Covalent Organic Polymers in Heterogeneous Catalysis and Sensors

Ph.D. Thesis

By
SAYAN MAITI

Under the guidance of

Dr. Apurba K Das

DEPARTMENT OF CHEMISTRY
INDIAN INSTITUTE OF TECHNOLOGY INDORE
AUGUST 2020

Covalent Organic Polymers in Heterogeneous Catalysis and Sensors

A THESIS

*Submitted in partial fulfillment of the
requirements for the award of the degree
of*
DOCTOR OF PHILOSOPHY

by
SAYAN MAITI
Under the guidance of

Dr. Apurba K Das

DEPARTMENT OF CHEMISTRY
INDIAN INSTITUTE OF TECHNOLOGY INDORE
AUGUST 2020

INDIAN INSTITUTE OF TECHNOLOGY INDORE

CANDIDATE'S DECLARATION

I hereby certify that the work which is being presented in the thesis entitled **Covalent Organic Polymers in Heterogeneous Catalysis and Sensors** in the partial fulfillment of the requirements for the award of the degree of **DOCTOR OF PHILOSOPHY** and submitted in the **DEPARTMENT OF CHEMISTRY, Indian Institute of Technology Indore**, is an authentic record of my own work carried out during the time period from July 2015 to July 2020 under the supervision of **Dr. APURBA K. DAS,** Associate Professor, Department of Chemistry.

The matter presented in this thesis has not been submitted by me for the award of any other degree of this or any other institute.

24.02.2021

SAYAN MAITI

This is to certify that the above statement made by the candidate is correct to the best of my/our knowledge.

Dr. APURBA K. DAS

SAYAN MAITI has successfully given his Ph.D. Oral Examination held on **24.02.2021**.

Dr. Satyajit Chatterjee	Dr. Tapas Kumar Maji	Dr. Apurba K. Das
Signature of Chairperson (OEB)	Signature of External Examiner	Signature(s) of Thesis Supervisor
Date: 24.02.2021	Date: 24.02.2021	Date: 24.02.2021
Signature of PSPC Member #1	Signature of PSPC Member #2	Signature of Convener, DPGC
Date: 24-02-2021	Date: 24-02-2021	Date: 24-02-2021

Dr. Biswarup Pathak
Signature of Head of Discipline
Date: 24.02.2021

ACKNOWLEDGEMENTS

Dedicated to My
Beloved
Parents and family

Abstract

Synthesis and characterization of covalent organic polymers (COPs) have gained great attention due to their structural periodicity and high tunable porosity. COPs show versatile applications in various fields such as storage of greenhouse gases like carbon dioxide, efficient heterogeneous catalysts, sensors and energy storage devices. In the past few years, various monomeric units with different functionalities are used to synthesize COPs. The ordered structures in COPs with organized π electron systems and presence of heteroatoms in the COPs (especially N and O center) serve various purposes including electronic properties, heterogeneous catalysis and detection of metal ions in solution or solid state. The development of efficient heterogeneous catalyst for diverse organic reactions is a successful application of COPs that has gained momentum in recent past. Presently, the focus is on the development of different metal integrated COPs to increase the efficiency in various applications. COPs provide large surface areas, defined pore size, low framework density and high thermal stability which help to increase their applicability. With the choice of binding block units in the polymeric backbone, COPs can be functionalized differently with several functional groups. Functionalized COPs act as efficient heterogeneous catalyst, for various chemical, electrochemical and photoelectrochemical reactions. COPs are considered as one of the most promising materials for the detection and removal of toxic metals. COPs/COFs with various functionalities on their surface facilitates in gas sensing and adsorption properties. A two dimensional covalent organic polymer based chemiresistive gas sensor was also developed for the selective gas sensing.

The overall aim of the work described in the thesis is to understand the fundamental mechanistic aspects towards synthesis, characterization and several applications of COPs. The specific objectives are as follows:

- ➢ To design and synthesize several functionalized COPs.
- ➢ To check the catalytic activity of COPs on various

organic transformation reactions.

➤ To investigate the catalytic activity on the electrochemical reactions.
➤ To explore the ability of COPs in metal ions removal efficiency.
➤ To fabricate chemiresistive device with COP and to investigate the efficiency and selectivity of COPs towards toxic gas sensing.

1. Benzoselenadiazole-based Nanoporous Covalent Organic Polymer (COP) as Efficient Room Temperature Heterogeneous Catalyst for Biodiesel Production.

In chapter 2, we report the synthesis of benzoselenadiazole-based nanoporous covalent organic framework **COP-1** *via* Sonogashira coupling reaction and **COP-2** functionalized with SO_3H group through HSO_3-Cl treatment with **COP-1**. The solid heterogeneous catalyst **COP-2** endows the synthesis of biodiesel *via* esterification of free fatty acids at room temperature at a faster rate. Solid-state ^{13}C NMR and FT-IR spectroscopic data confirm the synthesis of **COP-1** and **COP-2**. **COP-1** and **COP-2** show nanoporous structure with surface area of 471.8 and 158.66 m^2 g^{-1} and pore size of 11.42 nm and 4.49 nm. The sulfonated nanoporous **COP-2** shows excellent catalytic property in the esterification of fatty acids with TON 83.33 and 100% yield.

2. Picolinohydrazide Based Covalent Organic Polymer for Metal Free Catalysis and Removal of Heavy metals from Waste Water

In chapter 3, a picolinohydrazide based covalent organic polymer (**COP-3**) is synthesized. The **COP-3** acts as an efficient catalyst towards Knoevenagel reaction between aromatic aldehydes and malononitrile at 30 °C. Apart from the catalysis, **COP-3** could efficiently remove Hg^{2+}, Ca^{2+}, Cd^{2+}, Cu^{2+} and Pb^{2+} ions from waste water with adsorption capacity of >600 mg g^{-1}. Among these metals, Hg^{2+} is chosen for detailed adsorption study. XPS, Raman spectroscopy, solid state UV-Vis and density functional theory (DFT) were performed to investigate the detailed interactions between Hg^{2+} and **COP-3**. From the various studies, it can be summarized that the pyridine groups of **COP-3** are involved in non-covalent interactions with Hg^{2+}. Multifunctional **COP-3** is also responsible for removal of various other metal ions in a broad spectrum.

3. Covalent Organic Polymer as Hydrogen Sulfide Gas Sensor at Room Temperature

In chapter 4, a hydrazide based covalent organic polymer (**COP-4**) having pyridine groups has been used to fabricate efficient chemosensors for the detection of gaseous H_2S at 25 ºC. **COP-4** acts as an efficient chemiresistive H_2S gas sensor. Gas sensing behavior of **COP-4** has been measured in a dynamic flow through resistance measurement system. Enhancement of resistance has

been assigned to confirm H_2S sensing behavior of **COP-4**. Maximum response to 200 ppm of H_2S is found as > 50% at 25 °C. The **COP-4** fabricated sensor shows lower responsive time of 9 s with recovery time of 12 s respectively, when experiment has been with the H_2S concentrations of 200 ppm. It also shows high selectivity to H_2S gas compared to CO_2, NH_3, CO and NO_2.

4. Electrochemically Facile Hydrogen Evolution Using Ruthenium Encapsulated Two Dimensional Covalent Organic Framework (2D COF)

In chapter 5, a two dimensional crystalline ruthenium ion encapsulated 2D COF (Ru@COF) have been prepared from a synthesized COF. Here an electrochemical hydrogen evolution reaction using Ru@COF as electrocatalyst is performed. Moreover, Ru@COF shows better electrochemical hydrogen evolution reaction (HER) activity compared to bare $RuCl_3$ and COF. The HER activities are measured in 1.5 M H_2SO_4 medium. Ru@COF shows onset potential 159 mV with the Tafel slope of 79 mV dec^{-1}. The linear Tafel plot with the slope 79 mV dec^{-1} indicates Volmer-Heyrovsky-Tafel mechanism for the Ru@COF catalysed HER. COF plays a crucial role in maintaining stability and catalytic efficiency of the material. Interestingly, Ru@COF acts as an exemplary electrocatalyst material that is used as solid binder-free cathodic electrode on glassy carbon electrode surface.

List of Publications.
1. **Maiti**, **S**.; Roy Chowdhury, A.; Das, A. K. Benzoselenadiazole-Based Nanoporous Covalent Organic Polymer (COP) as Efficient Room Temperature Heterogeneous Catalyst for Biodiesel Production. *Microporous Mesoporous Mater.* **2019**, *283*, 39-47 (DOI: org/10.1016/j.micromeso.2019.03.046). (IF: 4.55)
2. **Maiti**, **S**.; Roy Chowdhury, A.; Das, A. K. Electrochemically Facile Hydrogen Evolution Using Ruthenium Encapsulated Two Dimensional Covalent Organic Framework (2-COF). *ChemNanoMat*, **2019**, *6*, 99-106 (DOI: org/10.1002/cnma.201900499) (IF: 3.38).
3. Roy Chowdhury, A.; **Maiti**, **S**.; Mondal, A.; Das, A. K. Picolinohydrazide Based Covalent Organic Polymer for Metal Free Catalysis and Removal of Heavy Metals from Waste Water. *J. Phys. Chem. C* **2020**, *124*, 7835–7843. (IF: 4.18)
4. **Maiti**, **S.**; Mandal, B.; Sharma, M.; Mukherjee, S.; Das, A. K. Covalent Organic Polymer as an Efficient Chemosensor For Highly Selective H_2S Detection Through Proton Conduction. *Chem. Commun.*, **2020** (Just accepted), DOI: 10.1039/D0CC02704A (IF: 5.99) .
5. **Maiti**, **S**.; Jadhav, R. G.; Mobin, S. M.; Mukherjee, T. K.; Das, A. K. Insights into the Aggregation Behaviour of Benzoselenadiazole-based Compound and

Generation of White Light Emission. *ChemPhysChem*, **2019**, *20*, 2221- 2229 (DOI: org/10.1002/cphc.201900476). (IF: 3.14)

6. Aaryashree.; Mandal, B.; Bhardwaj, R.; **Maiti**, **S**.; Sharma, D. S.; Das, A. K.; Mukherjee, S. Functionalized Oligo (p-phenylenevinylene) and ZnO based Nanohybrid for Selective Ammonia Sensing at Room Temperature. *IEEE Sensors J.* **2019**, *19*, 2847-2854 (DOI: 10.1109/JSEN.2018.2890092). (IF: 3.076)

7. Biswas, A.; **Maiti**, S.; Kalaskar, D. M.; Das, A. K. Redox Active Dynamic Self-Supporting Thixotropic 3D-Printable G-Quadruplex Hydrogel. *Chem. Asian J.* **2018**, *18*, 3928-3934 (DOI: org/10.1002/asia.201801409). (IF: 4.06)

8. Konda, M.; Jadhav, R. G.; **Maiti**, **S**.; Mobin, S. M.; Kauffmann, B.; Das, A. K. Understanding the Conformational Analysis of Gababutin Based Hybrid Peptides. *Org. Biomol. Chem.* **2018**, *16*, 1728-1735 (DOI: org/10.1039/C8OB00035B). (IF: 3.49)

9. Konda, M.; **Maiti**, **S**.; Jadhav, R. G.; Das, A. K. Redox-Active Peptide Functionalized Quinquethiophene Based Electrochromic π-gel. *Chem. Asian J.* **2018**, *13*, 204-209 (DOI: 10.1002/asia.201701460). (IF: 4.06)

10. Aaryashree, Sharma, P.; Mandal, B.; Biswas, A.; Manna, M. K.; **Maiti**, S.; Das, A. K.; Mukherjee, S. Synergetic Accrual of Lamellar Nano-Hybrids for Band-Selective Photodetection. *J. Phys. Chem. C*, **2017**, *121*, 14037-14044 (DOI: org/10.1021/acs.jpcc.7b04219). (IF: 4.18)

11. Jadhav, R. G.; Kumar, A.; Kumar, S.; **Maiti, S**.; Mukherjee, S.; Das, A. K. Benzoselenadiazole- Based Conjugated Molecules: Active Switching Layers with Nanofibrous Morphology for Nonvolatile Organic Resistive Memory Devices. *ChemPlusChem*, **2020**, *85*, 910-920. (DOI: org/10.1002/cplu.202000229). (IF: 2.75

12. Mandal, B.; **Maiti, S**.; Aaryashree, Siddharth, G.; Das, M.; Agarwal, A.; Das, A. K.; Mukherjee, S. Organo-di-benzoic-acidified ZnO nanohybrids for highly selective detection of CO at low temperature, *Journal of Physical Chemistry C* **2020**, *124*, 7307-7316. (DOI: org/10.1021/acs.jpcc.0c01044). (IF: 4.18)

Published Book Chapter

1. Das, A. K.; **Maiti**, **S**.; Roychowdhury, A. Light Induced Porous Organic Polymers: Design, Synthesis and Function, 2019, ISBN: 978-1-925823-24-0, Central West Publishing, Australia.

Conference Presentation

1**. Maiti, S**.; Das, A. K. Exploration of Peptide Self-assembly for the Fabrication of Photodetector and Electrochromic Devices, *sIPS-2018* A satellite symposium on Peptides in Biology and Material Science. (Shankarpur, west Bengal, India, 22 Feb, 2018 to 24 Feb, 2018)

Number of patent(s)/ patent applications

Mukherjee, S.; Das, A. K.; Agarwal, A.; Mondal, B.; Aaryashree, **Maiti**, **S**. Organo-Acidified Zinc Oxide Carbon Monoxide Gas Sensor. Patent Application Number. 201921026594, July 3, 2019.

Table of Contents

x

List of Schemes

ACRONYMS

Abbreviations used for chemicals, polymers and reagents are largely in acoordance with the recommendations of the IUPAC-IUB commission on Biochemical Nomenclature, 1974, Pure and Applied Chemistry, 40, 315-331. Additional abbreviations used in this thesis are listed below.

$CDCl_3$	Chloroform-d
DCM	Dichloromethane
DCC	Dicyclohexylcarbodiimide
DMSO	Dimethyl sulfoxide
DMF	Dimethyl Formamide
EtOAc	Ethyl Acetate
ESI-MS	Electrospray Ionization Mass Spectrometry
FTIR	Fourier Transform Infrared Spectroscopy
HCl	Hydrochloric Acid
HBA	4-Hydroxybenzyl Alcohol
MeOH	Methanol
Me	Methyl
M	Molar
NaCl	Sodium Chloride
NaOH	Sodium Hydroxide
$NaHCO_3$	Sodium Hydrogen Carbonate
NMR	Nuclear Magnetic Resonance
Ph	Phenyl
pH	The negative logarithm hydrogen-ion activity (-log10 $[H_3O^+]$)
PXRD	Powder X-ray Diffraction
SEM	Scanning Electron Microscope
TEM	Transmission Electron Microscope
TFA	Trifluoroacetic acid
THF	Tetrahydrofuran
TLC	Thin Layer Chromatograpy
TON	Turnover numbers

TOF	Turnover frequency
UV-Vis	UV-Visible Spectroscopy
ICP-AES	Inductively coupled plasma atomic emission spectroscopy
TGA	Thermogravimetric analysis
DSC	Differential Scanning Calorimetry
COF	Covalent organic framework
COP	Covalent organic polymer

NOMENCLATURE

θ	Angle
λ	Wavelength
α	Alfa
β	Beta
Å	Angstrom
nm	Nanometer
δ	delta
μm	Micrometer
π	Pi
σ	Sigma
γ	Gamma
μM	Micro molar
ppm	Parts per million

Chapter 1
Introduction

1.1 Background of covalent organic polymers (COPs).

Covalent organic polymers (COPs) are constructed by the strong covalent bonds between the organic secondary building block units (SBUs) through light elements such as carbon, nitrogen, oxygen, boron and sulfur atoms with high permanent porosity.[1-2] Secondary building units are assembled to generate porous polymeric network (Figure 1.1). Several number of porous polymeric structures can be constructed through various SBUs combinations which generate different material properties for various applications. Recently, COPs have been given a great attention in numerous applications due to its high chemical stability, enough surface area, tunable porosity and low framework density. Configuration of polymeric structure can be controlled by the tuning of the physiochemical properties of the building-block molecules.[3] This characteristic can be utilised in various applications. Here, we demonstrate various approaches to synthesize COPs. We characterize COPs using several spectroscopic and microscopic techniques. In this regard, COPs have been found to be a promising material in heterogeneous catalysis, gas adsorption, energy conversion, chemical vapour sensing, metal ions removal, gas separation, bioimaging, optoelectronics, energy storage and drug delivery.
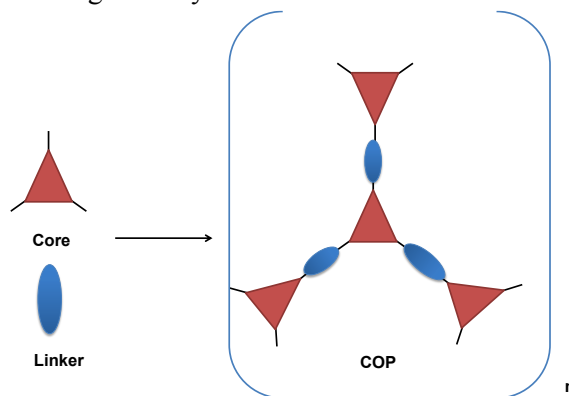
Figure 1.1 Pictorial representation of covalent organic polymer.

1.2 Design of the Secondary Building units and Synthesis.

Researchers are continuously finding the different ways to synthesize a wide varieties of COPs. However, it is very challenging task to construct porous organic polymer with discrete pores. After that, the term of reticular chemistry was introduced to synthesize COPs which uses topologically designed building block to synthesis these extended porous polymeric materials. To get a well ordered COP, the molecular structure of the SBUs needs two requirements: (1) the reaction for synthesizing COPs should be a reversible, and (2) the geometry and the properties of the SBUs should be well retained in the COPs backbones. Several reversible reactions have been developed for COP synthesis. A majority of the COPs rely on, -C-C- coupling, -C-N- coupling, (-C=N-) bond and boronate ester linkages (Figure 1.2).
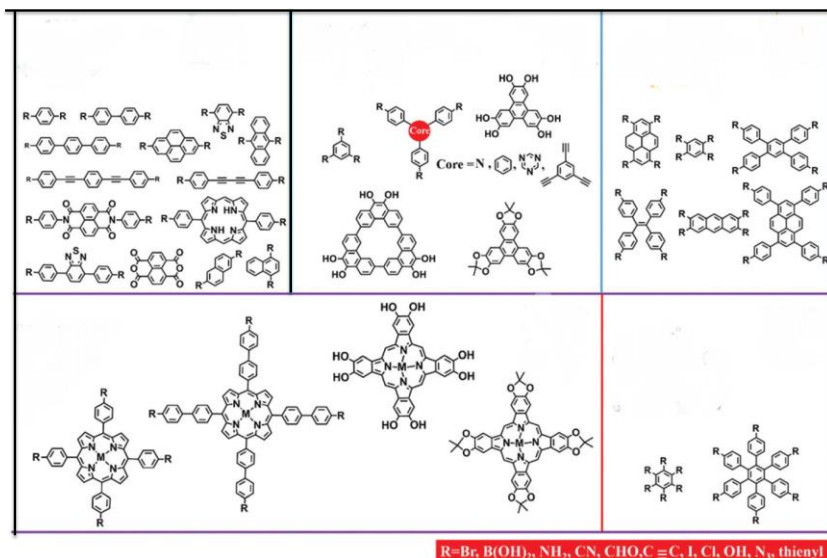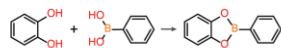
3
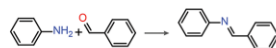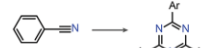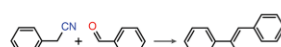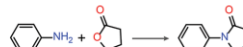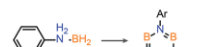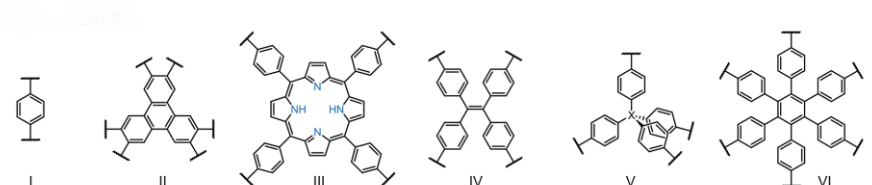
Figure 1.2 The representative molecular structures of the building blocks and linkers.

1.3 Classifications of COPs.

Based on the amorphous and crystalline nature, COPs can be classified into two part. More specifically crystalline COPs can be called as covalent organic frameworks (COFs). Generally, COFs are two-dimensional (2D) and three-dimensional (3D) pure organic solid in which monomeric units are linked by strong covalent bonds through light atoms. The irregular and uncontrolled linking of building units are resulting in amorphous COPs. The synthetic procedures are comparatively easy. Although, it is very difficult to maintain the high ordered symmetry throughout the reaction process to get the crystalline COPs.

1.4 Synthetic Methods.

COPs can be constructed through several well known reactions such as Suzuki - C-C- coupling, Schiff base, Heck coupling, Sonogashira coupling, Ulman coupling and radical type reactions. Dai *et al.* developed a sulfonamide polymer by capturing atmospheric sulfur dioxide (Figure 1.3) through the amine based monomers.[4] Recently, researchers are interested in developing COPs by light-induced photochemical reactions that are directly catalyzed by photons. Covalent organic polymers can be formed through the bond fission and bond fussion that is induced by the visible and UV light irradiation.
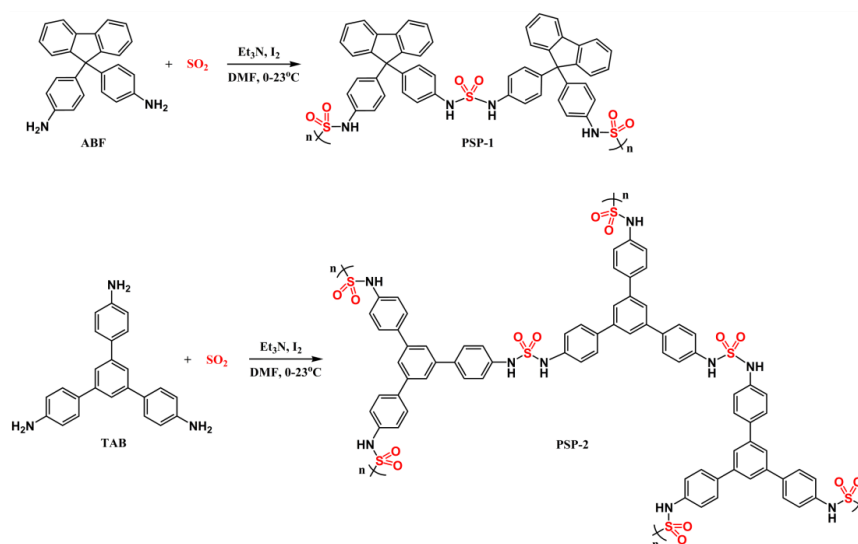
Figure 1.3 The preparation of porous sulfonamide polymers from amine precursors and SO_2 (1 bar).[4]

The first law of photochemistry describes the light mediated photochemical reactions. In addition, photochemical processes are specifically catalyzed by photons. Porous organic polymers are also produced from their corresponding monomers using co-ordinated and non-covalent interactions.[3-6] An efficient method was developed to obtain COPs (Figure 1.4) by the nickel(0)-catalyzed Yamamoto-Ullmann cross-coupling reaction.[7-9]
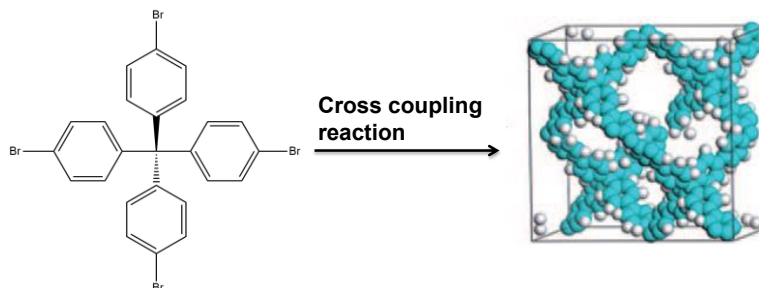
Figure 1.4 Synthesis of the microporous polymer network PAF-1 by a Yamamoto cross-coupling reaction.[8]

Recently, both Ben *et al.*[10-11] and Yuan *et al.*[12] developed a series of aromatic covalent organic polymers using a tetrahedral monomer, tetrakis(4-bromophenyl) methane (TBM) with exceptional high stability and porosity (Figure 1.5). These results inspired all material scientists to integrate TBM type T_d symmetry as a monomeric center for the tunable organic covalent polymers. Sometimes, the long linkers between two monomeric building block units generate other topologies that leads to less stability and porosity.

1.5 Choice of linkage.

Secondary building blocks are connected to each other *via* imine, azine, -C-C-, hydrazine, boronate ester, thiazole, triazine, diazine ring formation and -SO$_2$ linkers. Experimental environments require difficult conditions. The polymerization reactions are performed in a sealed pyrex tube or round bottom flask with long reaction times. Optimization of temperature is one of the crucial parameters to assure the reversibility of the polymerization reaction. In addition, ratios of the precursors and solvent combinations chosen for the condensation reactions are also the key parameters for scalable synthesis of polymers.

1.5.1 Imine linkages.

Huge number of COPs have been constructed using Schiff-base reaction. More specifically, they are enough stable in most of organic solvents, aqueous, acidic and basic conditions. The heteroatoms within the polymeric backbones facilitates in coordination with the metals ions. These properties provide the imine-based COPs with high potential in further applications. Choice of solvents is one of the important features in Schiff base reactions. Mesytilene/dioxane/AcOH are suitable solvent combinations for polymerization reactions. Certain solvent systems, such as dioxan/acetic acid and n-butanol/*ortho*-dichlorobenzene/acetic acid, have also been commonly used. The catalyst, usually acetic acid, plays a key role in the formation of polymers. Furthermore, in order to improve chemical stability, some researchers are preserving the inner portion of the polymer by adding H-bonded groups such as-OH,-SH.[13-14] A self-templated synthesis methods, utilizing H-bonding interactions has been developed to synthesize DhaTab COPs utilizing Schiff base reactions.[15] Highly organized COPs were developed due to H-bonding interactions between the functional imine and the hydroxyl groups. Thus, Jiang and coworkers developed porphyrine based imine-linked covalent organic polymers (Figure 1.6).[16] The interlayer interactions in COP layer increases with incorporation of the fluoro-substituted arenes into the building block units. In 2009, Yaghi *et al.* synthesized a diamond-like highly crystalline covalent organic polymer by Schiff base condensation reaction which was first of its kind.[17]

1.5.2 Hydrazone Linkages.

In 2011, the goal was to expand the spectrum of organic polymeric materials content that could be accomplished across a number of linkages.
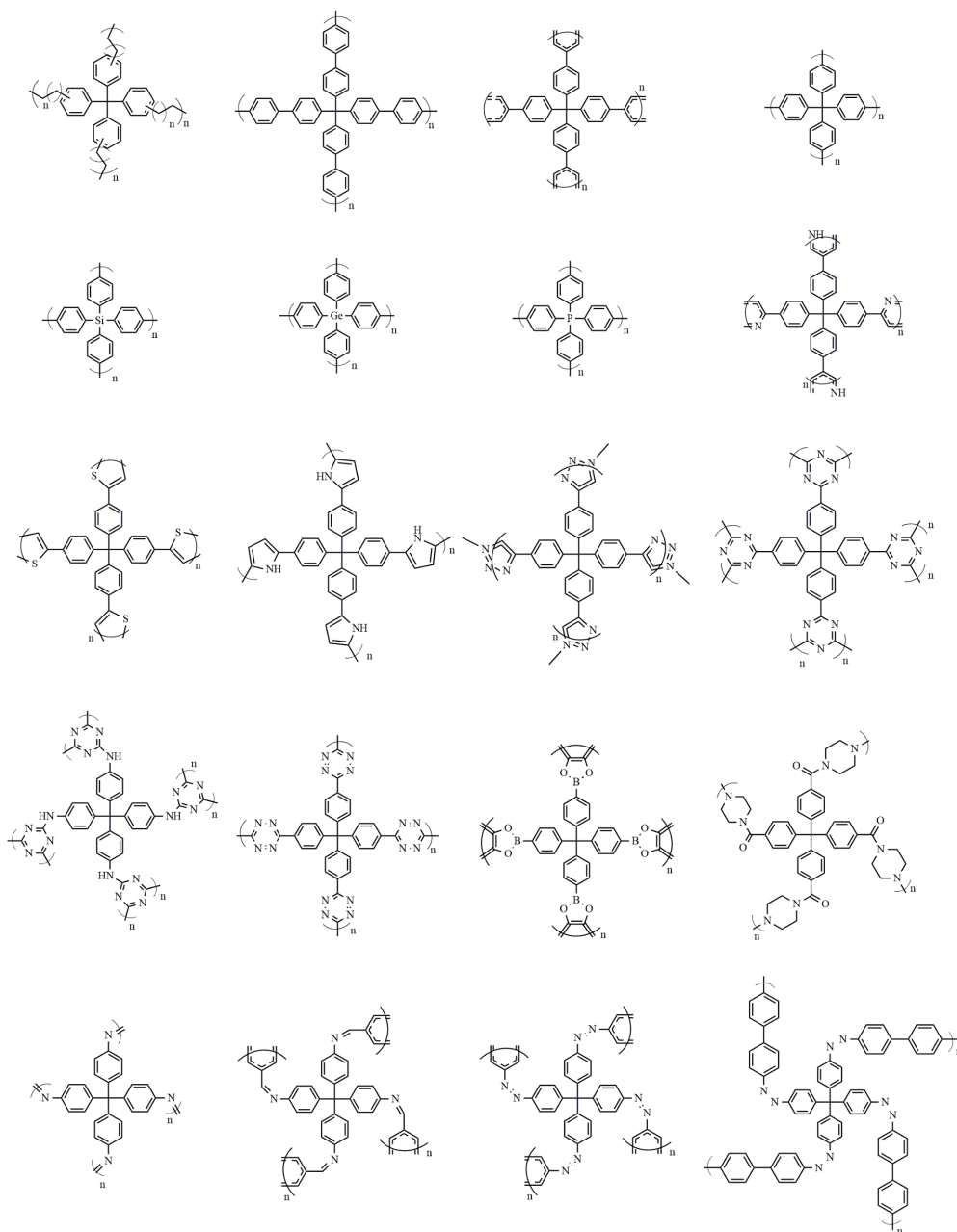
Figure 1.5 The structural summary of COPs with tetrahedral monomers and its derivatives.

Dichtel *et al*. synthesized a hydrazine based bulk exfoliated covalent organic polymer (COF-43) using aldehyde and hydrazine based building blocks with extra stability (Figure 1.7).[18]
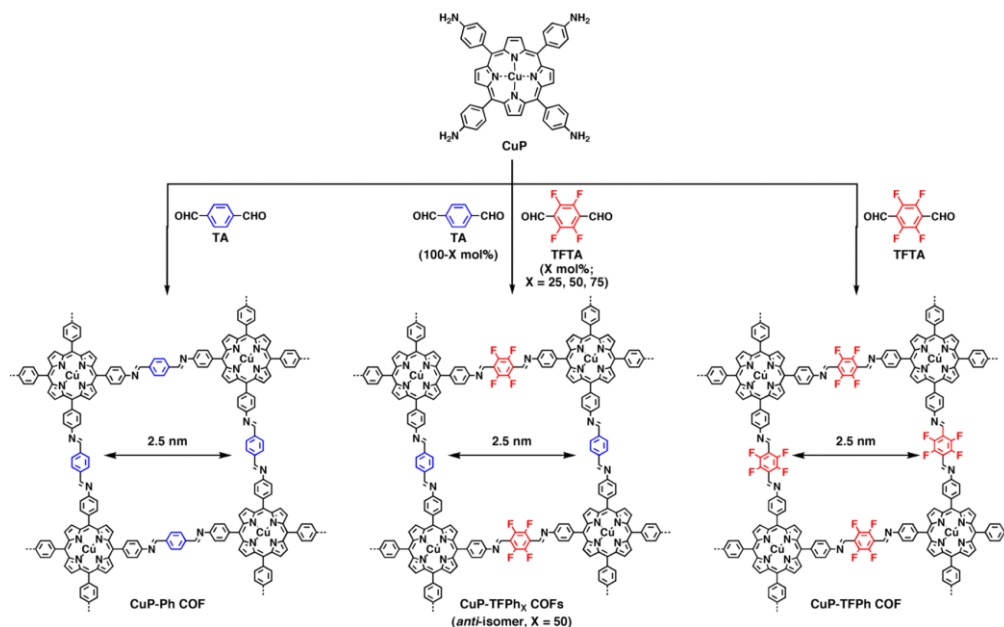
Figure 1.6 Porphyrine based imine-linked covalent organic polymers.[16]
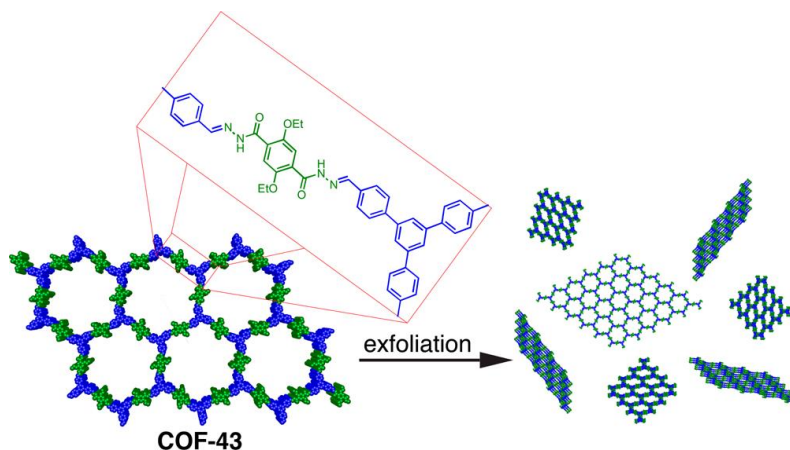
Figure 1.7 Exfoliation of COF-43 yields a suspension of few-layer 2D polymers.
[18]

Yaghi *et al*. reported scalable synthesis of COPs with hydrazone functionality as strong organic linkage.[19] COP based on hydrazine linkage was synthesized by easy condensation reaction of 2,5-dimethoxyterephthalohydrazide with 1,3,5-triformylbenzene under reflux conditions.[20] Commercially available hydrazine (2,5-diethoxyterephthalohydrazide) and (1,3,5-triformylbenzene, or 1,3,5-tris(4-formylphenyl)- benzene give strong hydrazone-linked structures. In order to promote activation in polymerization reaction, it is important to increase the solubility of the monomeric unit part. Interestingly hydrazones are more thermodynamically stable and less prone to hydrolysis than imine bonds. Stable hydrazines are typically built in acetic acid-catalyzed reversible condensation

reactions of the building blocks in dioxane/mesitylene (1:2) at 120 ºC in a sealed pressure vial under inert atmosphere at 72 h. In fact, acylhydrazones as linkages can promote thermal and hydrolytic stability. Hydrazone bonds can also be synthesized (Figure 1.8) by pure water.[21]
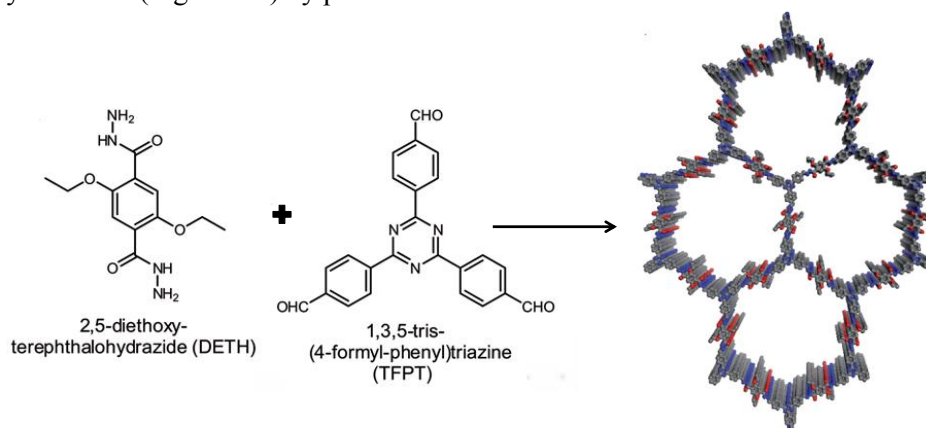
Figure 1.8 Showing the condensation of the two monomers to form the TFPT-COF.[21]

Banerjee *et al.* developed a methodology for the construction of hydrazine based COPs at a faster rate and in high yield, using liquid-assisted grinding (LAG) method.[22] Wu *et al.* a developed a stable hydrazine linkage-based (TFB-COF) polymer under solvothermal conditions.[23]

1.5.3 Azine Linkages.

Azine functionality is another significant linkage for the formation of COPs. Jiang *et al.* reported in 2013, the synthesis of a highly stable azine linked COP (Py-Azine COF) by condensation between hydrazine and 1,3,6,8-tetrakis(4-formylphenyl)pyrene (Figure 1.9).[24]
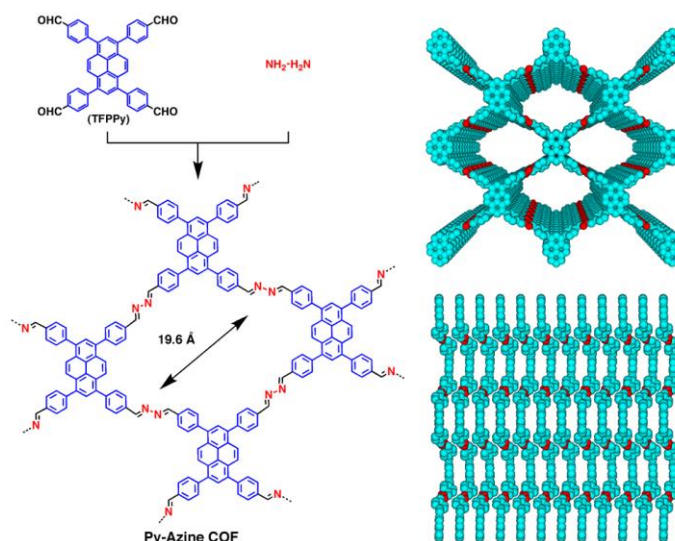
Figure 1.9 Synthetic scheme of the Py-Azine COF.

Thermodynamically stable azine bond is formed from hydrazine with aldehyde derivatives and water as by-product. Azine containing COPs exhibit robust chemical stability. *ortho*-dichlorobenzene (*o*-DCB), *o*-DCB/n-BuOH, 1,4 dioxane/mesitylene and 1,4 dioxane/*o*-DCB have commonly been used in the synthesizing of polymers in the presence of an acid catalyst.[25-27] Caro *et al.* presented a azine linked polymer (ACOF-1) which was synthesized on a porous support using solvothermal reactions.[28]

1.5.4 Phenazine linkages. To find out the new linkages, Jiang *et al*. synthesized phenazine-linked polymer (CS-COF), using C3-symmetrical triphenylene hexa (TPHA) and C2 symmetrical tertbutylpirene tetraone (PT) as monomeric units (Figure 1.10). Phenazine linkages based COPs allow to form nanowire like morphology and create nanochannels.[29]
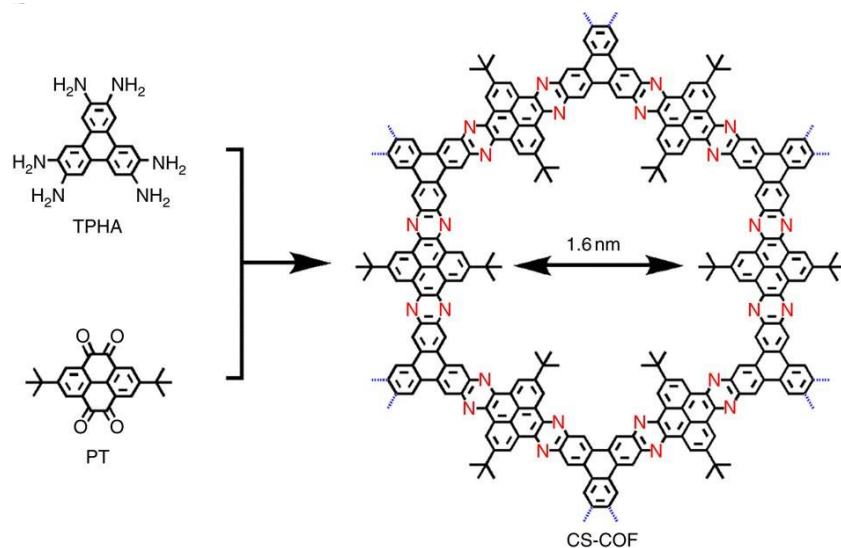
Figure 1.10 Schematic representation of the synthesis of CS-COF.[29]

Phenazine based conjugated polymers have extended π-delocalization which facilitate to interact with guest molecules and hole mobility. This unique nature of phenazine based polymer is useful for high electronic, optoelectronic and photovoltaic cells. Therefore, this phenazine center can constitute the organized semiconducting polymeric materials.

1.5.5 -C-C- linkages.
Suzuki cross-coupling and Yamamoto reaction are very common reaction for the polymerization reaction *via* -C-C- bond formation.[30-35] Cao *et al.* synthesized a porous luminescent COP through self-polycondensation of the monomer units of tris(4-bromophenyl)amine, 1,3,5-tris(4- bromophenyl)benzene, and 2,4,6-tris-(4-bromo-phenyl)-[1,3,5]triazine, using Ni-catalyzed Yamamoto reaction. Zhao *et al*. developed covalent organic polymers (PAF-1) through Yamamoto homo-

coupling reaction, using tetrahedral tetrakis(4-bromophenyl)methane monomeric unit. Cao *et al.* synthesized a series of COPs using Yamamoto coupling from the 1,3,5-tris((4-bromophenyl)ethynyl) benzene. After that researchers constructed COPs using (Figure 1.11) Sonogashira Hagihara coupling reaction.[36-37] Copper *et al.* synthesized few COPs (CMP-1 to CMP-5) from 1,3,5-triethynylbenzene and 1,4-dihalobenzene derivatives. A hypercrosslinked COP was synthesized *via* oxidative reaction using resin precursor.[38] Researchers also synthesized a wide range of COPs through Friedel Crafts arylation reaction under microwave or heating conditions.[39]
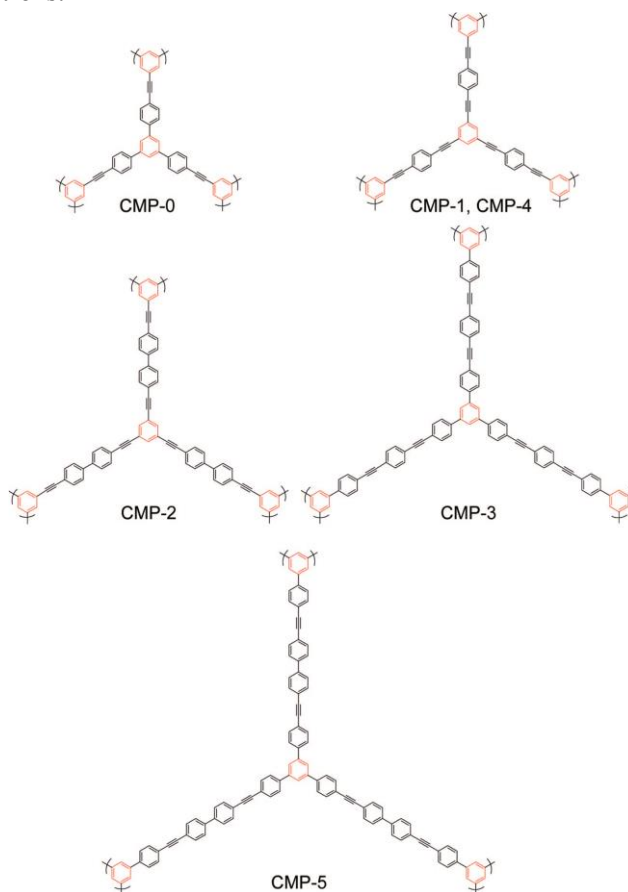
Figure 1.11 Construction of COPs through -C-C- coupling reactions.[36-37]

1.5.6 COPs formation through Topochemical transformations.

Stabilization of COPs is always a crucial feature in polymeric networking system. Very recently, post-synthetic locking strategies have been adopted to overcome all the obstacles towards stability issues. Lotsch *et al.* synthesized stable and highly crystalline thiazole based COF from imine linked COF *via* topochemical conversion of imine bonds. This post-synthetic modification enhanced electron beam stability which helps in investigation of the real framework structure.[40] Guo *et al.* synthesized a highly crystalline fibrous COF through the reversible imine linkage exchanging.[41] Liu *et al.* synthesized a

ultrastable COF *via* transformation of an imine based covalent organic framework.[42]

1.6 Synthetic route to synthesize COPs.

Synthesis methods of COPs are generally reversible in nature. High reversibile condition of the reaction pathway of COPs makes several difficulties in polymer formation. Therefore the successful synthesis of polymers with the desire polymeric backbones remains as a great challenge. In this regards, there are mainly five different synthetic methods for synthesize of COPs. These are, (i) solvothermal, (ii) ionothermal, (iii) microwave assisted synthesis, (iv) mechanochemical pathways, and (v) light assisted synthesis.

```
┌─────────────────────────────────┐
│     Synthetic methods of COPs    │
└─────────────────────────────────┘
```

| Solvothermal | Ionothermal | Mechanochemical synthesis | Microwave assisted synthesis | Light assisted synthesis |
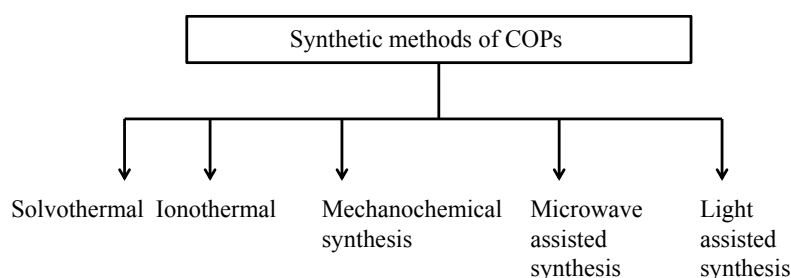
The above mentioned methods are widely used to synthesize COPs. Inspite of this, researchers developed several new methods to synthesize COPs. Banerjee *et al.* suggested a unique way to make ultrastable, solution-processable porous COPs from the homogeneous solution of amine and aldehyde through slow nucleation and growth process.[43]

1.6.1 Ionothermal process.

Ionothermal method serves a opportunity to get better polymeric materials. Thomas *et al.* synthesized a triazine based polymers by using $ZnCl_2$ as catalyst at 400 °C.[44] The COP material in this methods shows higher thermal stability. Although this method is not developed in broad spectrum due to its inability to construct regular ordered structure. Lotsch *et al.* synthesized a highly crystalline perylene based porous COF *via* ionothermal methods in presence of zinc chloride and eutectic salt mixtures. The reaction time is remarkably low compared to solvothermal methods.[45] Qiu *et al.* synthesized a series of ionic liquid (IL)-containing COFs (3D-IL-COFs) by using ionothermal method.[46] All reactions were performed at ambient temperature and pressure where IL was reused without loss of activity. (Figure 1.12).

1.6.2 Microwave process.

Synthesis of COPs/COFs *via* microwave methods was first introduced by Cooper and co-workers.[47] This method is quite faster, more efficient and greener compared to other reported methods for synthesizng COPs. The COF-5 can be synthesized only in few minutes by this methods.[47] The surface area and other

properties of COF-5 were improved in case of microwave assisted synthesis. This method was served better porosity of the material. The calculated surface area of COF-5 was observed as 2019 m^2 g^{-1}. Interestingly, surface area of COF-5 was found to be 1590 m^2 g^{-1} in solvothermal process.
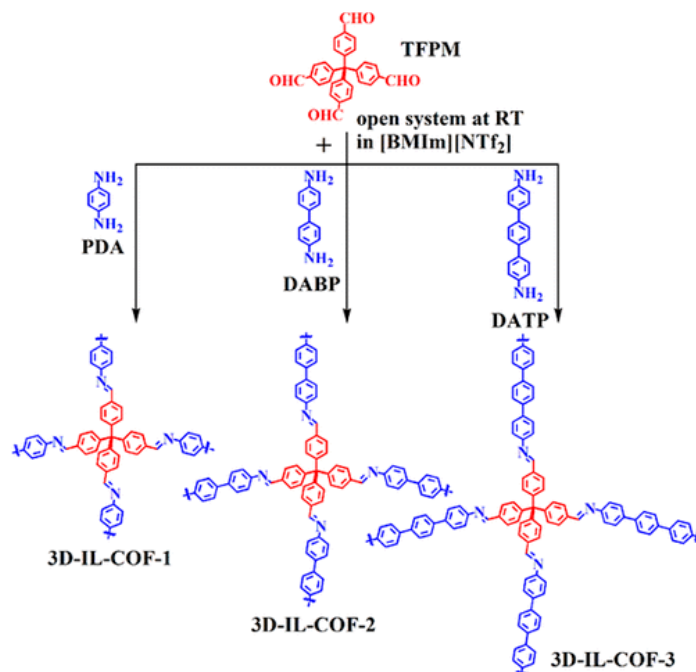
Figure 1.12 Synthetic strategy for synthesizing 3D ionic liquid-containing COFs.[46]

A two-dimensional enamine-linked COF was synthesized using microwave assisted solvothermal process from a 3:2 molar ratio solution of *p*-phenylenediamine and 1,3,5- triformylphloroglucinol solution in a solvent mixture of mesitylene/1,4-dioxane/3 M acetic acid (Figure 1.13).[48]
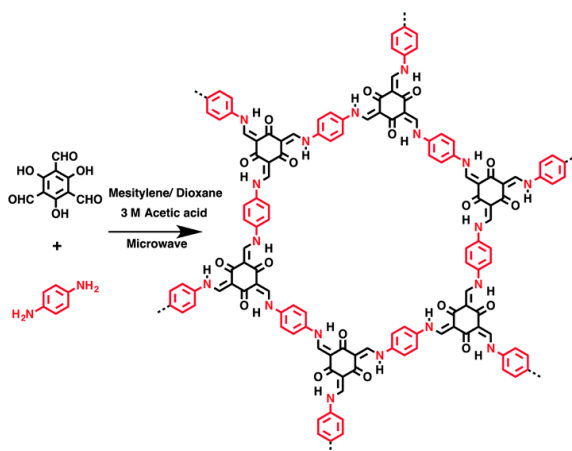
Figure 1.13 Synthetic scheme of TpPa-COF (MW).

Zhu *et al*. synthesized a highly fluorescent nanoparticles of melamine based COF (SNW-1) by using microwave-assisted synthesis method at 180 °C (Figure 1.14). The findings clearly showed that the microwave-assisted synthetic approach is a straightforward and highly effective technique for the processing of nanoscale porous COFs.[49]
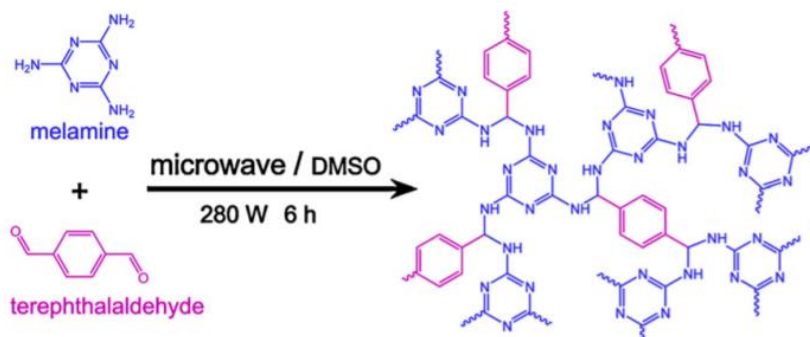
Figure 1.14 A schematic illustration melamine based polymeric network SNW-1 formation.[49]

1.6.3 Mechanochemical grinding.

Synthesis of COPs through mechanochemical grinding pathways has many advantageous steps. This is a very ancient concept that can be encouraged in a solid state reaction by utilizing limited quantities of monomers. Banerjee *et al*. reported few isoreticular COFs that were synthesized by mechanochemical method.[50-51] An amide bonds riched COF nanosheet clusture was synthesized by mechanical synthetic pathway *via* solid state reaction (Figure 1.15).[52] Dai *et al*. synthesized a pillar[5]quinone (P5Q) based multi-microporous organic polymers *via* solvent and catalyst-free mechanochemical process (Figure 1.16).[53]
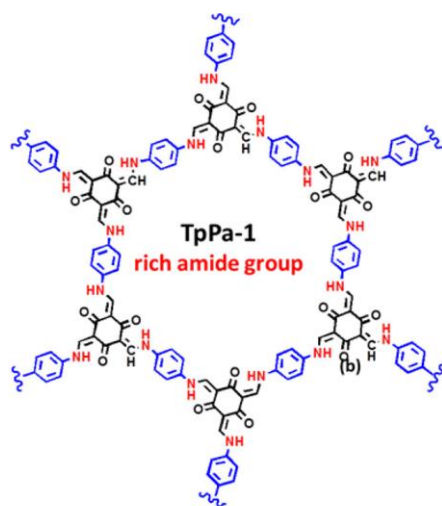
Figure 1.15 COF Structure with rich amide group.
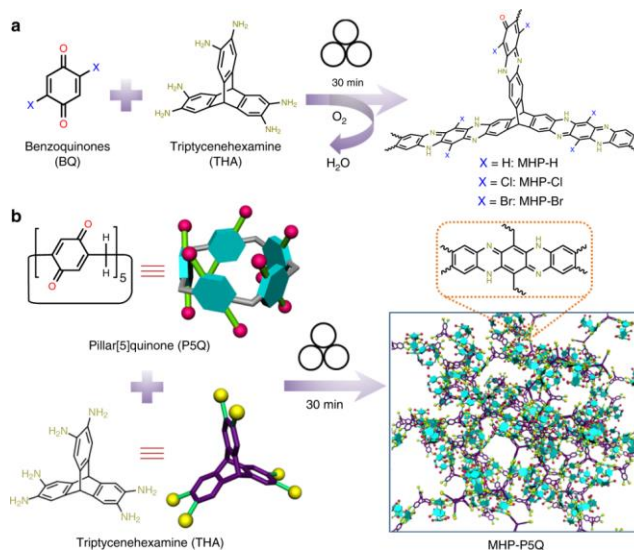
Figure 1.16 (a) Synthetic routes for synthesizing of MHP, MHP-Cl, and MHP-Br. (b) Synthetic scheme of the synthesis of MHP-P5Q using P5Q and THA.

1.6.4 Solvothermal process.

Solvothermal approaches for synthesizing COPs is a very well established strategy. In this process, all reactants are mixed together in a sealed tube such as an autoclave made-up of stainless steel at require temperature for few days. As per the literature report, 150 mTorr is the actual pressure that generates inside the vessel of 10 cm^3.[54] Solvothermal is controlled process over the shape, pore size and crystallinity of the polymers. After that Lavinge and co-workers developed a condensation process in presence of organic solvents under ambient pressure for synthesizing the COPs.[55] This method is very easier to handle and carry without using an autoclave. In context Dichtel *et al*. introduced a new solvothermal method to synthesize 2D COF using a single-layered graphene sheet as a template.[56] Kanatzidis *et al*. developed a series of microporous polymeric organic frameworks (POFs) through the solvothermal process.[57] The POFs were constructed from phlorglucinol and several aromatic benzaldehydes derivatives using Bakelite type chemistry.

1.6.5 Light assisted synthesis.

Choi *et al*. synthesized a two-dimensional (2D) covalent organic framework (COF) *via* the photon-assisted imine condensation reaction within 1 h.[58] Saito *et al*. developed organic polymer from bioinspired bis-thymine monomer through [2π + 2π] cycloaddition reaction.[59] Thymine is very sensitive towards light due to its isolated localized double bonds. Thymine core is very well familiar for the [2π + 2π] cycloaddition reaction under 270 nm UV light irradiation. Conjugated microporous polymeric thin film was developed[60] by light irradiation *via* free thiol-yne click coupling (TYC) reaction (Figure 1.17).[61]
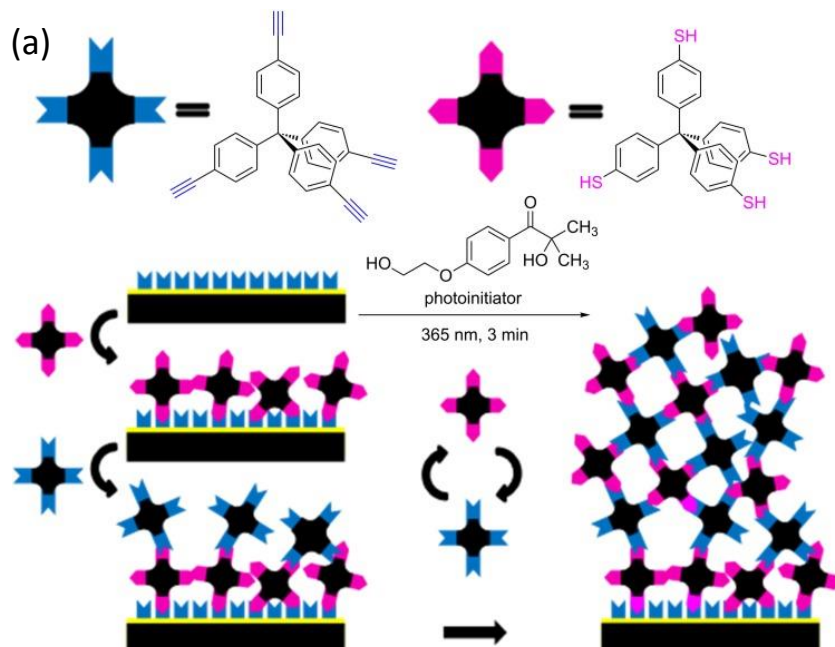
Figure 1.17 (a) Light assisted covalent organic polymer synthesis.

1.7 Characterization of COPs.

Several characterization techniques are adopted for synthesized COPs.
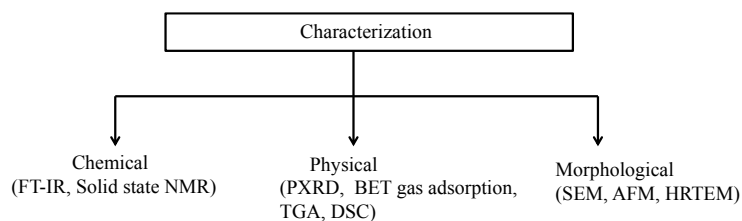
1.7.1 Fourier-transform infrared spectroscopy (FT-IR).

Primarily FT-IR stretching bands support the formation of polymer with desire connectivity of different linkages.

Few FT-IR stretching frequency of linkages are given in table 1.1

S.No	linkage	Streching frequency ($\overline{\nu}$ cm^{-1})	Ref.
1	HL-COP (-NH, -C=O, -C=N)	3429, 1672, 1549	62
2	TFTP-COF, (-C=N- bonds)	1670-1660, 1201-1210	63
3	TpDAB, -NH, -C=O, -C=C-	3100-3300, 1612, 1598	64
4	AB-COF, -C=N-	1620-1630	65
5	COF-66, -C=N-	1620 and 1249	66
6	COF-5, -B-O-, -B-C-, -C-O-	1347, 1026 and 1245	67
7	Am-MOP, -C=O, -NH	1664, 3270	68
8	POP-PU, -C=O, -N-H and C-N	1632, 3299, 1220	69

1.7.2 Solid state NMR.

Nuclear magnetic resonance (NMR) is a well familiar technique that allows us to identify the chemical environment of the chemical compounds. In general COPs are insoluble in deuterated NMR solvents. As a consequence, ^{13}C cross polarization magic angle spinning solid state NMR spectroscopy is appointed to identify the secondary building block units in polymeric network (Figure 1.18).[70]
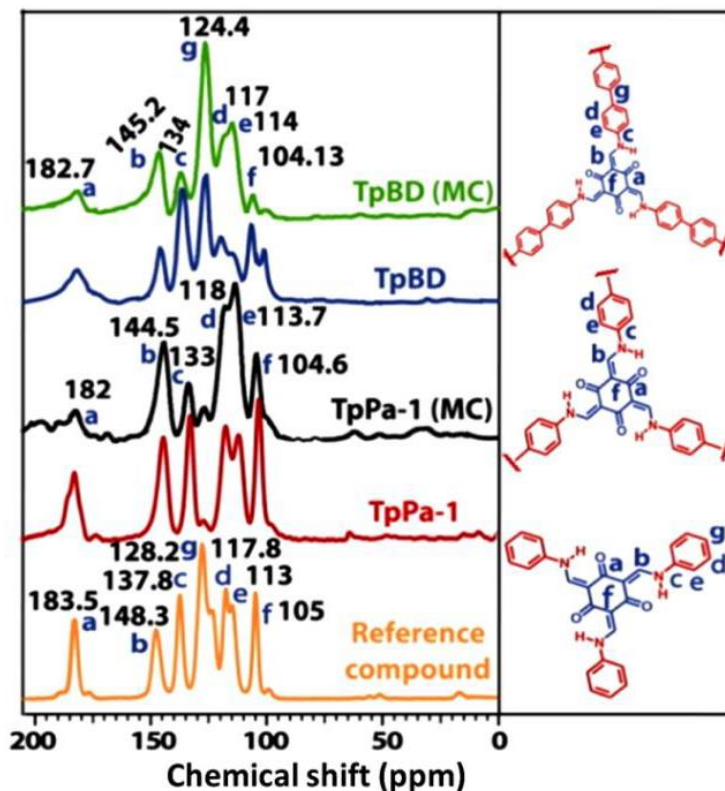
Figure 1.18 ^{13}C CP-MAS solid-state NMR spectra of COFs.

In contrast to solution state NMR, in solid state NMR there is no motion that leads to broading of the peaks and spectral resolution become poor. In solid state molecules do not tumble in all directions as they do in liquid state. As a result we will get broad and undetectable spectra. MAS (magic angle spinning) in solid state NMR removes a big extent of chemical anisotropy which can improve the spectral resolution. CPMAS provides better spectra as compared to MAS if sample molecule contains H atom attached with the carbon atom. Solid state NMR should be acquired if sample or system are not found to be suitable for solution state.

1.7.3 Powder XRD (PXRD).

Braggs law is used to explain interference the X-ray scattered by the crystal, powder or thin film samples.

$$AB+BC= 2dSin\theta=n\lambda$$

Where, the n= an integer

λ= Wavelength of the incident X-ray

d= is the interplannar spacing

In X-ray crystallography, wide angle X-ray scattering is the experiment of braggs peak scattered to the wide angles that causes the sub nanometer size structures. This experiment is commonly use to determine the crystalline nature of polymeric and fiberous compounds. In this technique a monochromatic X-ray radiation is used to generate a transmission diffraction pattern of a sample. PXRD is the fundamental physical characterization to distinguish the COPs. Broad structureless PXRD pattern assigns amorphous nature of COFs and sharp spectrum assigns crystalline nature of COPs (Figure 1.19 a and b).[71-72]
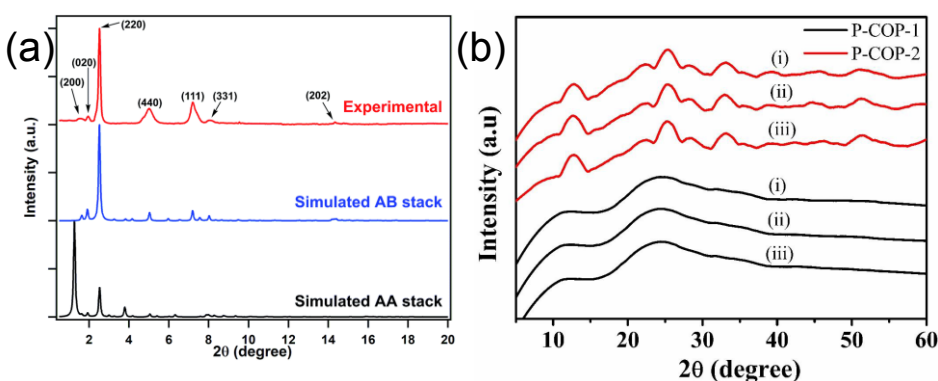
Figure 1.19 a) PXRD patterns of the PyVg-COF and b) P-COPs after treatment with (i) hot water, (ii) concentrated acid and (iii) base solutions.

1.7.4 Surface area analysis. To account the porous nature (specific surface area, pore size distribution and pore volume) of the polymers, (Brunauer, Emmett and Teller) BET surface area analysis experiment is performed. The specific surface area of a material is determined by amount of adsorption of a gas on the surface of the solid material and by calculating the volume of the adsorbate gas corresponding to the monomolecular layer on the surface. The quantity of gas adsorbed can be determined by a volumetric or continuous flow technique.

The BET equation

$$\frac{1}{W((\frac{P_0}{P}) - 1)} = \frac{1}{W_m C} + \frac{C - 1}{W_m C}(\frac{P}{P_0})$$

W= weight of gas adsorbed

P/P_0 =relative pressure

W_m = weight of adsorbate as monolayer

C = BET constant

This method involves adsorption-desorption process where liquid N_2 in general acts as adsorbate. Generally, the operative temperature is 77 K. The volume of adsorbed/desorbed liquid nitrogen in cc g^{-1} is plotted versus the relative pressure

to get the BET isotherm graph. Type- II and IV are quite common adsorption isotherms for COPs materials. Figure 1.20 shows different types of BET isotherms.[73] From the isotherm, the porosity can be calculated. Depending on the size of pores, COPs are classified as nano to macroporous nature.
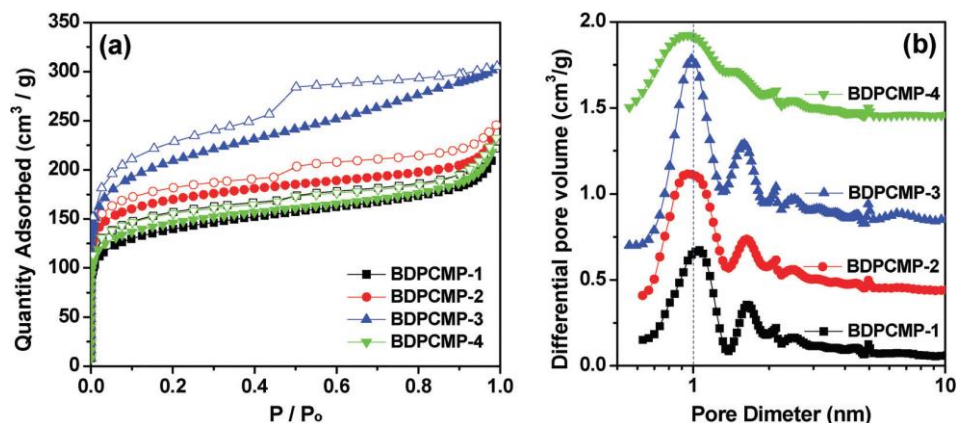
Figure 1.20 (a) Nitrogen adsorption /desorption isotherms of COP collected at 77 K. (b) Pore size distribution curves calculated by NLDFT methods.[73]

1.7.5 TGA (Thermogravimetric analysis).

Thermogravimetric analysis (TGA) measures weight shifts in a substance as a function of temperature (or time) in a regulated atmosphere. Its theory applies to the measurement of the thermal resilience of the substance, the composition of the polymer filler, the content of the moisture, residual solvent and the ratio of the components in the material.

The thermal stability of a molecule depends on the shape and size of a material or molecule, packing arrangement and intermolecular non covalent interactions (π-π or van der Waals interactions). Based on the above mentioned properties, the COPs exhibit exceptionally high thermal stability. TGA also allows us to understand the amounts of residual solvent or impurity present inside the pores of the COP materials (Figure 1.21).
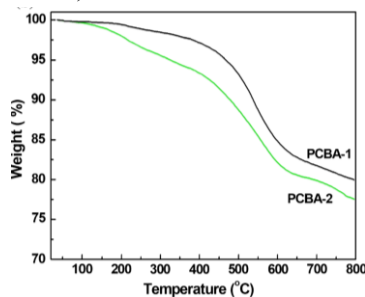
Figure 1.21 TGA plots of the obtained PCBA-1 and PCBA-2 polymers.[74]

1.7.6 Differential Scanning calorimetry (DSC).

Differential calorimetry scanning (DSC) is a very effective experimental tool for calculating the temperature differential between the sample and the reference

substance as a function of temperature. A specific temperature program is designed for DSC analysis such that the working temperature increases linearly as a function of time. Generally, DSC measures the phase transition temperature of the material such as the glass transition, melting, and crystallization. In addition, thermal curing, specific heat capacity, and purity analysis of chemical reactions are also measurable. Recently, with the development of the highly-functional polymeric material, DSC measurement is necessary to quantify the amount of heat on top (Figure 1.22).
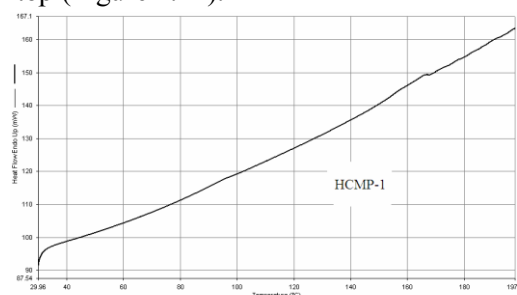
Figure 1.22 DSC measurement for polymer HCMP-1 (30–200 °C, 5 °C/min).[75]

1.7.7 Scanning electron microscopy (SEM) and Transmission electron microscopy (TEM).

The nanostructure and morphology of COPs were analyzed through scanning electron microscopy (SEM) and transmission electron microscopy (TEM) (Figure 1.23).[76] CSU-CPOPs-1 fomed a mulberry-like structure with honeycomb-like nanoparticles dispersed on the tubular surface. The nanotubes exhibited an average diameter of 25 nm with the length of 5 μm (Figure 1.23 a, b). Whereas CSU-CPOPs-2 exhibited a nanosheet (Figure 1.23 c and d). like morphology. SEM and TEM analysis of CSUCPOPs-3 indicated that its polymeric networks were made up by agglomerated of several nano spheres, which were connected through large and smooth nanotube-like structures (Figure 1.23 e,f). The anisotropic type morphology of COPs could be defined in terms of the geometry differences when forming the porous polymeric networks.
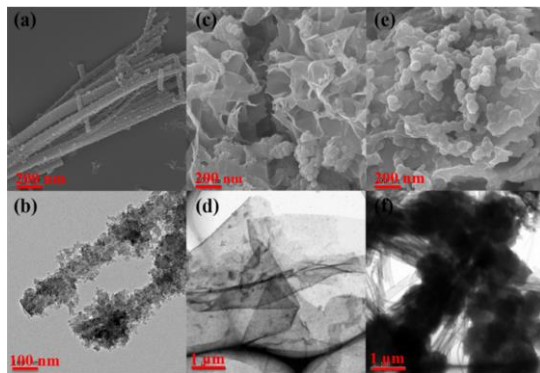
Figure 1.23 SEM images of (a) CSU-CPOPs-1, (c) CSU-CPOPs-2, and (e) CSU-CPOPs-3. Scale bar: 200 nm. TEM images of (b) CSU-CPOPs-1, (d) CSU-CPOPs-2, and (f) CSU-CPOPs-3. Scale bar: 100 nm and 1 μm.

1.7.8 Raman Spectroscopy.

Raman spectroscopy allows us to understand the interactions between COP and metal ions. POP-SH@Hg exhibited peaks at 276 and 290 cm^{-1}, (Figure 1.24) associated with the symmetric and unsymmetric Hg-S stretching vibrations.[77]
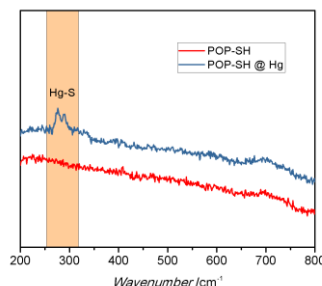
Figure 1.24 Raman spectra of POP-SH and POP-SH@Hg.[77]

1.7.9 Atomic force microscopy (AFM).

AFM measures the surface roughness of COPs and ascribe the reason for creating of hydrophobicity. The hydrophobicity of CPCMERI-1 is generated by formation of micro- as well as nano-level of surface roughness (Figure 1.25).[78]
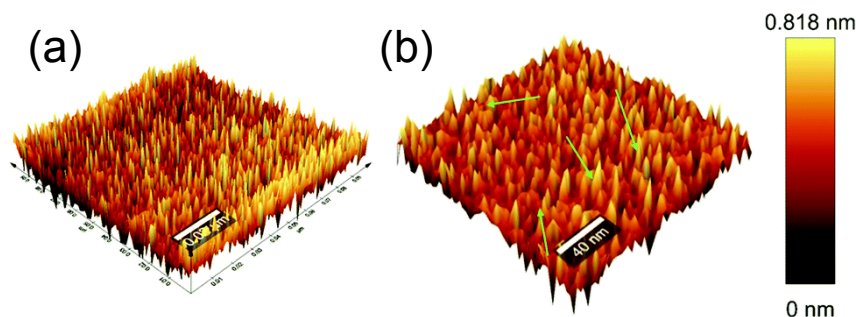
Figure 1.25 AFM Images of CPCMERI-1 (a) Micro scale image, and (b) nano scale image (with z-axis interpretation).

More importantly, Z-axis interpretation of AFM image of CPCMERI-1 shows several number of crests and troughs on the polymeric surface. The peaks are observed in the region of (0.5-1) nm which indicates the possibility of the presence of air pockets in-between the valley regions. This trapped air pockets make the polymer hydrophobic in nature.

1.8 Applications.

COPs exhibits a wide spectrum of uses in the field from material to medical sciences (Figure 1.26). COPs are made up of different functionalities of secondary building blocks with custom-built properties. Amongst these broad applications, a few emerging applications in the various fields have been explained below. Perhaps there lies a lot of scope to design and synthesis of novel COP materials and applications in the form of academic as well as industrial development.

1.8.1 Catalysis.

The integration of building blocks in COPs with specific functional moieties will demonstrate unparalleled catalytic property. COPs can be nucleated heterogeneously to act as heterogeneous catalyst. Wang and coworkers first developed the utility of COPs in catalysis by loading the Pd ion 2D COF (COF-LZU1) for Suzuki-Miyaura coupling reaction.[79] COF-LZU1 acts as a efficient catalyst with the 96-98% yield of the desired product. COPs are considered to be efficient and better templates for metal ions encapsulation since they have relatively more stable interactions and hydrophobic environments to increase their heterogeneity and surface efficiency. Recently, several COPs are developed that can act as efficient metal free organocatalyst for organic transformation reactions. Benzoselenadiazole based sulfonated nanoporous COP (COP-2) has been developed for efficient heterogeneous catalyst for biodiesel production at room temperature through the esterification and transesterification reactions of fatty acids.[80]

HOP

COP

COF

Structure- property correlation

Material   Application

Fine tunning/ optimization

Catalysis

Renewable energy device

Sensing

Chemical separation

Gas adsorption

Environmental toxic pollutant capture
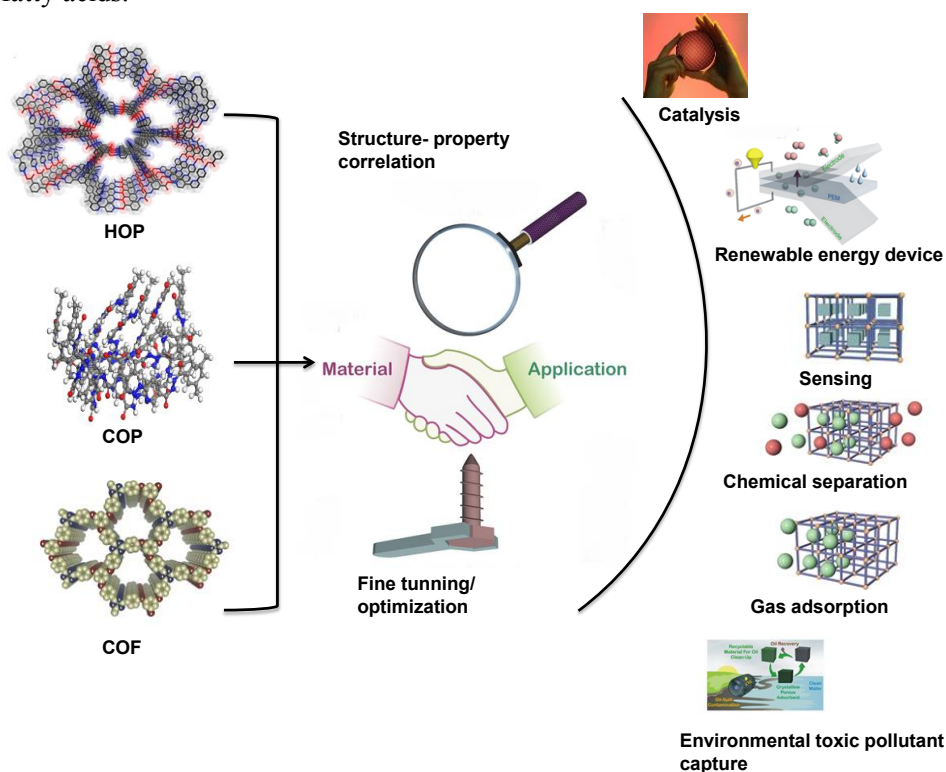
Figure 1.26 Schematic representation of severals applications of COP/COF/HOP.

Incorporation of benzoselenadiazole core in the COP increases the thermal stability[81] and chemical reactivity towards the sulfonation type aromatic electrophilic substitution reaction. Benzoselenadiazole unit is basic in nature due to the presence of diazole's nitrogen atoms. The nitrogen atoms make a polar region inside the pore of the polymer (COP-2). Polar pore can efficiently adsorb the substrate molecules (fatty acids) from the bulk solution through the hydrogen

bonding interaction. Selenium can also play the same role through the Se···H bonding interactions. So, the benzoselenadiazole core can act as a good host towards the polar substrate. Picolinohydrazide based covalent organic polymer is reported as metal free catalysis for Knoevenegal reaction at room temperature.[82] A catechol based COF has been introduced as organocatalyst for selective oxidation of benzyl alcohols.[83] The π-electronic polymers are further developed as a catalytic scaffold for Diels-Alder reactions.[84] Triazine-based covalent organic polymers (TMP) were reported as an efficient metal-free catalyst for the epoxidation of styrene in presence of H_2O_2 and $NaHCO_3$. A high yield over 98% selectivity to styrene oxide was obtained within 6 h. TMP shows higher catalytic activity for styrene oxidation reactions in aqueous conditions due to the stabilization of catalytically active peroxymonocarbonate ion (HCO4-) species with TMP networks.[85] Recently, researchers have tried to develope different metal integrated polymers[86-88] to improve the activity on various applications (Figure 1.27). The co-assembly of porous polymer materials and metal ions has been introduced an interdisciplinary research field.[89] Porous polymeric material encapsulates the metal ions or metal nanoparticles inside its cavity that possess relatively more stable interactions and creates a hydrophobic environment to increase their heterogeneity. A Pd NPs loaded on COP-4 was synthesized after hydrogen reduction in water, which exhibited excellent activity in the controlled oxidation of benzyl alcohol.[90] Prati *et al.* developed Pd/CTF as an efficient catalyst for selective oxidation of glycerol.[91] Schuth *et al.* reported Pt/CTF and $K_2[PtCl_4]$/CTF catalysts for the oxidation of methane at low temperature.[92] Ag-doped porous CIN-1 (Ag–CIN-1) was synthesized as an efficient catalyst for the selective reduction of nitriles to amides.[93-95] On the other hand metal integrated porous polymers also can act as efficient catalyst in electrocatalysis and photocatalysis. A ruthenium encapsulated 2D COF was develped as efficient electrocatalyst for facile hydrogen evolution reaction (HER).[96] Sun *et al.* developed a bimetallic COF as efficient electrocatalyst for water splitting.[97]

Lotsch *et al.* reported a Pt-encapsulated TFPT/COF as photocatalyst for water splitting reaction under visible light irradiation.[98] Nakanishi *et al*. synthesized a series of Pt-modified CTFs hybridized with carbon NPs as an efficient oxygen-reduction electro-catalyst (ORR) in an acidic condition.[99] Recently, a Re incorporated 2D COF was developed (Re-COF).[100] Interestingly, Re-COF exhibited excellent light absorption and charge separation (CS) properties. Re-COF acts as an efficient catalyst for the CO_2 to CO reduction under visible light irradiation (Figure 1.28). More than 98% conversion of CO_2 to CO was observed. Baeg *et al*. developed a triazine based covalent organic framework (2D CTF) as an excellent photocatalyst for CO_2 reduction under visible light. The visible light absorbing properties, optimum band gap and formation of π electron channels serves the impressive performance in photocatalytic application.[101] A highly crystalline electron rich TFPT-COF was synthesized for visible light photocatalysis for H_2 evolution reaction (Figure 1.29).[102]
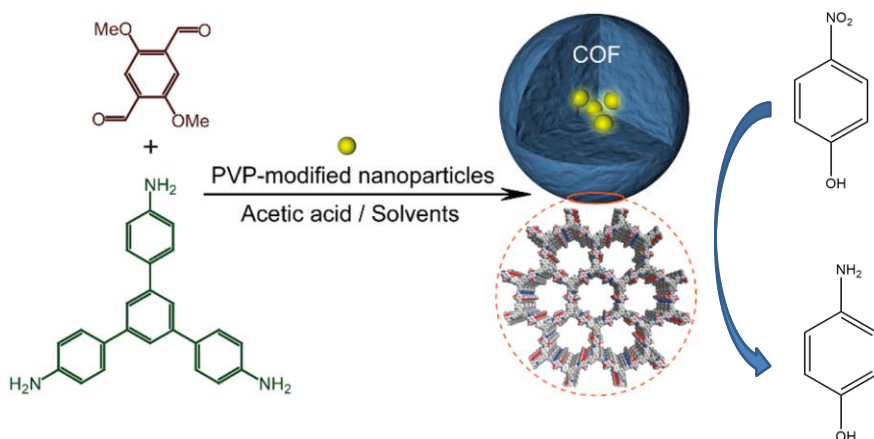
Figure 1.27 Schematic representation of Pd nanoparticle loaded COF as catalyst for reduction of 4-nitrophenol.[86]
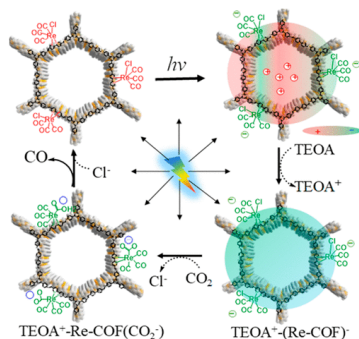
Figure 1.28 (a) Schematic representation of CO_2 reduction under visible light irradiation by Re-COF catalyst.[100]
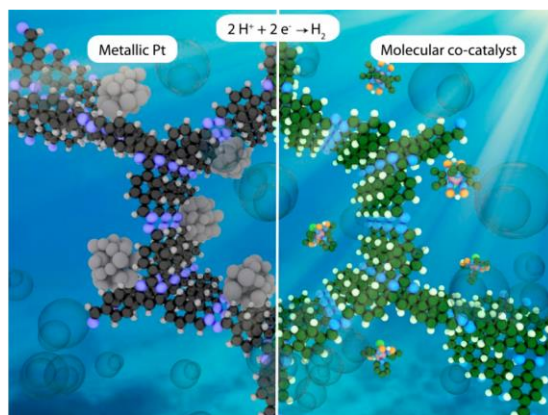
Figure 1.29 Schematic representation of photocatalytic H_2 evolution with Metallic Pt (left) and molecular cocatalysts (right)

Yang *et al*. designed and synthesized new kinds of novel bipyridine-based covalent organic polymers that exhibits excellent photocatalytic activity for the

water splitting reaction under visible light irradiation. In this reaction Pt acted as a proton reduction co- catalyst.[103] Schmidt and coworkers synthesized a highly stable acetylene and diacetylene based β-ketoenamine (COFs TP-EDDA and TP-BDDA COFs).[104] TP-EDDA and TP-BDDA show efficient photocatalytic activity for hydrogen evolution reaction from water. Diacetylene moieties based COFs (TP-BDDA) showed profound activity towards catalysis due to its high porosity, high surface area, easily accessible diacetylene functionalities, high chemical stability (Figure 1.30).
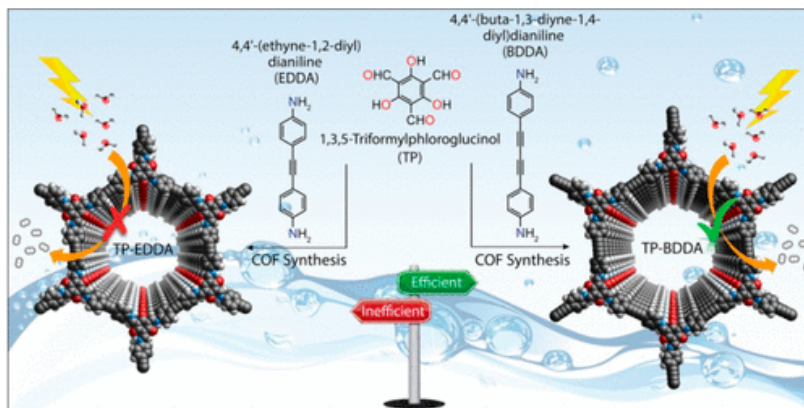
Figure 1.30 Schematic representation H_2 generation reaction by using TP-EDDA and TP-BDDA catalyst.[104]

Wang *et al*. demonstrated a platform for synthesizing a sp^2 based carbon polymeric frameworks (sp^2c-COF$_{ERDN}$) with extended π-conjugated to evolute of hydrogen from water under light irradiation.[105] sp^2c-COF$_{ERDN}$ serves a narrow band gap to absorb visible and near-infrared light. The band structure of the material (sp^2c-COF$_{ERDN}$) had been tuned by varying the electron-deficient units inside the polymeric backbones that generate electrons. Wang *et al*. synthesized a benzoxazole-linked ultrastable polymers for the efficient photocatalysis in organic transformation reactions (Ar-B(OH)$_2$ to Ar-OH) under visible light (Figure 1.31).[106]
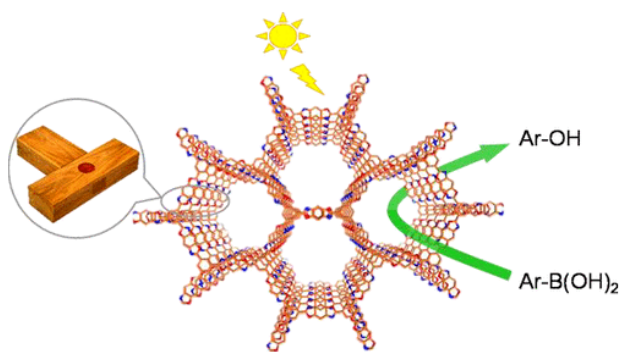
Figure 1.31 Schematic representation of photocatalytic organic transformation reaction.

1.8.2 Gas sensing, adsorption and storage.

From last few years, COPs have also gained a lot of attention in the electronics applications, specially in chemiresistive gas sensing devices. To the best of our knowledge, most of the pure organic based molecules or polymers are not suitable for chemiresistive gas sensors due to their poor conductivity or insulating nature.[107] Recently, Sakaushi *et al.* reported a amorphous covalent organic polymer based bipolar semiconducting organic material.[108-110] A triazine based amorphous covalent organic polymer (CTF-1) was reported as a high performance room temperature ammonia gas sensor material through dual (Figure 1.32) hydrogen bonding.[111]
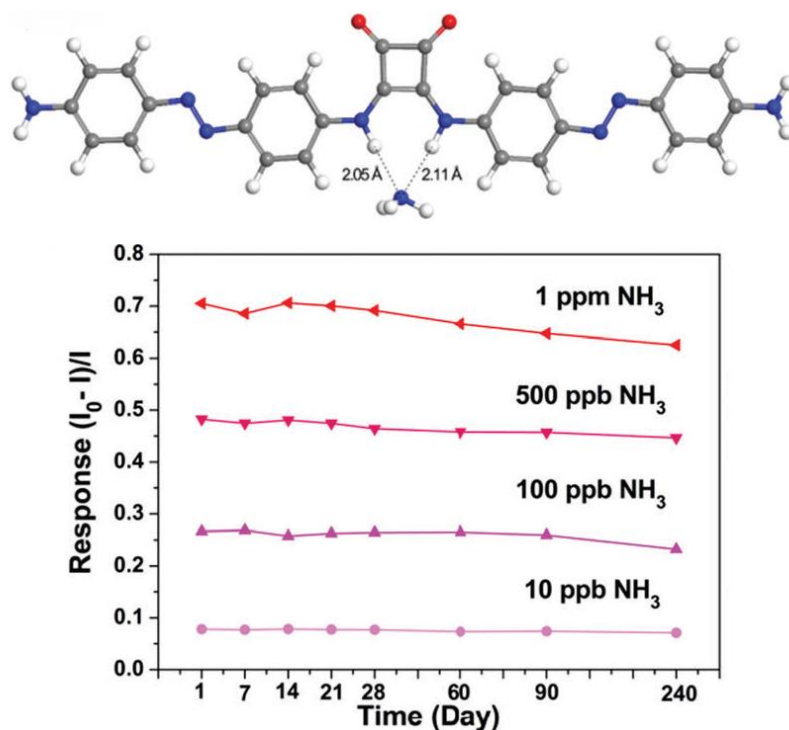
Figure 1.32 NH_3 sensing performance of thr PADS based sensor.[111]

CTF-1 based chemiresistive sensor shows high response efficiency. Polysquaramide-based (PADS) chemiresistor was developed for the detection of ammonia at room temperature (25 ℃). PADS acts as a sensing material with good selectivity, reproducibility, time stability and process-robustness matrix. Xia *et al.* developed a two dimensional polymer (T-2DP) based chemiresistive sensor for the efficient NO_2 sensing. The sensing effect is superfast (35-47 s) and fully reversibly operated at room temperature.[112] COPs have been also considered as promising materials for gas adsorption, separation and storage applications as they are constructed by the light atoms connected by strong covalent bonds to creats porous surface. Till the date, the adsorption, storage and separation capabilities of COPs for few gases, like H_2, CH_4, and CO_2 have been widely investigated. Primarily, these properties COPs depend primarily on the

elemental compositions and topologies of its surface and frameworks. Very recently, theoretical simulations and calculations predict that alkali metals encapsulated COFs serve a better gas adsorption and storage capacity, which illustrates the importance of introducing functional groups for several kinds of interactions with gases. Hydrogen gas adsorption and storage have given a great attention because it can serve as a future renewable energy resource and eco-friendly characteristics. Walton *et al*. developed a series of covalent organic polymer (PIMs) for hydrogen storage materials.[113] PIMs can uptake H_2 upto 2.7% by mass at 10 bar/77 K. A microcrystalline borazine-linked 2D covalent organic polymer (BLP-2H), was synthesized. BLP-2H exhibited high thermal stability and high surface area. BLP-2H can store H_2 up to 2.4 wt% at 77 K and 15 bar.[114] It has been observed that 3D polymers show better H_2 adsorption properties than 2D polymers. Yaghi and co-workers synthesized a series of 2D and 3D COFs to invesitigate the gas adsorption properties. Of the different COFs, 3D COF-102 exhibited the highest hydrogen storage capacity largest which uptakes upto 72 mg g^{-1} at 1 bar and 77 K.[115] On the other hand, 2D-COF-10 exhibited the highest hydrogen uptake up to 39.2 mg g^{-1} at 1 bar and 77 K. Methane gas can be a alternative source of vehicular fuel. However, a less efficient, high economic and safe on-board storage system is a major barrier that restricts methane-driven cars from competing with other commercially available fuels. The maximum CH_4 adsorption capacity was observed upto 187 mg g^{-1} COF for COF-102. Whereas COF-103 showed a high storage capacity of 175 mg g^{-1}.[115] These adsorption values are quite high compared to other reported porous materials.[116] Carbon dioxide is considered as a greenhouse gas that is highly responsible for global warming. Therefore, CO_2 capturing materials have been attracted in broad interest in many industries. In this regards, porous organic materials can be the promising materials for CO_2 capturing. Cao and co-workers designed and synthesized a series of COPs (COP-1 to COP-4) for CO_2 adsorption.[117] COP-4 exhibited highest CO_2 adsorption capacity compared to other synthesized COP. Incorporation of extra triazine group inside the polymeric backbone facilitates the better CO_2 adsorption behaviour of COP-4 (Figure 1.33).
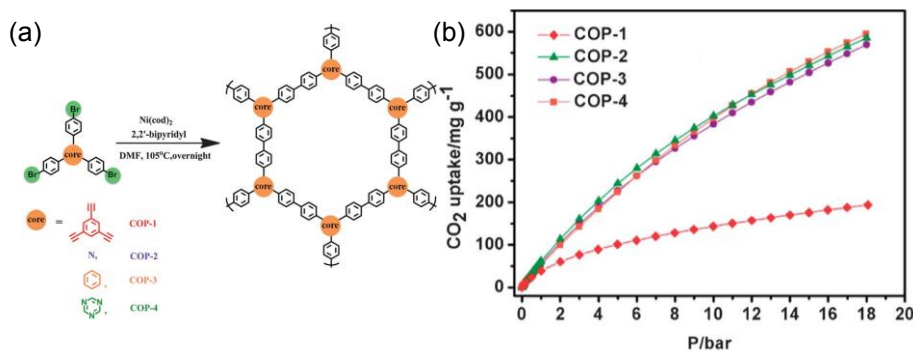
Figure 1.33 (a) Schematic representation of the synthesis of COP-1, COP-2, COP-3, COP-4, (b) CO_2 uptake profile.[117]

Azo-linkaged based porous organic polymers can be the better and efficient polymeric materials for the CO_2 adsorption. Several numbers of N_2-phobic nanoporous covalent organic polymers was syntheiszed for selective CO_2 adsorption.[118] Azo- COP-1 exhibited highest CO_2 adsorption capacity due to its larger surface area and huge no of azo-groups inside the polymeric backbone. Yavuz and co-workers synthesized a series of aromatic amide and ester based COPs for CO_2 capturing materials (COP-32, COP-33, COP-34, COP-35, COP-36 and COP-37).[119] It was observed that CO_2 adsorption capacity of amide based polymers (COP-32, COP-33, and COP-34) depend on the size of their pore volume and surface area. As a results, the trend in the CO_2 uptake capacity of amide based polymers is COP-33 > COP-32 > COP-34, which is similar to the amount of pore volume (0.2 > 0.139 > 0.095 cc g^{-1}). On the other hand, similar kinds of effect of pore volume on the CO_2 uptake capacity was also noticed in ester bond containing polymers. Covalent organic polymers show a high adsorption capacity for the adsorption of H_2, CH_4, and CO_2, although these gases are weakly interacted with the polymer's functionality. Polymers composed with boron atoms are useful for capturing ammonia because the ammonia (lewis base) has strong propensity to coordinate with vacant boron sites (Lewis acids).[120] Yaghi and coworkers synthesized a series of boronate ester-linked COFs. COF-10 (Figure 1.34) is promising material for efficient ammonia adsorption. COF-10 showed maximum NH_3 adsorption capacity of 15 mol kg^{-1} at 298 K under 1 bar pressure. Surprisingly, all such COF materials can be reused many times without any noticeable activity deterioration. These observations attribute that molecularly designed COFs containing functional groups on their polymer backbone or frame that can efficiently interact with gas molecules (Figure 1.34).
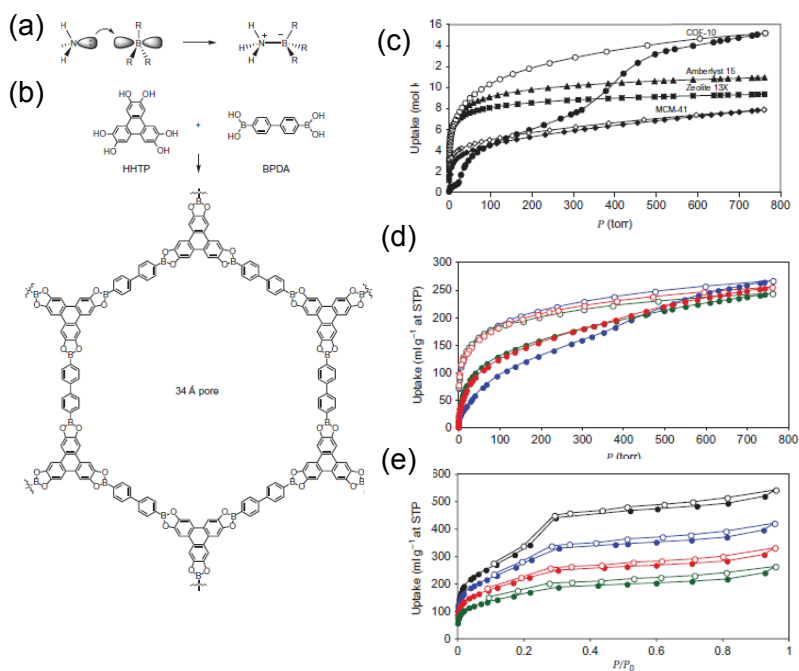
Figure 1.34 (a) Ammonia boron (Lewis acid-base) interactions. (b) Synthetic representation of COF 10 for ammonia storage. (c) Ammonia uptake in state-of-the-art materials and COF-10. (d) Ammonia adsorption and desorption isotherms in COF-10 of different cycles. (e) N_2 adsorption-desorption isotherms (77 K) of COF-10 material (black), after one cycle (blue), two cycles (red) and three cycles (green) of NH_3 adsorption.[120]

1.8.3 Conduction.

Since few years, exclusive research had been done in search for materials with various architectures and functionalities that could show better conductivity.[121] The well-ordered structure with proper ionic channel of polymer are required to acquire the well desired conductivity. Liu and co-workers synthesized a 2D-COF by condensing tetrathiafulvalene tetraaldehyde with 1,4 diaminobenzene that shows high conductivity.[122] A two dimensional COF, DAAQ-TFP was synthesized through electropolymerization with poly(3,4 ethylenedioxythiophene) (PEDOT).[123] This modified COF exhibits volumetric energies and high power densities. Significantly, 2D-COF with ordered π-conjugation and short intermolecular π···π interactions among the layers are established to have a potential application as conduction materials.[124] Several post synthetic modification of COPs have been done to get desired applications as required. Banerjee group developed the proton conducting polymer by surface modification of azo linked COF with phosphoric acid group.[125] Recently, sulfonic acid incorporated COP shows better conductivity which is better than Nafion (Figure 1.35).[126]
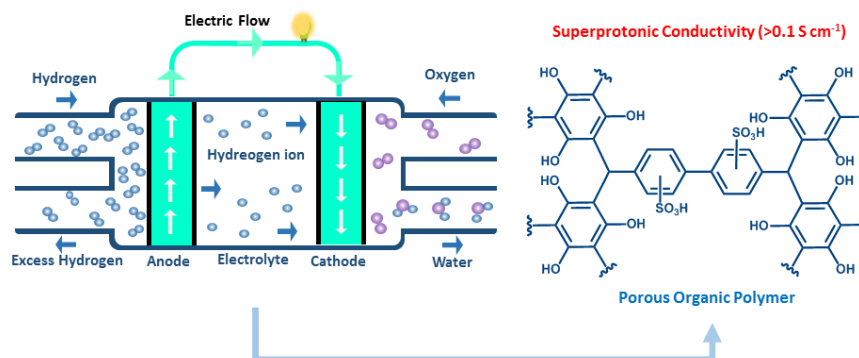
Figure 1.35 Sulfonic acid functionalized POP exhibits superprotonic conductivity.

Jiang and coworkers synthesized a π-electron rich 2D TP-COF from pyrene-2,7-diboronic acid (PDBA) and 2,3,6,7,10,11-hexahydroxytriphenylene (HHTP).[127] TP-COF creates of 2D long range interlocking hexagonal framework. Microscopic images of TP-COF support the formation of a belt-shaped morphology with a width of 300 nm, thickness of 100 nm. TP-COF can absorb a wide range of photons from the UV to the visible regions due to present of

pyrene and triphenylene moieties. Because of the formation of the layer by layer structure, TP-COF showed semiconducting properties that created hole transportation channels. Recently, metal integrated covalent organic polymers serve a new kinds of composite materials that show promising semiconducting behaviour. A metallophthalocyanine based COF (NiPc-COF) was synthesized to construct a efficient photoconductive material.[128] NiPc-COF exhibited high hole carrier mobility due to present of π-electron rich and redox active moieties inside the polymeric frame. The NiPc-COF was constructed from the [(OH)$_8$PcNi] and 1,4-benzenediboronic acid (BDBA) in dimethylacetamide (DMAc)/o-dichlorobenzene under solvothermal conditions. NiPc-COF forms sheet type layer by layer structure that also facilitates in hole conducting properties (Figure 1.36).[128] Porphyrine rings are also another moiety similar to phthalocyanines with extended π conjugation with various functionalities.[129] Copper and Zinc ions were incorporated inside the 2D porphyrine rings to construct COFs (MP-COFs). Metal ions encapsulated polyporphyrin are stacked in layer by layer arrangement. Metal-to-metal modes with discrete separations to form a charge carrier channel. Now this charge carriers of COFs is highly depended on the central metals in the porphyrine macrocycles. COFs without metal ions in porphyrin (H$_2$P-COF) showed hole conducting properties, whereas the Cu(II) porphyrin (CuP-COF) exhibited electron transport behavior. In contrast, the Zn(II) porphyrin (ZnP-COF) was ambipolar in nature.
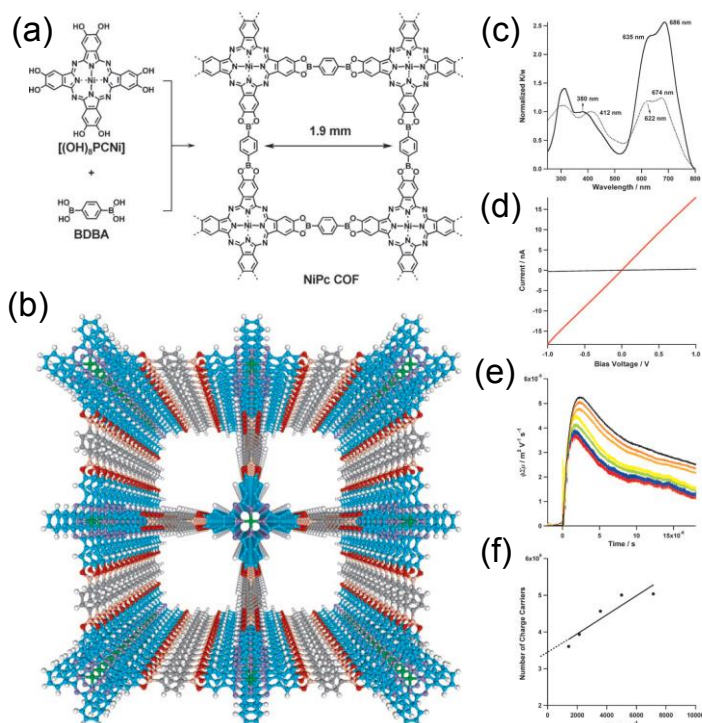
Figure 1.36 (a) Synthetic scheme of NiPc-COF. (b) Extended stacking 2D arrangement of phthalocyanine sheets and microporous channels in NiPc-COF.

(c) absorption spectra of NiPc-COF and [(MeO)$_8$PcNi]. (d) Current-voltage (I–V) curves of NiPc-COF (red curve) and [(MeO)$_8$PcNi] (black curve). (e) Transient conductivity profiles of NiPc-COF upon irradiation with a 355 nm pulsed laser. (f) Charge carriers measurement of NiPc-COF.

The developement of photoactive COP materials is challenging task for developing photosynthesis system, light energy harvesting, conversion, and optoelectronics. The molecular arrangement of the π electron rich units play a key role in determining the performance of above mentioned properties. Single crystalline π-conjugated materials serves a better photoconductive behavior because of exciton migration over the lattice with charge separation. A highly photoconductive COF (PPy-COF) was synthesized from pyrene-based units.[130] PPy-COF absorbed in a the narrow visible region whereas porphyrin and phthalocyanine ring based COFs exhibited a broad absorbance range from the UV to the NIR region. These broad range of absorption profiles are very much important for developing next generation optoelectronics applications.

1.8.4 Biomedicine.

COP based materials have also shown a significant impact in biomedicine applicatons. Their tunable structural skeleton, porous architecture, uniform pore distribution, low cytotoxicity, variable desired surface functionalities, high chemical and physical stability and biocompatibility properties have gathered huge attention towards biomedical applications.[131] In this regard, Yan *et al.* successfully synthesized a 3D polyimide based porous covalent organic polymers for controlled drug deliver in *vitro*.[132] They chose ibuprofen, captopril and caffeine for loading and control release. Zhao *et al.* developed a nanoporous polymer (PI-3-COF) that acts as good carrier for anticancer drug 5-fluorouracil with good biocompatibility[133] nanometal incorporated COP (MCOP) has been developed that can act as a photothermal agent for selective destruction of the cancer cells.[134]

1.9 Purpose, Significance, Scope and Definitions.

Tunable pore size, high surface area and unique molecular architecture play a key role for many properties of covalent organic polymers (COPs), including gas adsorption, catalysis, and electronic transport. Herein we anticipate that modification of additional surface functionality of COPs will assign an interdisciplinary research field for wide range of applications.

1.10 Thesis outline.

Chapter 2 presents a sulfonated acid group functionalized COP that acts as a efficient heterogeneous catalyst for esterification/transesterification reaction of fatty acids.

Chapter 3 exhibits metal-free catalysis and removal of heavy metals from waste water using picolinohydrazide group functionalized.

Chapter 4 describes COP as efficient chemiresistive gas sensor at room temperature.

Chapter 5 reports ruthenium encapsulated COF as an efficient electrochemical catalyst for H_2 evolution.

Chapter 6 closes the thesis and provides a brief deliberation on directions for future work.

1.11 References

1. Diercks, C. S.; Yaghi, O. M. The atom, the molecule, and the covalent organic framework. *Science*. **2017**, *355*, 1585 (doi:10.1126/science.aal1585)

2. Karak, S.; Kandambeth, S.; Biswal, B. P.; Sasmal, H. S.; Kumar, S.; Pachfule, P.; Banerjee, R. Constructing Ultraporous Covalent Organic Frameworks in Seconds *via* an Organic Terracotta Process, *J. Am. Chem. Soc*. **2017**, *139*, 5, 1856–1862. (doi.org/10.1021/jacs.6b08815)

3. Wang, H.; Wang, H.; Wang, Z.; Tang, L.; Zeng, G.; Xu, P.; Chen, M.; Xiong, T.; Zhou, C.; Li, X.; Huang, D.; Zhu, Y.; Wang, Z.; Tang, J. Covalent organic framework photocatalysts: structures and applications. *Chem. Soc. Rev*., **2020**, *49*, 4135-4165. (doi.org/10.1039/D0CS00278J)

4. Zhang, P.; Chen, D.; Chen, N.; Huang, K.; Tao, D.; Li, M.; Dai, S. Synthesis of Porous Sulfonamide Polymers by Capturing Atmospheric Sulfur Dioxide. **2018**, *11*, 1751-1755. (doi: org/10.1002/cssc.201800572)

5. Gao, Y.; Kuang, Y.; Guo, Z -F.; Guo, Z.; Krauss, I. J.; Xu. B. Enzyme-instructed molecular self-assembly confers nanofibers and a supramolecular hydrogel of taxol derivative, *J. Am. Chem. Soc*. **2009**, *131*, 13576-13577. (doi: org/10.1021/ja904411z)

6. Aida, T.; Meijer, E.; and Stupp, S. I. Functional supramolecular polymers. *Science* **2012**, *335*, 813-817. (doi:10.1126/science.1205962)

7. Trewin, A.; Cooper, A. I. Porous Organic Polymers: Distinction From Disorder? **2010,** *Angew. Chem., Int. Ed.* 49, 1533-1535. (doi:10.1002/anie.200906827)

8. Thomas, J. M. H.; Trewin, A. Amorphous PAF-1: Guiding the Rational Design of Ultraporous Materials. *J. Phys. Chem. C* **2014**, *118*, 19712-19722. (doi: org/10.1021/jp502336a)

9. Dawson, R.; Cooper, A. I.; Adams, D. J. Chemical functionalization strategies for carbon dioxide capture in microporous organic polymers. *Polym. Int.* **2013**, *62*, 345-352. (doi: org/10.1002/pi.4407)

10. Ben, T.; Ren, H.; Ma, S.; Cao, D.; Lan, J.; Jing, X.; Wang, W.; Xu, J.; Deng, F.; Simmons, J. M.; Qiu, S.; Zhu, G. Targeted Synthesis of a Porous Aromatic

Framework With High Stability and Exceptionally High Surface Area. *Angew. Chem. Int. Ed.* **2009**, *48*, 9457-9460. (doi: 10.1002/anie.200904637)

11. Pei, C.; Ben, T.; Qiu, S. Great Prospects for PAF-1 and its derivatives. *Mater. Horiz.* **2015**, *2*, 11-21. (doi: org/10.1039/C4MH00163J)

12. Yuan, D.; Lu, W.; Zhao, D.; Zhou, H.-C. Highly Stable Porous Polymer Networks with Exceptionally High Gas- Uptake Capacities. *Adv. Mater.* **2011**, *23*, 3723-3725. (doi: org/10.1002/adma.201101759)

13. Chen, X.; Addicoat, M.; Jin, E.; Zhai, L.; Xu, H.; Huang, N.; Guo, Z.; Liu, L.; Irle, S.; Jiang, D.; Locking Covalent Organic Frameworks with Hydrogen Bonds: General and Remarkable Effects on Crystalline Structure, Physical Properties, and Photochemical Activity. *J. Am. Chem. Soc.* **2015**, *137*, 3241-3247. (doi:10.1021/ja509602c)

14. Shinde, D. B.; Kandambeth, S.; Pachfule, P.; Kumar R. R.; Banerjee, R. Bifunctional covalent organic frameworks with two dimensional organocatalytic micropores. *Chem. Commun.* **2015**, *51*, 310-313. (doi:10.1039/C4CC07104B)

15. Kandambeth, S.; Venkatesh V.; Shinde, D. B.; Kumari, S.; Halder, A.; Verma S.; Banerjee, R. Self-templated chemically stable hollow spherical covalent organic framework. *Nat. Commun.* **2015**, *6*, 6786. (doi: org/10.1038/ncomms7786)

16. Chen, X.; Addicoat, M.; Irle, S.; Nagai A.; Jiang, D. Control of Crystallinity and Porosity of Covalent Organic Frameworks by Managing Interlayer Interactions Based on Self-Complementary π-Electronic Force. *J. Am. Chem. Soc.* **2013**, *135*, 546-549. (doi:10.1021/ja3100319)

17. Zhang, Y. B.; Su J; Furukawa, H.; Yun, Y.; Gandara, F.; Duong, A.; Zou X.; Yaghi, O. M. Single-crystal Structure of a Covalent Organic Framework. *J. Am. Chem. Soc.* **2013**, *135*, 16336-16339. (doi:10.1021/ja409033p)

18. Bunck, D. N.; Dichtel, W. R. Bulk Synthesis of Exfoliated Two-Dimensional Polymers Using Hydrazone-Linked Covalent Organic Frameworks. *J. Am. Chem. Soc.* **2013**, *135*, 14952-14955. (doi:10.1021/ja408243n)

19. Uribe-Romo, F. J.; Doonan, C. J.; Furukawa, H.; Oisaki K.; Yaghi, O. M. Crystalline Covalent Organic Frameworks with Hydrazone Linkages. *J. Am. Chem. Soc.* **2011**, *133*, 11478-11481. (doi:10.1021/ja204728y)

20. Rowan, S. J.; Cantrill, S. J.; Cousins, G. R. L.; Sanders J. K. M.; Stoddart, J. F. Dynamic Covalent Chemistry. *Angew. Chem., Int. Ed. Engl.* **2002**, *41*, 898-952. (doi:10.1002/1521-3773(20020315)41

21. Kundu, T,; Wang, J.; Cheng, Y.; Du, Y.; Qian, Y. Liu, G.; Zhao, D. Hydrazone-based covalent organic frameworks for Lewis acid catalysis. *Dalton Trans.* **2018**, *47*, 13824-13829. (doi: 10.1039/c8dt03005g)

22. Das, G.; Shinde, D. B.; Kandambeth, S.; Biswal, B. P.; Banerjee, R. Mechanosynthesis of imine, b-ketoenamine, and hydrogen-bonded imine-linked covalent organic frameworks using liquid-assisted grinding. *Chem. Commun.* **2014**, *50*, 12615-12618. (doi: org/10.1039/C4CC03389B)

23. Liu, W.; Su, Q.; Ju, P.; Guo, B.; Zhou, H.; Li, G.; Wu, Q. A Hydrazone-based Covalent Organic Framework as an Efficient and Reusable Photocatalyst for the

Cross-Dehydrogenative Coupling Reaction of N-Aryltetrahydroisoquinolines. *ChemSusChem.* **2017**, *10*, 664-669. (doi:10.1002/cssc.201601702)

24. Dalapati, S.; Jin, S.; Gao, J.; Xu, Y.; Nagai. A.; Jiang, D. An Azine-Linked Covalent Organic Framework. *J. Am. Chem. Soc*. **2013**, *135*, 17310-17313. (doi:10.1021/ja4103293)

25. Li, Z.; Zhi, Y.; Feng, X.; Ding, X.; Zou, Y.; Liu X.; Mu, Y. An Azine-Linked Covalent Organic Framework: Synthesis, Characterization and Efficient Gas Storage. *Chem. Eur. J.* **2015**, *21*, 12079-12084. (doi:10.1002/chem.201501206)

26. Li, Z.; Feng, X.; Zou, Y.; Zhang, Y.; Xia, H.; Liu, X.; Mu, Y. A 2D azine-linked covalent organic framework for gas storage applications. *Chem. Commun*. **2014**, *50*, 13825-13828. (doi:10.1039/C4CC05665E)

27. Vyas, V. S.; Haase, F.; Stegbauer, L.; Savasci, G.; Podjaski, F.; Ochsenfeld, C.; Lotsch, B. V. A tunable azine covalent organic framework platform for visible light-induced hydrogen generation. *Nat. Commun.* **2015**, *6*, 8508. (doi:10.1038/ncomms9508)

28. Fan, H.; Mundstock, A.; Gu, J.; Meng, H.; Caro, J. An azine-linked covalent organic framework ACOF-1 membrane for highly selective CO_2/CH_4 separation. *J. Mater. Chem. A* **2018**, *6*, 16849-16853. (doi:10.1039/C8TA05641B)

29. Guo, J.; Xu, Y.; Jin, S.; Chen, L.; Kaji, T.; Honsho, Y.; Addicoat, M. A.; Kim, J.; Saeki, A.; Ihee, H.; Seki, S.; Irle, S.; Hiramoto, M.; Gao J.; Jiang, D. Conjugated organic framework with three-dimensionally ordered stable structure and delocalized π clouds. *Nat. Commun.* **2013**, *4*, 2736. (doi: 10.1038/ncomms3736)

30. Xiang, Z. H.; Cao, D. P. Synthesis of Luminescent Covalent–Organic Polymers for Detecting Nitroaromatic Explosives and Small Organic Molecules. *Macromol. Rapid Commun.* **2012**, *33*, 1184-1190. (doi:10.1002/marc.201100865)

31. Ben, T.; Ren, H.; Ma, S.; Cao, D.; Lan, J.; Jing, X.; Wang, W.; Xu, J.; Deng, F.; Simmons, J. M.; Qiu, S.; Zhu, G. Targeted Synthesis of a Porous Aromatic Framework with High Stability and Exceptionally High Surface Area. *Angew. Chem., Int. Ed*. **2009**, *48*, 9457-9460. (doi:10.1002/anie.200904637)

32. Ben, T.; Qiu, S. Porous aromatic frameworks: Synthesis, structure and functions. *Cryst. Eng. Comm*. **2013**, *15*, 17-26. (doi:10.1039/C2CE25409C)

33. Yuan, D.; Lu, W.; Zhao, D.; Zhou, H.-C. Highly Stable Porous Polymer Networks with Exceptionally High Gas- Uptake Capacities. *Adv. Mater.* **2011**, *23*, 3723-3725. (doi:10.1002/adma.201101759)

34. Xiang, Z. H.; Cao, D. P.; Wang, W. C.; Yang, W. T.; Han, B. Y.; Lu, J. M. Postsynthetic Lithium Modification of Covalent-Organic Polymers for Enhancing Hydrogen and Carbon Dioxide Storage. *J. Phys. Chem. C* **2012**, *116*, 5974-5980. (doi:10.1021/jp300137e)

35. Xiang, Z. H.; Zhou, X.; Zhou, C. H.; Zhong, S.; He, X.; Qin, C. P.; Cao, D. P. Well-defined two dimensional covalent organic polymers: rational design, controlled syntheses, and potential applications. *J. Mater. Chem*., **2012**, *22*, 22663- 22669. (doi: 10.1039/c4py01383b)

36. Jiang, J.-X.; Su, F.; Trewin, A.; Wood, C. D.; Niu, H.; Jones, J. T. A.; Khimyak, Y. Z.; Cooper, A. I. Synthetic Control of the Pore Dimension and Surface Area in Conjugated Microporous Polymer and Copolymer Networks. *J. Am. Chem. Soc.* **2008**, *130*, 7710-7720. (doi:10.1021/ja8010176)

37. Jiang, J.-X.; Su, F.; Trewin, A.; Wood, C. D.; Campbell, N. L.; Niu, H.; Dickinson, C.; Ganin, A. Y.; Rosseinsky, M. J.; Khimyak, Y. Z.; Cooper, A. I. Conjugated Microporous Poly(aryleneethynylene) Networks. *Angew. Chem. Int. Ed.* **2007**, *46*, 8574-8578. (doi:10.1002/anie.200701595)

38. Lee, J-Y.; Wood, C. D.; Bradshaw, D.; Rosseinsky, M. J.; Cooper, A. I. Hydrogen adsorption in microporous hypercrosslinked polymers. *Chem. Commun.* **2006**, 2670-2672. (doi:10.1039/B604625H)

39. Germain, J.; Hradil, J.; Fréchet, J. M. J.; Svec, F. High Surface Area Nanoporous Polymers for Reversible Hydrogen Storage. *Chem. Mater*. **2006**, *18*, 4430-4435. (doi:10.1021/cm061186p)

40. Haase, F.; Troschke, E.; Savasci, G.; Banerjee, T.; Duppel, V.; Dörfler, S.; Grundei, M. M. J.; Burow, A. M.; Ochsenfeld, C.; Kaskel, S.; Lotsch, B. V. Topochemical conversion of an imine- into a thiazole-linked covalent organic framework enabling real structure analysis. *Nat. Commun*. **2018**, *9*, 2600. (doi:10.1038/s41467-018-04979-y)

41. Kong, W.; Jia, W.; Wang, R.; Gong, Y.; Wang, C.; Wu, P.; Guo, J. Amorphous-to-crystalline transformation toward controllable synthesis of fibrous covalent organic frameworks enabling promotion of proton transport *Chem. Commun*. **2019**, *55*, 75-78. (doi: org/10.1039/C8CC08590K)

42. Li, X.; Zhang, C.; Cai, S.; Lei, X.; Altoe, V.; Hong, F.; Urban, J. J.; Ciston, J.; Chan, E. M.; Liu, Y.; Facile transformation of imine covalent organic frameworks into ultrastable crystalline porous aromatic frameworks. (doi:10.1038/s41467-018-05462-4)

43. Sasmal, H. S.; Halder, A.; Kunjattu, H. S.; Dey, K.; Nadol, A.; Ajithkumar, T. G.; Bedadur, P. R.; Banerjee, R.; Covalent Self-Assembly in Two Dimensions: Connecting Covalent Organic Framework Nanospheres into Crystalline and Porous Thin Films *J. Am. Chem. Soc*. **2019**, *141*, 20371-20379. (doi: org/10.1021/jacs.9b10788)

44. Kuhn, P.; Antonietti, M.; Thomas, A. Porous, covalent triazine-based frameworks prepared by ionothermal synthesis. *Angewandte Chemie International Edition* **2008**, *47*, 3450-3453. (doi: doi.org/10.1002/anie.200705710).

45. Maschita, J.; Banerjee, T.; Savasci, G.; Haase, F.; Ochsenfeld, C.; Lotsch, B. V. Ionothermal Synthesis of Imide-Linked Covalent Organic Frameworks. *Angew. Chem. Int. Ed*. **2020**, 59, 15750-15758. (doi: 10.1002/anie.202007372)

46. Guan, X.; Ma, Y.; Li, H.; Yusran, Y.; Xue, M.; Fang, Q.; Yan, Y.; Valtchev, V.; Qiu, S. Fast, Ambient Temperature and Pressure Ionothermal Synthesis of Three-Dimensional Covalent Organic Frameworks. *J. Am. Chem. Soc*. **2018**, *140*, 13, 4494–4498. (doi: org/10.1021/jacs.8b01320)

47. Campbell, N. L.; Clowes, R.; Ritchie, L. K.; Cooper, A. I. Rapid microwave synthesis and purification of porous covalent organic frameworks. *Chemistry of Materials* **2009**, *21*, 204-206. (doi: org/10.1002/anie.202007372)

48. Wei, H.; Chai, S.; Hu, N.; Yang, Z.; Wei, L.; Wang, L. The microwave-assisted solvothermal synthesis of a crystalline two-dimensional covalent organic framework with high CO_2 capacity. *Chem. Commun.* **2015**, *51*, 12178-12181. (doi: 10.1039/c5cc04680g).

49. Zhang, W.; Qiu, L-G.; Yuan, Y.-P.;Xie, A.-J.; Shen, Y-H.; Zhu, J.-F. Microwave-assisted synthesis of highly fluorescent nanoparticles of a melamine-based porous covalent organic framework for trace-level detection of nitroaromatic explosives. *Journal of Hazardous Materials* **2012**, *221*, 147-154. (doi: org/10.1016/j.jhazmat.2012.04.025)

50. Biswal, B. P., Chandra, S.; Kandambeth, S.; Lukose, B.; Heine, T. Banerjee, R. Mechanochemical synthesis of chemically stable isoreticular covalent organic frameworks. *Journal of the American Chemical Society* **2013**, *135,* 5328-5331. (doi.org/10.1021/ja4017842)

51. Karak, S.; Kumar, S.; Pachfule, P.; Banerjee, R. Porosity prediction through hydrogen bonding in covalent organic frameworks. *Journal of the American Chemical Society* **2018**, *140*, 5138-5145. (doi: org/10.1021/jacs.7b13558).

52. Zou, C.; Li, Q.; Hua, Y.; Zhou, B.; Duan, J.; Jin, W. Mechanical Synthesis of COF Nanosheet Cluster and Its Mixed Matrix Membrane for Efficient CO_2 Removal. *ACS Appl. Mater. Interfaces* **2017**, *9*, 29093-29100. (doi: 10.1021/acsami.7b08032).

53. Jie, K.; Zhou, Y.; Sun, Q.; Li, B.; Zhao, R.; Jiang, D.; Guo, W.; Chen, H.; Yang, Z.; Huang, F.; Dai, S. Mechanochemical synthesis of pillar[5]quinone derived multi-microporous organic polymers for radioactive organic iodide capture and storage. *Nat Commun.* **2020**, *11*, 1086. (doi: org/10.1038/s41467-020-14892-y)

54. Côté, A. P.; Benin, A. I.; Ockwig, N. W.; O'keeffe, M.; Matzger, A. J.; Yaghi, O. M. Porous, crystalline, covalent organic frameworks. *Science*, **2005**, *310*, 1166-1170. (doi:10.1126/science.1120411).

55. Tilford, R. W.; Gemmill, W. R.; Zur Loye, H. C.; Lavigne, J. J. Facile synthesis of a highly crystalline, covalently linked porous boronate network. *Chemistry of Materials* **2006**, *18*, 5296-5301. (doi: org/10.1021/cm061177g).

56. Colson, J. W.; Woll, A. R.; Mukherjee, A.; Levendorf, M. P.; Spitler, E. L.; Shields, V. B.; Spencer, M. G.; Park, J.; Dichtel, W. R. Oriented 2D covalent organic framework thin films on single-layer graphene. *Science* **2011**, *332*, 228-231. (doi: 10.1126/science.1202747)

57. Katsoulidis, A. P.; Kanatzidis, M. G. Phloroglucinol Based Microporous Polymeric Organic Frameworks with -OH Functional Groups and High CO_2 Capture Capacity. *Chem. Mater*. **2011**, *23*, 1818-1824. (doi: org/10.1021/cm103206).

58. Kim, S.; Lim, H.; Lee, J.; Choi, H. C. Synthesis of a Scalable Two-Dimensional Covalent Organic Framework by the Photon-Assisted Imine

Condensation Reaction on the Water Surface. *Langmuir* **2018**, *34*, 8731-8738. (doi: org/10.1021/acs.langmuir.8b00951)

59. Johnston, P.; Braybrookb, C.; Saito, K. Topochemical photo-reversible polymerization of a bioinspired monomer and its recovery and repolymerization after photo-depolymerization. *Chemical Science* **2012**, *3*, 2301-2306. (doi: 10.1039/C2SC20380D)

60. An, Q.; Hassan, Y.; Yan, X.; Krolla-Sidenstein, P.; Mohammed, T.; Lang, M.; Bräse, M.; Tsotsalas, M. Fast and efficient synthesis of microporous polymer nanomembranes via light-induced click reaction. *Beilstein Journal of Organic Chemistry*, **2017**, *13*, 558-563. (doi: 10.3762/bjoc.13.54)

61. Xu, J.; Boyer, C. Visible light photocatalytic thiol-ene Reaction: an elegant approach for fast polymer post functionalization and Step-Growth polymerization. *Macromolecules,* **2015**, *48*, 520-529. (doi: org/10.1021/ma502460t)

62. Zhang, C.; Lia, G.; Zhang, Z. A hydrazone covalent organic polymer based micro-solid phase extraction for online analysis of trace Sudan dyes in food samples. *J. Chromatogr. A* **2015**, *1419*, 1-9. (doi: 10.1016/j.chroma.2015.09.059)

63. Stegbauer, L.; Schwinghammer, K.; Lotsch, B. V. A hydrazone-based covalent organic framework for photocatalytic hydrogen production. *Chem. Sci.* **2014**, *5*, 2789-2793. (doi: 10.1039/C4SC00016A)

64. Patra, B. C.; Khilari, S.; Satyanarayana, L.; Pradhan, D.; Bhaumik, A. A new benzimidazole based covalent organic polymer having high energy storage capacity. *Chem. Commun.* **2016,** *52*, 7592-7595. (doi: 10.1039/C6CC02011A)

65. Stegbauer, L.; Hahn, M. W.; Jentys, A.; Savasci, G.; Ochsenfeld, C.; Lercher, J. A.; Lotsch, B. V. Tunable Water and CO2 Sorption Properties in Isostructural Azine-Based Covalent Organic Frameworks through Polarity Engineering. *Chem. Mater.* **2015**, *27*, 7874−7881. (doi: 10.1021/acs.chemmater.5b02151)

66. Wan, S.; Gandara, F.; Asano, A.; Furukawa, H.; Saeki, A.; Dey, S. K.; Liao, L.; Ambrogio, M. W.; Botros, Y. Y.; Duan, X.; Seki, S.; Stoddart, J. F.; Yaghi, O. M. Covalent Organic Frameworks with High Charge Carrier Mobility. *Chem. Mater.* **2011**, *23*, 4094-4097. (doi: 10.1021/cm201140r)

67. Coˆteˊ, A. P.; Benin, A. I.; Ockwig, N. W.; O'Keeffe, M.; Matzger, A. J.; Yaghi, O. M. Porous, Crystalline, Covalent Organic Frameworks. *Science* **2005**, *310*, 1166-1170. (doi: 10.1126/science.1120411)

68. Suresh, V. M.; Bonakala, S.; Atreya, H. S.; Balasubramanian, S.; Maji, T. K. Amide Functionalized Microporous Organic Polymer (Am-MOP) for Selective CO2 Sorption and Catalysis *ACS Appl. Mater. Interfaces* **2014**, *6*, 4630-4637. (doi: 10.1021/am500057z)

69. Bhunia, S.; Chatterjee, N.; Das, S.; Saha, K. D.; Bhaumik, A, Porous Polyurea Network Showing Aggregation Induced White Light Emission, Applications as Biosensor and Scaffold for Drug Delivery. *ACS Appl. Mater. Interfaces* **2014**, *6*, 22569-22576. (doi: 10.1021/am5066859)

70. Biswal, B. P.; Chandra, S.; Kandambeth, S.; Lukose, B.; Heine, T.; Banerjee, R. Mechanochemical Synthesis of Chemically Stable Isoreticular Covalent

Organic Frameworks. *J. Am. Chem. Soc.* **2013**, *135*, 5328-5331. (doi: 10.1021/ja4017842)

71. Wang, L.; Zeng, C.; Xu, H.; Yin, P.; Chen, D.; Deng, J.; Li, M.; Zheng, N.; Gu, C.; Ma, Y. A highly soluble, crystalline covalent organic framework compatible with device implementation. *Chem. Sci.*, **2019**, *10*, 1023-1028. (doi: 10.1039/c8sc04255a).

72. Ravi, S.; Puthiaraj, P.; Yu, K.; Ahn, W.-S. Porous Covalent Organic Polymers Comprising a Phosphite Skeleton for Aqueous Nd(III) Capture. *ACS Appl. Mater. Interfaces* **2019**, *11*, 11488-11497. (doi: 10.1021/acsami.9b00546)

73. Xu, Y.; Chang, D.; Feng, S.; Zhang, C.; Jiang, J-X. BODIPY-containing porous organic polymers for gas adsorption. *New J. Chem.* **2016**, *40*, 9415-9423. (doi: 10.1039/C6NJ01812B)

74. Feng, L.; Zhang, S.; Sun, X.; Dong, A.; Chen, Q. Boronic acid-functionalized porous polycarbazoles: preparation, adsorption performance, and heterogeneous catalysts for selective oxidation. *J Mater Sci*. **2018**, *53*, 15025–15033. (doi: 10.1007/s10853-018-2682-9)

75. Jiang, J. -X.; Su, F.; Niu, H.; Wood, C. D.; Campbell, N. L.; Khimyak, Y. Z.; Cooper, A. I. Conjugated microporous poly(phenylene butadiynylene)s. *Chem. Commun.*, **2008**, 486-488. (doi: org/10.1039/B715563H).

76. Xiong, S.; Tang, X.; Pan, C.; Li, L.; Tang, J.; Yu, G. Carbazole-Bearing Porous Organic Polymers with a Mulberry-Like Morphology for Efficient Iodine Capture. *ACS Appl. Mater. Interfaces* **2019**, *11*, 27335-27342. (doi: 10.1021/acsami.9b07679)

77. Aguila, B.; Sun, Q.; Perman, J. A.; Earl, L. D.; Abney, C. W.; Elzein, R.; Schlaf, R.; Ma, S. Efficient Mercury Capture Using Functionalized Porous Organic Polymer. *Adv. Mater*. **2017**, *29,* 1700665. (doi: 10.1002/adma.201700665)

78. Dey, D.; Banerjee, P. Toxic organic solvent adsorption by a hydrophobic covalent polymer. *New J. Chem.*, **2019**, *43*, 3769-3777). (DOI: 10.1039/c8nj06249h)

79. Ding, S-Y.; Gao, J.; Wang, Q.; Zhang, Y.; Song, W-G.; Su, C-Y.; Wang, W. Construction of Covalent Organic Framework for Catalysis: Pd/COF-LZU1 in Suzuki Miyaura Coupling Reaction. |*J. Am. Chem. Soc.* **2011**, *133*, 19816-19822. (doi: 10.1021/ja206846p)

80. Maiti, S.; Chowdhury, A. R.; Das, A. K. Benzoselenadiazole-based nanoporous Covalent Organic Polymer (COP) as efficient room temperature heterogeneous catalyst for biodiesel production. *Microporous Mesoporous Mater.* **2019**, *283*, 39-47. (doi: 10.1016/j.micromeso.2019.03.046)

81. Xia, W. Interactions between metal species and nitrogen-functionalized carbon nanotubes. *Catal. Sci. Technol.* **2016**, *6*, 630-644. (doi: 10.1039/C5CY01694K)

82. Chowdhury, A. R.; Maiti, S.; Mondal, A.; Das, A. K. Picolinohydrazide-Based Covalent Organic Polymer for Metal-Free Catalysis and Removal of

Heavy Metals from Wastewater. *J. Phys. Chem. C* **2020**, *124*, 7835-7843. (doi: 10.1021/acs.jpcc.0c00664)

83. Khatioda, R.; Talukdar, D.; Saikia, B.; Bania, K. K.; Sarma, B. Constructing two dimensional amide porous polymer to promote selective oxidation reactions. *Catal. Sci. Technol*. **2017**, *7*, 3143-3150. (doi: 10.1039/C7CY00747G)

84. Wu, Y.; Xu, H.; Chen, X.; Gao, J.; Jiang, D. A π-electronic covalent organic framework catalyst π-walls as catalytic beds for Diels-Alder reactions under ambient conditions. *Chem. Commun.* **2015**, *51*, 10096-10098. (doi: 10.1039/C5CC03457D)

85. Ansari, M. B.; Jeong, E.-Y.; Park, S.-E. Styrene epoxidation in aqueous over triazine-based microporous polymeric network as a metal-free catalyst. *Green Sustain. Chem.* **2012**, *2*, 1-7. (doi: 10.4236/gsc.2012.21001)

86. Shi, X.; Yao, Y.; Xu, Y.; Liu, K.; Zhu, G.; Chi, L.; Lu, G. Imparting Catalytic Activity to a Covalent Organic Framework Material by Nanoparticle Encapsulation. *ACS Appl. Mater. Interfaces* **2017**, *9*, 7481-7488. (doi: 10.1021/acsami.6b16267)

87. Lin, S.; Diercks, C. S.; Zhang, Y.-B.; Kornienko, N.; Nichols, E. M.; Zhao, Y. Covalent organic frameworks comprising cobalt porphyrins for catalytic CO2 reduction in water. *Science* **2015**, *349*, 1208-1213. (doi: 10.1126/science.aac8343)

88. Chen, L.; Zhang, L.; Chen, Z.; Liu, H.; Luque, R.; Li, Y. A covalent organic framework-based route to the in situ encapsulation of metal nanoparticles in N-rich hollow carbon spheres. *Chem. Sci.* **2016**, *7*, 6015-6020. (doi: 10.1039/C6SC01659F)

89. White, R. J.; Luque, R.; Budarin, V. L.; Clark, J. H.; Macquarrie, D. J. Supported metal nanoparticles on porous materials. Methods and applications. *Chem. Soc. Rev.* **2009**, *38*, 481-494. (doi: 10.1039/B802654H)

90. Zhou, Y.; Xiang, Z.; Cao, D.; Liu, C.-J. Preparation and Characterization of Covalent Organic Polymer Supported Palladium Catalysts for Oxidation of CO and Benzyl Alcohol. *Ind. Eng. Chem. Res*. **2014**, *53*, 1359-1367. (doi: 10.1021/ie403279y)

91. Chan-Thaw, C. E.; Villa, A.; Katekomol, P.; Su, D.; Thomas, A.; Prati, L. Covalent Triazine Framework as Catalytic Support for Liquid Phase Reaction. *Nano Lett.* **2010**, *10*, 537-541. (doi: 10.1021/nl904082k)

92. Palkovits, R.; Antonietti, M.; Kuhn, P.; Thomas, A.; Sch¨uth, F. Solid Catalysts for the Selective Low- Temperature Oxidation of Methane to Methanol. *Angew. Chem. Int. Ed.* **2009**, *48*, 6909-6912. (doi: 10.1002/anie.200902009)

93. Baig, R. B. N.; Varma, R. S. A facile one-pot synthesis of ruthenium hydroxide nanoparticles on magnetic silica: aqueous hydration of nitriles to amides. *Chem. Commun.* **2012**, *48*, 6220-6222. (doi: 10.1039/C2CC32566G)

94. Battilocchio, C.; Hawkins, J. M.; Ley, S. V. Mild and Selective Heterogeneous Catalytic Hydration of Nitriles to Amides by Flowing through Manganese Dioxide. *Org. Lett.* **2014**, *16*, 1060-1063. (doi: 10.1021/ol403591c)

95. Hirano, T.; Uehara, K.; Kamata, K.; Mizuno, N. Palladium(II) Containing γ-Keggin Silicodecatungstate That Efficiently Catalyzes Hydration of Nitriles. *J. Am. Chem. Soc*. **2012**, *134*, 6425-6433. (doi: 10.1021/ja3006012)

96. Maiti, S.; Chowdhury, A. R.; Das, A. K. Electrochemically Facile Hydrogen Evolution Using Ruthenium Encapsulated Two Dimensional Covalent Organic Framework (2D-COF). *ChemNano Mat.* **2020**, *6*, 99-106. (doi: 10.1002/cnma.201900499)

97. Wu, D.; Xu, Q.; Qian, J.; Li, X.; Sun, Y. Bimetallic Covalent Organic Frameworks for Constructing Multifunctional Electrocatalyst **2019**, *25*, 3105-3111. (doi: 10.1002/chem.201805550)

98. Stegbauer, L.; Schwinghammer, K. Lotsch, B. V. A hydrazone-based covalent organic framework for photocatalytic hydrogen production. *Chem. Sci*. **2014**, *5*, 2789-2793. (doi: 10.1039/c4sc00016a)

99. Kamiya, K.; Kamai, R.; Hashimoto, K. Nakanishi, S. Platinum-modified covalent triazine frameworks hybridized with carbon nanoparticles as methanol-tolerant oxygen reduction electrocatalysts. *Nat. Commun*. **2014**, *5*, 5040. (doi: 10.1038/ncomms6040)

100. Yang, S.; Hu, W.; Zhang, X.; He, P.; Pattengale, B.; Liu, C.; Cendejas, M.; Hermans, I.; Zhang, X.; Zhang, J.; Huang, J. 2D Covalent Organic Frameworks as Intrinsic Photocatalysts for Visible Light-Driven CO_2 Reduction. *J. Am. Chem. Soc*. **2018**, *140*, 14614-14618. (doi: 10.1021/jacs.8b09705)

101. Yadav, R. K.; Kumar, A.; Park,N.-J.; Kong, K.-J.; Baeg, J.-O. A highly efficient covalent organic framework film photocatalyst for selective solar fuel production from CO_2. J. Mater. Chem. A, **2016**, *4,* 9413-9418. (doi: 10.1039/C6TA01625A)

102. Banerjee, T.; Gottschling, K.; Savasci, G. K.; Ochsenfeld, C.; Lotsch, B. V. H_2 Evolution with Covalent Organic Framework Photocatalysts. *ACS Energy Lett*. **2018**, *3*, 400-409. (doi: 10.1021/acsenergylett.7b01123)

103. Chena, J.; Tao, X.; Tao, L.; Lia, H.; Lia, C.; Wanga, X.; Li, C.; Li, R.; Yang, Q. Novel conjugated organic polymers as candidates for visible-light-driven photocatalytic hydrogen production. *Applied Catalysis B: Environmental* **2019**, *241*, 461-470. (doi.org/10.1016/j.apcatb.2018.09.011)

104. Pachfule, P.; Acharjya, A.; Roeser, J.; Langenhahn, T.; Schwarze, M.; Schomacker, R.; Thomas, A.; Schmidt, J. Diacetylene Functionalized Covalent Organic Framework (COF) for Photocatalytic Hydrogen Generation. *J. Am. Chem. Soc*. **2018**, *140*, 4, 1423–1427. (doi: 10.1021/jacs.7b11255)

105. Jin, E.; Lan, Z.; Jiang, Q.; Geng, K.; Li, G.; Wang, X.; Jiang, D. 2D sp^2 Carbon-Conjugated Covalent Organic Frameworks for Photocatalytic Hydrogen Production from Water. *Chem*. **2019**, *5*, 1632-1647. (doi: 10.1016/j.chempr.2019.04.015)

106. Wei, P.-F.; Qi, M.-Z.; Wang, Z.-P.; Ding, S.-Y.; Yu, W.; Liu, Q.; Wang, L.-K.; Wang, H.-Z.; An, W.-K.; Wang, W. Benzoxazole-Linked Ultrastable Covalent Organic Frameworks for Photocatalysis. *J. Am. Chem. Soc*. **2018**, *140*, 13, 4623-4631. (doi.org/10.1021/jacs.8b00571)

107. Tao, L-M.; Niu, F.; Zhang, D.; Wang, T-M.; Wang, Q-H. Amorphous covalent triazine frameworks for high performance room temperature ammonia gas sensing. *New J. Chem.* **2014**, *38*, 2774-2777. (doi: 10.1039/C4NJ00476K)

108. Sakaushi, K.; Hosono, E.; Nickerl, G.; Gemming, T.; Zhou, H.; Kaskel, S.; Eckert, J. Aromatic porous-honeycomb electrodes for a sodium-organic energy storage device. *Nat. Commun.* **2013**, *4*, 1485. (doi: 10.1038/ncomms2481).

109. Sakaushi, K.; Nickerl, G.; Wisser, F. M.; Nishio-Hamane, D.; Hosono, E.; Zhou, H.; Kaskel, S.; Eckert, J. An Energy Storage Principle using Bipolar Porous Polymeric Frameworks. *Angew. Chem. Int. Ed*. **2012**, *51*, 7850. (doi: 10.1002/anie.201202476)

110. Sakaushi, K.; Hosono, E.; Nickerl, G.; Zhou, H.; Kaskel, S. Eckert, J. Bipolar porous polymeric frameworks for low-cost, high-power, long-life all-organic energy storage devices. *J. Power Sources*, **2014**, *245*, 553. (doi: 10.1016/j.jpowsour.2013.07.007)

111. Zhou, J.; Lin, H.; Cheng, X-F.; Shu, J.; He, J-H.; Li, H.; Xu, Q-F.; Li, N-J.; Chen, D-Y.; Lu, J-M. Ultrasensitive and robust organic gas sensors through dual hydrogen bonding. *Mater. Horiz.* **2019**, 6, 554-562. (doi: 10.1039/C8MH01098F)

112. Yang, K.; Yuan, W.; Hua, Z.; Tang, Y.; Yin, F.; Xia, D. Triazine-Based Two-Dimensional Organic Polymer for Selective NO_2 Sensing with Excellent Performance, *ACS Appl. Mater. Interfaces* **2020**, *12*, 3919-3927. (doi: 10.1021/acsami.9b17450)

113. Budd, P. M.; Butler, A.; Selbie, J.; Mahmood, K.; McKeown, N. B.; Ghanem, B.; Msayib, K.; Book, D.; Walton, A. The potential of organic polymer-based hydrogen storage materials. *Phys. Chem. Chem. Phys.* **2007**, *9*, 1802-1808. (doi: 10.1039/b618053a)

114. Jackson, K. T.; Reich, T. E.; El-Kaderi, H. M. Targeted synthesis of a porous borazine-linked covalent organic framework. *Chem. Commun*. **2012**, *48*, 8823-8825. (doi: 10.1039/c2cc33583b)

115. Furukawa, H.; Yaghi, O. M. Storage of Hydrogen, Methane, and Carbon Dioxide in Highly Porous Covalent Organic Frameworks for Clean Energy Applications. *J. Am. Chem. Soc*. **2009**, *131*, 8875-8883. (doi:10.1021/ja9015765)

116. Furukawa, H.; Ko, N.; Go, Y. B.; Aratani, N.; Choi, S. B.; Choi, E.; Yazaydin, A. O.; Snurr, R. Q.; Keeffe, M. O.; Kim, J.; Yaghi, O. M. Ultrahigh porosity in metal-organic frameworks. *Science*, **2010**, *329*, 424-428. (doi: 10.1126/science.1192160)

117. Xiang, Z.; Zhou, X.; Zhou, C.; Zhong, C.; He, X.; Qin, C.; Cao, D. Covalent-organic polymers for carbon dioxide capture. *J. Mater. Chem*. **2012**, *22*, 22663–22669. (doi: 10.1039/c2jm35446b)

118. Patel, H. A.; Je, S. H.; Park, J.; Chen, D. P.; Jung, Y.; Yavuz, C. T.; Coskun, A. Unprecedented high-temperature CO_2 selectivity in N_2-phobic nanoporous covalent organic polymers. *Nature Communications* **2013**, *4*, 1357. (doi: 10.1038/ncomms2359)

119. Ullah, R.; Atilhan, M.; Anaya, B.; Al-Muhtaseb, S.; Aparicio, S.; Patel, H.; Thirion, D.; Yavuz, C. T. Investigation of Ester- and Amide-Linker-Based

Porous Organic Polymers for Carbon Dioxide Capture and Separation at Wide Temperatures and Pressures. *ACS Appl. Mater. Interfaces* **2016**, *8*, 20772-20785. (doi: 10.1021/acsami.6b05927)

120. Doonan, C. J.; Tranchemontagne, D. J.; Glover, T. G.; Hunt, J. R.; Yaghi, O. M. Exceptional ammonia uptake by a covalent organic framework. *Nature Chem*. **2010**, *2*, 235-238. (doi: org/10.1038/nchem.548).

121. Xu, H.; Tao, S.; Jiang, D. Proton conduction in crystalline and porous covalent organic frameworks. *Nature Materials*, **2016**, *15*, 722-726. (doi: 10.1038/nmat4611)

122. Cai, S. L.; Zhang, Y. B.; Pun, A. B.; He, B.; Yang, J.; Toma, F. M.; Sharp, I. D.; Yaghi, O. M.; Fan, J.; Zheng, S. R. Zhang, W. G. Tunable electrical conductivity in oriented thin films of tetrathiafulvalene-based covalent organic framework. *Chemical Science*, **2014**, *5*, 4693-4700. (doi: 10.1039/C4SC02593H)

123. Mulzer, C. R.; Shen, L.; Bisbey, R. P.; McKone, J. R.; Zhang, N.; Abruña, H. D.; Dichtel, W. R. Superior charge storage and power density of a conducting polymer-modified covalent organic framework. *ACS Cent. Sci*. **2016**, *2*, 667-673. (doi: 10.1021/acscentsci.6b00220)

124. Wan, S.; Gándara, F.; Asano, A.; Furukawa, H.; Saeki, A.; Dey, S. K.; Liao, L.; Ambrogio, M. W.; Botros, Y. Y.; Duan, X.; Seki, S. Covalent organic frameworks with high charge carrier mobility. *Chem. Mater*. **2011**, *23*, 4094-4097. (doi: 10.1021/cm201140r)

125. Chandra, S.; Kundu, T.; Kandambeth, S.; BabaRao, R.; Marathe, Y.; Kunjir, S. M.; Banerjee, R. Phosphoric Acid Loaded Azo (-N=N-) Based Covalent Organic Framework for Proton Conduction. *J. Am. Chem. Soc*. **2014**, *136*, 6570–6573. (Doi: 10.1021/ja502212v)

126. Kang, D. W.; Song, J. H.; Lee, K. J.; Lee, H. G.; Kim, J. E.; Lee, H. Y.; Kim, J. Y.; Hong, C. S. A conductive porous organic polymer with superprotonic conductivity of a Nafion-type electrolyte. *J. Mater. Chem. A*, **2017**, *5*, 17492-17498. (doi: 10.1039/C7TA05279K)

127. Wan, S.; Guo, J.; Kim, J.; Ihee, H.; Jiang, D. A Belt-Shaped, Blue Luminescent, and SemiconductingCovalent Organic Framework. *Angew. Chem. Int. Ed*. **2008**, *47*, 8826 -8830. (doi: 10.1002/anie.200803826).

128. Ding, X.; Guo, J.; Feng, X.; Honsho, Y.; Guo, J.; Seki, S.; Maitarad, P.; Saeki, A.; Nagase, S.; Jiang, D. Synthesis of Metallophthalocyanine Covalent Organic Frameworks That Exhibit High Carrier Mobility and Photoconductivity. *Angew. Chem. Int. Ed*. **2011**, *50*, 1289-1293. (doi: 10.1002/anie.201005919)

129. Feng, X.; Liu, L.; Honsho, Y.; Saeki, A.; Seki, S.; Irle, S.; Dong, Y.; Nagai, A.; Jiang, D. High-Rate Charge-Carrier Transport in Porphyrin Covalent Organic Frameworks: Switching from Hole to Electron to Ambipolar Conduction. *Angew. Chem. Int. Ed*. **2012**, *51*, 2618 -2622. (doi: 10.1002/anie.201106203.

130. Wan, S.; Guo, J.; Kim, J.; Ihee, H.; Jiang, D. A photoconductive covalent organic framework: self-condensed arene cubes composed of eclipsed 2D polypyrene sheets for photocurrent generation. *Angew. Chem., Int. Ed*. **2009**, *48*, 5439-5442. (doi: 10.1002/anie.200900881)

131. Li, Z.; Yang, Y. W. Creation and bioapplications of porous organic polymer materials. *Journal of Materials Chemistry B*, **2017**, *5*, 9278-9290. (doi: 10.1039/C7TB02647A)

132. Fang, Q.; Wang, J.; Gu, S.; Kaspar, R. B.; Zhuang, Z.; Zheng, J.; Guo, H.; Qiu, S.;Yan, Y. 3D porous crystalline polyimide covalent organic frameworks for drug delivery. *Journal of the American Chemical Society*, **2015**, *137*, 8352- 8355. (doi: 10.1021/jacs.5b04147)

133. Bai, L.; Phua, S. Z. F.; Lim, W. Q.; Jana, A.; Luo, Z.; Tham, H. P.; Zhao, L.; Gao, Q.; Zhao, Y. Nanoscale covalent organic frameworks as smart carriers for drug delivery. *Chem. Commun*. **2016**, 52, 4128-4131. (doi: 10.1039/C6CC00853D)

134. Shi, Y.; Deng, X.; Bao, S.; Liu, B.; Liu, B.; Ma, P.; Cheng, Z.; Pang, M.; Lin, Jun. Self-Templated Stepwise Synthesis of Monodispersed Nanoscale Metalation Covalent Organic Polymers for in *vivo. Bioimaging and Photothermal Therapy* **2017** 12, 2183-2188. (doi: 10.1002/asia.201700796)

Chapter 2

Benzoselenadiazole-based nanoporous Covalent Organic Polymer (COP) as efficient room temperature heterogeneous catalyst for biodiesel production

2.1 Introduction.

Biodiesel as an alternative source of fuel has gained more significance in recent years.[1–5] Biodiesel is renewable energy resource as compared to fossil fuels, which are nonrenewable natural resources. Biodiesel has the ability to extend the life of diesel engines. It also helps in the combustion of hydrocarbons and reduction of greenhouse gases. The growth in demand for biodiesel is resulting in rapid increase in their production at low cost, less hazardous, less time and easy synthetic routes. The conventional method of biodiesel production is the esterification or transesterification of long chain fatty acids. The reactions are typically catalyzed by either acid or alkali.[6–12] However, the acid and base catalyzed pathways are not sophisticated for the generation of biodiesel as there are several obstacles like slower reaction rate, longer reaction time, requirement of high temperature, difficulty in removal of the catalysts from the reaction medium and formation of byproducts.[13] Several metal based heterogeneous catalysts including mixed oxides of zinc, aluminium, calcium, potassium, tin and tungsten have been reported[14–17] which require heating and typical reaction conditions. There also have several reports on natural ways of biodiesel production[18–29] like pre-esterification of Calophyllum inophyllum oil.[30] Naturally occurring marine microalgal mats and marine microalgae have also been used for the production of biodiesel. Alternative ways of biodiesel production have been explored using polyoxometalates (POMs) based acid catalysts.[31–33] Metal organic frameworks (MOFs)[34–36] are another class of materials that have been explored as catalyst in biodiesel production. MOF-based catalysts show metal leaching during reactions. Considering the above factors, metal-free carbocatalysts are more advantageous. A metal-free acidic carbocatalyst worth mentioning here is a porous polymer which has been reported which was synthesized via Friedel-Crafts alkylation process and thereafter sulfonated.[37] The carbocatalyst upon sulfonation has been acted as an efficient acid catalyst towards esterification/transesterification reactions. Another type of metal free carbocatalyst is graphene-based catalyst, which has been investigated too. A graphitic nitride as catalyst has been prepared for esterification and transesterification reactions[38] while a sulfonated carbon-based graphene oxide has been reported for esterification of levulinic acid with benzyl alcohol.[39] Recently, researchers have been given great attention on the design and synthesis of porous materials.[40–42] Covalent organic frameworks (COFs) and porous organic polymers (POPs)[43–45] have been found as promising heterogeneous catalysts due to their large surface areas, defined pore size, low density, high stability, and greater hydrophobic part which increase their catalytic efficiency.[46–50] Porous polymers having basic N atoms can function as better gas storage and adsorption materials.[51-52] Recently, triphenylamine- and triphenyltriazinebased two-dimensional covalent organic frameworks have been reported as efficient CO_2 adsorption and energy storage capacitors.[53] POPs have been functionalized with sulfonic acid groups, which provide interesting results in catalytic property of the materials.[54-55] A novel functionalized sulfonated

polymer[56] with high surface area of 2625 m^2 g^{-1} has been prepared for proton conduction in water. About 92–98% yields of various biodiesel compounds have been obtained using this catalyst. Similarly, numerous possibilities as catalysts and gas adsorbents of COFs and COPs (covalent organic polymers) are still yet to be explored.[57,58] Relative ease in synthesizing these materials and relatively higher stability in organic and aqueous media make these materials as promising candidates in various applications especially as heterogeneous catalysts. Aromatic benzoselenadiazole based materials provide electronic, optical and optoelectronic behavior.[59] Benzoselenadiazole based porous MOF has been used as an active heterogeneous photocatalyst for cross-dehydrogenative coupling reactions.[60] In our quest of exploring COPs as gas adsorbent and as heterogeneous catalyst especially for biodiesel synthesis by esterification/transesterification of fatty acids, a benzoselenadiazole-based covalent organic porous framework named as sulfonated **COP-2** has been synthesized and reported here. We have incorporated benzoselenadiazole core in the covalent organic framework to increase the thermal stability[61] and chemical reactivity towards the sulfonation type aromatic electrophilic substitution reaction. Sulfonic groups have been attached on the organic framework by the covalent bond formation. Benzoselenadiazole core is basic in nature due to the presence of diazole's nitrogen atoms. The nitrogen atoms make a polar region inside the pore of the framework (**COP-2**). Polar pore can isolate or adsorb the substrate molecules (fatty acids) from the bulk solution through the hydrogen bonding interaction.[62] Selenium can also play the same role through the Se⋯H bonding interactions.[63] So, the benzoselenadiazole core can act as good host towards the substrates *i.e*. fatty acids. Considering the above facts, benzoselenadiazole-based sulfonated **COP-2** has been investigated as a solid heterogeneous catalyst for biodiesel synthesis. The surface area of **COP-2** has been calculated as 158 m^2 g^{-1} with a pore size of 4.49 nm. The sulfonated organic framework with fibrous nanoporous nature has functioned efficiently as heterogeneous catalyst in the esterification of fatty acids.

2.2 Experimental section.

2.2.1 Materials and methods. TMSA (trimethylsilylacetylene), 1,3,5 tribromobenzene, triethylamine, Pd(PPh₃)₂Cl₂, CuI, trimethylsilylacetylene, potassium carbonate, selenium dioxide, anhydrous sodium sulfate, chlorosulfonic acid, sulfuric acid, liquid bromine and deuterated solvents were purchased from Alfa Aesar, India. All solvents were purchased from Merck and distilled according to literature prior to use. Reactions were monitored by thinlayer chromatography (TLC). Silica gel was used as stationary phase for column chromatography. ^{1}H and ^{13}C NMR spectra were recorded on Bruker 400 MHz spectrometer for the characterization of relevant compounds. Chemical shifts (δ) are reported in ppm relative to the residual solvent signal. Solid state ^{13}C NMR spectra were recorded on JEOL; Model: ECX400 (Proton frequency: 400 MHz, using 10 KHz and 100 MHz CP-1).

Scheme 2.1 Synthetic scheme of **COP-1** and **COP-2.**
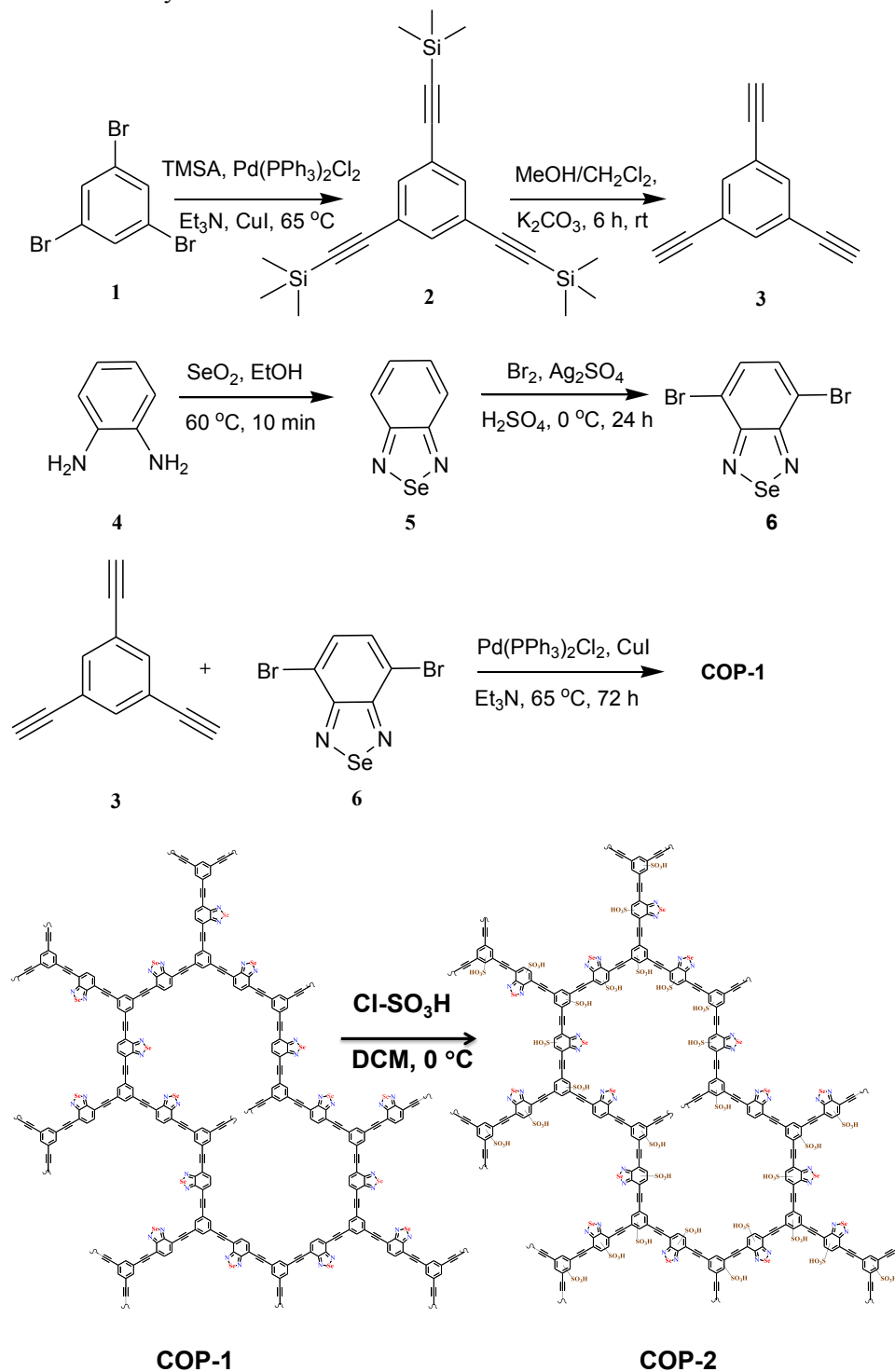
2.2.2 Synthesis of compounds.

2.2.2.1 Synthetic procedure of 1,3,5-tris(trimethylsilyl)ethynyl)benzene 2: To a solution of 1,3,5-tribromobenzene **1** (21 g, 66.7 mmol) in 200 mL dry

triethylamine, $Pd(PPh_3)_2Cl_2$ (5 mol%, 2.2 g) and CuI (5 mol %, 588 mg) were added in stirring condition under argon atmosphere. After purging the whole reaction mixture under argon atmosphere for 20 min, trimethylsilylacetylene (TMSA) (241.11 mmol, 34.33 mL) was added dropwise and the reaction was heated to 65 °C for 16 h. Then the reaction mixture was washed with 1 N HCl (100 mL × 3) and extracted with dichloromethane. After evaporation of solvent, the residue was purified by column chromatography on silica gel eluted with only hexane to give 12 g (32.7 mmol, yield 63%) of 1,3,5-tris(trimethylsilylethynyl)benzene **2** as pale yellow crystalline solid.

^{1}H NMR (400 MHz, CDCl3): δ 0.22 (27H, s), 7.49 (3H, s) ppm. ^{13}C NMR (100 MHz, CDCl3): δ 135.69, 123.82, 103.31, 95.74 ppm. MS (ESI) m/z: $(M + 2H)^+$ calcd. for $C_{21}H_{32}Si_3$ 368.1812; found 366.1948. Anal. Calcd for $C_{21}H_{30}Si_3$: C 68.78, H 8.25; found: C 69.3, H 8.1.
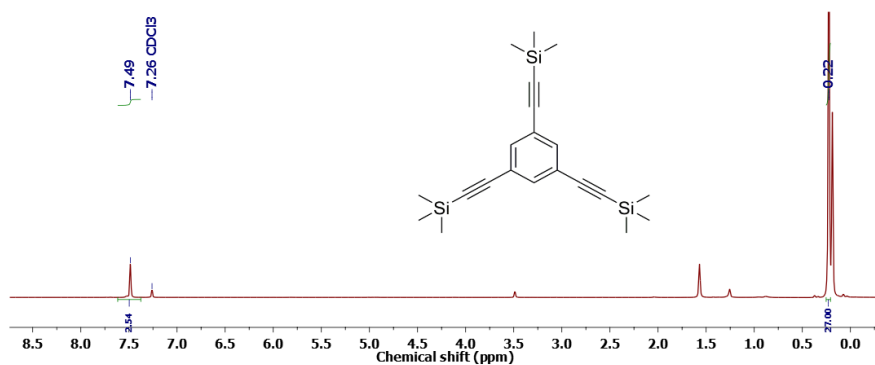
Figure 2.1 ^{1}H NMR (400 MHz, CDCl3) spectrum of **2**. (Peak at around 1.5 ppm is coming for H_2O).
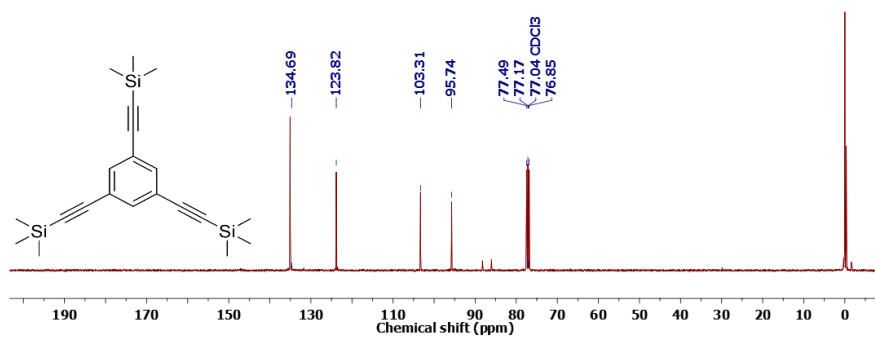
Figure 2.2 ^{13}C NMR (100 MHz, CDCl3) spectrum of **2**.
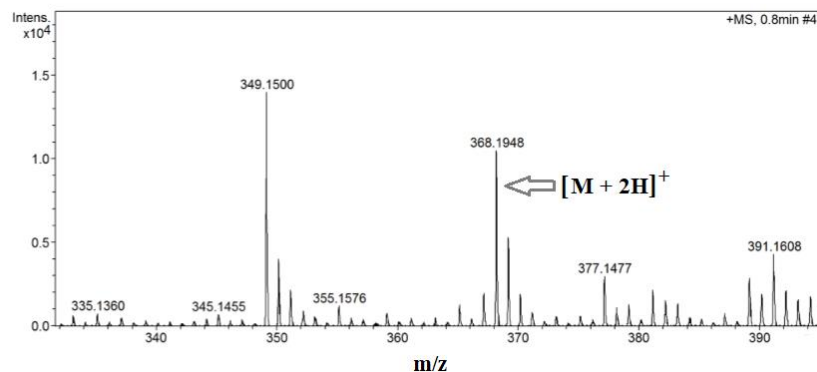
Figure 2.3 ESI-MS spectrum of **2.**

2.2.2.2 Synthetic procedure of 1,3,5-triethynylbenzene 3.

1,3,5-tris((trimethylsilyl)ethynyl)benzene (11.4 g, 31.12 mmol) was dissolved in dichloromethane (100 mL) and methanol (30 mL) and a solution of anhydrous potassium carbonate (735 mg) was added. The mixture was stirred at room temperature for 6 h and monitored by TLC. Then, water (90 mL) was added and the organic solvent was evaporated. The residue was extracted with dichloromethane, washed with water and brine, and dried over anhydrous sodium sulfate. Organic part was concentrated under vacuum and purified by flash column chromatography using 4% hexane in ethyl acetate as eluent to give 3.5 g (23.3 mmol, 93% yield) as off white solid product.

^{1}H NMR (400 MHz, CDCl$_3$): δ 7.50 (s, 3H), 3.03 (s, 3H) ppm.

^{13}C NMR (100 MHz, CDCl$_3$): δ 135.64, 122.93, 81.60, 78.67 ppm. MS (ESI) *m/z*: (2M + H)$^+$ calcd for C$_{24}$H$_{13}$ 301.1; found 301.1. Anal. Calcd for C$_{12}$H$_6$: C 95.97, H 4.03; found: C 95.15, H 4.85.
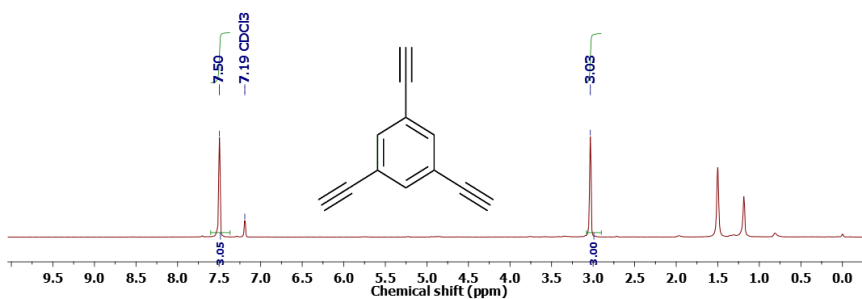
Figure 2.4 ^{1}H NMR (400 MHz, CDCl$_3$) spectrum of **3.** (Peak at around 1.5 ppm is coming for H$_2$O).
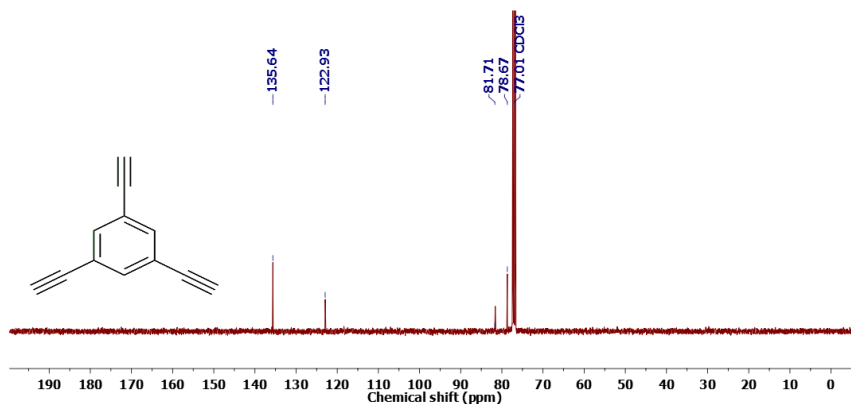
Figure 2.5 ^{13}C NMR (100 MHz, CDCl$_3$) spectrum of **3**.
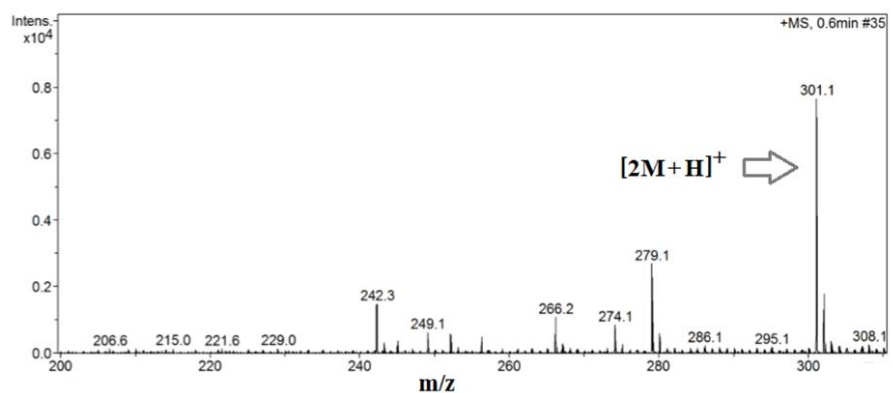
Figure 2.6 ESI-MS spectrum of **3**.

2.2.2.3 Synthetic procedure of benzo[2,1,3]selenadiazole 5.

An amount of *o*-phenylenediamine **4** (10.5 g, 97.1 mmol) and selenium dioxide (11.85 g, 106.8 mmol) were refluxed at 65 °C in absolute ethanol (100 mL) for 10 min. The reaction mixture was cooled to room temperature and ethanol was evaporated under vacuo. The product was precipitated from water to yield 17.6 g (96.1 mmol, 99% yield) as a faint pink colored solid.

^{1}H NMR (400 MHz, CDCl$_3$): δ 7.77-7.75 (2H, d), 7.39-7.37 (2H, d) ppm. ^{13}C NMR (100 MHz, CDCl$_3$): δ 160.41, 129.46, 123.60 ppm. Anal. Calcd for C$_6$H$_4$N$_2$Se: C 39.36, H 2.2, N 15.3; found: C 40.16, H 2.7, N 15.18.
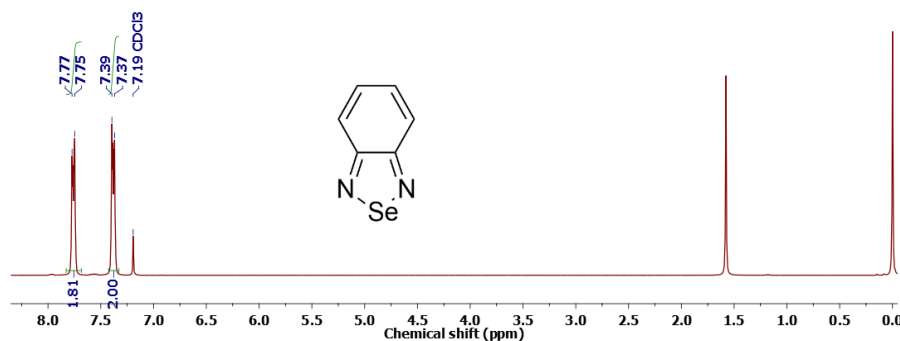
Figure 2.7 ^{1}H NMR (400 MHz, CDCl$_3$) spectrum of **5**. (Peak at around 1.5 ppm is coming for H$_2$O).
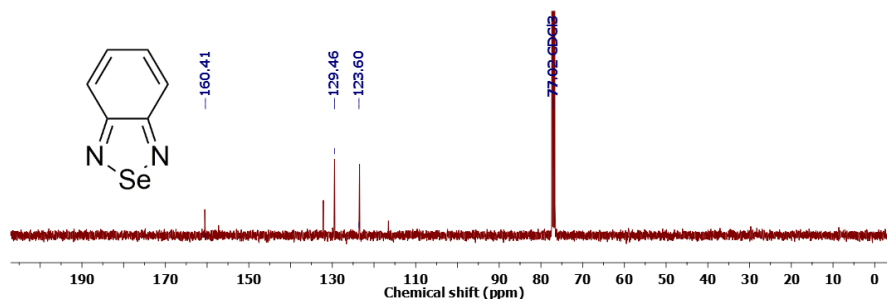
Figure 2.8 ^{13}C NMR (100 MHz, CDCl$_3$) spectrum of **5.**

2.2.2.4 Synthetic procedure of 4,7-dibromobenzo[2,1,3]selenadiazole 6.
Bromine (16.2 g, 0.01011 mol) was added dropwise to a solution of 2,1,3-benzoselenadiazole **5** (9.33 g, 0.051 mol) along with silver sulfate (15.9 g, 0.051 mol) in concentrated sulfuric acid (81 mL). The mixture was shaken at a room temperature for 24 h. The precipitate of silver bromide was filtered off, and the filtrate was poured into ice water. The precipitate was extracted by ethyl acetate and washed with water for three times and ethyl acetate (500 mL) then purified by column chromatography using hexane: dichloromethane (50:50) as eluent. This gave 4,7-dibromo-2,1,3-benzoselenadiazole **6** (10.5 g, 30.9 mmol, 60%) as golden yellow needles. ^{1}H NMR (400 MHz, CDCl$_3$): δ 7.57 (2H, s) ppm.
^{13}C NMR (100 MHz, CDCl$_3$): δ 157.23, 132.29, 116.31 ppm.
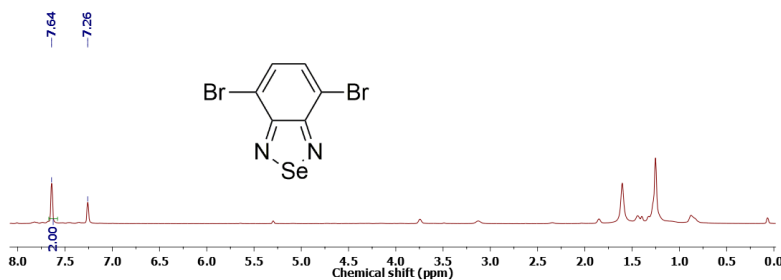
Figure 2.9 ^{1}H NMR (400 MHz, CDCl$_3$) spectrum of **6**. (Peak at around 1.5 ppm is coming for H$_2$O).
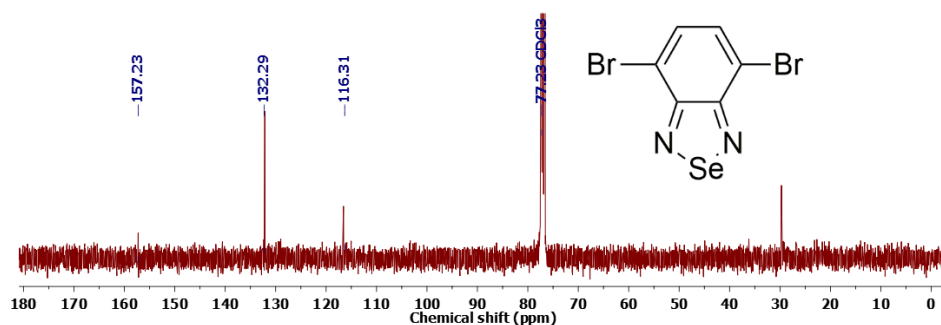
Figure 2.10 ^{13}C NMR (100 MHz, CDCl$_3$) spectrum of **6.**

2.2.2.5 Synthetic procedure of COP-1.

1,3,5-triethynylbenzene **3** (3 g, 19.9 mmol) and 4,7-dibromobenzo [2,1,3]selenadiazole **6** (9.9 g, 29.2 mmol) were taken in 100 mL triethylamine solvent in 250 mL single neck round bottom flask and the solution mixture was purged for 20 min under argon medium. Degassing was followed by addition of Pd(PPh$_3$)$_2$Cl$_2$ (8 mol%) and CuI (5 mol%) and the reaction mixture was kept for 3 days under argon atmosphere. After that residual solvent was removed in reduced pressure and precipitate was diluted with dichloromethane and washed with water by suction filtration set up. Then DCM was evaporated under vacuum and residue was washed with acetone, methanol and ethyl acetate for three times to obtain **COP-1** as brown solid. The product was dried in vacuum at 80 °C. 4.5 g of compound was obtained which was characterized by solid state ^{13}C NMR spectroscopy.

2.2.2.6 Synthetic Procedure of COP-2.

2.4 g of **COP-1** was taken in 40 mL dry DCM and 40 mL of ClSO$_3$H was added dropwise in ice bath at 0 °C and the solution mixture was stirred up to 48 h. The resultant mixture was poured into the ice bath and the solid was collected and poured into the ice water. The solid formed was collected by normal filtration. The brown powder was filtered and washed with distilled water repeatedly. It was dried in vacuum at 80 °C. 2 g of **COP-2** was obtained. **COP-2** was characterized by solid state ^{13}C NMR spectroscopy, FT-IR and powder XRD.

2.2.3 Calculation of acid strength of COP-2.

30 mg sulfonated polymer (**COP-2**) was stirred in 30 mL distilled water for 4 h at 313 K. After cooling to room temperature, 13 mL sodium hydroxide solution of strength 0.062 (N) was added to 10 mL aqueous mixture of sulfonated **COP-2**. After filtration, the excess NaOH solution was back titrated with 0.14 (N) oxalic acid solutions. 4.0 mL oxalic acid was needed to reach the first equivalence point of oxalic acid.

$$V_{NaOH} \times S_{NaOH} = V_{OX} \times S_{OX}$$

$V_{NaOH} \times 0.062$ (N) $= 4.0 \times 0.14$(N)

$V_{NaOH} = 9.03$ mL

So the NaOH required to neutralize the acidic site of **COP-2** $= (13-9.03)$ mL $= 3.97$ mL.

$V_{NaOH} \times S_{NaOH} = V_{COP-2} \times S_{COP-2}$

3.97×0.062 (N) $= 10 \times S_{COP-2}$

$S_{COP-2} = 0.0246$ (N)

The molecular weight of sulfonic acid group ($-SO_3H$) is 81.

So, 30 mL 0.024 (N) **COP-2** solution contains 0.059 g free sulfonic acid group. Calculation: 1000 mL 1(N) **COP-2** = 81 g free sulfonic acid in the solid matrix (**COP-2**). 30 mL 0.024 (N) **COP-2** = 0.059 g free sulfonic acid = 0.7284 mmol free sulfonic acid. 30 mg sample (**COP-2**) contains 0.7284 mmol free sulfonic acid. 1000 mg sample (**COP-2**) contains 24.28 mmol free sulfonic acid. So free sulfonic acid site of the solid **COP-2** is 24.28 mmol/gm. By using the same procedure, we have calculated the free sulfonic acid site of **COP-2A** and **COP-2B.**

2.2.4 Characterization techniques.

Mass spectra were obtained on a Bruker MicrOTOF-Q II by positive mode electrospray ionization. All NMR spectra were recorded on a 400 MHz Bruker AV400 NMR. UV-Vis was done in Varian Cary 100 Bio UV Visible spectrophotometer. Powder XRD was done in Rigaku SmartLab, Automated Multipurpose X-ray Diffractometer equipped with a high-accuracy theta-theta goniometer featuring a horizontal sample mount. BET surface area analysis was done in quantachrome, Autosorb iQ2. Thermogravimetric analysis (TGA) was carried out using a METTLER TOLEDO TGA instrument. The samples were heated from 25 °C to 1000 °C at a constant rate of 5 °C min^{-1} in a nitrogen gas environment. Differential Scanning Calorimeter was done in DSC 214 SET MFC LN2 at 10 °C min^{-1} heating rate. XPS (X-ray photoelectronic spectroscopy) was performed using AXIS Supra instrument (Kratos Analytical, UK, SHIMADZU group). FT-IR spectra of all reported compounds were performed using a Bruker (Tensor-27) FT-IR spectrophotometer. The GC-MS QP 2010 Ultra mass spectrometer from Shimadzu Analytical India Pvt. Ltd was used. In GC-MS helium as inert carrier gas was used and could detect up to ppm level masses. The mass range is 10–1000 Da, which allows analysis over a wide range of low and high molecular weight compounds. NIST Mass spectra library is available for separation/identification of organic compounds and molecules.

2.3 Results and discussion.

In the present work, a benzoselenadiazole-based covalent organic porous framework named as **COP-1** was synthesized *via* Sonogashira coupling. **COP-1** was functionalized with -SO$_3$H group through HSO$_3$-Cl acid treatment, which is named as **COP-2** (Scheme 2.1). **COP-2** was investigated as a solid heterogeneous catalyst for biodiesel synthesis. In order to characterize the molecules, UV-vis spectra of the **COP-1** and **COP-2** were recorded in the solid state (Figure 2.11a). Two COPs show broad absorption peaks across the wavelength range of 390-440 nm which are very similar with the COF/COP materials available in literature.[64] **COP-1** shows adsorption peak at 430 nm due to n-π* transition which is sharper than that of **COP-2**. The absorbance maxima value at this region was found to be somewhat less than in case of **COP-2**. Followed by UV-Vis, FT-IR spectra as shown in Figure 2.11b were recorded to investigate the structural arrangement. The low intensity peaks at 2921 cm^{-1} and 2854 cm^{-1} of **COP-1** correspond to the aromatic sp^2 C-H stretching frequency. The peak at 2338 cm^{-1} corresponds to C≡C frequency. The sharp intensity peaks at 1632 cm^{-1} and 1579 cm^{-1} correspond to -C=C- stretching and -C=N- frequencies. The peak at 1367 cm^{-1} suggests sp^3 C-H bending. Other peaks at 1116 cm^{-1} and 675 cm^{-1} correspond to aromatic sp^2 C-H bend. With the incorporation of -SO$_3$H group in the **COP-1** backbone, the intensities of all the relevant peak positions of **COP-2** increased along with the appearance of two new stretching frequencies at 1034 cm^{-1} and 1198 cm^{-1} which correspond to S=O stretching. With extra -SO$_3$H groups in **COP-2**, stretching frequencies of sp^2 -C-H, aromatic -C=C-, aromatic -C=N and –C≡C shift towards 2925 cm^{-1}, 1680 cm^{-1}, 1625 cm^{-1} and 2360 cm^{-1}.
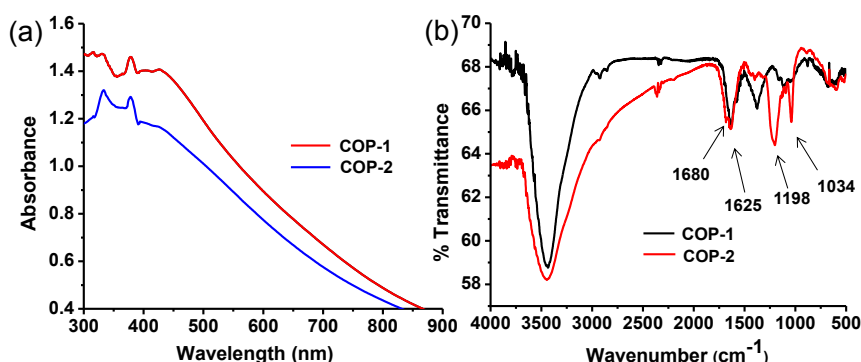
Figure 2.11 Solid state UV-vis spectra of **COP-1** and **COP-2**, (b) FT-IR spectra of **COP-1** and sulphonated acid catalyst **COP-2**.

The solid state ^{13}C NMR spectrum of **COP-1** (Figure 2.12a) shows signals at 77.52, 83.45, 124.44 ppm and in the range of 140-150 ppm. The ^{13}C NMR peaks at 77.52 and 83.45 ppm correspond to carbon atoms of –C≡C- group which acts as bridge joining the two aromatic groups. The response at 124 ppm is attributed to the carbon atom of the symmetric aromatic group. The remaining carbon

atoms between 140 and 150 ppm are the carbon atoms of benzoselenadiazole group. For ^{13}C NMR spectrum of **COP-2** (Figure 2.12b), the ^{13}C signals of the -C≡C- group as observed in **COP-1** shifted up-field at 73.45 ppm and 76.43 ppm. All the aromatic carbon atoms generate one single broad signal from 120 to 150 ppm.
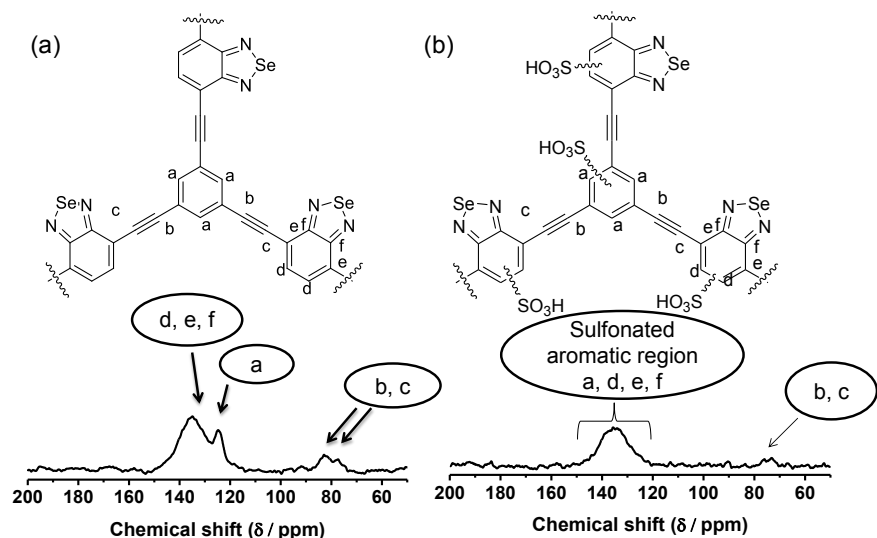
Figure 2.12 Solid state ^{13}C NMR spectra of (a) **COP-1** and (b) **COP-2**.

PXRD patterns of both the **COP-1** (Figure. 2.13a) and **COP-2** (Figure 2.13b) reveal broad peaks that indicate amorphous nature of the frameworks. For **COP-1**, 2θ at 22.28° (d = 0.399 nm) and another peak at 5.5° (d = 1.64 nm) are observed and for **COP-2**, 2θ at 22.15° (d = 0.4 nm) and 5.29° (d = 1.67 nm) are observed. The d spacing at 0.399 nm for **COP-1** and 0.4 nm for **COP-2** suggests π- π stacking interaction[65] among aromatic functional groups.
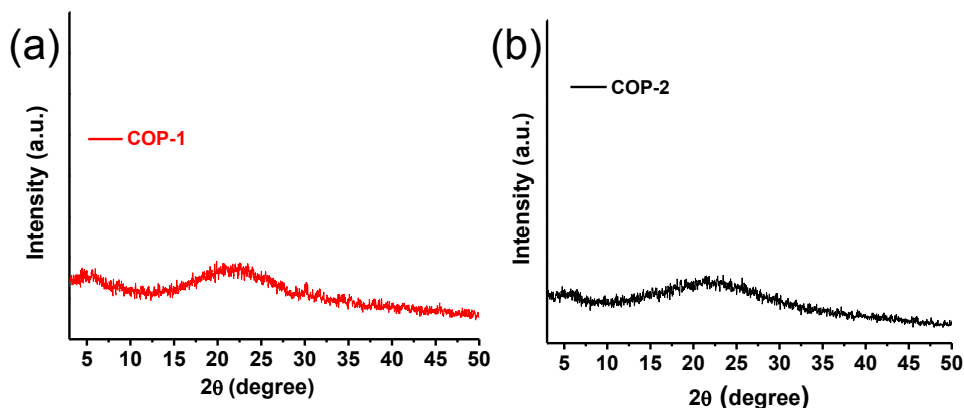
Figure 2.13 Wide angle powder XRD of (a) **COP-1** and (b) **COP-2**.

The surface morphology as observed from the SEM images at 10 μm shows fibrous nature of the frameworks with high porosity (Figure 2.14a and 2.14b). SEM images of **COP-1** and **COP-2** show difference in pore size.
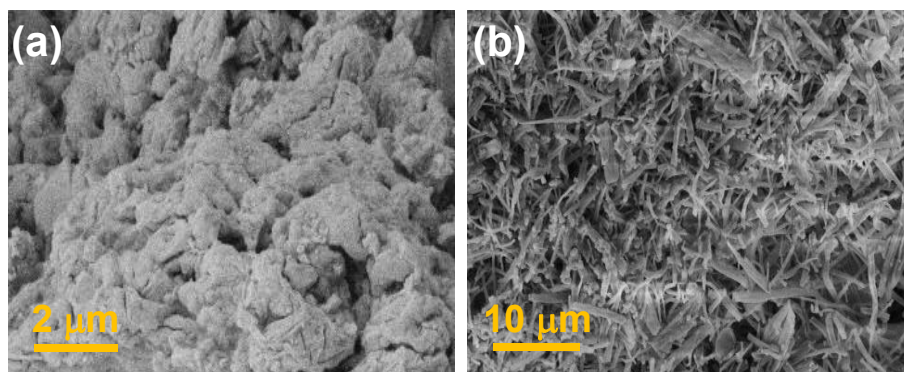
Figure 2.14 SEM images of (a) **COP-1** and (b) **COP-2.**

Upon sulfonation, non-covalent interactions (H-bonding) between -SO₃H groups and other organic moieties may be the caused of different morphology. The robustness of the COPs was demonstrated by thermogravimetric analysis (TGA). Figure 2.15a and Figure 2.15b suggest high thermal stability of both the **COP-1** and **COP-2**. **COP-1** is quite stable up to 150 °C. A weight loss of 52% is observed between 150 and 360 °C for **COP-1**. The next step is the degradation of the molecules from 360 °C to 680 °C of about 48%. For the catalyst **COP-2**, four steps of degradation process are observed. Initial weight loss of 10.6% is seen from 30 to 100 °C due to the release of the residual solvent molecules trapped inside the pores of the **COP** network. Then in the second step, the weight loss of 21.46% is seen from 100 to 300 °C. In the third step, the weight loss of 58.51% is observed from 300 to 540 °C. In the fourth step, weight loss of 9% is observed from 540 to 980 °C. Sulfonated **COP-2** shows slower thermal degradation process compare to the non sulfonated **COP-1**.
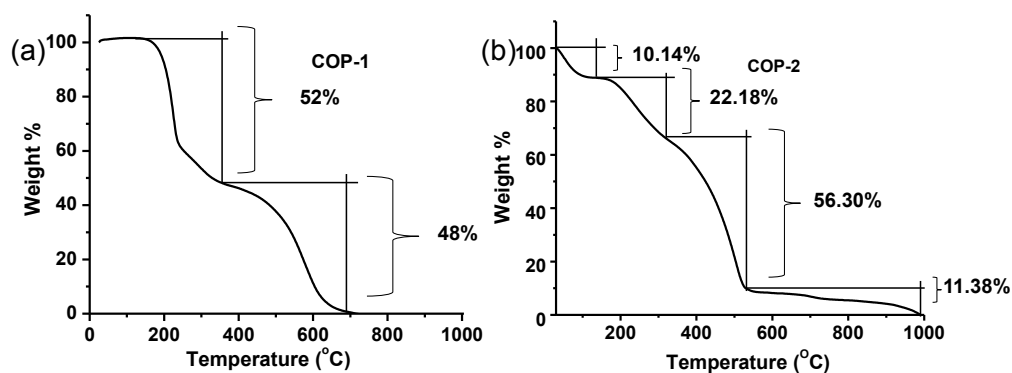
Figure 2.15 Thermogravimetric analysis of (a) **COP-1** and (b) **COP-2.**

Differential scanning calorimetry (DSC) data (Figure 2.16) of benzoselenadiazole based **COP-1** and **COP-2** show Tg (glass transition temperature) values of 127.7 °C, which suggest a reversible transition in amorphous COP materials from glassy-like state to rubbery state with increase in temperature. Incorporation of sulfonic acid group does not show any discrimination in Tg value in the sulfonated **COP-2**.
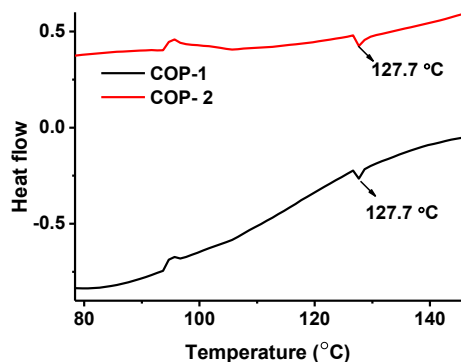
Figure 2.16 Differential scanning calorimetry (DSC) thermograms of **COP-1** and **COP-2.**

The porous nature of the **COP-1** and **COP-2** were discerned by BET at 77 K using N_2 gas adsorption analyzing the surface area and pore size distribution of the COPs (Figure 2.17a, b, c and d). The N_2 sorption shows type-IV BET isotherm for both the **COP-1** and **COP-2**. From this study, the surface area of **COP-2** is observed as 158.66 m^2 g^{-1}. However, in case of **COP-1**, the surface area is observed as 471.8 m^2 g^{-1} (Table 2.1). The decrease in surface area and pore volume for **COP-2** is observed due to the incorporation of extra -SO$_3$H groups. Pore size distribution of the COPs was done using carbon slit pore model at 77 K and determined by the NLDFT (nonlocal density functional theory) model. The study exhibits an average pore size of 4 nm for **COP-2**.

Figure 2.18 shows the XPS spectra of the deconvoluted peaks of **COP-2** for the elements C1s, N1S, S2p, O1s and Se3d.[66–68] The deconvoluted C1s spectrum in **COP-2** shows five peaks including C=CH-C at 284.76 eV, C-C=C at 285.5 eV, -C-C=N at 286.3 eV, -C≡C- at 287.0 eV and -CSO$_3$H at 290.03 eV. N1s core level spectrum shows peak at 398.8 eV, which suggests -C=N. Two peaks of S2p3/2 at 168.48 eV and S2p1/2 at 170.7 eV correspond to S2p spectrum of SO$_3$H. The peaks in between 168.48 eV and 170.7 eV correspond to a higher oxidation state of sulfur in **COP-2**. A peak centered at 531.25 eV (S=O) is associated with O1s spectrum. O1s core level spectrum shows that all the peaks arise between 536 and 530 eV with peak maxima at 531.2 eV.
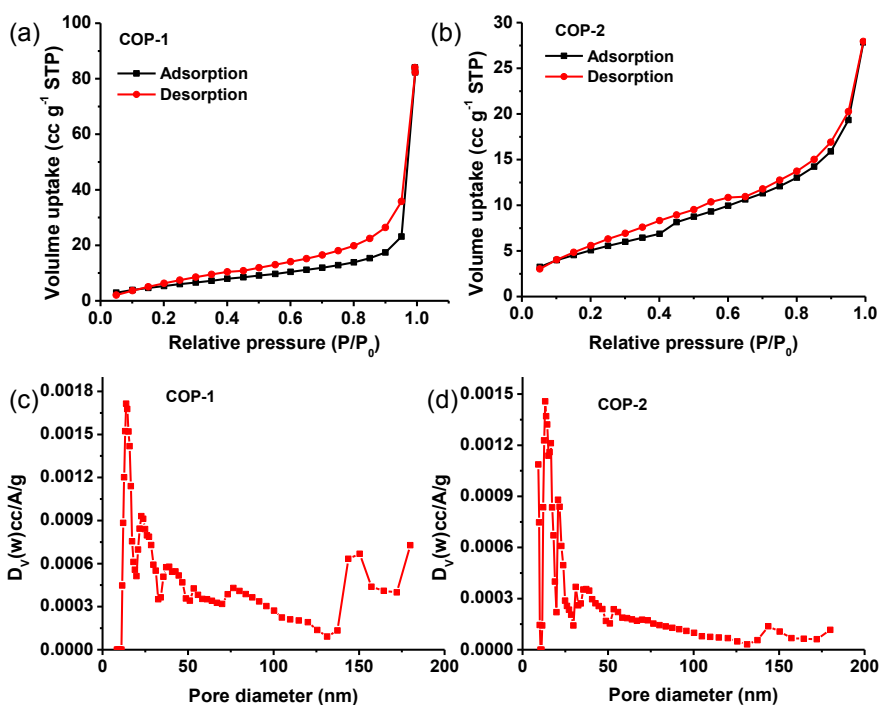
Figure 2.17 (a) N_2 adsorption/desorption isotherms of (a) **COP-1** and (b) **COP-2** Pore size distribution of (c) **COP-1** and (d) **COP-2** by using the NLDFT methods.

Table 2.1 The BET isotherm model parameters for the adsorption of N_2 gas by **COP-1** and **COP-2**

Compound	Surface area ($m^2 g^{-1}$)	Pore Volume (cc g^{-1})	Pore Size (nm)	Isotherm type	Max gas adsorption (cc g^{-1})
COP-1	417.8	0.127	11.42	IV	84.30
COP-2	158.66	0.043	4.49	IV	27.96

The core level spectrum of O1s suggests that the oxygen is in -2 oxidation state. Se3d shows only one peak at 56.6 eV (Se-N) (green and red curves are merged in Figure 2.18f). Additionally, the degree of sulfonation is estimated by using the XPS elemental analysis. All the sulfur content exists in the form of sulfonic acid groups which is revealed by FT-IR spectra. The surface atomic concentrations of C1s, N1s, S2p, O1s and Se3d are calculated and shown in Table 2.2. The XPS results show the high -SO_3H density on **COP-2** surface.

Table 2.2 Surface atomic concentration (atomic%) from XPS of **COP-2**

Element	C1s	N1s	S2p	O1s	Se3d
Atomic (%)	71.95	1.48	3.26	23.25	0.06
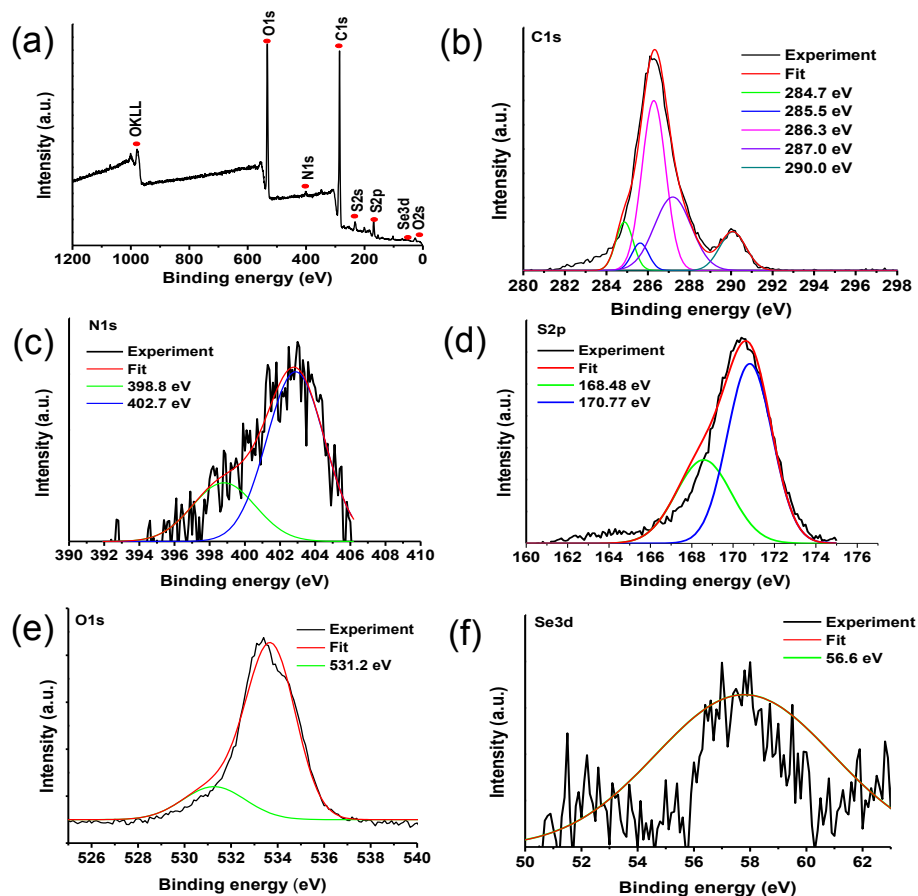
Figure 2.18 (a) XPS survey spectrum of **COP-2**. (b), (c), (d), (e) and (f) are the XPS spectra for the deconvoluted peaks for the elements of C1s, N1s, and S2p on **COP-2** surface.

2.3.1 Catalytic performance.

COP-2 was utilized as a catalyst for the conversion of methyl esters of long chain fatty acids like lauric acid, myristic acid, palmitic acid, stearic acid, sebacic acid, adipic acid and oleic acid, which serve as the feedstock for biodiesel (**Scheme 2.2**). 0.5 wt% of **COP-2** was loaded for the catalytic reactions. The reactions were carried out at room temperature with high conversion percentage suggesting high efficiency of the catalyst. The -SO$_3$H groups act as Bronsted acids, which enhance the catalytic activity with higher efficiency. GC was carried out in RTX-5MS as stationary phase to monitor the catalytic efficiency along with ^{1}H NMR and ^{13}C NMR (**Appendix-A**) experiments.

Lauric acid converted to methyl laurate in 7 h reaction time with 100% conversion with 0.5 wt% of **COP-2** catalyst loading. 15% methyl laurate conversion was observed at 0.5 h. The efficiency of the catalyst **COP-2** was also investigated with the esterification of lauric acid to methyl laurate at room temperature at different time scales from 0.5 to 7 h. The progress of the reaction is shown in Figure **2.19** a.

Esterification reactions
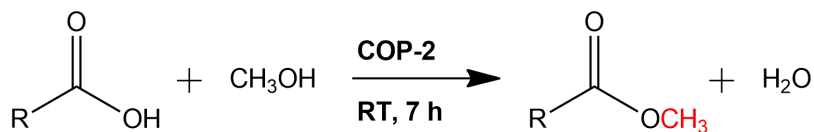
R = CH_3(CH_2)_9, CH_3(CH_2)_12, CH_3(CH_2)_14, CH_3(CH_2)_16, CH_3(CH_2)_7CH=CH(CH_2)_7, HOOC(CH_2)_8, HOOC(CH_2)_4

Transesterification reactions

CH_3(CH_2)_9COOCH_3 + CH_3CH_2OH $\xrightarrow[\text{RT, 24 h}]{\text{COP-2}}$ CH_3(CH_2)_9COOCH_2CH_3

Methyl laurate   **Ethyl laurate**

CH_3(CH_2)_9COOCH_2CH_3 + MeOH $\xrightarrow[\text{RT, 24 h}]{\text{COP-2}}$ CH_3(CH_2)_9COOCH_3

Ethyl laurate   **Methyl laurate**
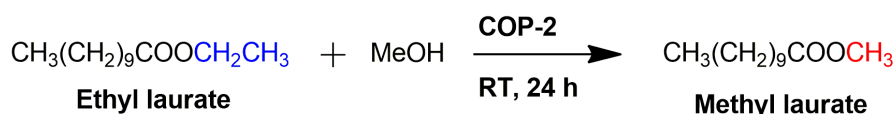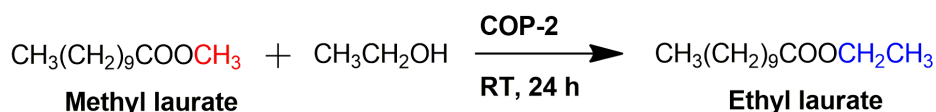
Scheme 2.2 COP-2 catalysed esterification/ transesterification reactions of fatty acids at room temperature.
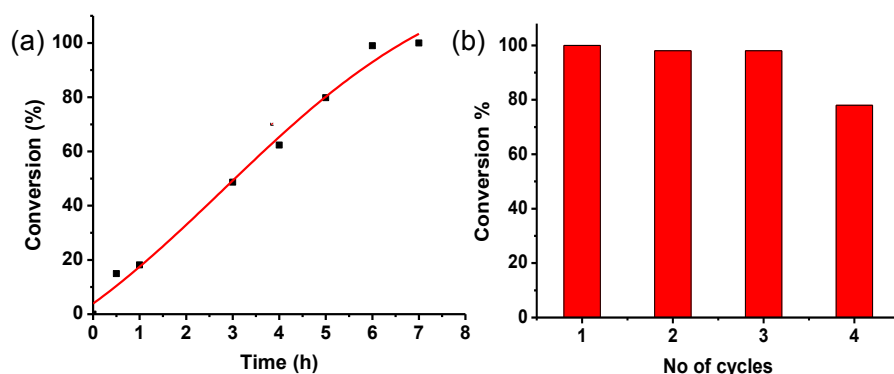
Figure 2.19 (a) Reaction time *vs* conversion (%) curve for lauric acid at room temperature with **COP-2**, (b) Recyclability of **COP-2** catalyst in the esterification of lauric acid.

For the conversion of myristic acid into its corresponding methyl ester, the product conversion is 99% at 7 h (Table 2.3). **COP-2** can also respond in transesterification reaction. Here, **COP-2** was used to perform transesterification of methyl laurate to ethyl laurate and vice versa at room temperature for 24 h using 5 wt% of the catalyst. The transesterification reaction resulted in 59% conversion of ethyl laurate to methyl laurate (Table 2.3) which was supported through Gas Chromatographic, ^{1}H NMR and ^{13}C NMR studies (**Appendix A**). The transesterification of methyl laurate to ethyl laurate was also monitored for 24 h and 29% conversion was observed from GC (**Appendix A**).

Table 2.3 Summary of the esterification and transesterification reactions catalyzed by **COP-2.**

S. No	Reactants (Fatty Acids)	Products (Biodiesel)	Time (h)	Conversion[a]
1	$CH_3(CH_2)_{10}COOH$ (Lauric acid)	$CH_3(CH_2)_{10}COOCH_3$	7	100%
2	$CH_3(CH_2)_{10}COOH$ (with recycled catalyst)	$CH_3(CH_2)_{10}COOCH_3$	7	99%
3	$CH_3(CH_2)_{12}COOH$ (Myristic acid)	$CH_3(CH_2)_{12}COOCH_3$	7	99%
4	$CH_3(CH_2)_{14}COOH$ (Palmitic Acid)	$CH_3(CH_2)_{14}COOCH_3$	7	100%
5	$CH_3(CH_2)_{16}COOH$ (Stearic Acid)	$CH_3(CH_2)_{16}COOCH_3$	7	100%
6	$CH_3(CH_2)_7CH=CH(CH_2)_7COOH$ (Oleic Acid)	$CH_3(CH_2)_7CH=CH(CH_2)_7COOCH_3$	7	100%
7	$(HOOC)(CH_2)_8(COOH)$ (Sebacic Acid)	$(H_3COOC)(CH_2)_8(COOCH_3)$	7	100%
8	$(HOOC)(CH_2)_4(COOH)$ (Adipic Acid)	$(H_3COOC)(CH_2)_4(COOCH_3)$	7	100%
Transesterification Reactions				
9	$CH_3(CH_2)_{10}COOCH_3$	$CH_3(CH_2)_{10}COOC_2H_5$	24	29%
10	$CH_3(CH_2)_{10}COOC_2H_5$	$CH_3(CH_2)_{10}COOCH_3$	24	59%

[a]Conversion determined by GC.

The screening of the catalyst was carried out with different wt% of catalyst ranging from 0.5 to 3 wt% for 7 h. In all the cases, 100% conversion was observed as shown by the corresponding GC data (**Appendix A**). We also accomplished some other reactions of fatty acids to its methyl ester conversion at room temperature, which is given below in Table 2.3. Four fatty acids including myristic, palmitic, stearic and oleic acids with 2 mL MeOH and 0.5 wt% catalyst were used to study the progress of the reaction starting from 0 to 7 h similar to that of lauric acid. After 4-5 h, the methyl ester conversion as obtained from GC was found to be 100% for all the four acids. Thus the catalyst is found to be more efficient in these cases (**Appendix A**). To show the effect of degree of modification ratio on its catalytic activity, the catalyst **COP-2** was modified as **COP-2A** and **COP-2B**. **COP-2A** and **2B** are the two modified forms of catalyst **COP-2** based on the degree of sulfonation. **COP-2** contains greater no of free sulfonic acids group than that of **COP-2A** and **2B**. The order of catalytic activity for conversion of lauric acid to methyl laurate is **COP-2** > **COP-2A** > **COP-2B** which exactly follows the order of number of free sulfonic acid groups existing on the COP surface (Table 2.4).

Table 2.4 The catalytic effect of degree of modified catalyst **COP-2.**

S. No	COP-1 / HSO₃Cl (mg mL⁻¹)	Catalyst	Free sulfonic acidic sites (mmol g⁻¹)	Methyl ester conversion (%) of lauric acid after 7 h
1	30	**COP-2**	24.28	100
2	100	**COP-2A**	8.5	97
3	150	**COP-2B**	3.5	44

COP-2 contained 24.28 mmol g⁻¹ free sulfonic acid group (experimental section 2.2.3) which is used for acid catalysed biodiesel or biofuel production. The catalytic activity definitely depends on the free sulfonic acids existing on the surface of **COP** backbone. The formation of methyl esters from fatty acids follows acid-catalyzed nucleophilic substitution reaction (**Figure 2.20**).

COP-2 catalysed esterification reaction of fatty acids

R = long carbon chain of fatty acid
R¹ = -CH₃, R²= -CH₂CH₃
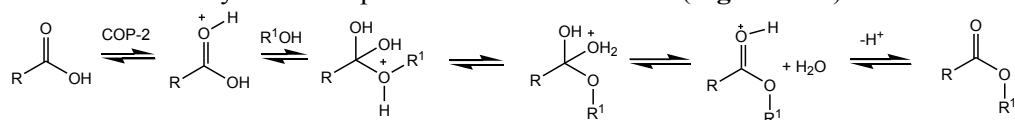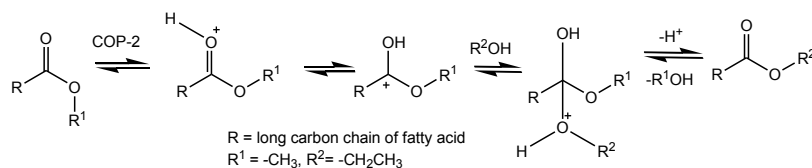
COP-2 catalysed transesterification reaction of fatty acid ester

Figure 2.20 Reaction mechanism of **COP-2** catalysed esterification and transesterification of fatty acids.

2.3.2 Recyclability and efficiency.

The recyclability experiment with 0.5 wt% catalyst **COP-2** was monitored in a very simple way with the esterification of lauric acid to methyl laurate for 7 h at room temperature via GC analysis. After completion of one cycle, the catalyst was easily recovered with minimal amount of loss by simple filtration, washed several times with water-methanol mixture and dried under 60 °C temperature. After drying, the recovered catalyst was weighed and used again for the same reaction under same reaction conditions. Every time gas chromatographic analysis was performed to monitor the conversion. Up to 3rd cycle, catalytic activity was retained after which it started diminishing. Figure 2.19b shows the histogram of catalytic efficiency of **COP-2**. The recycled **COP-2**, upto 4th cycle (Figure 2.21) shows similar XRD peaks at 22.46° and a small peak at 5.28°. The sulfonated **COP** with fibrous mesoporous nature has functioned efficiently as acid catalyst in the esterification of fatty acids with 99% yield.
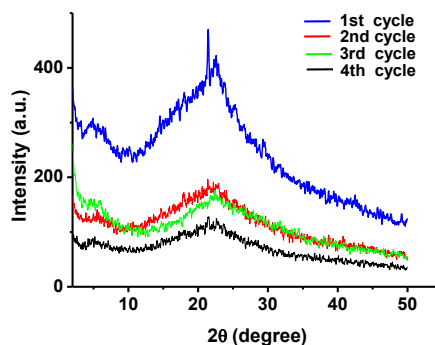
Figure 2.21 Wide angle powder XRD of **COP-2** upto 4th cycles.

Sulfonation in the COP backbone has many advantages such as it leads to better interaction with the incoming substrate. The reaction time was reduced to 4-5 h with almost 100% yield. The heterogeneous catalyst could be reused several times with almost similar efficiency. The catalyst could be recovered from the reaction medium by simple filtration technique. A catalytic reaction of lauric acid to methyl laurate with sulfonated benzoselenadiazole core (5 wt%) for 7 h was performed as control experiment. In this case, 91% conversion of methyl laurate was observed. However, the sulfonated benzoselenadiazole catalyst is soluble in the reaction mixture resulting in homogeneous environment. A comparative study of **COP-**2 for conversion of lauric acid to methyl laurate with other heterogeneous catalysts reported in literature is shown in Table 2.5. From the Table 2.5, it is observed that although catalysts PVDTASO₃H[69] and HMP-1SO₃H[70] showed greater than 90% conversion in esterification reaction of lauric acid to methyl laurate at room temperature but more time and more catalyst loading are required in these cases. In case of SPPOP-1,[37] negligible amount of catalyst is required for the conversion, however, more time is required. On the other hand, the catalysts Amberlyst-15,[71] sPS-S,[71] PDVB-xs-SO₃H,[72] PES-H,[73] PS-SO₃H@DSNs[74] and PS/nPMA-SiO₂HNs[75] required higher temperature to get the significant percentage of conversion of lauric acid to methyl laurate. Thus considering the time, temperature and catalyst loading mentioned in Table 2.5, benzoselenadiazole-based **COP-2** can be used as a promising catalyst for the esterification of fatty acids to esters in presence of mild condition.

Table 2.5 Summary of different catalysts used in esterification of lauric acid.

S. No	Catalyst	BET Surface (m^2g^{-1})	Reaction Conditions				Conversion (%)	Ref.
			Alcohol : Free Fatty Acid	Time (h)	Catalyst (wt%)	T (°C)		
1	PVDTA-SO₃H	406	109:1	10	20	25	98	69
2	HMP-1SO₃H	350	50:1	10	7	25	93	70
3	SPPOP-1	280	50:1	10	0.05	25	90	37
4	Amberlyst-15	45	16:1	6	0.5	65	57	71
5	sPS-S	0.1	16:1	8	0.5	65	100	71
6	PDVB-xs-SO₃H	380	20:1	5	19	70	99	72
7	PES-H	1.0	6:1	5	1.0	80	96	73
8	PS-SO₃H@ DSNs	410	5:1	6	2	85	90	74
9	PS/nPMA-SiO₂HNs	120-330	4:1	3	4.5	80	88	75
10	**COP-2**	158.66	80:1	7	0.5	25	100	This work

2.4 Conclusion.

Covalent organic frameworks are emerging class of porous compounds, which have huge possibilities in various application fields. Huge scope lies in their exploration. In summary, a covalent organic porous framework with large surface area 471.8 m^2 g^{-1} named as **COP-1** has been reported in this work. On sulfonation of **COP-1**, benzoselenadiazole-based catalyst **COP-2** was obtained which showed excellent catalytic activity for biodiesel production from long chain fatty acids at room temperature. **COP-2** contained 24.28 mmol g^{-1} free sulfonic acid group which is almost 6-8 times more than the previously reported. COPs for acid catalysed biodiesel or biofuel formation. The reaction time has been reduced as compared to literature and the catalyst could be removed by simple filtration techniques. The PXRD of the reused catalyst suggests that the catalyst is stable under reaction conditions even after successive reaction cycles. Catalysis of transesterification of methyl laurate to ethyl laurate was also found to be successful. Thus the catalyst is found to be promising in several aspects. In future more of such functionalized covalent organic frameworks will be investigated as heterogeneous catalysts in a variety of chemical reactions due to their structural diversity.

2.5 References

1. Hoekmana, S.; Broch, K. A.; Robbins, C.; Ceniceros, E.; Natarajan, M. Review of biodiesel composition, properties, and specifications. *Renew. Sust. Energ. Rev.* **2012**, *16*, 143-169 (DOI: org/10.1016/j.rser.2011.07.143).

2. Lee, A. F.; Bennett, J. A.; Manayil, J. C.; Wilson, K. Heterogeneous catalysis for sustainable biodiesel production via esterification and transesterification. *Chem. Soc. Rev.* **2014**, *43*, 7887-7916 (DOI:10.1039/C4CS00189C).

3. Leung, D. Y. C.; Wu, X.; Leung, M. K. H. A review on biodiesel production using catalyzed transesterification. *Appl. Energy* **2010**, *87* 1083-1095 (DOI:org/10.1016/j.apenergy.2009.10.006).

4. Atabani, A. E.; Silitonga, A. S.; Badruddin, I. A.; Mahlia, T. M. I.; H. H. Masjuki, S. A. Mekhilef. A comprehensive review on biodiesel as an alternative energy resource and its characteristics. *Renew. Sust. Energ. Rev.* **2012**, *16*, 2070-2093 DOI: org/10.1016/j.rser.2012.01.003).

5. Trombettoni, V.; Lanari, D.; Prinsen, P.; Luque, R.; Marrocchi, A.; Vaccaro, L. Recent advances in sulfonated resin catalysts for efficient biodiesel and bio-derived additives production. *Prog. Energy Combust.Sci.* **2018**, *65*, 136-162 (DOI: org/10.1016/j.pecs.2017.11.001).

6. Lotero, E.; Liu, Y.; Dora, E. L.; Suwannakarn, K.; Bruce, D. A.; Goodwin, J. G. Synthesis of Biodiesel via Acid Catalysis. *Ind. Eng. Chem. Res.* **2005**, *44*, 5353-5363 (DOI: org/10.1021/ie049157g).

7. Aranda, D. A. G.; Santos, R. T. P.; Tapanes, N. C. O.; Ramos, A. L. D.; Antunes, O. A. C. Acid Catalyzed Homogeneous Esterification Reaction for Biodiesel Production from Palm Fatty Acids. *Catal. Lett.* **2008**, *122*, 20–25 (DOI: org/10.1007/s10562-007-9318-z).

8. Marchetti, J. M.; Errazu, A. F. Esterification of free fatty acids using sulfuric acid as catalyst in the presence of triglycerides. *Biomass Bioenerg.* **2008**, *32*, 892-895 (DOI: org/10.1016/j.biombioe.2008.01.001).

9. Peng, B.-X.; Shu, Q.; Wang, J.-F.; Wang, G.-R.; Wang, D.-Z.; Han, M.-H. Biodiesel production from waste oil feedstocks by solid acid catalysis. *Process Saf. Environ. Prot.* **2008**, *86*, 441-447 (DOI: org/10.1016/j.psep.2008.05.003).

10. Felizardo, P.; Correia, M. J. N.; Raposo, I.; Mendes, J. F.; Berkemeier, R.; Bordado, J. M. Production of biodiesel from waste frying oils. *Waste Manag.* **2006**, *26*, 487-494 (DOI: org/10.1016/j.wasman.2005.02.025).

11. Canakci, M. The potential of restaurant waste lipids as biodiesel feedstocks. *Bioresour. Technol.* **2007**, *98*, 183-190 (DOI: 10.1016/j.biortech.2005.11.022).

12. Shahbazi, M. R.; Khoshandam, B.; Nasiri, M.; Ghazvini, M. Biodiesel production via alkali-catalyzed transesterification of Malaysian RBD palm oil - Characterization, kinetics model. *J. Taiwan Inst. Chem. Eng.* **2012**, *43*, 504-510 (DOI: org/10.1016/j.jtice.2012.01.009).

13. Atapour, M.; Kariminia, H.-R.; Moslehabadi, P. M. Optimization of biodiesel production by alkali-catalyzed transesterification of used frying oil. *Process Saf. Environ. Prot.* **2014**, *92*, 179-185 (DOI: org/10.1016/j.psep.2012.12.005).

14. Hillion, G.; Delfort, B.; Pennecle, D.; Bournay, L.; Chodorge, J.-A. Biodiesel production by a continuous process using a heterogeneous catalyst. *Prepr. Pap.-Am. Chem. Soc. Div. Fuel Chem.* **2003**, *48*, 636-638.

15. Wang, J.; Yang, L.; Luo, W.; Yang, G.; Miao, C.; Fu, J.; Xing, S.; Fan, P.; Lv, P.; Wang, Z. Sustainable biodiesel production via transesterification by using recyclable $Ca_2MgSi_2O_7$ catalyst. *Fuel* **2017**, *196*, 306-313 (DOI: org/10.1016/j.fuel.2017.02.007).

16. Bournay, L.; Casanave, D.; Delfort, B.; Hillion, G.; Chodorge, J. A. New heterogeneous process for biodiesel production: A way to improve the quality and the value of the crude glycerin produced by biodiesel plants. *Catal. Today* **2005**, *106*, 190-192 (DOI: org/10.1016/j.cattod.2005.07.181).

17. Furuta, S.; Matsuhashi, H.; Arata, K. Catalytic action of sulfated tin oxide for etherification and esterification in comparison with sulfated zirconia. *Appl. Catal. A: Gen.* **2004**, *269*, 187–191 (doi.org/10.1016/j.apcata.2004.04.017).

18. Ghesti, G. F.; de Macedo, J. L.; Resck, I. S.; Dias, J. A.; Dias, S. C. L. FT-Raman Spectroscopy Quantification of Biodiesel in a Progressive Soybean Oil Transesterification Reaction and Its Correlation with ^{1}H NMR Spectroscopy Methods. *Energy Fuels* **2007**, *21*, 2475–2480 (DOI: org/10.1021/ef060657r).

19. Santos, E. M.; Piovesan, N. D.; de Barros, E. G.; Moreira, M. A. Low linolenic soybeans for biodiesel: Characteristics, performance and advantages. *Fuel* **2013**, *104*, 861-864 (DOI: org/10.1016/j.fuel.2012.06.014).

20. Zhang, X.; Lu, J.; Zhang, J. Porosity Enhancement of Carbazolic Porous Organic Frameworks Using Dendritic Building Blocks for Gas Storage and Separation. *Chem. Mater.* **2014**, *26*, 4023-4029 (DOI: org/10.1021/cm501717c).

21. Martin, R. L.; Simon, C. M.; Smit, B.; Haranczyk, M. In silico Design of Porous Polymer Networks: High-Throughput Screening for Methane Storage Materials. *J. Am. Chem. Soc.* **2014**, *136*, 5006–5022 (DOI: org/10.1021/ja4123939).

22. Chisti, Y. Biodiesel from microalgae. *Biotechnol. Adv.* **2007**, *25*, 294-306 (DOI: 10.1016/j.biotechadv.2007.02.001).

23. Wang, Y.; Wang, L.; Liu, C.; Wang, R. Benzimidazole- Containing Porous Organic Polymers as Highly Active Heterogeneous Solid- Base Catalysts, *ChemCatChem* **2015**, *7*, 1559–1565 (DOI: org/10.1002/cctc.201500244).

24. Schade, A.; Monnereau, L.; Muller, T.; Braese, S. A Rigid Pseudo-Octahedral Core at the Service of Three- Dimensional Porous Frameworks. *ChemPlusChem* **2014**, *79*, 1176–1182 (DOI: org/10.1002/cplu.201402093).

25. Sun, Q.; Dai, Z.; Liu, X.; Sheng, N.; Deng, F.; Meng, X.; Xiao, F.-S. Highly Efficient Heterogeneous Hydroformylation over Rh-Metalated Porous Organic Polymers: Synergistic Effect of High Ligand Concentration and Flexible Framework. *J. Am. Chem. Soc.* **2015**, *137*, 5204-5209 doi.org/10.1021/jacs.5b02122).

26. Pimentel, D.; Patzek, T. W. Ethanol Production Using Corn, Switchgrass, and Wood; Biodiesel Production Using Soybean and Sunflower. *Nat. Resour. Res.* **2005**, *14*, 65–76 (DOI: doi.org/10.1007/s11053-005-4679-8).

27. Borah, P.; Mondal, J.; Zhao, Y. Urea–pyridine bridged periodic mesoporous organosilica: An efficient hydrogen-bond donating heterogeneous organocatalyst

for Henry reaction. *J. Catal.* **2015**, *330*, 129-134 (DOI: doi.org/10.1016/j.jcat.2015.07.011).

28. Voelker, T. A.; Worrell, A. C.; Anderson, L.; Bleibaum, J.; Fan, C.; Hawkins, D. J.; Radke, S. E.; Davies, H. M. Fatty acid biosynthesis redirected to medium chains in transgenic oilseed plants. *Science* **1992**, *257*, 72–74 (DOI: 10.1126/science.1621095).

29. Wibowo, S. H.; Sulistio, A.; E. Wong, H. H.; Blencowe, A.; Qiao, G. G. Functional and Well- Defined β- Sheet- Assembled Porous Spherical Shells by Surface- Guided Peptide Formation. *Adv. Funct. Mater.* **2015**, *25*, 3147-3156 (DOI: org/10.1002/adfm.201404091).

30. Marso, T. M. M.; Kalpage, C. S.; Udugala-Ganehenege, M. Y. Metal modified graphene oxide composite catalyst for the production of biodiesel via pre-esterification of Calophyllum inophyllum oil. *Fuel* **2017**, *199*, 47-64 (DOI: org/10.1016/j.fuel.2017.01.004).

31. Avramidou, K. V.; Stamatia, F. Z.; Karakoulia, A.; Triantafyllidis, K. S.; Ravasio, N. Esterification of free fatty acids using acidic metal oxides and supported polyoxometalate (POM) catalysts. *Mol. Catal.* **2017**, *439*, 60-71 (DOI: 10.1016/j.mcat.2017.06.009).

32. Janssens, N.; Wee, L. H.; Martens, J. A. Esterification Reaction Utilizing Sense of Smell and Eyesight for Conversion and Catalyst Recovery Monitoring. *J. Chem. Educ.* **2014**, *91*, 876−879 (DOI: org/10.1021/ed400356j).

33. Du, D.-Y.; Qin, J.-S.; Sun, Z.; Yan, L.-K.; M. O'Keeffe, Su, Z.-M.; Li, S.-L.; Wang, X.-H.; Wang, X.-L.; Lan, Y.-Q. An unprecedented (3,4,24)-connected heteropolyoxozincate organic framework as heterogeneous crystalline Lewis acid catalyst for biodiesel production. *Sci. Rep.* **2013**, *3*, 2616 (DOI: 10.1038/srep02616).

34. Chen, J.; Liu, R.; Gao, H.; Chen, L.; Yeb, D. J. Amine-functionalized metal-organic frameworks for the transesterification of triglycerides. *J. Mater. Chem. A* **2014**, *2*, 7205-7213 (DOI: 10.1039/C4TA00253A).

35. Kou, J.; Sun, L.-B. Fabrication of Metal-Organic Frameworks inside Silica Nanopores with Significantly Enhanced Hydrostability and Catalytic Activity. *ACS Appl. Mater. Interfaces* **2018**, *10*, 12051-12059 (DOI: org/10.1021/acsami.8b01652).

36. Macgillivray, L. R. Metal-Organic Frameworks: Design and Application, Wiley 368 (2010) ISBN: 978-0-470-19556-7.

37. Kundu, S. K.; Bhaumik, A. Pyrene-Based Porous Organic Polymers as Efficient Catalytic Support for the Synthesis of Biodiesels at Room Temperature. *ACS Sustainable Chem. Eng.* **2015**, *3*, 1715-1723 (DOI: org/10.1021/acssuschemeng.5b00238).

38. Samanta, S.; Srivastava, R. A novel method to introduce acidic and basic bifunctional sites in graphitic carbon nitride for sustainable catalysis: cycloaddition, esterification, and transesterification reactions. *Sustainable Energy Fuels* **2017**, *1*, 1390-1404 (DOI: 10.1039/C7SE00223H).

39. Nakhate, A. V.; Yadav, G. D. Synthesis and Characterization of Sulfonated Carbon-Based Graphene Oxide Monolith by Solvothermal Carbonization for Esterification and Unsymmetrical Ether Formation. *ACS Sustainable Chem. Eng.* **2016**, *4*, 1963–1973 (DOI: org/10.1021/acssuschemeng.5b01205).

40. Atuchin, V. V.; Andreeva, O. P.; Gavrilova, T. A.; Kalyzhnyi, N. A.; Korolkov, I. V.; Maximovskiy, E. A. Synthesis of Mesoporous CaMoO$_4$ in Aqueous Solution. Solid State Phenomena. **2016**, *245*, 80-85 (DOI: org/10.4028/www.scientific.net/SSP.245.80).

41. Troitskaiaa, I. B.; Gavrilovab, T. A.; Atuchin, V. V. Structure and micromorphology of titanium dioxide nanoporous microspheres formed in water solution. *Physics Procedia* **2012**, *23*, 65-68 (DOI:10.1016/j.phpro.2012.01.017).

42. Kitagawa, S. Future Porous Materials. *Acc. Chem. Res.* **2017**, *50*, 514-516 (DOI: org/10.1021/acs.accounts.6b00500).

43. Bhunia, A.; Vasylyeva, V.; Janiak, C. From a supramolecular tetranitrile to a porous covalent triazine-based framework with high gas uptake capacities. *Chem. Commun.* **2013**, *49*, 3961-3963 (DOI: 10.1039/C3CC41382A).

44. Ren, S.; Bojdys, M. J.; Dawson, R.; Laybourn, A.; Khimyak, Y. Z.; Adams, D. J.; Cooper, A. I. Porous, fluorescent, covalent triazine-based frameworks via room-temperature and microwave-assisted synthesis. *Adv. Mater.* **2012**, *24*, 2357–2361 (DOI: 10.1002/adma.201200751).

45. Mukherjee, G.; Thote, J.; Aiyappa, H. B.; Kandambeth, S.; Banerjee, S.; Vanka, K.; Banerjee, R. A porous porphyrin organic polymer (PPOP) for visible light triggered hydrogen production. *Chem. Commun.* **2017**, *53*, 4461-4464 (DOI: 10.1039/C7CC00879A).

46. Kaur, P.; Hupp, J. T.; Nguyen, S. T. Porous Organic Polymers in Catalysis: Opportunities and Challenges. *ACS Catal.* **2011**, *1*, 819–835 (DOI: org/10.1021/cs200131g).

47. Cote´, A. P.; El-Kaderi, H. M.; Furukawa, H.; Hunt, J. R.; Yaghi, O. M. Reticular Synthesis of Microporous and Mesoporous 2D Covalent Organic Frameworks. *J. Am. Chem. Soc.* **2007**, *129*, 12914-12915 (doi.org/10.1021/ja0751781).

48. Zhang, Y.; Riduan, S. N. Functional porous organic polymers for heterogeneous catalysis. *Chem. Soc. Rev.* **2012**, *41*, 2083–2094 (DOI: 10.1039/C1CS15227K).

49. Bhowmik, S.; Jadhav, R. G.; Das, A. K. Nanoporous Conducting Covalent Organic Polymer (COP) Nanostructures as Metal-Free High Performance Visible-Light Photocatalyst for Water Treatment and Enhanced CO$_2$ Capture. *J. Phys. Chem. C* **2018**, *122*, 274−284 (DOI: org/10.1021/acs.jpcc.7b07709).

50. Bleschke, C.; Schmidt, J.; Kundu, D. S.; Blechert, S.; Thomas, A. A Chiral Microporous Polymer Network as Asymmetric Heterogeneous Organocatalyst. *Adv. Synth. Catal.* **2011**, *353*, 3101 -3106 (DOI: doi.org/10.1002/adsc.201100674).

51. Zhu, Y.; Long, H.; Zhang, W. Imine-Linked Porous Polymer Frameworks with High Small Gas (H_2, CO_2, CH_4, C_2H_2) Uptake and CO_2/N_2 Selectivity. *Chem. Mater.* **2013**, *25*, 1630-1635 (DOI: org/10.1021/cm400019f).

52. Gorji, A. H.; Belmabkhout, Y.; Sayari, A. Polyethylenimine-Impregnated Mesoporous Silica: Effect of Amine Loading and Surface Alkyl Chains on CO_2 Adsorption. *Langmuir* **2011**, *27*, 12411–12416 (DOI: org/10.1021/la202972t).

53. EL-Mahdy, A. F. M.; Kuo, C-H.; Alshehri, A.; Young, C.; Yamauchi, Y.; Kim, J.; Kuo, S-W. Strategic design of triphenylamine- and triphenyltriazine-based two-dimensional covalent organic frameworks for CO_2 uptake and energy storage. *J. Mater. Chem. A* **2018**, *6*, 19532-19541 (10.1039/C8TA04781B).

54. Chaikittisilp, W.; Ariga, K.; Yamauchi, Y. A new family of carbon materials: synthesis of MOF-derived nanoporous carbons and their promising applications, *J. Mater. Chem. A* **2013**, *1*, 14-19 (DOI: 10.1039/C2TA00278G).

55. Carvalho, W. A.; Galhardo, T. S.; Simone, N.; Gonçalves, M.; Figueiredo, F.; Mandelli, D. Preparation of Sulfonated Carbons from Rice Husk and Their Application in Catalytic Conversion of Glycerol. *ACS Sustainable Chem. Eng.* **2013**, *1*, 1381-1389 (DOI: org/10.1021/sc400117t).

56. Klumpen, C.; Gödrich, S.; Papastavrou, G.; Senker, J. Water mediated proton conduction in a sulfonated microporous organic polymer. *Chem. Commun.* **2017**, *53*, 7592-7595 (DOI: 10.1039/C7CC02117H).

57. Andrew, R. D.; Cooper, A. I.; Adams, D. J. Nanoporous organic polymer networks. *Prog. Polym. Sci.* **2012**, *37*, 530-563 (DOI: org/10.1016/j.progpolymsci.2011.09.002).

58. Nagai, A.; Chen, X.; Feng, X.; Ding, X.; Guo, Z.; Jiang, D. A. A Squaraine-Linked Mesoporous Covalent Organic Framework. *Angew. Chem. Int. Ed.* **2013**, *52*, 3770 -3774 (DOI: org/10.1002/anie.201300256).

59. Mondal, S.; Konda, M.; Kauffmann, B.; Manna, M. K.; Das, A. K. Effects of Donor and Acceptor Units Attached with Benzoselenadiazole: Optoelectronic and Self-Assembling Patterns. *Cryst. Growth Des.* **2015**, *15*, 5548-5554 (DOI: org/10.1021/acs.cgd.5b01179).

60. Zhang, W.-Q.; Li, Q.-Y.; Zhang, Q.; Lu, Y.; Lu, H.; Wang, W.; Zhao, X.; Wang, X-J. Robust Metal–Organic Framework Containing Benzoselenadiazole for Highly Efficient Aerobic Cross-dehydrogenative Coupling Reactions under Visible Light. *Inorg. Chem.* **2016**, *55*, 1005-1007 (DOI: org/10.1021/acs.inorgchem.5b02626).

61. Xia, W. Interactions between metal species and nitrogen-functionalized carbon nanotubes. *Catal. Sci. Technol.* **2016**, *6*, 630-644 (DOI: 10.1039/C5CY01694K).

62. Shenoy, S. R.; Stomo, F. R. P. C.; Iwasawa, T.; Rebek, J. J. Organocatalysis In a Synthetic Receptor with an Inwardly Directed Carboxylic Acid. *J. Am. Chem. Soc.* **2008**, *13*, 5658 -5659 (DOI: org/10.1021/ja801107r).

63. Plano, D.; Palop, J. A.; Sanmartín, C. Thermal Analysis of Sulfur and Selenium Compounds with Multiple Applications, Including Anticancer Drugs. *IntechOpen.* **2013**, 365-384 (DOI: 10.5772/53048).

64. Stegbauer, L.; Schwinghammer, K.; Lotsch, B. V. A hydrazone-based covalent organic framework for photocatalytic hydrogen production. *Chem. Sci.* **2014**, *5*, 2789-2793 (DOI: 10.1039/C4SC00016A).

65. Biswas, S.; Jadhav, R. G.; Das, A. K. Construction of Porous Organic Nanostructures using Cooperative Self-assembly for Lipase Catalyzed Inclusion of Gastrodigenin. *ACS Appl. Nano Mater.* **2018**, *1*, 175-182 (doi.org/10.1021/acsanm.7b00085).

66. Guan, Q.; Li, Y.; Chen, Y.; Shi, Y.; Gu, J.; Li, B.; Miao, R.; Chen, Q.; Ning, P. Sulfonated multi-walled carbon nanotubes for biodiesel production through triglycerides transesterification. *RSC Adv.* **2017**, *7*, 7250-7258 (DOI: 10.1039/C6RA28067F).

67. Fahlman. X.-L. W.; Epstein, A. J. XPS Study of Highly Sulfonated Polyaniline. *Macromolecules* **1999**, *32*, 3114-3117 (DOI: org/10.1021/ma981386p).

68. Adams, L.; Oki, A.; Grady, T.; McWhinney, H.; Luo, Z. Preparation and characterization of sulfonic acid-functionalized single-walled carbon nanotubes. *Physica E Low Dimens. Syst. Nanostruct.* **2009**, *41*, 723-728 (DOI: 10.1016/j.physe.2008.11.018).

69. Gomes, R.; Bhanja, P.; Bhaumik, A. A Sulfonated porous organic polymer as a highly efficient catalyst for the synthesis of biodiesel at room temperature, J. *Mol. Catal. A: Chem.* **2016**, *411*, 110-116 (DOI: org/10.1016/j.molcata.2015.10.016).

70. Bhunia, S.; Banerjee, B.; Bhaumik, A. A new hypercrosslinked supermicroporous polymer, with scope for sulfonation, and its catalytic potential for the efficient synthesis of biodiesel at room temperature. *Chem. Commun.* **2015**, *51*, 5020-5023 (DOI: 10.1039/C4CC09872B).

71. Chang, Y.; Lee, C.; Bae, C. Polystyrene-based superacidic solid acid catalyst: synthesis and its application in biodiesel production. *RSC Adv.* **2014**, *4*, 47448-47454 (DOI: 10.1039/C4RA07747D).

72. Liu, F.; Meng, X.; Zhang, Y.; Ren, L.; Nawaz, F.; Xiao, F.-S. Efficient and stable solid acid catalysts synthesized from sulfonation of swelling mesoporous polydivinylbenzenes. *J. Catal.* **2010**, *271*, 52-58 (DOI: org/10.1016/j.jcat.2010.02.003).

73. Wang, Z.; Wang, Z.; Bai, Y.; Fu, B.; Liu, H.; Song, A.; Zhang, Z.; Zhang, M. Sulfonated polyethersulfone directly synthesized through sulfonic monomer as a new stable solid acid catalyst for esterification. *Catal. Commun.* **2012**, *27*, 164-168 (DOI: org/10.1016/j.catcom.2012.07.015).

74. Zhang, X.; Zhao, Y.; Xu, S.; Yang, Y.; Liu, J.; Wei, Y.; Yang, Q. *Nat. Commun.* **2014**, *5*, 3170 (DOI:10.1038/ncomms4170).

75. Zhang, X.; Zhang, L.; Yang, Q. Designed synthesis of sulfonated polystyrene/mesoporous silica hollow nanospheres as efficient solid acid catalysts. *J. Mater. Chem. A* **2014**, *2*, 7546-7554 (DOI: 10.1039/C4TA00241E).

Chapter 3
Picolinohydrazide Based Covalent Organic Polymer for Metal Free Catalysis and Removal of Heavy metals from Waste Water

3.1 Introduction.

Development and synthesis of covalent organic polymers (COPs) have gained great attention due to their highly tunable porosity. COPs show versatile applications in various fields, such as storage of greenhouse gases (i.e., carbon dioxide), efficient heterogeneous catalysts, sensors, and energy storage devices.[1–4] In the past few years, various monomeric units with different functionalities have been used to synthesize COPs for the exploration of numerous applications. The presence of heteroatoms in COPs (especially N and O centers) serves various purposes including heterogeneous catalysis and detection of metal ions in solution or in the solid state. The development of efficient heterogeneous catalysts for diverse organic reactions is a successful application of COPs that has gained momentum in the recent past. COPs provide large surface areas, defined pore size, low framework density, and high thermal stability, which help in increasing their catalytic efficiency.[5–10] With the choice of binding units in the polymeric backbone, COPs can be functionalized differently for different catalytic reactions. Knoevenagel reaction is one such type of organic reaction, which could be catalyzed by a porous polymer with a basic surface site. Typically, Knoevenagel reaction involves a condensation reaction between an active methylene group and an aldehyde carbonyl group. The importance of Knoevenagel reaction lies in the fact that it gives rise to a number of products used for medicinal purposes. In the recent past, a 3D microporous COF was synthesized for size-selective catalysis in Knoevenagel reaction,[11] while a bifunctional COF was synthesized for cascade catalysis.[12] In recent days, water contaminated with toxic heavy metal ions has become a serious issue due to their bioaccumulation, uncontrollable release, and persistence in nature.[13] Several techniques, including electrolysis, precipitation, filtration, reduction, and adsorption, have been developed for the removal of heavy metal ions from contaminated water.[14] The adsorption method is one of the efficient, easiest, and simplest techniques for the removal of toxic heavy metal ions. A few adsorbents, such as metal oxides and activated carbon, are widely used for the treatment of wastewater. However, their adsorption performance is low due to lower binding affinity with the metal ions. There is a need to develop modified adsorbent materials for the removal of toxic metal ions. Functionalized COPs are considered one of the promising materials, which could be used to detect and remove toxic metal ions from polluted water due to their variable porosity, surface area, low framework density, and chemical diversity. Several surface modifications (triazole, ester, sulfide, and ether groups) have been done on COP surfaces to remove metal ions selectively from waste water. In general, waste water contains various toxic heavy metal ions. Therefore, there is a need to develop a broad-spectrum COP with effective adsorbing ability toward different metal ions. Incorporation of suitable functionalities inside the COP can serve the purpose of the removal and detection of toxic metal ions. Recently, a few encouraging results reported in the literature motivated us to synthesize a COP that could detect and select a broad spectrum of metal ions.[15-

[19] Heptazine- and tetraphenylmethane-based polymers for the detection of iron ions[20-21] and imidazolium-based polymers for the removal of $Cr_2O_7^{2-}$ ions[22] are reported. In the recent past, removal of Hg^{2+} ions using COFs was reported by Jiang *et al.*[23] In another report, a sulfur-rich triazine polymer is used for the detection and removal of Hg^{2+} ions.[24] Therefore, it is important to construct a COP using nitrogen-rich building blocks. The picolinohydrazide group is a well-known binding ligand due to its efficient adsorption capacity toward metal ions. To the best of our knowledge, there is no report on a picolinohydrazide based COP that has been used for the removal of metal ions. In this regard, our objectives are (1) to synthesize a nitrogen-rich picolinohydrazide-based covalent organic polymer, (2) to investigate its catalytic activity on Knoevenagel reaction and (3) to remove toxic heavy metal ions from polluted water. In this work, we have synthesized a covalent organic polymer (**COP-3**) by the hydrazide coupling reaction between 6-hydrazinonicotinic hydrazide and 1,3,5-benzenetricarbonyl trichloride. Nitrogen-rich **COP-3** functioned appreciably as a heterogeneous catalyst at 30 °C for the Knoevenagel condensation between malononitrile and aromatic benzaldehyde derivatives. In addition, **COP-3** could efficiently remove Ca^{2+}, Cu^{2+}, Cd^{2+}, Hg^{2+}, and Pb^{2+} from contaminated water. Among the above-mentioned metal ions, the Hg^{2+} ion is considered for a detailed adsorption study with **COP-3**. Only the pyridinic group of **COP-3** is capable of interacting with Hg^{2+} ions, which is discussed in this article.

3.2 Experimental section.
3.2.1 Materials and methods.

1,3,5-Benzenetricarbonyl trichloride, 6-hydrazinonicotinic hydrazide hydrate, pyridine, aromatic aldehydes, malononitrile and metal salts were purchased from Sigma Aldrich USA. All solvents like tetrahydrofuran (THF), acetone, methanol and ethyl acetate were purchased from Merck and distilled prior to use. Reactions progression were monitored by thin-layer chromatography (TLC). Silica gel was used as stationary phase for column chromatography.

UV-Vis spectra were collected using Varian Cary 100 Bio UV-Visible spectrophotometer. Powder XRD were recorded using Rigaku SmartLab, Automated Multipurpose X-ray Diffractometer equipped with a high-accuracy theta-theta goniometer featuring a horizontal sample mount. The fluorescence spectra were recorded in Fluoromax-4 spectrofluorimeter (HORIBA Jobin Yvon model FM-100) with excitation and emission slit widths at 5 nm using quartz cuvette (10×10 mm^2). BET surface area analysis was performed using quantachrome, Autosorb iQ2. Solid state ^{13}C NMR was recorded on JEOL ECX 400 (100 MHz CP-1). Thermogravimetric analysis (TGA) was carried out using a METTLER TOLEDO TGA instrument. The samples were heated from 25 °C to 600 °C at a constant rate of 5 °C min^{-1} in a N_2 gas environment. Differential Scanning Calorimeter was done in DSC 214 SET MFC LN2 at 10 °C/min heating rate. FT-IR spectra of all reported compounds were performed using a Bruker (Tensor-27) FT-IR spectrophotometer. The GC-MS QP 2010 Ultra mass

spectrometer from Shimadzu Analytical India Pvt. Ltd was used. In GC-MS, helium as inert carrier gas was used and could detect up to ppm level masses. The mass range is 10-1000 Da, which allows analysis over a wide range of low and high molecular weight compounds. NIST Mass spectra library is available for separation/identification of organic compounds and molecules. The polymers were visualized under a Scanning Electron Microscope from Carl Zeiss at working voltage of 5.0 kV. Atomic Emission Spectrometry (ICP-AES) was done in model ARCOS, Simultaneous ICP Spectrometer. XPS (X-ray photoelectronic spectroscopy) was carried out on AXIS Supra instrument (Kratos Analytical, UK, SHIMADZU group). Raman experiment of materials were analyzed. (Manufacturing Company: Horiba Scientific, Model LabRAMHR Evolution).

3.2.2 Synthesis of COP-3.

In a typical experiment, 6-hydrazinonicotinic hydrazide hydrate (472 mg, 2.8 mmol) in 30 mL tetrahydrofuran (THF) within a round bottom flask was degassed and purged with argon for 20 minutes. To this, 5 mL pyridine was added dropwise under the continuous flow of Ar. The mixture was allowed to stir at 0 °C for 1 h. After that 1,3,5-benzenetricarbonyl trichloride (500 mg, 1.8 mmol) in THF was added dropwise by dropping funnel. The whole reaction mixture was allowed to stir for 48 h. The reaction mixture was quenched in H_2O and washed several times by acetone, methanol, dichloromethane and ethyl acetate. The resultant residue was dried at 90 °C to a greenish white colored polymer (450 mg) which was insoluble in most organic solvents. The synthetic scheme is shown in **scheme 3.1**.

3.2.3 General Procedure for the Catalytic Reactions.

Benzaldehyde derivative (1 equiv.) and malononitrile (1 equiv.) were taken in 100 mL round bottom flask. THF (3 mL) was added for dissolution. It was stirred initially for five minutes at 25 °C followed by the addition of **COP-3** (2 wt%). The reaction mixture was then stirred at 30 °C for 2 h. The reaction mixture was filtered and washed several times by acetone, methanol and ethyl acetate. The residue was dried to recover the catalyst. The filtrate was concentrated under reduced pressure. The product was characterized by GC-MS analyzer, ^{1}H and ^{13}C NMR spectroscopy.

3.2.4 Density function theory (DFT) calculation.

DFT calculations were performed using Turbomole (v7.0) software.[25-30] The geometry optimizations were performed at the B3LYP level of DFT. The Ahlrichs group documented all-electron Gauussian base sets.[29-30] Triple-ξ quality basis sets (TZVP) with one set of polarization functions were used for nitrogen, and oxygen like atoms. The carbon and hydrogen atoms were described by smaller polarized split-valence SV(P) basis sets, double-ξ quality in the valence region with a polarizing set of d-functions on the non-hydrogen atoms. The self-consistent field (SCF) calculations were tightly converged [1 × 10^{-8} Eh

(Hartree Energy) in energy, 1×10^{-7} Eh in the density change, and 1×10^{-7} in the maximum element of the DIIS error vector]. The geometries were considered to be converged after the energy change was less than 5×10^{-6} Eh, the gradient norm and maximum gradient element were smaller than 1×10^{-4} Eh/Bohr and 3×10^{-4} Eh/Bohr, respectively, and the root-mean square and maximum displacements of atoms were smaller than 2×10^{-3} Bohr and 4×10^{-3} Bohr, respectively. The DFT energy is expressed as a functional of the molecular electron density ρ (r) which is shown in equation 3.1.

$E_{DFT} [\rho] = T [\rho] + V_{ne} [\rho] + J[\rho] + E_x[\rho] + E_c [\rho] + V_{nuc}$　　　　　Eq. 3.1

where $T [\rho]$ is the kinetic energy, $V_{ne} [\rho]$ is the nuclei-electron interaction, $E_x [\rho]$ and $E_c [\rho]$ are the exchange and correlation energy functionals.

3.2.5 Sorption Experiments.

0.27 g $HgCl_2$ was taken in 250 mL distilled water to prepare an 800 ppm Hg^{2+} stock solution. Different concentration of Hg^{2+} solutions were obtained by diluting the stock solution. The concentrations of Hg^{2+} for all experiments were measured by inductively coupled plasma-atomic emission spectroscopy (ICP-AES) for ppm level of concentrations.

3.2.6 Hg^{2+} sorption isotherm.

To get adsorption isotherm for **COP-3**, 10 mg of adsorbent was placed in 20 mL aqueous solutions of different Hg^{2+} concentrations (50-800 ppm). Then solutions were stirred for overnight. All the solution mixtures were filtered. The filtration process was done through a 0.45 μm membrane filter. After that the filtrates were analyzed *via* ICP-AES to measure the residual Hg^{2+} concentrations.

The Hg^{2+} adsorption capacity, q_e (mg g^{-1}), at equilibrium was calculated using Equation 3.2.

$$q_e = \frac{(C_0 - C_e)V}{m}$$　　　　　Eq. 3.2

Where C_0 is the initial concentration

　　　C_e is the equilibrium (final concentration) concentrations,

　　　V is the volume of solution taken in mL and m is the mass of **COP-3**
taken for experiment.

3.2.7 Hg^{2+} sorption kinetics.

To evaluate the kinetics of Hg^{2+} ion adsorption through **COP-3**, 10 mg of **COP-3** was taken in 200 mL 100 ppm Hg^{2+} solution in a conical flask. The mixture was then stirred overnight at room temperature. 20 mL aliquots were taken out from solution mixture with increasing time intervals and filtered by 0.45 μm membrane filter. Finally, filtrate was send for ICP-AES for the residual Hg^{2+} concentration.

The initial adsorption rate and rate constants were calculated and the kinetics were evaluated using pseudo-second-order kinetics fitting with the following equation 3.3.

$$\frac{t}{q_t} = \frac{1}{k_2 q_e^2} + \frac{t}{q_e}$$

Eq 3.3

where k_2 (g mg^{-1} min^{-1}) is the rate constant of adsorption, q_e is the equilibrium adsorption capacity and q_t is the adsorption capacity at time t.

Distribution coefficient values (K_d) were calculated from the adsorption kinetic study with help of equation 3.4.

$$K_d = \frac{(C_0 - C_e)}{C_e} \times \frac{V}{m}$$

Eq. 3.4

Where C_0 is the initial concentration

C_e is the equilibrium (final concentration) concentrations,

V is the volume of solution taken in mL and m is the mass of **COP-3** taken for experiment.

3.2.8 Selectivity test. A mixed metal solution was made with either Cl$^-$ salts of Hg^{2+}, Ca^{2+}, Cd^{2+}, Pb^{2+} and Cu^{2+}, with equal concentrations of 5 ppm. 10 mg of **COP-3** was added to 20 mL of the mixture of metal solution and this was then sonicated to full dispersion and stirred for 12 h. The solutions were filtered through a 0.45 μm membrane filter, and the filtrate was analyzed by ICP for the remaining metal concentrations. The removal efficiency was calculated by equation 3.5.

Removal percentage $(\%) = \frac{(C_0 - C_e) \times 100}{C_0}$

Eq. 3.5

Where C_0 is the initial concentrations of Hg^{2+}.

and C_e is the equilibrium concentration (final concentration) of the Hg^{2+}.
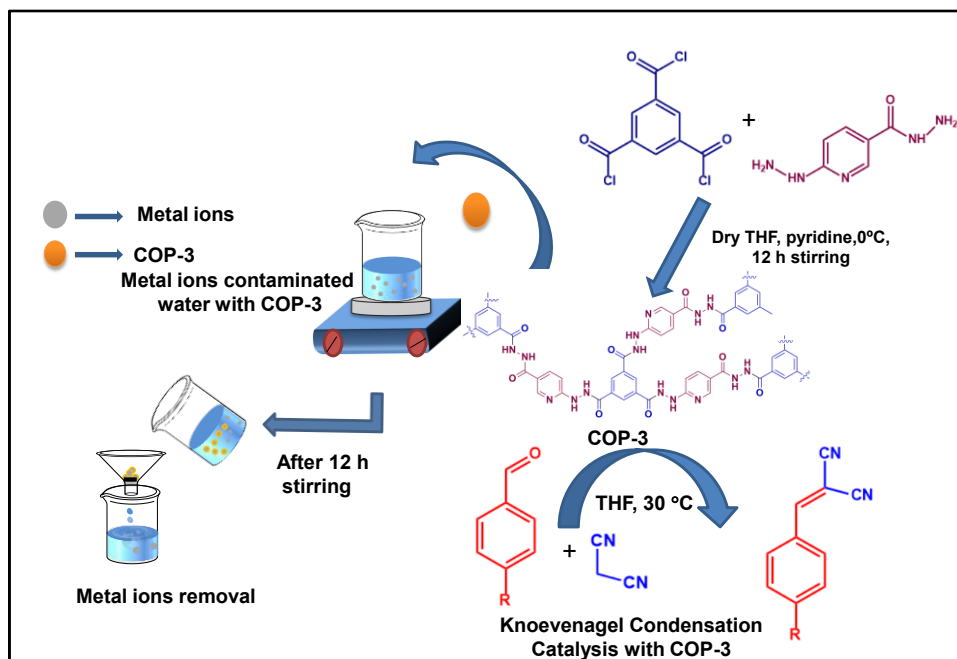
Scheme 3.1 Schematic representation of synthesis of **COP-3** and its applications.

3.3 Results and discussion.

In the present work, a covalent organic polymer **COP-3** was synthesized from 6-hydrazinylnicotino hydrazide and 1,3,5-benzenetricarbonyl trichloride (Scheme 3.1). UV-Vis, FT-IR, solid state NMR studies, TGA, DSC and BET analysis were performed for the characterization of **COP-3**. The FT-IR frequencies of **COP-3** is observed at 3240 cm^{-1} (typical for N-H stretching), 1670 cm^{-1} for C=O stretching and 1605 cm^{-1} for C=N stretching. The C=O stretching and C=N stretching exhibit sharp peaks while that of N-H reveals a broad peak (Figure 3.1).
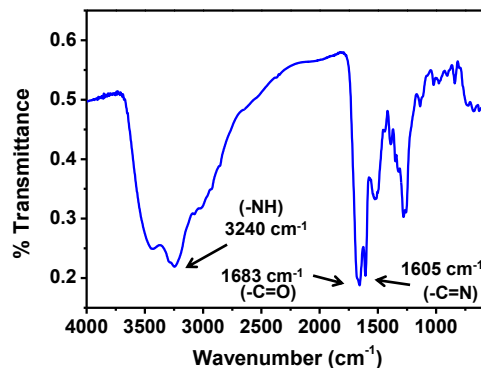
Figure 3.1 FT-IR spectrum of **COP-3.**

PXRD pattern (Figure 3.2 a) reveal two peaks (one intense at 26.28° and another small at 13.48°). PXRD shows amorphous nature of **COP-3**. Differential scanning calorimetry (DSC) as shown in Figure 3.2 b portrays some interesting

81

results about **COP-3**. The glass transition temperature T_g is found at 60 °C and the entire transition ranges from 40 to 80 °C. The presence of a sharp dip at 122 °C indicates that **COP-3** has reached its melting temperature T_m.
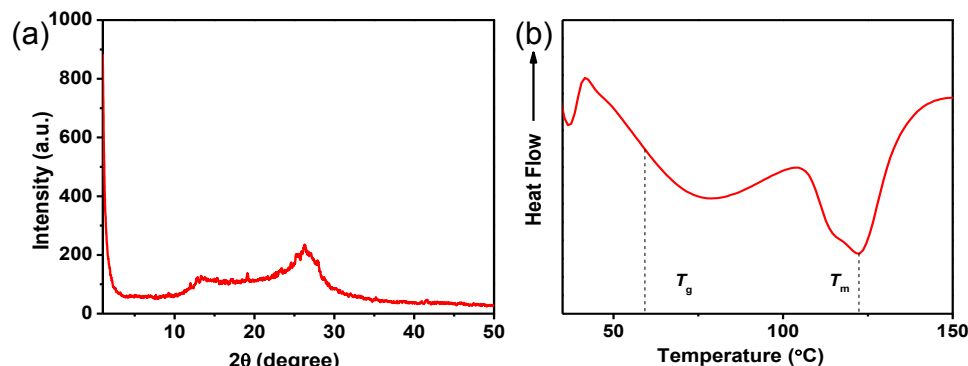
Figure 3.2 (a) Powder XRD of **COP-3** and (b) DSC of **COP-3**.

The robustness of the material was analyzed by TGA (Thermogravimetric Analysis). A weight loss of 41.75% is observed from 23 °C to 188 °C in the first step due to residual solvent (water or moisture). A weight loss of 39.55 % is observed from 188 °C to 506 °C in the second step and a weight loss of 8.13 % is observed from 506 °C to 855 °C in the third step as shown in Figure 3.3
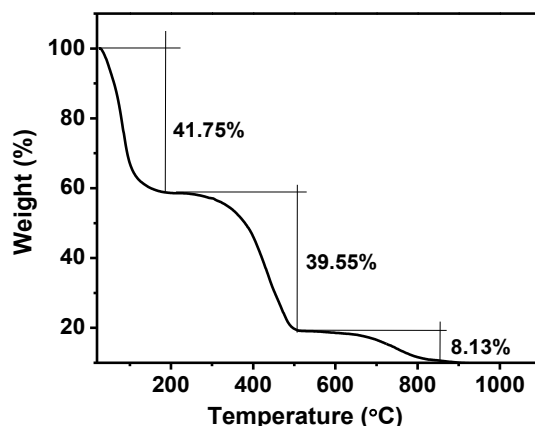
Figure 3.3 Thermogravimetric analysis of **COP-3**.

The solid state ^{13}C NMR spectrum (Figure 3.4 a) shows prominent signals at 170 ppm and 131 ppm. The peak from 120-140 ppm consists of most of the aromatic carbons (*i.e.* from a-f and from i-j). The carbon atoms (h, l) adjacent to N give signals at 157 ppm and 148 ppm. The signal at 170 ppm reveals the carbon atom (g) of carbonyl carbon.
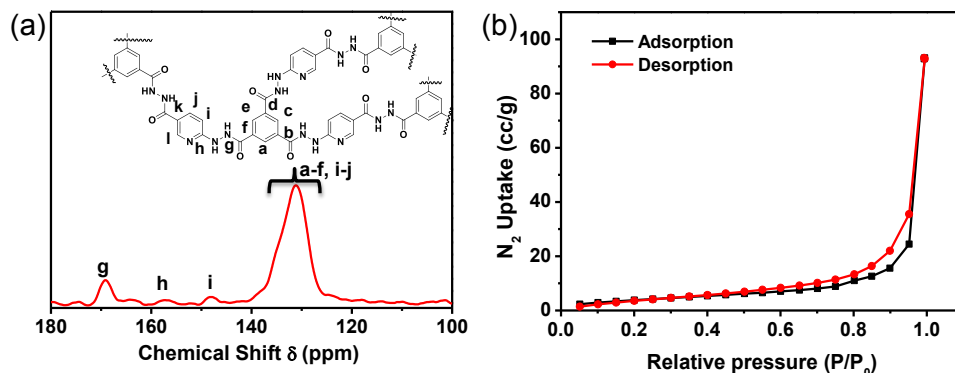
Figure 3.4 (a) Solid state ^{13}C NMR spectrum of **COP-3** and (b) N$_2$ adsorption-desorption isotherm of **COP-3**.

To account the porosity and surface area of the **COP-3**, nitrogen sorption analysis was performed at 77 K and 1 bar pressure (Figure 3.4 b). The BET isotherm of **COP-3** can be classified as type IV. Hysteresis loops is seen in the range of 0.7-1.0 P/P$_0$ which suggests a typical mesoporous structure of **COP-3**. Barrett-Joyner-Halenda (BJH) pore size distribution curve also supports this phenomenon (Figure 3.5). **COP-3** shows multipoint BET surface area of 22.113 m^2 g^{-1}. Pore size distribution of the **COP-3** is calculated *via* BJH method. **COP-3** exhibits average pore size and pore volume of 4.8 nm and 0.14 cc g^{-1}. The PSD curves agree with the shape of the nitrogen isotherms and suggest that **COP-3** is predominantly mesoporous in nature.
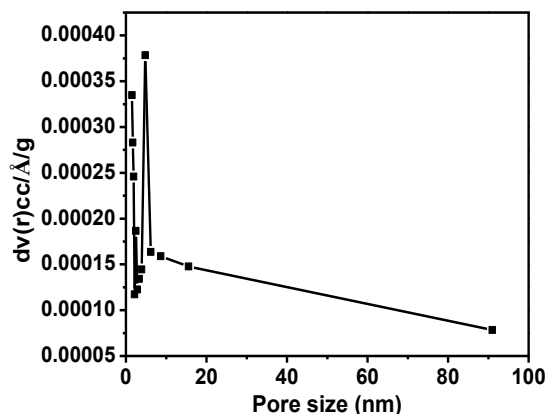
Figure 3.5 Pore size distribution of **COP-3** by using the BJH methods.

To measure the surface roughness, AFM (atomic force microscopy) is done. AFM images show surface roughness and describe the reason to generate hydrophobicity inside the pore. The hydrophobic nature of **COP-3** is executed by micro to nano-level surface roughness. The **COP-3** polymer aggregates to spherical assembly during coating on glass surface, which is one of the primary features of hydrophobic materials.[31] Figure. 3.6 shows nano roughness of **COP-3** material. It has been observed from 3D view that surface contains some crests

and troughs. The peaks are observed in the region of (0.5 -1) μm which indicates the presence of air pockets between the peaks (valley regions). These trapped air pocket in the valley region makes the pore of **COP-3** hydrophobic in nature.
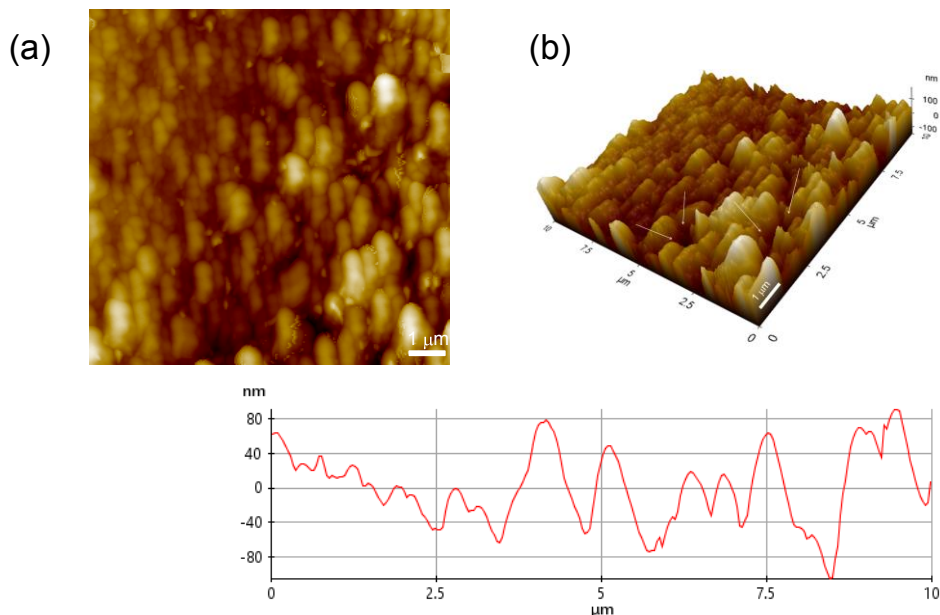
Figure 3.6 (a) AFM Images of COP-3. (b) micro scale 3D image (with z-axis interpretation) of **COP-3**.

3.3.1 Catalytic Performance.

In this catalytic investigation, **COP-3** acts as basic heterogeneous catalyst for the Knoevenagel condensation between the aromatic aldehydes and malononitrile. Aromatic aldehydes (1 mmol) with different *para* substituted groups and malononitrile (1 mmol) were used for the Knoevenagel condensation using **COP-3** as a heterogeneous catalyst as shown in Scheme 3.2. Various external parameters like temperature, solvents and amount of loaded catalyst were changed to optimize the best catalytic activity. Catalytic reactions were performed at 30 °C in THF for 2 h (Table 3.1). To account the conversion, different weight percent of catalyst (**COP-3**) was loaded. It is seen that 2 wt% of catalyst is ideal for good conversion. No conversion was observed without catalyst. The reaction propagation time was also varied. After 2 h, maximum conversion was observed. The propagation of the reaction was monitored by the thin layer chromatography (TLC). All the desired products were characterized by ^{1}H, ^{13}C NMR spectroscopy and GCMS spectrometry (**Appendix-B**). Appearance of benzylic proton at 7.7 ppm in ^{1}H NMR and benzylic carbon at 87.6 ppm in ^{13}C NMR confirms the formation of desired products. ^{13}C NMR data also support the results. Furthermore, purity and conversion were confirmed by the GCMS analysis. SEM image of fresh and recycled catalyst (Figure 3.7 a, 3.7 b) shows a negligible deformation of surface morphology and the crystallinity. Reaction time *vs* conversion (%) graph for the reaction between nitrobenzaldehyde and

COP-3 is shown in Figure 3.7 c. **COP-3** retains its catalytic activity and frameworks up to 4 cycles (Figure 3.7 d, 3.8). Summary of different catalysts used in Knoevenagel condensation is shown in Table 3.2.[32-38]
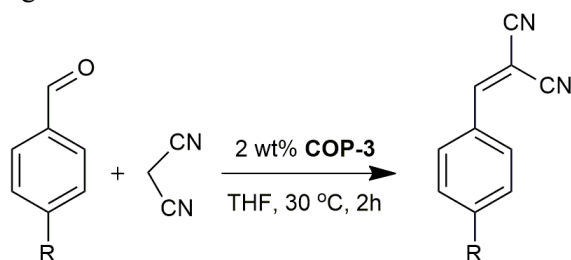
R = H (1A), NO$_2$ (2A), Cl (3A), Br (4A), OMe (5A)

Scheme 3.2 COP-3 Catalyzed Knoevenagel reactions.

Table 3.1 Summary of the Knoevenagel reactions catalyzed by **COP-3**

S. No	Reactants	Wt% of catalyst (mg)	Reaction Time (h)	Temperature	Conversion[a]
1	1A	2	2	30 °C	100%
2	2A	2	2	30 °C	100%
3	3A	2	2	30 °C	100%
4	4A	2	2	30 °C	100%
5	5A	2	2	30 °C	100%

'a' GC product conversion.
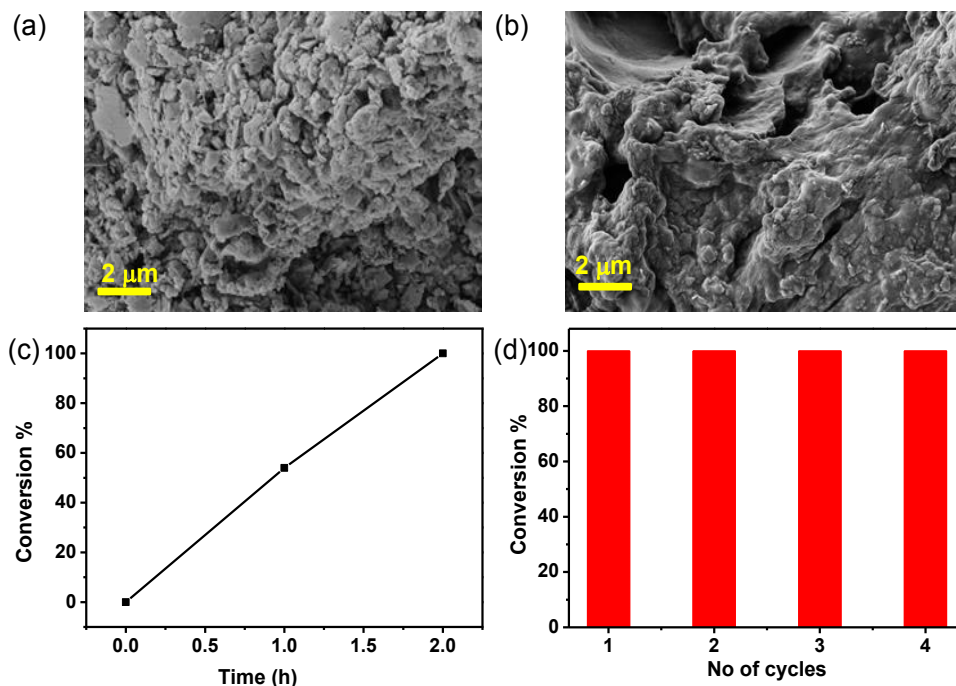
Figure 3.7 SEM images of **COP-3** (a) before catalysis and (b) after catalysis. (c) Reaction time *vs* conversion (%) curve for the product obtained between

nitrobenzaldehyde with **COP-3** and (d) recyclability of **COP-3** in the Knoevenagel reaction.
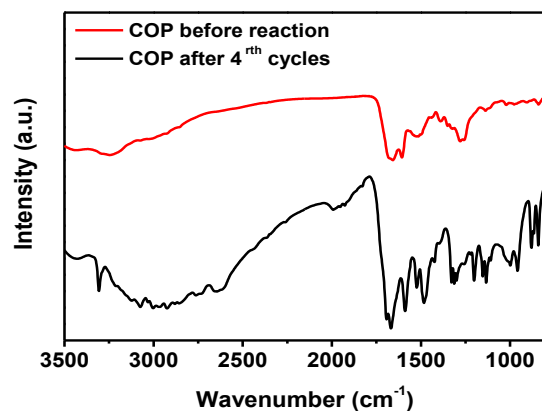
Figure 3.8 FT-IR specta of **COP-3** before and after 4th cycle catalysis.

Table 3.2 Summary of different catalysts used in Knoevenagel condensation reaction

S. No.	Catalyst	Time (h)	Catalyst Loading	Temperature (°C)	Conversion (%)	Ref.
1	Am-MOP	14	0.9 mol%	40 °C	62.64	32
2	HG xerogel	4	1 mol%	40 °C	90	33
3	2,3-DhaTph	1.5	15 wt%	80 °C	96	34
4	BF-COF	10	5 wt%	25 °C	96	35
5	Cy-pip	4	1.0 wt%	25 °C	95.8	36
6	Pd/COF-TpPa-Py	4	4 wt%	80 °C	98	37
7	{Zn(oba)$_3$bpdh)$_{0.5}$}$\propto$·2H$_2$O	2	2 wt%	25 °C	96	38
8	**COP-3**	2	2 wt%	25 °C	99	This work

3.3.2 Removal of Hg using COP-3 from Waste Water.

Considering the strong coordination ability of –C(=O)NHNH-, -C=N and pyridinic groups in the **COP-3** backbone, the **COP-3** is assumed to be a promising material for adsorption of metal ions. Five metal ions including Pd^{2+}, Hg^{2+}, Cu^{2+}, Cd^{2+} and Ca^{2+} are chosen as target metal ions for adsorption evaluation. Among the mentioned metal ions, we have taken Hg^{2+} as standard metal ion for kinetic studies. It is found that **COP-3** achieved a maximum Hg

adsorption capacity of 627.8 mg g^{-1} (using eq. 3.2). Figure 3.9 a displays adsorption isotherm at equilibrium. Adsorption isotherm is obtained from aqueous solutions with initial Hg^{2+} concentrations ranging from 50 to 800 ppm. The Langmuir model is well fitted with the adsorption isotherm with a correlation coefficient of 0.989.

A detailed kinetic (Figure 3.9 b, c and d) study was investigated on **COP-3** in removing Hg from water. We had started with 100 ppm solution of Hg^{2+} ion. After that the solution mixture was analyzed at different time intervals following treatment with **COP-3**. Remaining Hg^{2+} ion concentration was analyzed using inductively coupled plasma-atomic emission spectroscopy (ICP-AES). Hg^{2+} ion concentration is lowered to 58.76 ppm within 20 min and after 2 h the concentration is as low as 16.13 ppm.
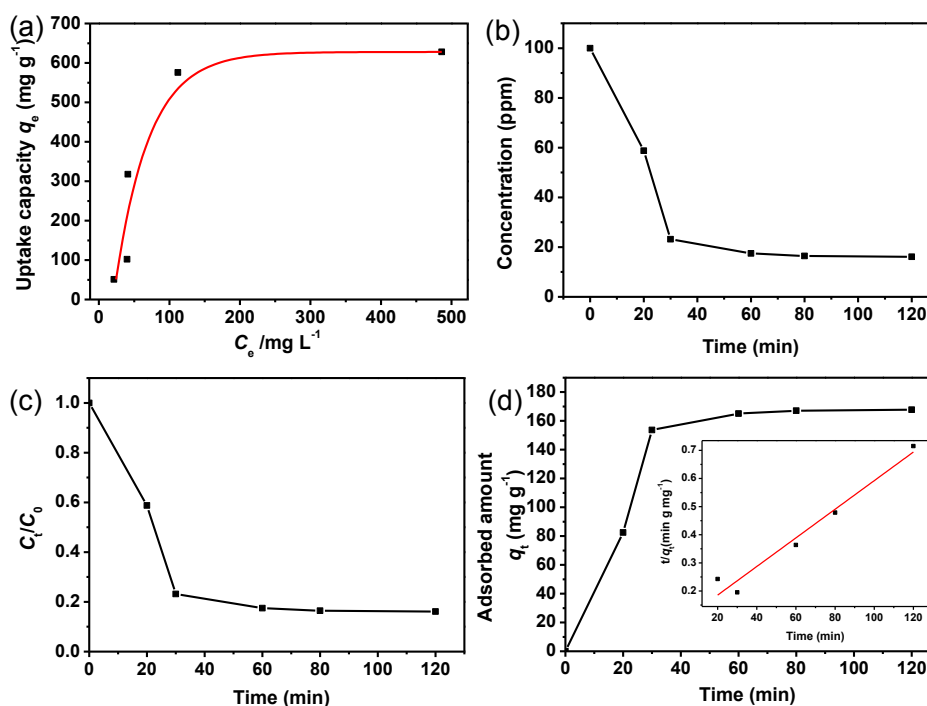
Figure 3.9 (a) Hg^{2+} adsorption isotherm for **COP-3.** (b) Hg^{2+} adsorption kinetics of **COP-3** with Hg^{2+} initial concentration of 100 ppm (c) adsorption curve of Hg^{2+} concentration versus time in aqueous solution using **COP-3**. (d) adsorption capacity curve of Hg^{2+} versus time in aqueous solution using **COP-3**, Inset shows the pseudo-second order kinetic plot for the adsorption.

From figure 3.9 d, The initial adsorption rate, ($k_2 q_e^2$), is calculated as 12.04 mg g^{-1} min^{-1} which assigns the rapid removal of mercury from water. A pseudo-second order kinetic is well fitted with the experimental kinetic data using eq. 3.3. Distribution coefficient (K_d) value of **COP-3** for the Hg adsorption is found to be (using eq. 3.4) 1.02×10^5 mL g^{-1}. It is necessary to check selective removal of mercury in the presence of other ions. The selectivity test (Figure 3.10) of

mercury in presence of Pb^{2+}, Cu^{2+}, Ca^{2+} and Cd^{2+} with equal concentrations was performed.
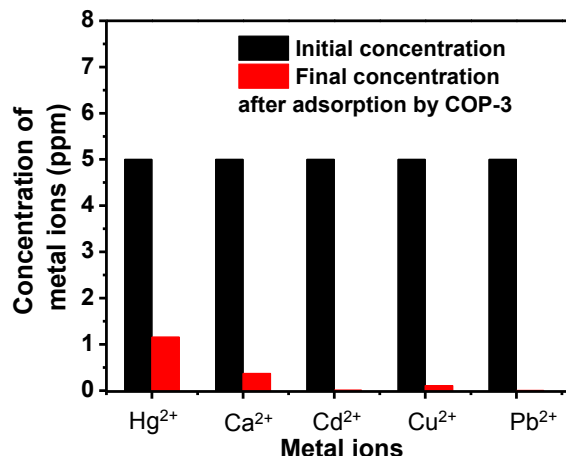
Figure 3.10 Selectivity test of Hg^{2+} adsorption in presence of other metal ions using **COP-3** (The final concentration of Cd^{2+} and Pb^{2+} after adsorption was as low as 0.10 ppb, reaching the detection limit of the instrument).

After treatment with **COP-3**, the final concentration of Cd^{2+} and Pb^{2+} after adsorption is found as low as 10 ppb (reaching the detection limit of the instrument) along with Hg^{2+} 80% removal efficiency (Table 3.3). **COP-3** shows versatility in metal ions adsorption due to having large number of binding ligand group in its polymeric back bone. Removal efficiency is calculated using eq. 3.5.

Table 3.3 Removal efficiency table of heavy metal ions using **COP-3**

Metal ion	Hg^{2+}	Ca^{2+}	Cd^{2+}	Cu^{2+}	Pb^{2+}
Initial concentration	5 ppm	5 ppm	5 ppm	5 ppm	5ppm
Final concentartion	1.15 ppm	0.37 ppm	<10 ppb	0.19 ppm	<10ppb
Removal efficiency %	80%	93%	>99%	96%	>98%

In this regard, Ma *et al.*[39-41] reported few thiol (-SH) modified covalent organic polymers for the efficient Hg^{2+} adsorption via the formation of strong coordination bond. Their -SH groups on the surface of the polymer provide huge number of coordinating sites for metal ions. The Hg^{2+} or other metal ions are exclusively bound with -SH via intermolecular co-operative bond in -SH functionalized polymer. After every use, the Hg^{2+} loaded polymer needs to be stirred and washed with 12 M concentrated HCl to get its initial structure or mercury free form. **COP-3** contains pyridine group in polymeric backbone which

efficiently interact with Hg^{2+} (explained later) to remove it from the aqueous solution. Now this high concentration might damage the polymeric architecture and functionality, pore size and linkages. So after every use, **Hg-COP-3** is vigorously washed with only distilled water to get Hg^{2+} free **COP-3**. Water cannot deform the original polymeric structure of **COP-3**.

3.3.3 Investigation of Hg^{2+} binding interaction with COP-3.

To check the binding interaction of Hg^{2+} with **COP-3**, we have performed XPS, solid state UV, Raman spectroscopy and FT-IR. XPS technique[39-42] was applied to reveal the interaction between **COP-3** and Hg(II) ions (Figure 3.11 a, b). **COP-3** shows several peaks between 200 eV to 550 eV which implies C1s, N1s, and O1s orbitals. Core level deconvoluted spectra of N1s and O1s for **COP-3** are shown in Figure 3.11 c, d. Core level spectra for N1s in **COP-3** shows three peaks at 400.78, 400.00 and 399.68 eV due to the pyridinic ring -C=N and -C(=O)N. Peaks appeared at region of 531.90 to 533.00 eV for the carbonyl O1s in **COP-3**. Now binding energy of atoms in a blend is varied or shifted to higher binding energy due to specific interactions with metal ions.[43] After Hg(II) adsorption onto **COP-3**, the binding energy of O1s for –C=O is not changed significantly whereas the binding energies of nitrogen centres (N1s) are significantly shifted to higher energy. 0.58 eV (pyridinic -C=N), 0.23 eV Schiff base -C=N) and 0.51 eV -C(=O)N) red shifting in binding energy is observed after Hg(II) adsorption onto **COP-3** (Figure 3.11 e, f). These above results shows that Hg^{2+} ions significantly interact with the N centre of pyridinic -C=N than with other nitrogen centre and oxygen centre. The reason is that nitrogen atoms existed in a more oxidized state on the **COP-3** surface after interacting with Hg(II), forming Hg(II)···N=C complex (which is also explained by DFT and Raman experiments). The nitrogen atoms donate their electron pairs to the Hg(II) to form coordination bonds between them. Electron density on nitrogen atoms is then reduced and peaks are shifted to higher binding energy.[44] The N1s XPS spectra indicate the significant binding interactions of Hg(II) to pyridinic nitrogen atoms of **COP-3**. After adsorption of Hg(II) ion on **COP-3** surface, two new peaks are generated at 102.23 and 105.20 eV (Hg4f$_{7/2}$ and Hg 4f$_{5/2}$) due to Hg. This result indicates that Hg(II) ion is adsorbed onto **COP-3** (Figure 3.12).

Thin film solid state UV -Vis experiment was performed. An apparent red shift at the region of 400 nm is observed at the characteristic band in UV-Vis (Figure 3.13 a) which is ascribed to the interaction of pyridine group after introduction of Hg^{2+}. Additionally, Raman spectra (Figure 3.13 b) of **Hg-COP-3** displays peak at 280 cm^{-1} which is associated with the (-N-Hg) stretching. SEM image of **Hg-COP-3** shows induced morphological changes in the polymeric framework of **COP-3** (Figure 3.14 a). FT-IR (Figure 3.14 b) was performed with the precipitate (**Hg-COP-3**). The stretching frequency of C=N shifts upfield to 1599 cm^{-1} (**Hg-COP-3**) from 1605 cm^{-1} (**COP-3**) due to the interaction between pyridine N and Hg^{2+}. The C=O stretching frequency also changes from 1683 cm^{-1} to 1674 cm^{-}

[1].[45-46] Organic ligands for the detection of Hg^{2+} are reported in literature in huge numbers, [47-49] however, removal of Hg^{2+} by them are rare (Table 3.4).
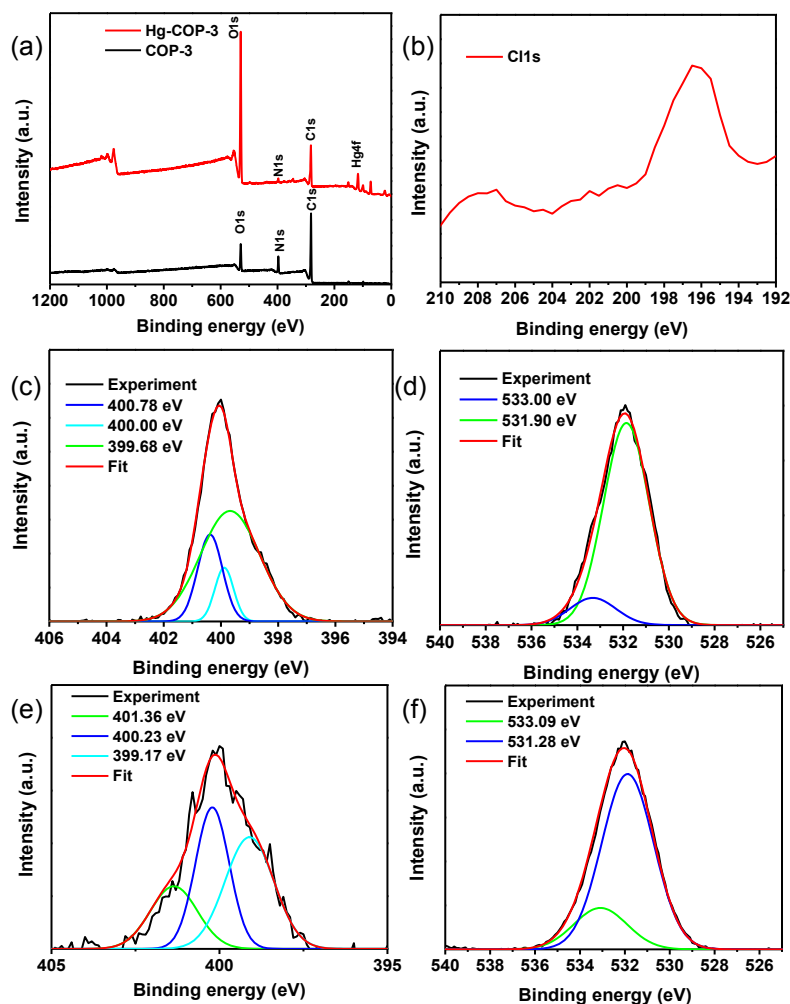
Figure 3.11 (a) XPS wide scan spectra of **COP-3** and **Hg-COP-3.** (b) **XPS** wide scan spectra of Cl in **Hg- COP**. Deconvoluted XPS spectra of (c) N1s, (d) O1s in **COP-3**. Deconvoluted XPS spectra of (e) N1s, (f) O1s in **Hg-COP-3**.
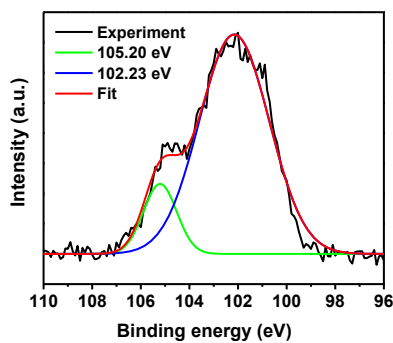
Figure 3.12 Deconvoluted XPS spectra of Hg^{2+} in **Hg-COP-3.**
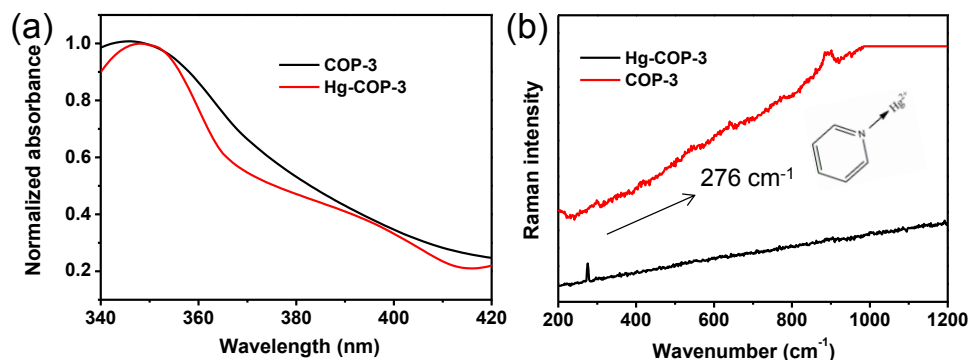
Figure 3.13 (a) Solid state UV-Vis spectrum and (b) Raman spectrum **COP-3** and **Hg-COP-3**.

Table 3.4 Comparative study with other polymer based Hg^{2+} ion sensors

S. No	Materials	Detection limit and adsorption of Hg^{2+}	Reference
1	COF-LZU8	236 mg g^{-1}	24
2	TAPB-BMTTPA-COF	ND and 734 mg g^{-1}	23
3	NOP-28	12.0 ppb and 658 mg g^{-1}	50
4	S-FMC-700	451 mg g^{-1} adsorption	19
5	**COP-3**	627. 8 mg g^{-1}	This work
	ND: Not Done		

COF-LZU8 was reported by Wang *et al*. that could detect (detection limit of 33.3 μM and adsorption capacity of 236 mg g^{-1}) and remove Hg^{2+}.[24] Another two materials named as TAPB-BMTTPA-COF[23] and S-FMC[19] could remove Hg^{2+} from aqueous medium with an adsorption capacity of 743 mg g^{-1} and 452 mg g^{-1} respectively. In another case, NOP-28 was found to have a 12 ppb detection of Hg^{2+} and 658 mg g^{-1} of adsorption capacity.[50]
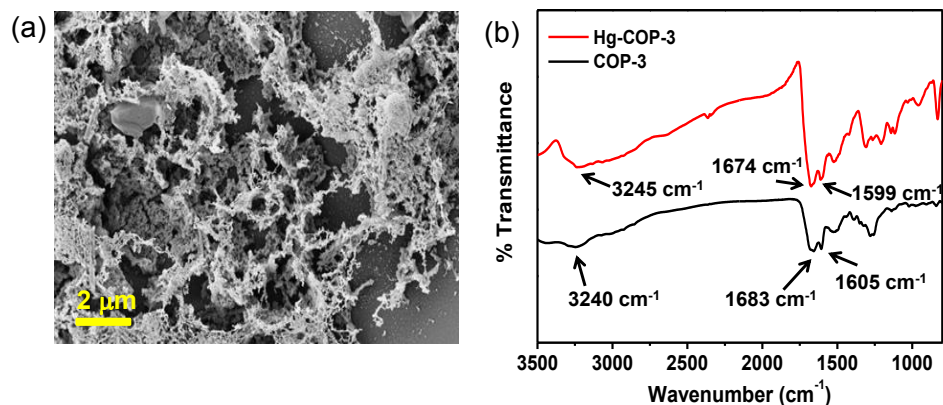
Figure 3.14 (a) SEM image of **COP-3** after adsorption with Hg^{2+} and (b) FT-IR spectra of **COP-3** and **Hg-COP-3**.

3.3.4 Density Functional Theory Studies.

DFT calculations are completed in Turbomole (v7.0) software.[25-30] First the geometry of the truncated **COP-3** was optimized as in Figure 3.15 a. Figure 3.15 b shows the geometry optimized structure of **COP-3** with labels), which enabled us to find the distances between the various bonds. The calculation was performed with truncated version of **COP-3**, three molecules of $HgCl_2$ and water in the system (Figure 3.16 a).The energy of **COP-3** before interaction with Hg^{2+} is found as -3347.36 kJ with a HOMO-LUMO gap of 3.029 eV prior to interaction.
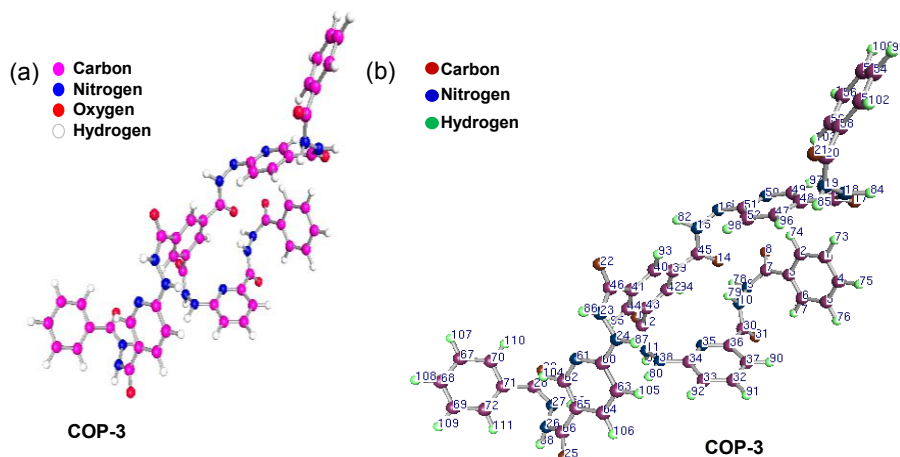
Figure 3.15 (a) Geometry optimized structure of **COP-3** and (b) geometry optimized structure of **COP-3** with labels.

The lowest energy structure is shown here. On comparison with geometry optimized structure of **COP-3**, it is found that HOMO-LUMO gap and the total energy of the **Hg-COP-3** system are lowered (became more negative) on interaction of Hg^{2+} ions with **COP-3**. In **Hg-COP-3** interaction, three Hg^{2+} ions interact with three pyridine Ns of **COP-3**.
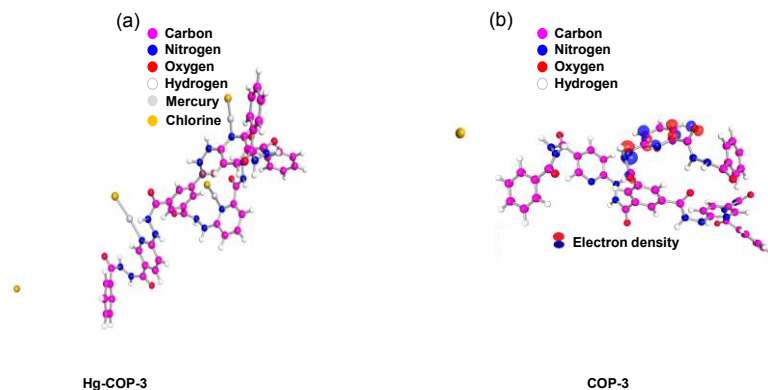
Figure 3.16 (a) Geometry optimized structure of **Hg-COP-3** and (b) geometry optimized structure of **COP-3** with labels, (b) geometry optimized structure of **COP-3** showing HOMO.

It was primarily observed that the interactions occur between the pyridine N and Hg^{2+}. One Hg^{2+} interacts with one pyridine N (N61) which forms a distance of 2.139 Å. The other Hg^{2+} interacts with another pyridine N (N50) atom to form a bond of about 2.145 Å. The third Hg^{2+} interacts with pyridine N (*i.e.* N35). The distance is calculated as 2.197 Å. The distances suggest covalent interaction between Hg-N. The HOMO-LUMO gap is reduced to 0.298 eV (in **Hg-COP-3**) from 3.029 eV in **COP-3**. The reduced HOMO-LUMO gap indicates facile electron transfer. HOMO-LUMO gap of less than 1.00 eV indicates kinetically stable species.[51] All the C-N distances adjacent to the pyridine moiety are increased in length considerably after the pyridine N interacts with Hg^{2+} ion as given in Table 3.5. The increase in distances suggest electron shift from polymeric backbone towards Hg^{2+}.

Table 3.5 Comparison of C-N distances before and after interaction with Hg^{2+}

	Before interaction with Hg^{2+} (Å)	After interaction with Hg^{2+} (Å)
N61-C60	1.351	1.362
N61-C62	1.346	1.369
N35-C34	1.348	1.354
N35-C36	1.354	1.370
N50-C51	1.355	1.368
N50-C49	1.341	1.366

The interaction energy is calculated by the following equation:

$$\Delta E_{int} = E (A, B) - [E (A) + E (B)] \qquad \text{Eq. 3.6}$$

where, E (A, B) is the energy of the **Hg-COP-3** (-6750.27 kJ), E (A) is the energy of **COP-3** (-3347.36 kJ) and E (B) is the energy of $HgCl_2$ ($3 \times$ -1073.91 kJ). Thus ΔE_{int} is calculated as -181.18 kJ. The negative interaction energy suggests facile interaction between **COP-3** and Hg^{2+}. When the HOMO of the **COP-3** (Figure 3.16 b) and **Hg-COP-3** (Figure 3.17) are compared, to see the electronic distribution before and after interaction with Hg^{2+}, it is seen that the electronic distribution is almost removed from the polymeric framework. From the atomic population analysis, it is found that prior to the interaction with Hg^{2+}, the charge densities on the three pyridine Ns of **COP-3** are as follows: N35 with -0.1049.4; N50 with -0.10867 and 61N with -0.11106. After interaction with Hg^{2+}, the charges on the above mentioned N atoms change from negative to positive suggesting shift in electron density from N center to Hg^{2+}. The charges are now calculated as 35N with 0.03744; 50N with 0.05771 and 61N with 0.05776.
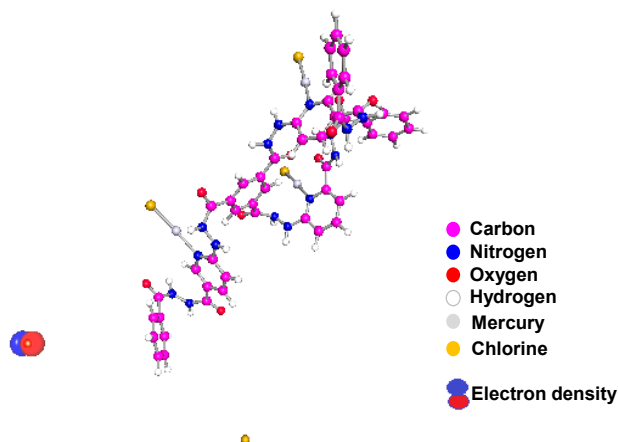
Figure 3.17 Geometry optimized structure of **Hg-COP-3** showing HOMO.

3.4 Conclusion.

In summary, a new robust covalent organic polymer **COP-3** with a picolinohydrazide linkage was synthesized and explored elaborately in this work. Here, we investigated the role of the pyridine moiety in **COP-3** in various applications. **COP-3** acted as a heterogeneous catalyst for Knoevenagel condensation at 30 °C, which was reused for up to four cycles. Hydrazide and pyridine groups of **COP-3** provided a better basic host toward the Knoevenagel reactants, which increased its catalytic efficiency under mild conditions. **COP-3** exhibited promising efficiency in removal of heavy metal ions, including Ca^{2+}, Cu^{2+}, Cd^{2+}, Hg^{2+}, and Pb^{2+}. For all of the mentioned metal ions, **COP-3** showed significant adsorption capacity with removal efficiencies of >95% for Ca^{2+}, Cu^{2+}, Cd^{2+}, and Pb^{2+} and 80% for Hg^{2+}. Insight into this interaction was obtained through a theoretical approach. The unique combination of suitable binding sites, such as pyridine N and hydrazide units, in the polymeric framework was the key reason for such diverse properties of this material. Such predesigned polymers can be used in various areas and could constitute important starting materials for several industrial applications in future. The Hg^{2+} ion removal capacity might be explored further in future for full-scale environmental applications.

3.5 References

1. Kitagawa, S. Future Porous Materials. *Acc. Chem. Res.* **2017**, *50*, 514-516 (DOI: org/10.1021/acs.accounts.6b00500).

2. Bhunia, A.; Vasylyeva, V.; Janiak, C. From A Supramolecular Tetranitrile to a Porous Covalent Triazine-Based Framework with High Gas Uptake Capacities. *Chem. Commun.* **2013**, *49*, 3961-3963 (DOI: 10.1039/C3CC41382A).

3. Ren, S.; Bojdys, M. J.; Dawson, R.; Laybourn, A.; Khimyak, Y. Z.; Adams, D. J.; Cooper, A. I. Porous, Fluorescent, Covalent Triazine-Based Frameworks Via Room Temperature and Microwave-Assisted Synthesis. *Adv. Mater.* **2012**, *24*, 2357-2361 (DOI: org/10.1002/adma.201200751).

4. Segura, J. L.; Mancheno, M. J.; Felix, Z. Covalent Organic Frameworks Based on Schiff-Base Chemistry: Synthesis, Properties and Potential Applications. *Chem. Soc. Rev.* **2016**, *45*, 5635 (DOI: 10.1039/C5CS00878F).

5. Puthiaraj, P.; Lee, Y-R.; Zhang, S.; Ahn, W-S. Triazine-based covalent organic polymers: design, synthesis and applications in heterogeneous catalysis. *J. Mater. Chem. A* **2016**, *4*, 16288-16311 (DOI: 10.1039/C6TA06089G).

6. Côté, A. P.; Benin, A. I.; Ockwig, N. W.; O'Keeffe, M.; Matzger, A. J.; Yaghi, O. M. Porous, crystalline, covalent organic frameworks. *Science* **2005**, *310*, 1166-1170. (DOI: 10.1126/science.1120411)

7. Feng, X.; Ding, X.; Jiang, D. Covalent organic frameworks. *Chem. Soc. Rev.* **2012**, *41*, 6010-6022 (DOI: 10.1039/C2CS35157A).

8. Ding, S.-Y.; Wang, W. Covalent organic frameworks (COFs): from design to applications. *Chem. Soc. Rev.* **2013**, *42*, 548-568 (10.1039/C2CS35072F).

9. Ascherl, L.; Sick, T.; Margraf, J. T.; Lapidus, S. H.; Calik, M.; Hettstedt, C.; Karaghiosoff, K.; Doblinger, M.; Clark, T.; Chapman, K. W.; Auras, F.; Bein, T. Molecular docking sites designed for the generation of highly crystalline covalent organic frameworks. *Nat. Chem.* **2016**, *8*, 310-316 (DOI: org/10.1038/nchem.2444).

10. Pang, Z.-F.; Xu, S.-Q.; Zhou, T.-Y.; Liang, R.-R.; Zhan, T.-G.; Zhao, X. Construction of Covalent Organic Frameworks Bearing Three Different Kinds of Pores through the Heterostructural Mixed Linker Strategy. *J. Am. Chem. Soc.* **2016**, *138*, 4710-4713 (DOI: 10.1021/jacs.6b01244).

11. Fang, Q.; Gu, S.; Zheng, J.; Zhuang, Z.; Qiu S.; Yan, Y. 3D Microporous Base- Functionalized Covalent Organic Frameworks for Size- Selective Catalysis. *Angew. Chem. Int. Ed.* **2014**, *53*, 2878-2882 (DOI: org/10.1002/anie.201310500).

12. Li, H.; Pan, Q.; Ma, Y.; Guan, X.; Xue, M.; Fang, Q.; Yan, Y.; Valtchev, V.; Qiu, S. Three-Dimensional Covalent Organic Frameworks with Dual Linkages for Bifunctional Cascade Catalysis. *J. Am. Chem. Soc.* **2016**, *138*, 14783-14788 (DOI.org/10.1021/jacs.6b09563).

13. Roy Chowdhury, A.; Ghosh, P.; Roy, B. G.; Mukhopadhyay, S. K.; Mitra, P.; Banerjee, P. A simple and dual responsive efficient new Schiff base chemoreceptor for selective sensing of F^- and Hg^{2+}: application to bioimaging in living cells and mimicking of molecular logic gates. *RSC Adv.* **2015**, *5*, 62017-62023 (DOI: 10.1039/c5ra06105a).

14. Fu, F.; Wang, Q. Removal of heavy metal ions from wastewaters: A review. *Journal of Environmental Management* **2011**, *92*, 407-418. (doi.org/10.1016/j.jenvman.2010.11.011).

15. Guo, L.; Cao, D. Color tunable porous organic polymer luminescent probes for selective sensing of metal ions and nitroaromatic explosives. *J. Mater. Chem. C* **2015**, *3*, 8490-8494 (DOI: 10.1039/c5tc01649e).

16. Rui, X.; Guo, H.; Wang, T.; Gong, L.; Wang, Y.; Ai, J.; Huang, D.; Chena, H.; Yang, W.; Fluorescence properties and analytical applications of covalent

organic frameworks. *Anal. Methods* **2017**, *9*, 3737-3750 (10.1039/C7AY01261F).

17. Räupke, A.; Palma-Cando, A.; Shkura, E.; Teckhausen, P.; Polywka, A.; Görrn, P.; Scherf, U.; Ried, T. Highly sensitive gas-phase explosive detection by luminescent microporous polymer networks. *Scientific Reports* **2016**, *6*, 29118 (DOI: org/10.1038/srep29118).

18. Zhang, Z-H.; Duan, F-H.; Tian, J-Y.; He, J-Y.; Yang, L-Y.; Zhao, H.; Zhang, S.; Liu, C-S.; He, L-H.; Chen, M.; Chen, D-M.; Du, M. Aptamer-Embedded Zirconium-Based Metal-Organic Framework Composites Prepared by De Novo Bio-Inspired Approach with Enhanced Biosensing for Detecting Trace Analytes. *ACS Sens*. **2017**, *2*, 982-989 (DOI: org/10.1021/acssensors.7b00236).

19. Shin, Y.; Fryxell, G. E.; Um, W.; Parker, K.; Mattigod, S. V.; Skaggs, R. Sulfur-Functionalized Mesoporous Carbon. *Adv. Funct. Mater*. **2007**, *17*, 2897-2901 (DOI: 10.1002/adfm.200601230).

20. Ma, D.; Li, B.; Cui, Z.; Liu, K.; Chen, C.; Li, G.; Hua, J.; Ma, B.; Shi, Z.; Feng, S. Multifunctional Luminescent Porous Organic Polymer for Selectively Detecting Iron Ions and 1,4-Dioxane via Luminescent Turn-off and Turn-on Sensing. *ACS Appl. Mater. Interfaces* **2016**, *8*, 24097-24103 (DOI: org/10.1021/acsami.6b07470).

21. Guo, L.; Zeng, X.; Lan, J.; Yun, J.; Cao, D. Absorption competition quenching mechanism of porous covalent organic polymer as luminescent sensor for selective sensing Fe^{3+}. *Chemistry Select* **2017**, *2*, 1041-1047 DOI: org/10.1002/slct.201602076).

22. Su, Y.; Wang, Y.; Li, X.; Li, X.; Wang, R. Imidazolium-Based Porous Organic Polymers: Anion Exchange Driven Capture and Luminescent Probe of $Cr_2O_7^{2-}$. *ACS Appl. Mater. Interfaces* **2016**, *8*, 18904-18911 (DOI: org/10.1021/acsami.6b05918).

23. Huang, N.; Zhai, L.; Xu, H.; Jiang, D. Stable Covalent Organic Frameworks for Exceptional Mercury Removal from Aqueous Solutions. *J. Am. Chem. Soc.* **2017**, *139*, 2428-2434 (DOI: org/10.1021/jacs.6b12328).

24. Ding, S-Y.; Dong, M.; Wang, Y-W.; Chen, Y-T.; Wang, H-Z.; Su, C-Y.; Wang, W. Thioether-Based Fluorescent Covalent Organic Framework for Selective Detection and Facile Removal of Mercury (II). *J. Am. Chem. Soc*. **2016**, *138*, 9, 3031-3037 (DOI: org/10.1021/jacs.5b10754).

25. University of Karlsruhe and Forschungszentrum Karlsruhe GmbH 1989−2007.http://www.cosmologic.de/files/downloads/manuals/TURBOMOLE-Users-Manual_70.pdf (Since 2007).

26. Becke, A. D. Density functional calculations of molecular bond energies. *J. Chem. Phys*. **1986**, *84*, 4524-4529 (DOI: org/10.1063/1.450025).

27. Becke, A. D. Density- functional thermochemistry. III. The role of exact exchange. *J. Chem. Phys*. **1993**, *98*, 5648-5652 (DOI: org/10.1063/1.464913).

28. Lee, C.; Yang, W.; Parr, R. G. Development of the Colle-Salvetti correlation-energy formula into a functional of the electron density. *Phys. Rev. B*. **1988**, *37*, 785-789 (DOI: org/10.1103/PhysRevB.37.785).

29. Schafer, A.; Horn, H.; Ahlrichs, R. Fully optimized contracted Gaussian basis sets for atoms Li to Kr. *J. Chem. Phys*. **1992**, *97*, 2571-2577 (DOI: org/10.1063/1.463096).

30. Schafer, A.; Huber, C.; Ahlrichs R. Fully optimized contracted Gaussian basis sets of triple zeta valence quality for atoms Li to Kr. *J. Chem. Phys*. **1994**, *100*, 5829-5835 (DOI: org/10.1063/1.467146).

31. Carne´-Sa´nchez, A.; Stylianou, K. C.; Carbonell, C.; Naderi, M.; Imaz, I.; Maspoch, D. Protecting Metal-Organic Framework Crystals from Hydrolytic Degradation by Spray- Dry Encapsulating Them into Polystyrene Microspheres. *Adv. Mater*. **2015**, *27*, 869-873 (DOI: org/10.1002/adma.201403827).

32. Suresh, V. M.; Bonakala S.; Atreya, H. S.; Balasubramanian, S.; Maji, T. K. Amide Functionalized Microporous Organic Polymer (Am-MOP) for Selective CO_2 Sorption and Catalysis. *ACS Appl. Mater. Interfaces* **2014**, *6*, 4630-4637 (DOI: org/10.1021/am500057z).

33. Sutar, P.; Maji, T.K. Bimodal self-assembly of an amphiphilic gelator to hydrogelnanocatalyst and organogel of different morphologies and photophysical properties. *Chem. Commun.* **2016**, *52*, 13136-13139 (DOI: 10.1039/C6CC06971A).

34. Shinde, D. B.; Kandambeth, S.; Pachfule, P.; Kumara R. R.; Banerjee R. Bifunctional covalent organic frameworks with two dimensional organocatalytic micropores. *Chem. Commun*. **2015**, *51*, 310-313 (DOI: 10.1039/C4CC07104B).

35. Fang, Q.; Gu, S.; Zheng, J.; Zhuang, Z.; Qiu S.; Yan Y. 3D Microporous Base- Functionalized Covalent Organic Frameworks for Size Selective Catalysis. *Angew. Chem. Int. Ed*. **2014**, *53*, 2878 -2882 (DOI: org/10.1002/anie.201310500).

36. Dang, Q-Q.; Zhan, Y-F.; Wang, X-M.; Zhang, X-M. Heptazine-Based Porous Framework for Selective CO_2 Sorption and Organocatalytic Performances. *ACS Appl. Mater. Interfaces* **2015**, *7*, 28452-28458 (DOI: org/10.1021/acsami.5b09441.

37. Sun, Q.; Aguila, B.; Ma, S. A Bifunctional Covalent Organic Framework As An Efficient Platform For Cascade Catalysis. *Mater. Chem. Front*. **2017**, *1*, 1310-1316 (DOI: 10.1039/C6QM00363J).

38. Jiajia, W.; Wang, X.; Xu, H.; Zhao, X.; Zheng, Z.; Zhen-liang, X. A new Zn (Ⅱ) porous metal-organic framework and the catalytic properties in Knoevenagel condensation controlled by its morphology *ChemPlusChem.* **2017**, *9*, 1182-1187 (DOI: org/10.1002/cplu.201700327).

39. Aguila, B.; Sun, Q.; Perman, J. A.; Earl, L. D.; Abney, C. W.; Elzein, R.; Schlaf, R.; Ma, S. Efficient Mercury Capture Using Functionalized Porous Organic Polymer. *Adv. Mater*. **2017**, *29*, 1700665 (DOI: org/10.1002/adma.201700665).

40. Sun, Q.; Aguila, B.; Perman, J.; Earl, L. D.; Abney, C. W.; Cheng, Y.; Wei, H.; Nguyen, N.; Wojtas, L.; Ma, S. Postsynthetically Modified Covalent Organic Frameworks for Efficient and Effective Mercury Removal. *J. Am. Chem. Soc*. **2017**, *139*, 2786-2793 (DOI: org/10.1021/jacs.6b12885).

41. Li, B.; Zhang, Y.; Ma, D.; Shi, Z.; Ma, S. Mercury nano-trap for effective and efficient removal of mercury(II) from aqueous solution. *Nat. Commun*. **2014**, *5*, 5537 (DOI: org/10.1038/ncomms6537).

42. Huang, S.; Ma, C.; Liao, Y.; Min, C.; Du, P.; Jiang, Y. Removal of Mercury(II) from Aqueous Solutions by Adsorption on Poly(1-amino-5-chloroanthraquinone) Nanofibrils: Equilibrium, Kinetics, and Mechanism Studies. *Journal of Nanomaterials* **2016**, 1-11 (DOI: org/10.1155/2016/7245829).

43. Chen, C.; Dong, L.; Cheung, M. K. Preparation and characterization of biodegradable poly(l lactide)/chitosan blends. *Eur. Polym. J*. **2005**, *41*, 958-966 (DOI: org/10.1016/j.eurpolymj.2004.12.002).

44. Zhang, X.; Bai, R. B. Mechanisms and kinetics of humic acid adsorption onto chitosan-coated granules. *J. Colloid Interface Sci*. **2003**, *264*, 30-38 (DOI: 10.1016/s0021-9797(03)00393-x).

45. Uribe-Romo, F. J.; Doonan, C. J.; Furukawa, H.; Oisaki, K.; Yaghi, O. M. Crystalline Covalent Organic Frameworks with Hydrazone Linkages. *J. Am. Chem. Soc*. **2011**, *133*, 11478-11481 (DOI: org/10.1021/ja204728y).

46. Maiti, S.; Chowdhury, A. R.; Das, A. K. Electrochemically Facile Hydrogen Evolution Using Ruthenium Encapsulated Two Dimensional Covalent Organic Framework (2D COF). *ChemNanoMat*. **2019,** *5*, 1-9 (DOI: org/10.1002/cnma.201900499).

47. Zhang, Y. M.; Qu, W. J.; Gao, G. Y.; Shi B. B.; Wu, G. Y.; Wei, T. B.; Lin, Q.; Yao, H. A highly selective dual-channel chemosensor for mercury ions: utilization of the mechanism of intramolecular charge transfer blocking. *New J. Chem*. **2014**, *38*, 5075-5080 (DOI: 10.1039/C4NJ00599F).

48. Biswas, S.; Bhowmik, S.; Rasale, D. B.; Das, A. K. A Highly Selective Colorimetric Detection of Hg(II) *via* Enzymatic Dephosphorylation Reaction. *Macromol. Symp*. **2016**, *369*, 108-113. (doi: org/10.1002/masy.201600069)

49. Kim, H. N.; Ren, W. X.; Kim, J. S.; Yoon, J. Fluorescent and colorimetric sensors for detection of lead, cadmium, and mercury ions. *Chem. Soc. Rev*. **2012**, *41*, 3210-3244 (DOI: 10.1039/C1CS15245A).

50. Fu, Y.; Yu, W.; Zhang, W.; Huang, Q.; Yan, J., Pan, C.; Yu, G. Sulfur-rich covalent triazine polymer nanospheres for environmental mercury removal and detection. *Polym. Chem*. **2018**, *9*, 4125-4131 (DOI: 10.1039/C8PY00419F).

51. Aihara, J. Reduced HOMO-LUMO Gap as an Index of Kinetic Stability for Polycyclic Aromatic Hydrocarbons. *J. Phys. Chem. A* **1999**, *103*, 7487-7495 (DOI: org/10.1021/jp990092i).

Chapter 4

Covalent organic polymer as an efficient chemosensor for highly selective H₂S detection through proton conduction

4.1 Introduction.

H_2S is one of the well-known toxic gases which is mainly generated from drainage water, rubbish dump, laboratory chemical waste, coal mine, oil and paper industries.[1-2] According to national Institute for occupational safety and health (NIOSH), 100-1000 ppm of H_2S causes serious respiratory, central nervous and cardiovascular system problems. Therefore, it is important to design and develop H_2S gas sensors. Several types of gas sensors have been developed to detect toxic and explosive gases such as resistive, impedance and fluorescent gas sensors.[3-5] Specifically, resistive gas sensors have several advantages compared to other gas sensors due to easy device fabrication, simplest operation technique, lower cost of production and easy miniaturization. Moreover, a better resistive gas sensor holds a sensing layer whose resistance is highly sensitive to the surrounding ambience. Several organic-inorganic nanohybrid materials have been developed as gas sensor devices.[6-7] In 1960, a metal oxide based gas sensor was developed and commercialized.[8] After that researchers are engaged to explore and improve the efficiency of the gas sensor.[9-11] In_2O_3 and bipyramidal nano-crystals based chemiresistive sensor was developed for H_2S sensing.[12] Several ZnO and CuO based nanorod-bundles were reported for H_2S sensing materials at high temperature.[13] α-Fe_2O_3 nanotube was fabricated as H_2S sensing material at higher temperature.[14] A huge number of metal oxide based H_2S sensors is reported in literature. Several drawbacks with metal oxide based sensors are observed such as, air sensitivity, lack of selectivity and high temperature responsive devices. There are limited number of reports on nanostructured materials which were developed to increase the selectivity and efficiency in gas sensing properties.[15-16] Nanostructured materials show efficient performance in gas sensing experiment due to their large surface to volume ratio, large surface area and huge no of surface active sites.[17-18] The interaction between gas molecules and materials mainly takes place on the active surface sites, hence the functional groups residing on a material's surface is crucial for controlling the sensor performance.[19-20] Recently, covalent organic polymers (COPs) have gained significant attention due to their emerging nanostructured architecture and structural diversity. The shape and size selectivity of the COPs can be controlled by variation of pore dimensions, chemical functionalization (presence of hydrophobic and hydrophilic groups) and orientation of surface functional groups, which can facilitate in detection and discrimination among various gases. COPs also possess more active sites on surface, large surface area, intrinsic periodic pore structures and abundant functional groups, which can facilitate in ultrafast sensitivity and high selectivity in gas sensing performance.[21-24] A luminescent porous covalent organic polymer has been developed as efficient H_2S gas sensor.[25] A two dimensional covalent organic framework as chemiresistive gas sensor has also been developed for selective gas sensing.[26] In this regard, our objectives are i) to design and synthesize nanostructured covalent organic polymers (COP), ii) to fabricate a device with the synthesized COP and iii) to analyze the gas sensing properties using the

device. In this work, a mesoporous hydrazide based covalent organic polymer (**COP-4**) has been synthesized and used as sensing layer in chemiresistive gas sensor device. The **COP-4** fabricated sensor exhibits an excellent response to H_2S gas at 25 °C. Experimental results reveal that the **COP-4** sensor can selectively distinguish H_2S from the interference toxic gases including CO_2, NH_3, CO and NO_2. The **COP-4** has been synthesized from the Schiff base reaction between 1,3,5-tricaboxaldehyde and 6-hydrazinonicotinic hydrazide hydrate under thermal reaction in ethanol and 6 M acetic acid solution (**Scheme 4.1**).

4.2 Experimental Section.
4.2.1 Materials.
6-Hydrazinonicotinic hydrazide hydrate, benzene-1,3,5-tricarboxaldehyde, acetic acid, dimethyl sulfoxide (DMSO), and all other solvents were purchased from Sigma Aldrich and Merck.

4.2.2 Synthesis of COP-4.
6-Hydrazinonicotinic hydrazide hydrate and benzene-1,3,5-tricarboxaldehyde in ethanol and 6M acetic acid solution were refluxed in 100 mL round bottom flask for 48 h at 90 °C. After that the reaction mixture was filtered and washed with methanol, acetone, dichloromethane, dimethyl sulfoxide and water. The reddish brown solid residue was dried over 80 °C for 24 h. The reddish brown solid **COP-4** powder was characterized by ^{13}C solid state NMR and FT-IR spectroscopy.

4.2.3 Gas sensor fabrication and sensing measurements.
A Corning glass slide with the dimension of $3 \times 3 \times 0.5$ mm was used for the sensor substrate. Two interdigitated Pt electrodes on the top of glass substrate was used to fabricate the sensor. Each Pt electrode consists of 5 fingers ($250 \times 25 \times 1$ μm), and the distance between two fingers was 25 μm. The **COP-4** powder (10 mg) in 3 mL ethanol in a 10 mL beaker was stirred and sonicated for 30 min. After that dispersed solution of the **COP-4** was directly drop-casted on the interdigitated electrodes coated glass substrate and dried it for the overnight at 120 °C.

The gas sensing experiment was carried out by the dynamic flow-through measurement technique (**Scheme 4.1**). The sensor resistance was monitored by Keithley-2612A source meter interfaced with PC at a direct-current (DC) voltage of 2 V. Optimal concentration of H_2S in the chamber was gained by flowing a certain amount (sccm) of synthetic air to a mixing chamber where certain amount (sccm) of test gas (H_2S) was flown. The flow rates of the respective gases were controlled by a separate mass flow controller, MFC (model: Alicat®, MC 1slpm, USA). The temperature of the system was controlled by a PID temperature controller (with an accuracy of ±1 °C). Efficiency of the sensor corresponds to the response% is given by:

$$\text{Response (\%)} = \frac{R_g - R_a}{R_a} \times 100$$

Where R_g and R_a are the resistance of the sensor in presence of sensing gas and air.

4.2.4 Material Characterization.

Solid state ^{13}C NMR spectrum was recorded using 400 MHz solid state NMR spectrometer (JEOL, model: ECX400; proton frequency: 400 MHz). Powder XRD was done on Rigaku SmartLab, Automated Multipurpose X-ray Diffractometer. Thermogravimetric analysis (TGA) was analyzed using Mettler Toledo Thermal Analyzer with heating rate of 10 °C/min. BET surface area was analyzed on Quantachrome, Autosorb iQ2. FT-IR spectra of the **COP-4** were recorded using Bruker, Tensor-27 FT-IR spectrophotometer. High resolution transmission electron (HRTEM) microscopy analysis was carried out using Field Emission Gun-Transmission Electron Microscope 200 kV (model no Tecnai G2, F30). The field-emission scanning electron microscopy (FESEM) measurements were performed out using a field-emission scanning electron microscope, (Supra 55 Zeiss). For FESEM measurements, the dried samples were coated with gold for subsequent imaging experiments. Atomic force microscopy (AFM) images were taken by drop-casting the samples on mica substrates *via* tapping mode at a scan frequency of 0.65-1.0 Hz and analyzed the data using SmartScan software (model park NX10).
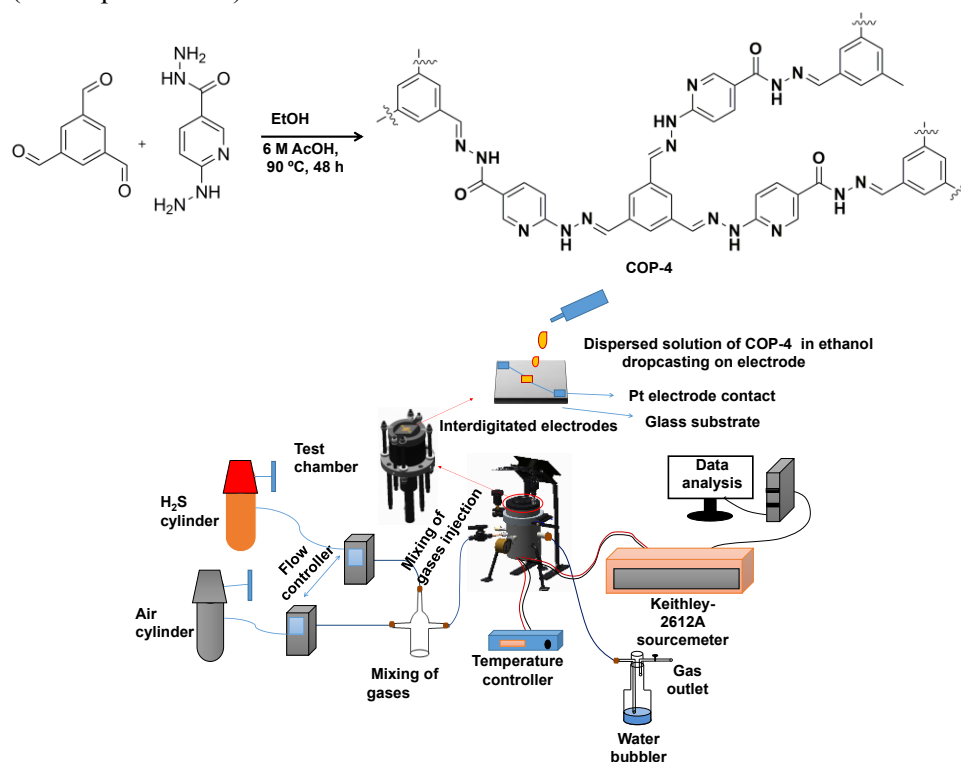
Scheme 4.1: Synthetic scheme of **COP-4** and schematic of the H$_2$S gas sensing set-up.

4.3 Results and discussion.

The FT-IR spectrum of the **COP-4** shows that the **COP-4** is successfully constructed through the -C=N linkage from its building blocks. The FT-IR spectrum of the **COP-4** indicates the presence of desired functionalities and linkages of the polymeric backbone.[27-28] The FT-IR peaks at 1530 and 1605 cm^{-1} are appeared due to the presence of aromatic -C=C- and Schiff base -C=N stretching vibration. FT-IR peak at 1653 cm^{-1} is appeared for the **COP-4** due to C=O stretching vibration of -C(=O)NHN- group (Figure 4.1 a). Broad powder XRD of the **COP-4** at the region of 20 to 30° diffraction angle (2θ) assigns its amorphous polymeric nature (Figure 4.1 b). The robustness of the **COP-4** is demonstrated by thermogravimetric analysis (TGA). Figure 4.1 c suggests high thermal stability of the **COP-4**. The **COP-4** is not fully decomposed within the temperature range of 24-800 °C. Initial degradation in TGA spectrum is observed due to the evaporation of residual solvents or moisture. The **COP-4** is stable up to 240 °C. A weight loss of 5% is observed between the temperature range of 240-360 °C. The next stage is the degradation of the material from 360 to 410 °C, which is about 11%. In the third stage, 16% of the weight loss is observed from 430 to 800 °C. Solid-state ^{13}C CP-MAS NMR of the **COP-4** was acquired to establish the connectivity of the **COP-4** (Fig. 4.1 d). The peaks from 120-150 ppm suggest the existence of the phenyl groups and acylhydrazone Schiff base groups present in the **COP-4**. A peak at 166 ppm suggests the presence of carbonyl group of -C(O)NHN- groups. The peaks at 162 and 158 ppm are appeared due to the presence of -C=N bond of the pyridine ring. To find out the surface morphology of the COP, scanning electron microscopy (SEM), high-resolution transmission emission microscopy (HRTEM) and atomic force microscopy (AFM) analysis were performed. SEM image (Figure 4.2 a) of the **COP-4** shows spherical morphology. HRTEM analysis supports the formation of amorphous spherical morphology with an average diameter of 100 nm (Figure 4.2 b). The **COP-4** is enough stable to retain its structure under high electron beam diffraction (200 kV). AFM image of the **COP-4** reveals the surface roughness. The hydrophobic nature of the **COP-4** is executed by micro level surface roughness. The **COP-4** aggregates to spherical assembly (Figure 4.2 c) during coating on glass surface, which is one of the general features of highly hydrophobic materials.[29] The 3D view of the **COP-4** surface shows some crests and troughs. Air pockets between the peaks (valley regions) are observed in 3D view of AFM image (Figure. 4.2 d). The trapped air pocket in the valley region makes the pore of the **COP-4** hydrophobic nature. **COP-4** is enough stable to retain their form under high (200 kV) electron beam diffraction. Figure 4.3 shows porous texture of **COP-4**.
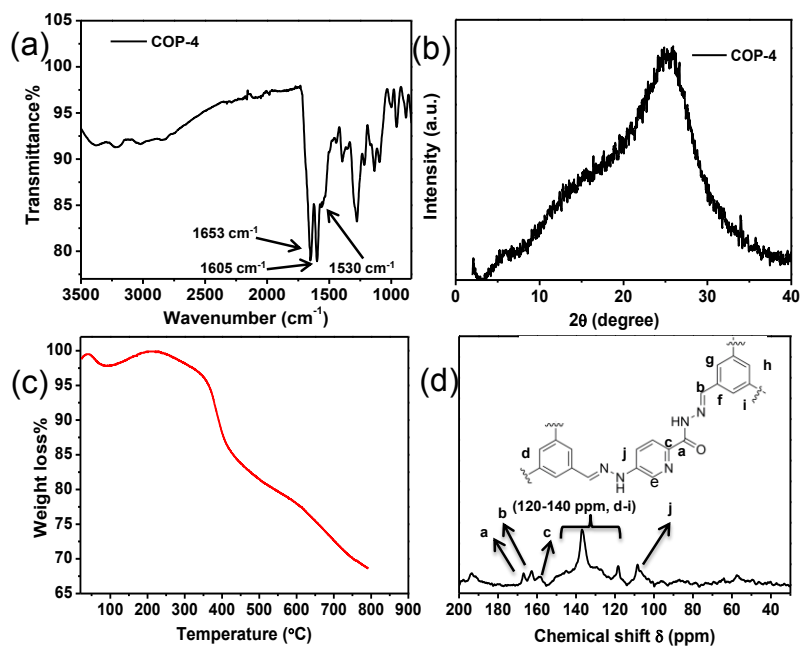
Figure 4.1 (a) FT-IR spectra of **COP-4** (b) PXRD of **COP-4** (c) TGA of **COP-4** (d) solid state ^{13}C NMR of **COP-4**.
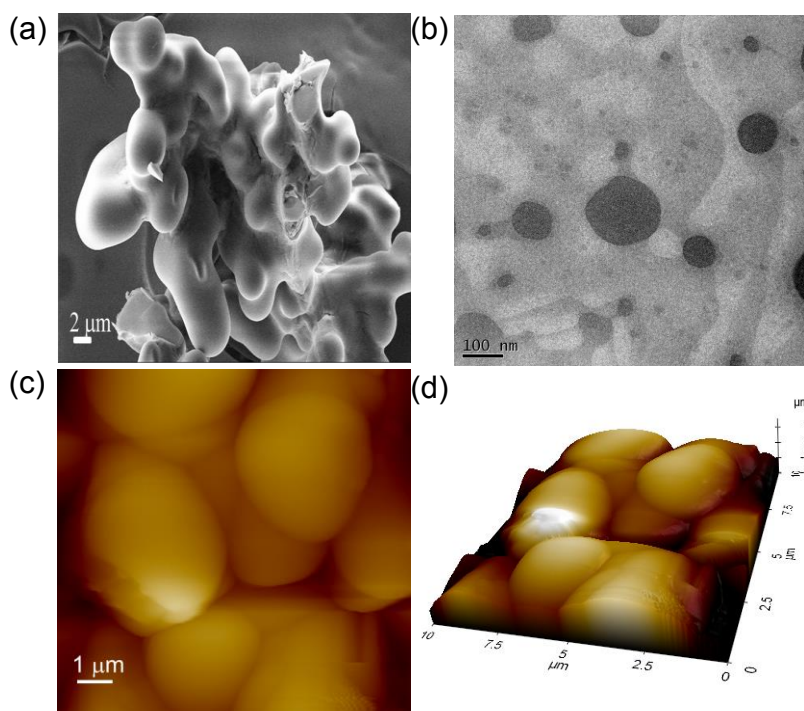
Figure 4.2 (a) SEM (b) HRTEM image of **COP-4**. (c) AFM image of **COP-4**. (d) micro scale 3D image (with z-axis interpretation) of **COP-4.**
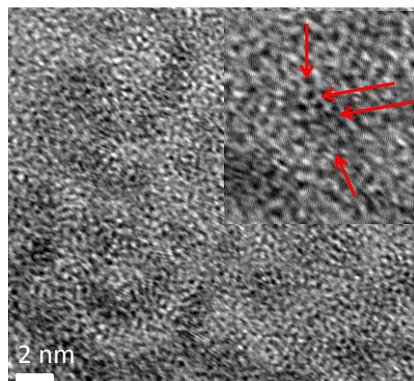
Figure 4.3 HRTEM of **COP-4** (porous texture of **COP-4**).

To determine porosity of **COP-4**, BET surface area analysis by nitrogen sorption was performed at 77K and 1 bar pressure (Figure 4.4 a). According to the IUPAC classification, both **COP-4** shows type IV isotherm. The calculated surface area of **COP-4** is 452 $m^2 g^{-1}$ (Table 4.1). **COP-4** shows the average pore size of 17.5 nm which is calculated *via* NLDFT method (Figure 4.4 b). Calculated average pore volume of **COP-4** is 0.29 cc.g^{-1}. Pore size distribution curve indicates mesoporous nature of **COP-4**.
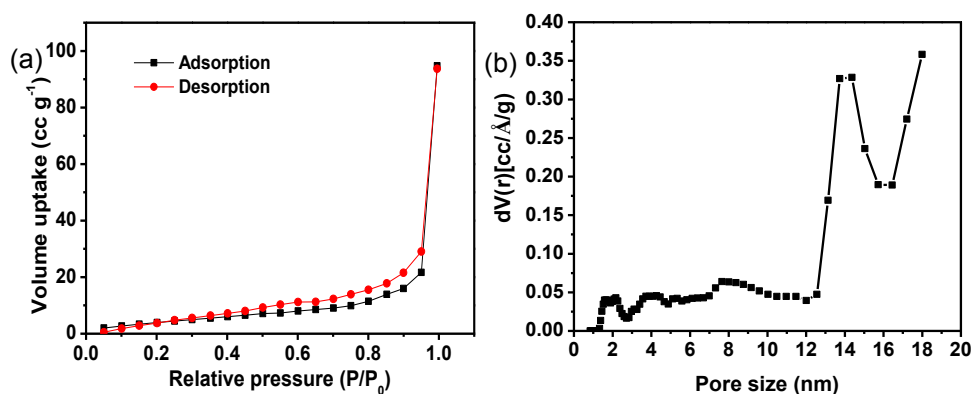
Figure 4.4 (a) BET surface area analysis by N_2 adsorption and (b) Pore size distribution of **COP-4** by using the NLDFT methods.

Table 4.1 Summary of BET surface area analysis

Material	N_2 uptake (cc g^{-1})	Surface area ($m^2 g^{-1}$)	Pore size (nm)	Pore volume cc g^{-1}
COP-4	97.74	452	17.5	0.29

4.3.1 Gas sensing properties.
The sensor device prepared with the **COP-4** was used to investigate the H_2S gas sensing properties. To begin with, 200 ppm of H_2S gas was flown through a test chamber where the **COP-4** based sensor device was placed horizontally formonitoring the electrical resistance. Initially, the electrical resistance of the **COP-4** based sensor device increases quickly when H_2S gas is introduced into

the test chamber. Next the electrical resistance decreases quickly when H_2S gas is withdrawn from the test chamber. The **COP-4** based sensor device exhibits a maximum response of 51% to 200 ppm of the gas at 25 $^\circ$ C (Figure 4.5 a). For the development of low-cost gas sensors, room temperature sensors are the natural choice. Here, the porous **COP-4** based sensor plays an important role in the development of a room temperature H_2S sensor. To check the effect of the H_2S concentration on the device sensitivity, the sensor response was measured at 50, 100 and 200 ppm of H_2S. The sensor response increases slightly with the increase in the concentrations of H_2S. The **COP-4** based sensor was exposed to 200 ppm of H_2S continuously for 3 cycles to check the repeatability of the sensor. The response in the second and third cycles decreased slightly (Figure 4.5 b). The reason for this can be attributed to the incomplete desorption of H_2S from the pore of the **COP-4** materials. Figure 4.5 c represents the single cycle response and recovery characteristics of the **COP-4** based sensor to 200 ppm of H_2S.
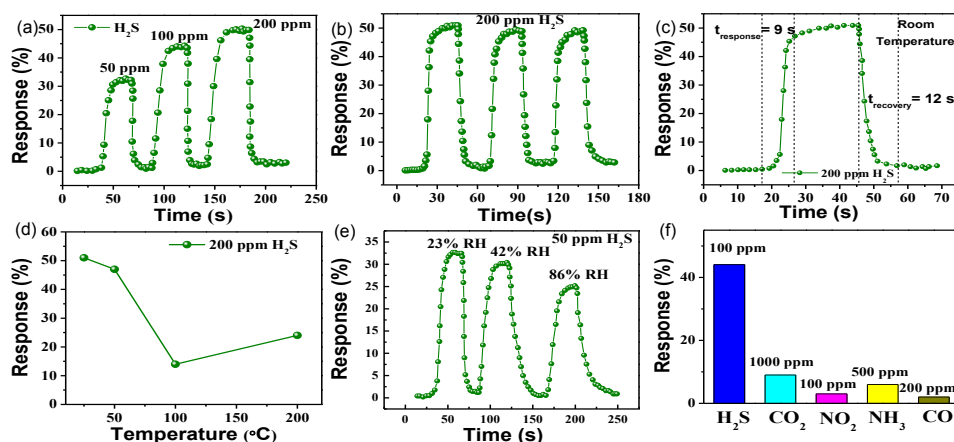
Figure 4.5 (a) Real-time dynamic response and recovery characteristics for the **COP-4** based sensor. (b) Repeatability of **COP-4** based sensor at 25 °C. (c) Single transient response and resistance of **COP-4** fabricated sensor. (d) Gas response of the **COP-4** based sensor vs operating temperature to 200 ppm H_2S. (e) Effect of humidity on the H_2S sensing properties of the **COP-4** fabricated sensor device. (f) Selectivity of the **COP-4** based sensor towards H_2S over other gases such as CO_2, NO_2, NH_3 and CO.

The **COP-4** fabricated sensor device shows a very short response and recovery time, about 9 s and 12 s, respectively. The operating temperature dependent gas sensitivity is a well-known phenomenon in a chemiresistive sensor device. To check the operating temperature dependent H_2S response in the **COP-4** based sensor, a sensing experiment was performed at different temperatures (25 to 200 $^\circ$ C). An interesting sensing response was observed for the **COP-4** based sensor at different temperatures. The **COP-4** based sensor shows the highest response at room temperature (25 $^\circ$ C). The response decreases gradually with the increase in temperature and reaches the lowest value at 100 $^\circ$ C (Figure 4.5 d). Humidity is

an important parameter to consider when the sensing measurement is done at 25 º C. The response of the **COP-4** based sensor was measured under different humid conditions of 42 and 83% relative humidity (RH). Under 42% RH conditions, the sensor response decreases by 9%, whereas under 83% RH, the sensor response decreases by 21% with respect to 23% RH conditions (Figure 4.5 e). The **COP-4** fabricated device also shows significant selectivity towards H_2S compared to CO_2, CO, NH_3 and NO_2 gases (Figure 4.5 f). The base resistance of the **COP-4** remains almost constant up to 200 º C (Figure 4.6).
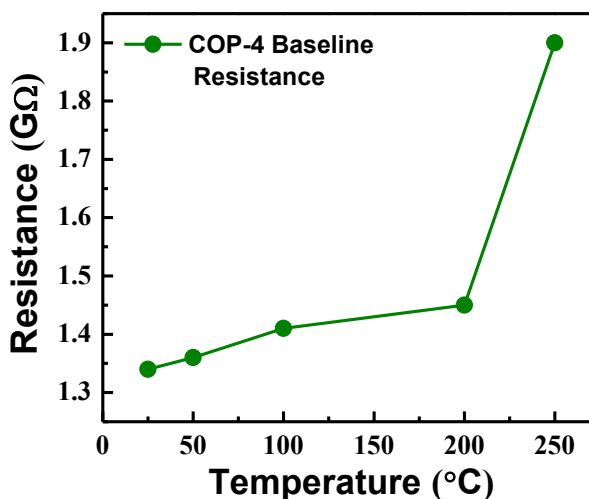
Figure 4.6 Resistance of the **COP-4** based sensor vs operating temperature.

In general, the conductivity of amine based organic polymers is generated due to a proton conduction process through -NH bonds.[30-32] Organic polymers containing primary, secondary or tertiary amine groups are somewhat sensitive to acidic gases.[30] Here, the **COP-4** contains several numbers of basic hydrazide amine (-CONH-N-) groups. On the other hand, H_2S is a weak acid in nature. The increase in the electrical resistance or decrease in the electrical conductance of the **COP-4** is attributed to the reduction of the proton mobility on the **COP-4** surface. Hydrazide -NH protons in the polymer can help in the proton conduction process through the enol form of hydrazide groups (Figure 4.7). In the presence of H_2S gas, the -CONH- groups of the **COP-4** interact with H_2S [$-CONH\cdots SH_2$], which restricts the formation of the enol form of hydrazide groups (Fihure 4.7). Consequently, the proton conduction process in the polymer is collapsed. As a result, the resistance of the **COP-4** increases. The H_2S sensing performance of the **COP-4** decreases with the increase in temperature.

The interaction of H_2S is hindered at a higher temperature due to an increase of molecular vibration of the **COP-4**. Consequently, the sensing response becomes lower with the increase in temperature. At higher humidity, the presence of water molecules facilitates an alternating pathway for proton conduction. So, proton conduction can take place through the water molecules adhered to the backbone of the **COP-4**.[33] Thus the conductivity of **COP-4** is increased at higher

humidity. Consequently, the response of **COP-4** to H_2S gas is decreased. An insignificant change in the base resistance of the precursors is observed and shows almost 0% response upon exposure to H_2S gas. Mostly metal oxide and inorganic-organic based hybrid materials have been used in the fabrication of chemi-resistive gas sensors.[34-41] Previously, researchers have reported a few **COP-4** based nanomaterials for chemi-resistive gas sensors. A two dimensional organic polymer based chemiresistive sensor has been developed for selective NO_2 sensing at 25 º C.[42] A tetraphenylethene-based covalent organic polymer has been prepared for sensing gaseous HCl.[22] Swager *et al*. developed a polythiophene based chemiresistive chemical sensor.[43] Here, we have used a **COP-4** as a H_2S sensing material. H_2S gas ensing using the **COP-4** fabricated sensor device was carried out through a proton conduction process.
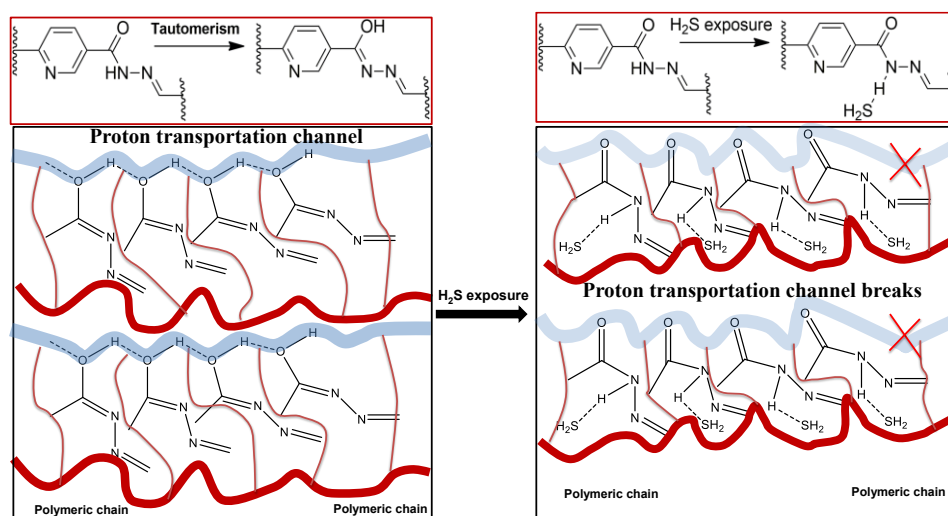
Figure 4.7 Proposed H_2S sensing mechanism of **COP-4** through proton conduction phenomenon.

Here, we proposed chemiresistive gas sensing mechanism. The **COP-4** creates a proton transportation channel inside the polymeric chain due to proton transfer of the enol form of hydrazide groups (-C(-OH)N-N=).[44-47] After H_2S exposure, the proton transportation channel gradually collapses due to $H_2S\cdots H$-N-(C=O) interaction.[48] Obviously, in H_2S environment the stability or percentage of enol form becomes lower due to $H_2S\cdots H$-N-(C=O) interaction. As a result, the electrical resistance of **COP-4** increases in presence of H_2S and we get very fast response. We observed that the response time becomes less at higher ppm of H_2S and very fast increment of electrical resistance of the system.

Here, the gas sensing mechanism does not occur only through the acid base interaction, however it also depends on the surface area of adsorbant, pore size and rate of adsorption-desorption of the analytes (here gases).

However, we tried to establish this through the theoretical insight. Density functional theory (DFT) calculations have been performed using Gaussian 09

software. First, the geometry of the truncated **COP-4 (**Named COPT**)** with C(=O)NH-N=) functionality has been optimized as -C(=O)NH-N=) groups which mainly involves the sensing mechanism. Then the calculation is performed with a truncated version of **COP-4**, one molecule of H_2S and CO_2. The energy of COPT before the interaction with H_2S and CO_2 is -737.293 Hartree. Now the total energy of the H_2S-COPT system is lowered (became more negative) value of -1134.694 Hartree than CO_2-COPT with energy of -924.809 Hartree. From the energy calculation study, we conclude that H_2S-COPT system is more energetically stable and favourable system than CO_2-COPT system. So H_2S should have more tendency to interact with **COP-4** than CO_2.
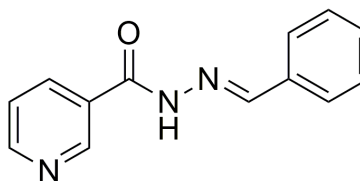
COPT

We have gone through several literatures to find out the pKa value of the material and tried to establish the sensing mechanism with the acid-base interactions. Here, we have calculated the pK_a value of **COPT** (AH) using DFT calculation.[49] The pK_a value of **COPT** is calculated as high as 51.072. Now **COPT** behaves almost like a aliphatic hydrocarbons compound due to very high pK_a value. So acid-base type of interactions with external analytes (acidic gases) are quite absurd here or insignificant.

Calculation of pK$_a$ value:
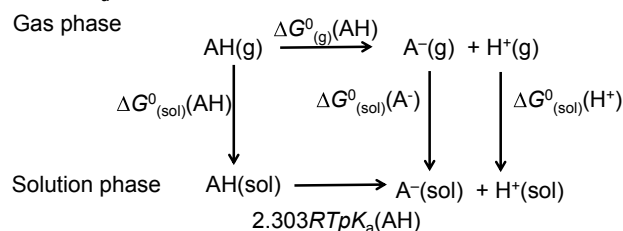
Thermodynamic cycled used for the calculation of pK$_a$ values.

$$\Delta G^0_{(g)}(AH) = \Delta G^0_{(sol)}(A^-) + \Delta G^0_{(sol)}(H^+) - \Delta G^0_{(sol)}(AH)$$

$$\Delta G^0_{(g)}(AH) = 2.303\ RTpK_a(AH)$$
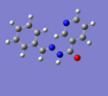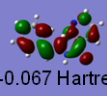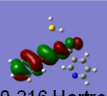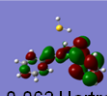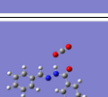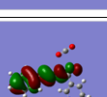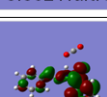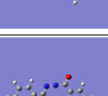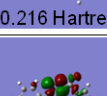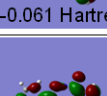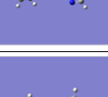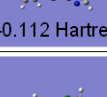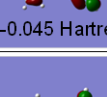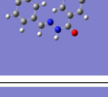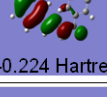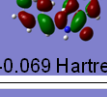
$$\text{Direct p}K_a(AH) = \frac{\Delta G^0_{(g)}(AH)}{2.303\ RT}$$

Linear correction pK_a = (Direct pK_a+ 7.281)/1.194

Now, if we include the effect of moisture, H_2S (week acid) generates HS^- and S^{2-} after reaction with moisture whereas CO_2 forms H_2CO_3 (week acid) upon reaction with moisture.

$$H_2S + H_2O = HS^- + H_3O^+$$
$$HS^- + H_2O = S^{2-} + H_3O^+$$
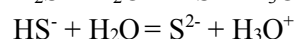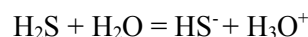
Now HS$^-$ will more prone to interact with –HN-C(=O) rather than H_2CO_3. After exposure with H_2S, the proton transportation channel gradually collapses due to $H_2S\cdots H$-N-(C=O) interaction. In H_2S environment, the stability or percentage of enol form becomes lower due to $H_2S\cdots H$-N-(C=O) interaction. As a result, the electrical resistance of **COP-4** increases or suddenly changes in presence of H_2S and very fast response was observed for H_2S.

System	Molecular structure	HOMO	LUMO
COPT (gas phase)		-0.223 Hartree	-0.067 Hartree
H_2S-COPT (gas phase)		-0.216 Hartree	-0.062 Hartree
CO_2-COPT (gas phase)		-0.216 Hartree	-0.061 Hartree
Deprotonated COPT (solution phase)		-0.112 Hartree	-0.045 Hartree
COPT (solution phase)		-0.224 Hartree	-0.069 Hartree
Deprotonated COPT (gas phase)		-0.021 Hartree	-0.074 Hartree

Summary of all DFT calculations (Basis set =3-21G, Basis function= B3LYP, Solvation= The conductor-like polarizable continuum model CPCM/water)).

Furthermore, the reddish brown colour of the **COP-4** changed to faint brown colour upon exposure to H_2S gas with a response time of less than 2 seconds (Figure 4.8), which is quite fast. Interestingly, the **COP-4** regains its original brown colour after exposure to air. This is the main advantage of the faster colour change under day light. Considering the response efficiency, response time, recovery, temperature and other parameters mentioned in Table 4.2, the COP-based sensor can be used as a promising device for H_2S sensing.

Reddish brown   **Faint brown**
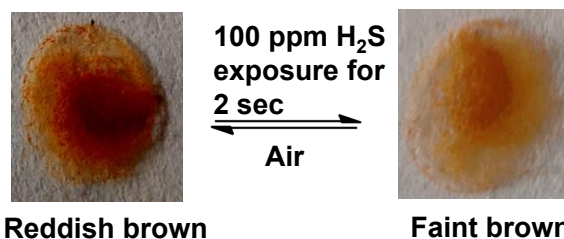
Figure 4.8 The reddish brown coloured **COP-4** transformed into faint brown colour after exposure of 100 ppm H_2S gas for 2s, which further transformed into reddish brown colour after exposure under air.

Table 4.2 Comparison table of H_2S sensing of **COP-4** with other reported nanomaterials.

S. No	Material	Sensor device	Maximum response%	Temp. (^{o} C)	Ref.
1	Zn-doped-Fe_2O_3	Chemiresitive	23.5 (5 ppm H_2S)	175	37
2	Fe_2O_3@CNT-3.0	Chemiresitive	$\approx$ 9 (100 ppm H_2S)	25	38
3	$MoSe_2$	Chemiresitive	19-20 (5.45 ppm)	200	39
4	Au-nanowire	Chemiresitive	30-40 (0.5 ppm)	25	40
5	SnO_2/rGO	Chemiresitive	60-70 (100 ppm)	22	41
6	**COP-4**	Chemiresitive	>50 (200 ppm), >30 (50 ppm)	25	This work

4.4. Conclusion.

In summary, we synthesized a hydrazide-based **COP-4**. The **COP-4** was used as an efficient chemiresistive gas sensing material for H_2S at 25 ^{o} C. Gas sensing measurement of the **COP-4** fabricated device was carried out in a dynamic flow-through resistance measurement system. The sensing effect was fully reversible and operated at a low temperature. The maximum response to 200 ppm of H_2S was found to be 450% at 25 ^{o} C. The **COP-4** fabricated chemiresistive device showed a very fast response time of 9 s with a recovery time of 12 s, respectively, with 200 ppm of H_2S at 25 ^{o} C. The **COP-4** fabricated device showed high selectivity to H_2S compared to CO_2, CO, NH_3 and NO_2. Here, the gas sensing of H_2S using the **COP-4** fabricated sensing device occurred through a proton conduction process. The proton transportation process inside the **COP-4** backbone was restricted after adsorption of H_2S that enhanced the resistance of the **COP-4** fabricated device.

4.5 References

1. D. K. Aswal and S. K. Gupta, Science and Technology of Chemiresistor Gas Sensors, Nova Science Publishers: New York, 2007;. (ISBN: 9781600215148 1600215149)

2. Mortezaali, A.; Moradi, R. The correlation between the substrate temperature and morphological ZnO nanostructures for H_2S gas sensors. *Sens. Actuators A* **2014**, *206*, 30. (DOI: 10.1016/j.sna.2013.11.027)

3 Song, Z.; Wei, Z.; Wang, B.; Luo, Z.; Xu, S.; Zhang, W.; Yu, H.; Li, M.; Huang, Z.; Zang, J.; Yi, F.; Liu, H. Sensitive Room-Temperature H_2S Gas Sensors Employing SnO_2 Quantum Wire/Reduced Graphene Oxide Nanocomposites. *Chem. Mater.* **2016**, *28*, 1205-1212. (DOI: org/10.1021/acs.chemmater.5b04850)

4. Balasubramani, V.; Sureshkumar, S.; Rao, T. S.; Sridhar, T. M. Impedance Spectroscopy-Based Reduced Graphene OxideIncorporated ZnO Composite Sensor for H_2S Investigations. *ACS Omega* **2019**, *4*, 9976-9982. (DOI: org/10.1021/acsomega.9b00754)

5. Guo, Z.; Chen, G.; Zeng, G.; Li, Z.; Chen, A.; Wang, J.; Jiang, L. Fluorescence chemosensors for hydrogen sulfide detection in biological systems. *Analyst*, **2015**, *140*, 1772. (DOI: 10.1039/C4AN01909A)

6. Aaryashree, Mandal, B.; Bhardwaj, R.; Maiti, S.; Sharma, D. S.; Das, A. K.; Mukherjee, S. Functionalized oligo(p-phenylenevinylene) and ZnO based nanohybrid for selective ammonia sensing at room temperature. *IEEE Sens. J.*, **2019**, *19*, 2847-2854. (DOI: 10.1109/JSEN.2018.2890092)

7. Mandal, B.; Biswas, A.; Aaryashree, Sharma, D. S.; Bhardwaj, R.; Das, M.; Rahman, M. A.; Kuriakose, S.; Bhaskaran, M.; Sriram, S.; Htay, M. T.; Das, A. K. π-Conjugated Amine-ZnO Nanohybrids for the Selective Detection of CO_2 Gas at Room Temperature. *ACS Appl. Nano Mater*. **2018**, *1*, 12, 6912-6921. (DOI: org/10.1021/acsanm.8b01731)

8. Zhang, J.; Liu, X.; Neri, G.; Pinna, N. Nanostructured Materials for Room-Temperature Gas Sensors. *Adv. Mater*. **2016**, *28*, 795-831. (DOI: 10.1002/adma.201503825)

9. Deng, J. F.; Fu, Q. Y.; Luo, W.; Tong, X. H.; Xiong, J. H.; Hu, Y. X. Enhanced H_2S Gas Sensing Properties of Undoped ZnO Nanocrystalline Films from QDs by Low-Temperature Processing. *Sens. Actuators, B* **2016**, *224*, 153-158. (DOI: org/10.1016/j.snb.2015.10.022)

10. Wang, Y. Y.; Duan, G. T.; Zhu, Y. D.; Zhang, H. W.; Xu, Z. K.; Dai, Z. F. Room Temperature H_2S Gas Sensing Properties of In_2O_3 Micro/Nanostructured Porous Thin Film and Hydrolyzation-Induced Enhanced Sensing Mechanism *Sens. Actuators, B* **2016**, *228*, 74-84. (DOI: org/10.1016/j.snb.2016.01.002)

11. Yu, T. T.; Cheng, X. L.; Zhang, X. F.; Sui, L. L.; Xu, Y. M.; Gao, S.; Zhao, H.; Huo, L.; Highly sensitive H_2S detection sensors at low temperature based on hierarchically structured NiO porous nanowall arrays. *J. Mater. Chem. A* **2015**, *3*, 11991-11999. (DOI: 10.1039/c5ta00811e)

12. Kaur, M.; Jain, N.; Sharma, K.; Bhattacharya, S.; Roy, M.; Tyagi, A. K.; Gupta, S. K.; Yakhmi, J. V. Room-temperature H_2S gas sensing at ppb level by single crystal In_2O_3 whiskers. *Sensors and Actuators B* **2008**, *133*, 456-461. (DOI: org/10.1016/j.snb.2008.03.003)

13. Kim, J.; Kim, W.; Yong, K. CuO/ZnO Heterostructured Nanorods: Photochemical Synthesis and the Mechanism of H_2S Gas Sensing. *J. Phys. Chem. C* **2012**, *116*, 15682-15691. (DOI: org/10.1021/jp302129j)

14. Sun, Z.; Yuan, H.; Liu, Z.; Han, B.; Zhang, X. A Highly Efficient Chemical Sensor Material for H_2S: α- Fe_2O_3 Nanotubes Fabricated Using Carbon Nanotube Templates. *Adv. Mater*. **2005**, *17*, 2993-2997. (DOI: org/10.1002/adma.200501562)

15. Vander Wal, R. L.; Hunter, G. W.; Xu, J. C.; Kulis, M. J.; Berger, G. M.; Ticich, T. M. Metal-oxide nanostructure and gas-sensing performance. *Sens. Actuators, B* **2009**, *138*, 113. (DOI: org/10.1016/j.snb.2009.02.020)

16. Cadena, G. J.; Riu, J.; Rius, F. X. Gas sensors based on nanostructured materials. *Analyst*, **2007**, *132*, 1083-1099. (DOI: 10.1039/B704562J).

17. Huang, X.-J.; Choi, Y.-K. Chemical sensors based on nanostructured materials. *Sens. Actuators, B* **2007**, *122*, 659. (DOI:org/10.1016/j.snb.2006.06.022)

18. E. Comini. Metal oxide nano-crystals for gas sensing. *Anal. Chim. Acta*. **2006**, *568*, 28. (DOI: org/10.1016/j.aca.2005.10.069)

19. Sun, Y.-F.; Liu, S.-B.; Meng, F.-L.; Liu, J.-Y.; Jin, Z.; Kong, L.-T.; Liu, J.-H. Metal Oxide Nanostructures and Their Gas Sensing Properties: A Review. *Sensors* **2012**, *12*, 2610-2631. (DOI: org/10.3390/s120302610)

20. Li, Y.-X.; Guo, Z.; Su, O. Y.; Jin, X.-B.; Tang, X.-H.; Huang, J.-R.; Huang, X.-J.; Li, M.-Q.; Liu, J.-H. *ACS Sens*. **2017**, *2*, 102-110. (DOI: org/10.1021/acssensors.6b00597)

21. Byun, J.; Je, S.-H.; Patel, H. A.; Coskun, A.; Yavuz, C. T. Nanoporous covalent organic polymers incorporating Troger's base functionalities for enhanced CO_2 capture. *J. Mater. Chem. A* **2014**, *2*, 12507-12512. (DOI: 10.1039/C4TA00698D)

22. Cui, F.-Z.; Xie, J.-J.; Jiang, S.-Y.; Gan, S.-X.; Ma, D.-L.; Liang, R.-R.; Jiang, G.-F.; Zhao, X. A gaseous hydrogen chloride chemosensor based on a 2D covalent organic framework. *Chem. Commun*. **2019**, *55*, 4550-4553. (DOI: 10.1039/C9CC01548E)

23. Byun, Y.; Je, S. H.; Talapaneni, S. N.; Coskun, A. Advances in Porous Organic Polymers for Efficient Water Capture. *Chem.Eur.J.* **2019**, *25*, 10262-10283. (DOI: org/10.1002/chem.201900940)

24. Xiang, Z.; Mercado, R.; Huck, J. M.; Wang, H.; Guo, Z.; Wang, W.; Cao, D.; Haranczyk, M.; Smit, B. Systematic Tuning and Multifunctionalization of Covalent Organic Polymers for Enhanced Carbon Capture. *J. Am. Chem. Soc*. **2015**, *137*, 13301-13307. (DOI: org/10.1021/jacs.5b06266)

25. Guo, L.; Wang, M.; Zeng, X.; Cao, D. Mater. Luminescent porous organic polymer nanotubes for highly selective sensing of H_2S. *Chem. Front*. **2017**, *1*, 2643-2650. (DOI: 10.1039/C7QM00423K)

26. Meng, Z.; Stolz, R. M.; Mirica, K. A. Two-Dimensional Chemiresistive Covalent Organic Framework with High Intrinsic Conductivit. *J. Am. Chem. Soc*. **2019**, *141*, 11929-11937. (DOI: org/10.1021/jacs.9b03441).

27. U.-Romo, F. J.; Doonan, C. J.; Furukawa, H.; Oisaki, K.; Yaghi, O. M. Crystalline Covalent Organic Frameworks with Hydrazone Linkages. *J. Am. Chem. Soc.* **2011**, *133*, 11478-11481. (DOI: org/10.1021/ja204728y).

28. Maiti, S.; Chowdhury, A. R.; Das, A. K. Electrochemically Facile Hydrogen Evolution Using Ruthenium Encapsulated Two Dimensional Covalent Organic Framework (2D COF). *ChemNanoMat.* (DOI: https://doi.org/10.1002/cnma.201900499).

29. Dey, D.; Banerjee, P. Toxic organic solvent adsorption by a hydrophobic covalent polymer. *New J. Chem.* **2019**, *43*, 3769-3777. (DOI: 10.1039/C8NJ06249H).

30. Tanaka, R.; Yamamoto, H.; Shono, A.; Kubo, K.; Sakurai, M. Proton conducting behavior in non-crosslinked and crosslinked polyethylenimine with excess phosphoric acid. *Electrochim. Acta.* **2000**, *45*, 1385-1389. (DOI: org/10.1016/S0013-4686(99)00347-3).

31. Yardeni, J. L.; Amit, M.; Ashkenasy, G.; Ashkenasy, N. Sequence dependent proton conduction in self-assembled peptide nanostructures. *Nanoscale* **2016**, *8*, 2358-2366. (DOI: 10.1039/C5NR06750B).

32. Scheiner, S.; Wang, L. Hydrogen bonding and proton transfers of the amide group. *J. Am. Chem. Soc.* **1993**, *115*, 1958-1963. (DOI: org/10.1021/ja00058a049).

33. Doan, T. C. D.; Baggerman, J.; Ramaneti, R.; Tong, H. D.; Marcelis, A. T. M.; Rijn, C. J. M. V. Carbon dioxide detection with polyethylenimine blended with polyelectrolytes. *Sensors and Actuators B* **2014**, *201*, 452-459. (DOI: org/10.1016/j.snb.2014.05.023).

34. Xue, D.; Zhou, R.; Lin, X.; Duan, X.; Li, Q.; Wang, T. A highly selective and sensitive H_2S sensor at low temperatures based on Cr-doped α-Fe_2O_3 nanoparticles. *RSC Adv.* **2019**, *9*, 4150-4156. (DOI: 10.1039/c8ra07365a).

35. Wagh, M. S.; Patil, L. A.; Seth, T.; Amalnerkar, D. P. Surface cupricated SnO_2-ZnO thick films as a H_2S gas sensor. *Materials Chemistry and Physics* **2004**, *84*, 228-233. (DOI: org/10.1016/S0254-0584(03)00232-3).

36. Shirsat, M. D.; Bangar, M. A.; Deshusses, M. A.; Myung, N. V.; Mulchandani, A. Surface cupricated SnO_2-ZnO thick films as a H_2S gas sensor *Appl. Phys. Lett.* **2009**, *94*, 083502. (DOI: org/10.1063/1.3070237).

37. Wei, K.; Zhao, S.; Zhang, W.; Zhong, X.; Li, T.; Cui, B.; Gao, S.; Wei, D.; Shen, Y. Controllable Synthesis of Zn-Doped α-Fe_2O_3 Nanowires for H_2S Sensing. *Nanomaterials* **2019**, *9*, 994. (DOI: org/10.3390/nano9070994).

38. Kim, W.; Lee, J. S.; Jang, J. Facile synthesis of size-controlled Fe_2O_3 nanoparticle-decorated carbon nanotubes for highly sensitive H_2S detection. *RSC Adv.* **2018**, *8*, 31874-31880. (DOI: 10.1039/C8RA06464D).

39. Jha, R. K.; Costa, J. V. D.; Sakhuja, N.; Bhat, N. $MoSe_2$ nanoflakes based chemiresistive sensors for ppb-level hydrogen sulfide gas detection. *Sensors & Actuators: B. Chemical* **2019**, *297*, 126687. (DOI: org/10.1016/j.snb.2019.126687).

40. Moon, C. H.; Zhang, M.; Myung, N. V.; Haberer, E. D. Highly sensitive hydrogen sulfide (H$_2$S) gas sensors from viral-templated nanocrystalline gold nanowires. *Nanotechnology* **2014**, *25*, 135205. (DOI:10.1088/0957-4484/25/13/135205).

41. Song, Z.; Wei, Z.; Wang, B.; Luo, Z.; Xu, S.; Zhang, W.; Yu, H.; Li, M.; Huang, Z.; Zang, J.; Yi, F.; Liu, H Sensitive Room-Temperature H$_2$S Gas Sensors Employing SnO$_2$ Quantum Wire/Reduced Graphene Oxide Nanocomposites *Chem. Mater.* **2016**, *28*, 1205-1212. (DOI: org/10.1021/acs.chemmater.5b04850).

42. Yang, K.; Yuan, W.; Hua, Z.; Tang, Y.; Yin, F.; Xia, D. Triazine-Based Two-Dimensional Organic Polymer for Selective NO$_2$ Sensing with Excellent Performance. ACS *Appl. Mater. Inter.*, **2020**, *12*, 3919-3927. (DOI: doi.org/10.1021/acsami.9b17450)

43. Wang, F.; Gu, H.; Swager, T. M. Carbon Nanotube/Polythiophene Chemiresistive Sensors for Chemical Warfare Agents. . *J. Am. Chem. Soc.*, **2008**, *130*, 5392-5393. (DOI: 10.1021/ja710795k)

44. Oklejas, V.; Uibel, R. H.; Horton, R.; Harris, J. M. Electric-Field Control of the Tautomerization and Metal Ion Binding Reactivity of 8-Hydroxyquinoline Immobilized to an Electrode Surface. *Anal. Chem.* **2008**, *80*, 1891-1901. (DOI: org/10.1021/ac701808z)

45. Mohan, M.; Satyanarayan, M. N.; Trivedi, D. R. Photophysics of proton transfer in hydrazides: a combined theoretical and experimental analysis towards OLED device application. *New J. Chem.* **2019**, *43*, 10413- 10428. (DOI: 10.1039/c9nj01503e)

46. Mondal, S.; Agam, S. Y.; Nandi, R.; Amdursky, N. Exploring long-range proton conduction, the conduction mechanism and inner hydration state of protein biopolymers. *Chem. Sci.* **2020**, *11*, 3547-3556. (DOI: 10.1039/c9sc04392f)

47. Rani, S.; Kumar, M.; Garg, R.; Sharma, S.; Kumar, D. Amide Functionalized Graphene Oxide Thin Films for Hydrogen Sulfide Gas Sensing Applications. *IEEE Sens. J*, **2016**, *16* , 2929 - 2934. (DOI: 10.1109/JSEN.2016.2524204)

48. Krepps, M. K.; Parkin, S.; Atwood, D. A. Hydrogen Bonding with Sulfur. *Crystal Growth & Design* **2001**, *1*, 291-297. (DOI: 10.1021/cg015505v)

49. Kelly, C. P.; Cramer, C. J.; Truhla, D. G. Single-ion solvation free energies and the normal hydrogen electrode potential in methanol, acetonitrile, and dimethyl sulfoxide. *J. Phys. Chem. B* **2007**, *111*, 408-422. (DOI: 10.1021/jp065403l).

Chapter 5
Electrochemically Facile Hydrogen Evolution Using Ruthenium Encapsulated Two Dimensional Covalent Organic Framework (2D COF)

5.1 Introduction.

Covalent organic frameworks (COFs) are an unique class of porous crystalline two or three dimensional material with structural periodicity and uniform porosity.[1–6] COFs often show potential applications in optoelectronic,[7] gas adsorption,[8–9] gas separation,[10–11] energy storage,[12–13] molecular catalysis,[14–15] electrocatalysis[16–19] and drug delivery[20] due to their uniform porosity resulting from strong covalent bond formation between the light atoms (H, B, C, N, and O). The synthesis of 2D COFs has become important in recent times. The 2D COFs could be tuned structurally.[21–23] The importance of these COFs lies in the fact that they show good stability and enhanced hydrogen evolution. The ordered structures in 2D COFs with organized π electron systems exhibit several potential applications.[24] Presently, the focus is on the development of different metal integrated COFs[25–27] to increase the efficiency in various applications. Recently, the assembly of porous materials and metal ions has been assigned an interdisciplinary research field for the design of new materials as efficient heterogeneous catalysts.[28] Porous materials which can encapsulate metal ions or metal nanoparticles inside its cavity, function as heterogeneous catalysts for various kinds of organic reactions.[29–31] COFs are considered as efficient and better templates for the encapsulation of metal ions because they possess relatively more stable interactions and hydrophobic environment to increase their heterogeneity. In recent time, entire world suffers in energy crisis and continuously researchers are finding new alternative and renewable sources of energy. Molecular hydrogen is considered as an alternative source of energy. Several methods are adopted to generate molecular hydrogen using chemical,[32–33] electrochemical[34–39] and photoelectrochemical[40–43] reactions. Electrochemical hydrogen evolution reaction (HER) is one of the promising methods, which involves several steps of electrochemical processes to generate molecular hydrogen. In the last decade, a few transition metal-based alloys (Ru, Co, Ni, Mo, Pd and Rh)[44–47] have been used for the HER catalyst. In addition to metals, metal oxides could be an efficient material for electrochemical HER. Oxides of iridium (IrO_2) and ruthenium (RuO_2) have been explored to have great abilities for HERs.[48–51] Although several obstacles including corrosion of metal, lower conductivity, poor stability and catalytic activity have been observed with these transition metal catalyts in HER. Researchers are engaged to design and modify several HER catalysts and systems to improve their activity and stability. Feng *et al.* developed a highly efficient HER catalyst by the construction of Ru nanoparticles over the Te nanorod.[52] Chen *et al.* synthesized N-dopped carbon coated nanorod on a Ti mesh as HER electrocatalyst.[53] Rao *et al.* also developed an efficient HER catalyst from the nanocomposite of MoS_2 and boron nitride.[54] On the other hand, several metal free catalyst for HER have also been reported. N-doped hexagonal carbon,[55] porous g-C_4N_4,[56] N,S-doped carbon[57] and PCN@graphene[58] have been reported as metal free efficient HER catalyst. Recently, Kitagawa *et al.* developed few porous coordinating polymers (PCPs),

which provided dynamic narrow pore channel for the efficient gas storage and separation.

In the present work, our objective is to design and synthesize metal encapsulated 2D COFs where porous framework of 2D COFs will act as a good template in heterogeneous catalysis with increased catalytic activity and stability in electrochemical hydrogen evolution reaction (HER). Here we have synthesized an imine linked crystalline 2D **COF** by the condensation of benzene-1,3,5-tricarboxaldehyde and 3,4-diaminobenzohydrazide. This **COF** is an ideal support to load Ru to generate **Ru@COF**. **Ru@COF** acts as an electrocatalyst for the electrochemical H_2 evolution reaction in 1.5 M H_2SO_4. Interestingly, **Ru@COF** acts as an exemplary electrocatalyst material that could form solid binder-free cathodic electrode on glassy carbon electrode surface.

5.2 Experimental Section.

5.2.1 Materials and Methods. 3,4-Diaminobenzohydrazide, benzene- 1,3,5 tricarboxaldehyde, dimethyl sulfoxide (DMSO), ruthenium trichloride and all solvents were purchased from Sigma Aldrich and Merck. Chemical shifts (δ) in ppm relative to the residual solvent signal were reported. Solid state ^{13}C NMR spectra was recorded on 400 MHz solid state NMR spectrometer (Instrument make: JEOL, model: ECX400; proton frequency: 400 MHz).

5.2.2 Synthesis of the COF. 3,4-Diaminobenzohydrazide and benzene- 1,3,5 tricarboxaldehyde in DMSO were refluxed in 100 mL round bottom flask for 72 h at 110°C. After that the reaction mixture was filtered and washed with methanol, dichloromethane and DMSO. The brown solid residue was dried over 90 °C for 1 day. This brown solid was characterized by the ^{13}C solid state NMR and FT-IR spectroscopy.

5.2.3 Preparation of Ru@COF. Ruthenium trichloride (30 mg) and COF (100 mg) in dichloromethane (10 mL) were stirred at 0 °C for 72 h. After that the whole mixture was centrifuged and washed with water and methanol. Resultant black residue was dried at 60 °C for 1 day. Then it was used for experimentation. This black residue was characterized by XPS and FT-IR.

5.2.4 Characterization Techniques. Powder XRD was performed using Rigaku SmartLab, Automated Multipurpose X-ray Diffractometer. Thermogravimetric analysis (TGA) was performed using by Mettler Toledo Thermal Analyzer with heating rate of 10 °C/min and heated from 25°C to 800 °C in N_2 environment. BET surface area analysis was performed using quantachrome, Autosorb iQ2. Differential Scanning Calorimeter was carried out in DSC 214 SET MFC LN2 with heating rate of 10 °C min^{-1}. XPS (X-ray photoelectronic spectroscopy) was done using AXIS Supra instrument (Kratos Analytical, UK, SHIMADZU group). FT-IR spectra of all materials were recorded in a Bruker (Tensor-27) FT-IR spectrophotometer. (HRTEM) High resolution transmission electron microscopy

analysis was carried out using Field Emission Gun-Transmission Electron Microscope 300 kV (model no Tecnai G2, F30). Electrochemical experiments were performed on a Metrohm autolab potentiostat (PGSTAT302N) instruments with the three electrodes system at room temperature. Three electrode system consist of an Ag/AgCl/KCl (3.0 M) as reference electrode, glassy carbon (GC) as working electrode and platinum wire as counter electrode. The potential measured values were corrected to the reversible hydrogen electrode (RHE).

5.2.5 Electrochemical measurements. The HER catalyst (5 mg, **Ru@COF**) was dispersed in ethanol and sonicated for 2 h to yield a dispersed solution. The dispersed solution (10 μL) was drop casted onto a glassy carbon electrode surface (d=5.00 mm). It was then dried with slow evaporation inside the incubator and performed the electrochemical experiment with a loading of 0.6 mg **Ru@COF** catalyst. 1.5 M H_2SO_4 solution was used as electrolyte. The electrolyte solution was purged with nitrogen gas at least 1 h before the experiments. 0.6 mg of each material was deposited on the glassy carbon electrode surface. All linear sweep voltammetry measurements were carried out with the scan rate of 10 mV s^{-1}. CV (Cyclic voltammetry) study with the potential window of 0.4 V to 0.8 V was taken to check the stability of the material at a scan rate of 10 mV s^{-1}. Impedence measurements were carried out with the range of 100 kHz to 10 mHz. The observed working electrode potential (E_{obs}) was converted to the potential versus RHE (E) using equation.

The observed working electrode potential (E_{obs}) was converted to the potential versus RHE (E) using equation

$$E = E_{obs} + 0.213 + 0.059 \text{ pH} \qquad \text{Eq. 5.1}$$

5.2.6 Electrochemical reaction steps.

Volmer reaction

$$H^+ + e^- = H_{ads} \qquad \text{Eq. 5.2}$$

Heyrovsky reaction

$$H^+ + H_{ads} + e^- \rightarrow H_2 \qquad \text{Eq. 5.3}$$

Tafel reaction

$$2H_{ads} \rightarrow H_2 \qquad \text{Eq. 5.4}$$

The Tafel equation is presented as

$$\eta = a + b \log(i/i_0) \qquad \text{Eq. 5.5}$$

where, 'η' is the overpotential, 'i' is current density, 'i_0' is the exchange current density, 'b' is the Tafel slope and 'a' is the constant term.

5.2.7 Calculation of quantification of evolved H_2 from electrode.

Hydrogen moles = (Current in amperes × Time in seconds)/(2 × Faraday)

Hydrogen moles = ($i \times t$)/(2 × Faraday)

Hydrogen moles = (Q)/(2 × 96500)

$Q = (i \times t)$

where Q is the charge carried by the working electrode, F is Faraday constant (96485.3 C/mol), the number 2 means 2 mole electrons per mole H_2, the number 1 means 1 mole H_2.

5.3 Results and Discussion.

A two dimensional covalent organic framework (2D COF) has been synthesized from the reaction between the 3,4-diaminobenzohydrazide and benzene-1,3,5-tricarboxaldehyde. **Ru@COF** has been prepared using $RuCl_3$ and 2D COF. Synthetic route for the preparation of COF and **Ru@COF** is shown in **Scheme 5.1**.
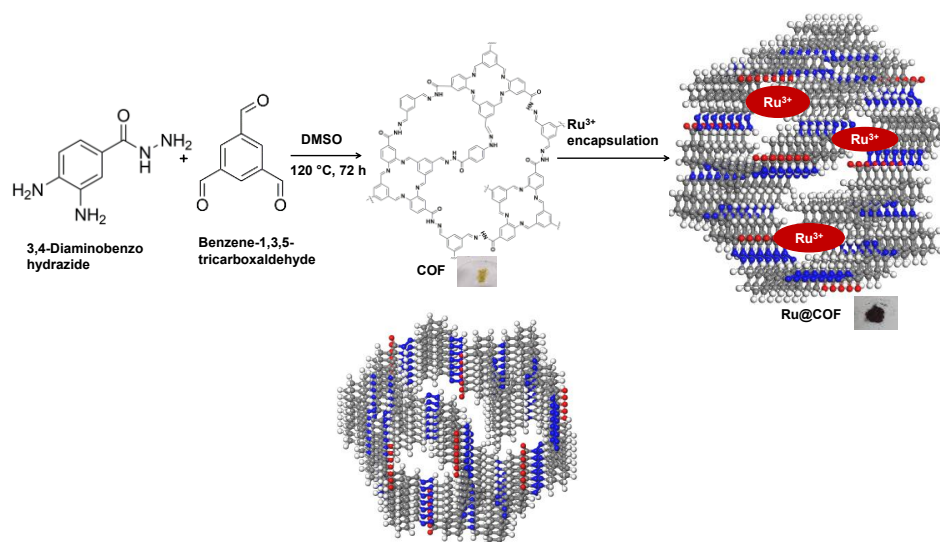
Scheme 5.1. Schematic representation for the preparation of **COF** and **Ru@COF**.

The FT-IR spectrum of **COF** shows a peak at 1620 cm^{-1} for the presence of acyl hydrazone linkage which is formed from the condensation between benzene-1,3,5-tricarboxaldehyde and 3,4-diaminobenzohydrazide. Furthermore, the >C=O stretching band is observed at 1662 cm^{-1} for the presence of -C(O)NHNH- groups in **COF**.[60] The acyl hydrazone linkage and -C=O band are observed at 1626 and 1670 cm^{-1} in **Ru@COF**. Both the **COF** and **Ru@COF** show stretching band at 1557 cm^{-1} due to the presence of aromatic -C=C- bond. **Ru@COF** shows significant change in the stretching frequency other than **COF** (Figure 5.1 a and b). The FT-IR spectrum of **Ru@COF** indicates no sign of decomposition of **COF** which is perfectly same with the pure matrix. Solid-state ^{13}C CP-MAS NMR is also used to establish the connectivity of the **COF** species as shown in Figure 5.2 a. Peaks in the range of 130 ppm-140 ppm suggest the existence of the phenyl groups. Peaks in the range of 160-170 ppm suggest the formation of acylhydrazone groups in **COF**. Powder X-ray diffraction (PXRD) pattern of **COF** reveals a crystalline material. The sharp PXRD peaks support the formation of the highly crystalline organic framework.[61] Sharp peaks at 7.16°, 10.2°,

12.4°, 16.1°, 20.4°, 21.6°, 23.9°, 26.0°, 27.1°, 29.9°, 30.8°, 34.1° and 32.6° of **COF** suggest highly crystalline nature.
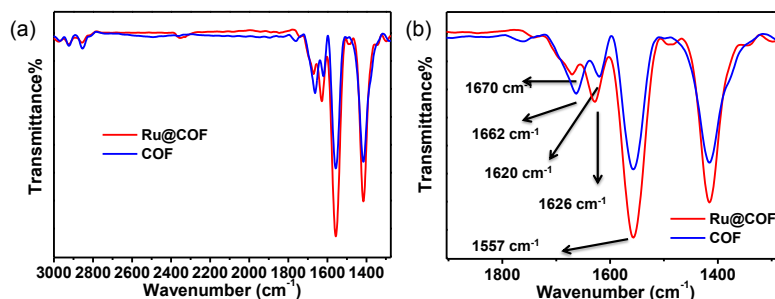
Figure 5.1. FT-IR spectra of **COF** and **Ru@COF** (a) within the range of 1000-4000 cm^{-1} and (b) within the range of 1500-1900 cm^{-1}.

PXRD pattern of **Ru@COF** reveals that no significant change in polymeric framework occurs after the incorporation of Ru ions inside the pore of **COF** (Figure 5.2 b). From powder XRD data, it is clear that **COF** gained much higher degree of crystallinity than their precursors (Figure 5.2 b). Powder XRD of **COF** clearly shows its district nature of polymeric architecture. Powder XRD pattern of **COF** implies that **COF** could not only from frameworks structure but also can form several types of cages types structures inside the frameworks due to presence of adjacent amine groups in 3,4-diaminobenzohydrazide.
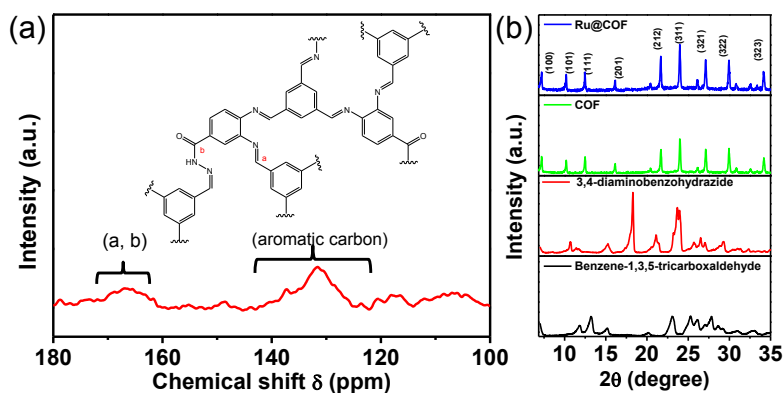
Figure 5.2 (a) Solid state ^{13}C NMR of **COF** (b) PXRD of 3,4-diaminobenzohydrazide, benzene-1,3,5-tricarboxaldehyde, **COF** and **Ru@COF**.

The robustness of the **COF** and **Ru@COF** is demonstrated by thermogravimetric analysis (TGA) (Figure 5.3 a). **COF** is stable up to 310°C. A weight loss of almost 100% is observed within the range of 310-400°C for **COF**. In case of **Ru@COF**, the polymer is stable up to 290 °C and almost 100% mass loss is observed within the range of 290 °C to 400°C. The Differential Scanning Calorimetry of both **COF** and **Ru@COF** have been performed (Figure 5.3 b and c). It is seen from the figures that an endothermic peak i.e. T_m (melting

temperature) for **COF** is found at 104 °C while for **Ru@COF** the T_m is found to be at 98 °C. It indicates the decrease in rigidity and the increase in flexibility after the incorporation of RuCl$_3$ inside the pores of the **COF**.
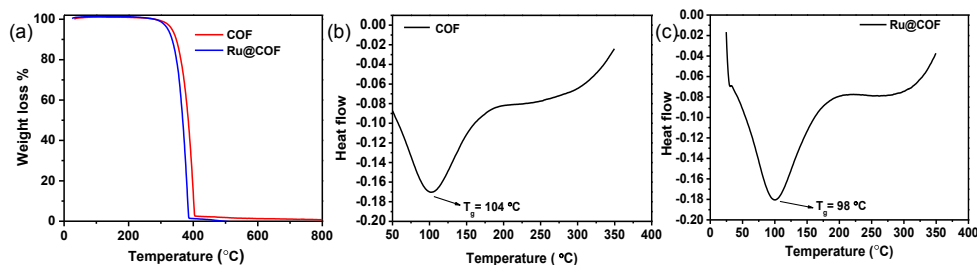
Figure 5.3 (a) Thermogravimetric analysis (TGA) of **COF** and Differential scanning calorimetry of (b) **COF** and (c) **Ru@COF**.

X-ray photoelectron spectroscopy (XPS)[62-67] was performed to provide more insight of Ru encapsulation inside the **COF** cavities (Figure 5.4 a). The deconvoluted C1s spectrum shows five peaks including C=CH-C at 284.7 eV, C-C=C at 285.5 eV, -C(=O)N at 286.1 eV, -C=O at 288.7 eV and -C=N 286.3 eV which is assigned for imine (Figure 5.4 b) groups. The deconvoluted Ru3d spectrum shows one peak at 282.4 eV that indicates Ru in +3 oxidation state (Figure 1d). Deconvoluted N1s spectrum shows three peaks including Schiff imine -C=N at 398.8 eV, -C(=O)N at 397.7 eV and -N-N- at 400 eV (Figure 5.4 c). The core level spectrum of O1s shows peak at 531.5 eV due to -C=O bond (Figure 5.4 d).
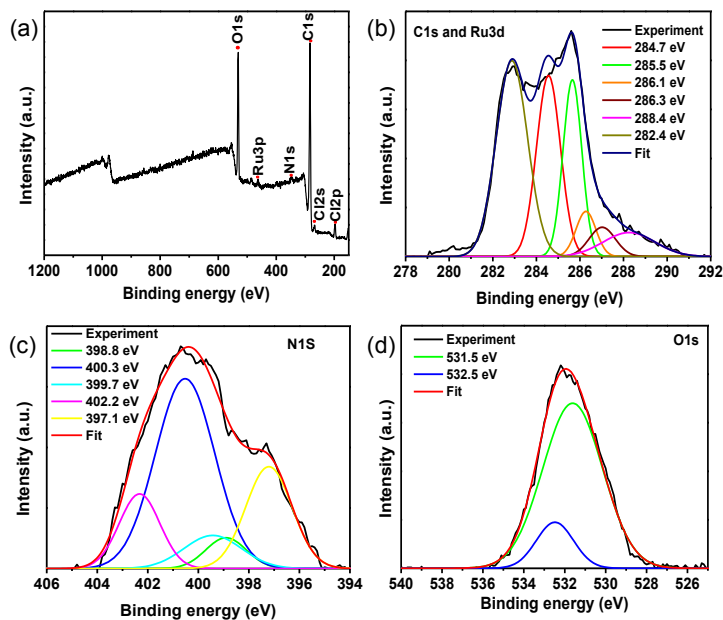
Figure 5.4 (a) XPS survey spectra of **Ru@COF** (b) XPS spectra for the deconvoluted peaks for the elements of C1s and Ru3d on **Ru@COF** surface,

XPS spectra for the deconvoluted peaks for the element of (c) nitrogen and (d) oxygen on **Ru@COF** surface.

XPS data also reveals that $RuCl_3$ does not form any complex with polymeric backbone. $RuCl_3$ only resides inside the pore of **COF**. Calculated atomic% of the relevant elements are given in Table 5.1

Table 5.1 Surface atomic concentration (atomic%) from XPS of **Ru@COF.**

Element	C1s	N1s	Cl2p	O1s	Ru3d
Atomic (%)	79.81	0.70	1.91	16.09	1.49

To determine the porosity and surface area of **COF** and **Ru@COF**, nitrogen sorption analysis was performed at 77K and 1 bar pressure (Figure 5.5 a and b). According to the IUPAC classification, both **COF** and **Ru@COF** show type IV isotherm. The calculated surface area of **COF** and **Ru@COF** is 425.48 and 248 $m^2 g^{-1}$ (Table 5.2).
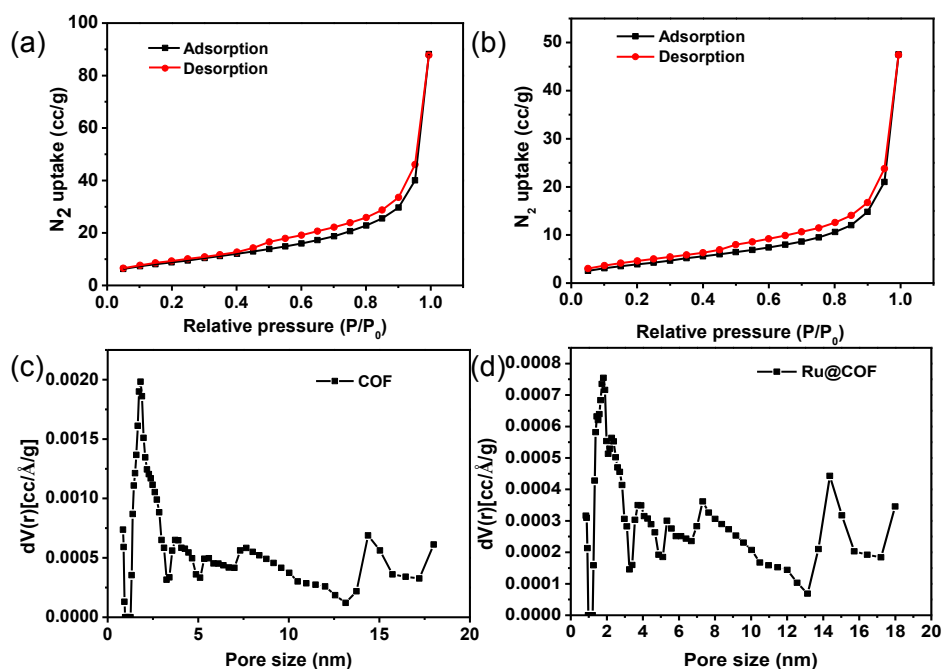
Figure 5.5 N_2 adsorption desorption isotherms of (a) **COF** and (b) **Ru@COF**, pore size distribution curve of (c) **COF** and (d) **Ru@COF**.

Average pore sizes of **COF** and **Ru@COF** are 11 nm and 0.9 nm respectively, which are calculated via BJH method (Figure 5.5 c and d). Total pore volume of **COF** and **Ru@COF** are 0.13 and 0.07 cc.g^{-1} respectively. It clearly depicts that the material has changed its porous nature from mesoporous to microporous after the incorporation of Ru atom. It also indicates the placement of Ru inside the pores.

Table 5.2 Summary of gas adsorption studies of **COF** and **Ru@COF.**

Material	N$_2$ uptake (cc.g^{-1})	Surface area (m^2.g^{-1})	Pore size (nm)	Pore volume (cc.g^{-1})
COF	88.19	425.48	11	0.13
Ru@COF	47.64	248	0.9	0.07

SEM images (Figure 5.6 a and b) of **COF** and **Ru@COF** show spherical morphology. The composition of **Ru@COF** is further confirmed by EDS (Figure 5.6 c -i) elemental mapping spectrum. The study shows that the weight percentage for the elements (Table 5.3).
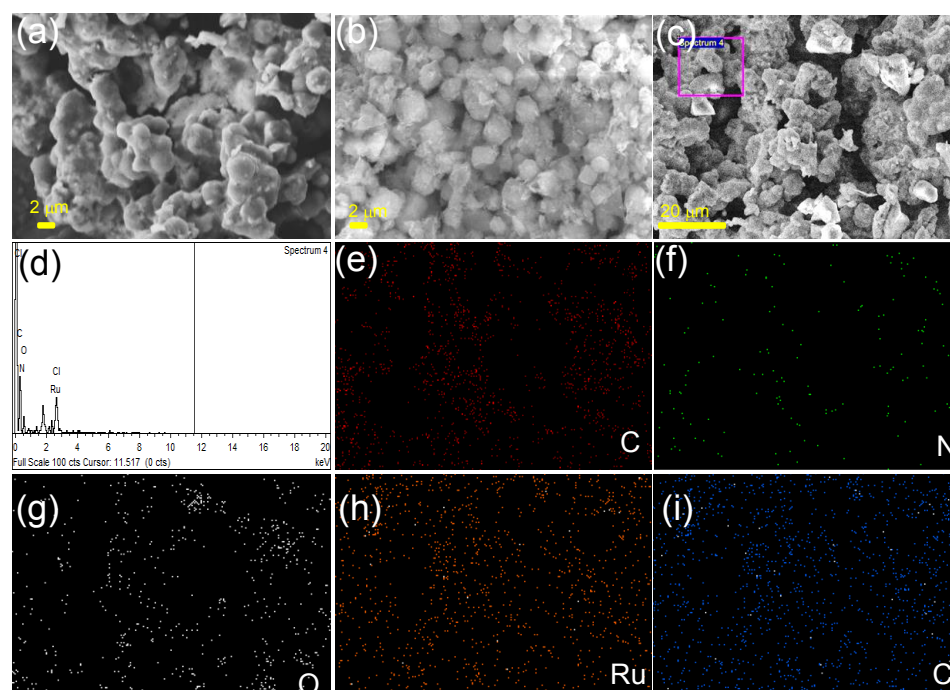
Figure 5.6 SEM images of (a) **COF** and (b) **Ru@COF**. (c) to (i) EDS mapping of **Ru@COF**.

Table 5.3 Atomic% from EDS of **Ru@COF.**

Element	C1s	N1s	Cl2p	O1s	Ru3d
Atomic (%)	53.73	6.13	9.63	14.65	15.88

High resolution transmission emission microscopy (HRTEM) analysis provides the evidence of 2D long range order and layer stacking structure of **COF** and **Ru@COF** (Figure 5.7). HRTEM images of **COF** show formation of nanosphere (Figure 5.7 a and b) with the average size of 6.34 nm. Fast Fourier Transform (FFT) studies of **COF** show higher crystalline nature. A cross view of **COF**

sample shows layer by layer stacking with the inter layer distance of 0.25 nm as shown in Figure 5.7 b.
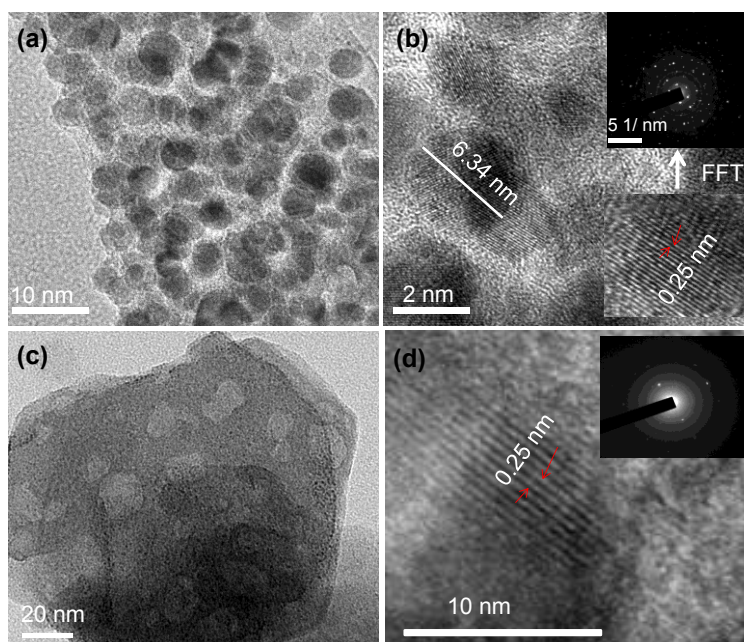
Figure 5.7 (a) HRTEM image of **COF**. (b) Lattice resolution HRTEM image of a **COF** particle with consistent lattice fringes extending across the entire particle. Inset: FFT of the image, cropped at the predominant fringe spacing (aligned parallel with the 0.25 nm fringes). (c) and (d) are the HRTEM images of ruthenium loaded **COF** (**Ru@COF**).

HRTEM image of **COF** shows clear lattice fringes with the d spacing of 0.25 nm that is close to interspacing of (323) plane. On the other hand several **Ru@COF** layers are agglomerated to construct bulk structure. HRTEM image of Ru loaded **COF** (**Ru@COF**) shows sheet-type crystalline porous nanostructure (Figure 5.7 c). FFT analysis of **Ru@COF** shows the d spacing of 0.25 nm between the inter layers (Figure 5.7 d). Figure 5.8 shows the presence of **COF** crystal orderly and dispersly loaded Ru metal salt.
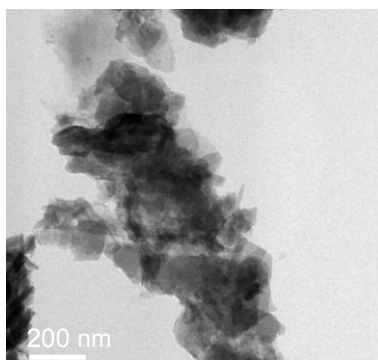
Figure 5.8. HRTEM image of **Ru@COF**.

5.3.1 Electrochemical HER catalytic activity of Ru@COF.

The HER activity of the **Ru@COF** was performed by linear sweep voltammetry (LSV) in 1.5 M H_2SO_4 solution (Figure 5.9 a). All the LSV plots show a rapid increment of the cathodic current upon a certain negative bias potential. Glassy carbon (GC) electrode was used to perform electrocatalytic activity. The sharp increments of the cathodic current occur due to the initiation of hydrogen evolution reaction on the **Ru@COF** coated GC electrode surface. Lower cathodic current response from the **COF** coated GC electrode and bare GC electrode shows their negligible HER activity. **Ru@COF** loaded GC (glassy carbon electrode) achieves high cathodic current which suggests significant HER catalytic activity. The efficiency of the HER depends on the value of overpotential (η). Lower value of η shows better catalytic activity for H_2 generation reaction upon a lower cathodic bias. **Ru@COF** shows onset overpotential value of 159 mV for HER. Catalytic activity of HER catalyst can be determined from the required onset overpotential values to gain current density of 10 mA cm^{-2}. In present work, the **Ru@COF** has achieved a current density of 10 mA cm^{-2} at an overpotential of 212 mV. Surprisingly very low overpotential (280 mV) is required to achieve 60 mA cm^{-2} exchange current density. This result confirms efficient HER activity for the **Ru@COF** electrocatalyst. The overpotential for HER with **Ru@COF** is comparable to other recently reported HER electrocatalysts (Table 5.4).[68-77]

Table 5.4 Comparison for the hydrogen evolution reaction materials with **Ru@COF.**

S. No	Material for HER	Overpotential (η) mV	Tafel slope (b) (mV dec^{-1})	Ref.
1	SB-PORPy **COF**	380 @ 5 mA.cm^{-2}	116	68
2	CoP nanosheets	100 @ 10 mA.cm^{-2}	76	69
3	MoC$_x$	142 @ 10 mA.cm^{-2}	53	70
4	Mo$_2$C@NPC	260 @ 10 mA.cm^{-2}	126.4	71
5	NU-1000_Ni-S	238 @ 10 mA.cm^{-2}	111	72
6	NENU-500	237 @ 10 mA.cm^{-2}	96	73
7	Co-(MOFs)	324 @ 10 mA.cm^{-2}	33	74
8	C-Fe, Co-**COF**	260 @ 10 mA.cm^{-2}	150	75
9	TpPAM	250 @ 10 mA.cm^{-2}	160	76
10	Cu-CMP850	350 @ 10 mA.cm^{-2}	135	77
11	**Ru@COF**	159 @ 1 mA.cm^{-2} and 212 @ 10 mA.cm^{-2}	79	This work

It is noteworthy to mention here that Sun *et al.*[75] developed a bimetallic **COF** which exhibited better catalytic performance towards electrochemical HER with overpotential value of 260 mV in acidic medium at a current density of 10 mA cm^{-2}.
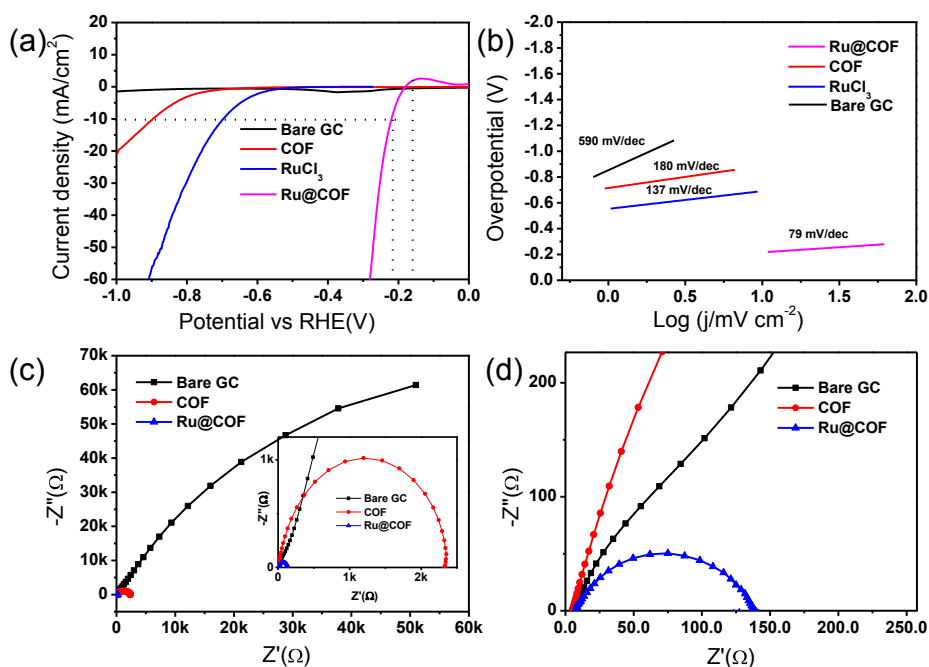
Figure 5.9 (a) LSV plot of **Ru@COF**, bare RuCl₃ and **COF**. (b) Tafel plot of **Ru@COF**, **COF**, RuCl₃ and bare GC. (c) Nyquist plot of impedance spectra of the bare GC, **COF** and **Ru@COF** at onset overpotential of 159 mV. Inset: impedance spectra in lower frequency range. (d) Impedance spectra of the **COF** and **Ru@COF** at lower frequency range to visualize the EIS plot of **COF** and **Ru@COF**.

HER mechanism and kinetics can be determined from the Tafel slope (Figure 5.9 b) value 'b'. A lower Tafel slope value suggests faster electrode reaction. The **Ru@COF** catalyst exhibits 'b' value of 79 mV dec^{-1}. Figures 5.9 c and d show the Nyquist plot of impedance spectra of **COF** and **Ru@COF**. The diameter of semicircle in the impedance spectra provides the charge transfer resistance (R$_{ct}$) values of the electrode-electrolyte interface. **COF** shows higher R$_{ct}$ value of 2330 Ω whereas the estimated R$_{ct}$ value is 138 Ω for **Ru@COF**.
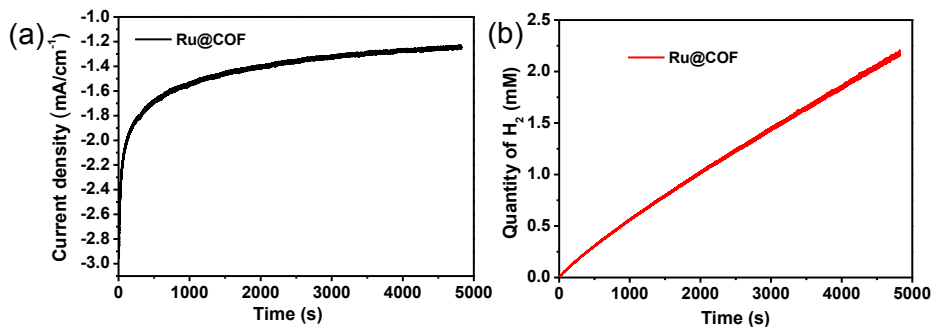

Figure 5.10 (a) Chronoamperometry (i-t) plot with **Ru@COF** at -0.2 V vs RHE (b) Quantity of H₂ evolution by **Ru@COF**.

131

Ru@COF gives excellent electrochemical hydrogen generation activity (Figure 5.10) with an onset overpotential of 200 mV. A chronoamperometry (CA) test of **Ru@COF** also shows good stability at -0.2 V vs RHE during a 5000 second electrolysis (Figure 5.10 a). Figure 5.10 b shows the amount of H_2 with the charge consumed by **Ru@COF**. The acidic solution (electrolyte) was purged with inert Ar gas before the measurement. LSV was conducted at a sweep rate of 10 mV s^{-1}.

5.3.2 Stability and efficiency of Ru@COF.

COFs are more robust in comparison to other porous polymers. **COF**s are also stable even in strong acid, basic and organic medium. As stated earlier, the reported **COF** acts as a template for Ru which increases the heterogeneity, stabililty and robustness of the whole composite. **Ru@COF** in 1.5 M H_2SO_4 medium shows better HER efficiency in comparison to $RuCl_3$ and **COF**. The working electrode (GC) was fabricated without any external binder and conducting materials. The electrocatalyst **Ru@COF** was reused upto 100 cycles. The HER activity of **Ru@COF** after 100 cycles was not changed in terms of exchange in current density and onset overpotential (Figure 5.11).
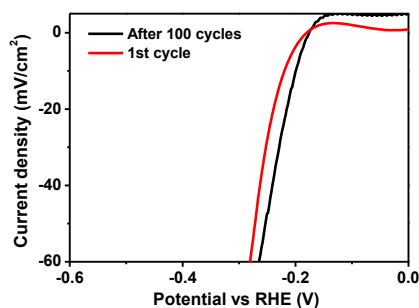
Figure 5.11 LSV plot of the recyclability of the hydrogen evolution reaction by **Ru@COF**.

Powder XRD of recycled **Ru@COF** shows negligible change in polymeric framework as compared to fresh **Ru@COF** (Figure 5.12 a). SEM image of the recycled **Ru@COF** catalyst is shown in Figure 5.12 b These results suggest good efficiency and stability of **Ru@COF** in acidic medium.
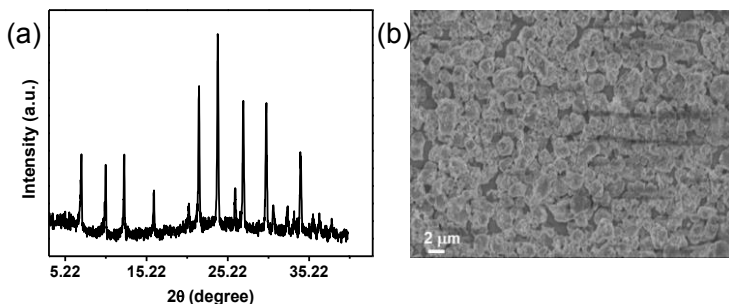
Figure 5.12 (a) Powder XRD of the recycled **Ru@COF** catalyst, (b) SEM image of the recycled **Ru@COF** catalyst.

5.4 Conclusion.

In summary, we have reported a porous 2D **COF** and Ru encapsulated **COF** (**Ru@COF**). These 2D **COF** and **Ru@COF** have been well characterized using solid state ^{13}C NMR, TGA, DSC, powder XRD, XPS, BET, SEM and HRTEM. **COF** and **Ru@COF** are robust, highly crystalline in nature and stable in acidic medium. Both the 2D **COF** and **Ru@COF** showed spherical morphology. Furthermore, we have investigated the catalytic activity of **Ru@COF** modified GC electrode in electrochemical HER. **Ru@COF** showed lower overpotential value of 159 mV for HER. Lower Tafel slope of 79 mV dec^{-1} indicated its faster rate and better catalytic activity for H$_2$ generation reaction upon lower cathodic potential. Lower overpotential 212 mV was required to achieve 10 mA cm^{-2} in acidic solution. In conclusion, **COF** was considered as efficient and better template for the encapsulation of Ru. The 2D **COF** possessed relatively more stable interactions and hydrophobic environment to increase its heterogeneity which increased its stability on the GC electrode surface with advantages of its cost-effective, easy binder free electrode fabrication.

5.5 References

1. Ding, S.-Y.; Wang, Covalent organic frameworks (COFs): from design to applications. W. *Chem. Soc. Rev*. **2013**, *42*, 548. (DOI: 10.1039/C2CS35072F)

2. Thomas, A. Functional materials: from hard to soft porous frameworks. *Angew. Chem. Int. Ed*. *2010*, 49, 8328-8344. (DOI: 10.1002/anie.201000167)

3. Côté, A. P, Benin, A. I, Ockwig, N. W.; O'Keeffe, M.; Matzger, A. J.; Yaghi O. M. Porous, crystalline, covalent organic frameworks. *Science* **2005**, *310*, 1166-1170. (DOI: 10.1126/science.1120411)

4. Dogru, M.; Sonnauer, A.; Zimdars, S.; Do¨blinger, M.; Knochel, P.; Bein, T. Facile synthesis of a mesoporous benzothiadiazole-COF based on a transesterification process. *CrystEngComm*. **2013**, *15*, 1500-1502. (DOI: 10.1039/C2CE26343B)

5. Li, Z.; Feng, X.; Zou, Y.; Zhang, Y.; Xia, H.; Liu, X.; Mu, Y. A 2D azine linked covalent organic framework for gas storage applications. *Chem. Commun.* **2014**, *50*, 13825-13828. (DOI: 10.1039/c4cc05665e)

6. Wan, S.; Guo, J.; Kim, J.; Ihee, H.; Jiang, D. A photoconductive covalent organic framework: self-condensed arene cubes composed of eclipsed 2D polypyrene sheets for photocurrent generation. *Angew. Chem. Int. Ed*. **2009**, *48*, 5439 -5442. (DOI: 10.1002/anie.200900881)

7. Wang, L.; Zeng, C.; Xu, H.; Yin, P.; Chen, D.; Deng, J.; Li, M.; Zheng, N.; Gu, C.; Ma, Y. A highly soluble, crystalline covalent organic framework compatible with device implementation. *Chem. Commun*. **2014**, *50*, 13825-13828. (DOI: 10.1039/C8SC04255A)

8. Zhu, L.; Zhang, Y.-B. *Molecules* **2017**, *22*, 1149. Crystallization of Covalent Organic Frameworks for Gas Storage Applications. (DOI: org/10.3390/molecules22071149)

9. Li, Z.; Zhi, Y.; Feng, X.; Ding, X.; Zou, Y.; Liu, X.; Mu, Y. An Azine-Linked Covalent Organic Framework: Synthesis, Characterization and Efficient Gas Storage. *Chem. Eur. J.* **2015**, *21*, 12079-12084. (DOI: org/10.1002/chem.201501206)

10. Lee, G. Y, Lee, J.; Vo, H. T.; Kim, S.; Lee, H.; Park, T. Amine-Functionalized Covalent Organic Framework for Efficient SO_2 Capture with High Reversibility. *Sci Rep.* **2017**, *7*, 557. (DOI: 10.1038/s41598-017-00738-z)

11. Fan, H.; Mundstock, A.; Feldhoff, A.; Knebel, A.; Gu, J.; Meng, H.; Caro, J. Covalent Organic Framework-Covalent Organic Framework Bilayer Membranes for Highly Selective Gas Separation. *J. Am. Chem. Soc.* **2018**, *140*, 10094-10098. (DOI: org/10.1021/jacs.8b05136)

12. Lv, J.; Tan, Y.; Xie, J.; Yang, R.; Yu, M.; Sun, S.; Li, M.; Yuan, D.; Wang, Y. Direct Solar-to-Electrochemical Energy Storage in a Functionalized Covalent Organic Framework. *Angew. Chem. Int. Ed.* **2018**, *57*, 12716-12720. (DOI: 10.1002/anie.201806596)

13. Feng, S.; Xu, H.; Zhang, C.; Chen, Y.; Zeng, J.; Jiang, D.; Jiang, J.-X. Bicarbazole-based redox-active covalent organic frameworks for ultrahigh-performance energy storage. *Chem. Commun.* **2017**, *53*, 11334-11337. (DOI: 10.1039/C7CC07024A)

14. Sun, Q.; Aguila, B.; Ma, S. A bifunctional covalent organic framework as an efficient platform for cascade catalysis, *Mater. Chem. Front.* **2017**, *1*, 1310-1316. (DOI: 10.1039/C6QM00363J)

15. Mu, Z. J.; Ding, X.; Chen, Z. Y. Han, B. H. Zwitterionic Covalent Organic Frameworks as Catalysts for Hierarchical Reduction of CO_2 with Amine and Hydrosilane. *ACS Appl Mater Interfaces* **2018**, 10, 41350-41358. (DOI: 10.1021/acsami.8b1467)

16. Lin, C.-Y.; Zhang, D.; Zhao, Z.; Xia, Z. Covalent Organic Framework Electrocatalysts for Clean Energy Conversion. *Adv.Mater.* **2018**, *30*, 1703646. (DOI: org/10.1002/adma.201703646)

17. Peng, P.; Zhou, Z.; Guo, J.; Xiang, Z. Well-Defined 2D Covalent Organic Polymers for Energy Electrocatalysis. *ACS Energy Lett.* **2017**, *2*, 1308-1314. (DOI: 10.1021/acsenergylett.7b00267)

18. Aiyappa, H. B.; Thote, J.; Shinde, D. B.; Banerjee, R.; Kurungot, S. Cobalt-Modified Covalent Organic Framework as a Robust Water Oxidation Electrocatalyst. *Chem. Mater.* **2016**, *28*, 4375-4379. (DOI: org/10.1021/acs.chemmater.6b01370)

19. Xu, Q.; Tang, Y. Zhang, X.; Oshima, Y.; Chen, Q.; Jiang, D. Template Conversion of Covalent Organic Frameworks into 2D Conducting Nanocarbons for Catalyzing Oxygen Reduction Reaction. Q. Xu, Y. Tang, X. Zhang, Y. Oshima, Q. Chen, D. Jiang, *Adv. Mater.* **2018**, *30*, 1706330. (DOI: org/10.1002/adma.201706330)

20. Mitra, S.; Sasmal, H. S.; Kundu, T.; Kandambeth, S.; Illath, K.; Díaz, D. D.; Banerjee, R. Targeted Drug Delivery in Covalent Organic Nanosheets (CONs)

via Sequential Postsynthetic Modification. *J Am Chem Soc*. **2017**;*139*, 4513-4520. (DOI: 10.1021/jacs.7b00925)

21. Vyas, V. S.; Haase, F.; Stegbauer, L.; Savasci, G.; Podjaski, F.; Ochsenfeld, C.; Lotsch, B. V. A tunable azine covalent organic framework platform for visible light-induced hydrogen generation. *Nat Comm*. **2015**, *6*, 8508. (DOI:10.1038/ncomms9508)

22. Wang, P.; Zhou, F.; Zhang, C.; Yin, S.-Y.; Teng, L.; Chen, L.; Hu, X.-X.; Liu, H. W.; Yin, X.; Zhang, X.-B. Ultrathin two-dimensional covalent organic framework nanoprobe for interference-resistant two-photon fluorescence bioimaging. *Chem. Sci*. **2018**, *9*, 8402-8408. (DOI: 10.1039/C8SC03393E)

23. Haase, F.; Gottschling, K.; Stegbauer, L.; Germann, L. S.; Gutzler, R.; Duppel, V.; Vyas, V. S.; Kern, K.; Dinnebier, R. E.; Lotsch, B. V. Tuning the stacking behaviour of a 2D covalent organic framework through non-covalent interactions. *Mater. Chem. Front*. **2017**, *1*, 1354-1361. (DOI: 10.1039/C6QM00378H)

24. Spitler, E. L.; Koo, B. T.; Novotney, J. L.; Colson, J. W.; Uribe-Romo, F. J.; Gutierrez, G. D.; Clancy, P.; Dichtel, W. R. A 2D Covalent Organic Framework with 4.7-nm Pores and Insight into Its Interlayer Stacking. *J. Am. Chem. Soc*. **2011**, *133*, 19416-19421. (DOI: org/10.1021/ja206242v)

25. Shi, X.; Yao, Y.; Xu, Y.; Liu, K.; Zhu, G.; Chi, L.; Lu, G. Imparting Catalytic Activity to a Covalent Organic Framework Material by Nanoparticle Encapsulation. *ACS Appl. Mater. Interfaces* **2017**, *9*, 7481-7488. (DOI: org/10.1021/acsami.6b16267)

26. Lin, S.; Diercks, C. S.; Zhang, Y. B.; Kornienko, N.; Nichols, E. M.; Zhao, Y.; Paris, A. R.; Kim, D.; Yang, P.; Yaghi, O. M.; Chang, C. J. Covalent organic frameworks comprising cobalt porphyrins for catalytic CO_2 reduction in water. *Science* **2015**;349, 1208-13. (DOI: 10.1126/science.aac8343)

27. Chen, L.; Zhang, L.; Chen, Z.; Liu, H.; Luque, R.; Li, Y. A covalent organic framework-based route to the in situ encapsulation of metal nanoparticles in N-rich hollow carbon spheres. *Chem. Sci*. **2016**, *7*, 6015-6020. (DOI: 10.1039/C6SC01659F)

28. White, R. J.; Luque, R.; Budarin, V. L.; Clark, J. H.; Macquarrie, D. J. Supported metal nanoparticles on porous materials. Methods and applications. *Chem. Soc. Rev*. **2009**, *38*, 481-494. (DOI: 10.1039/B802654H)

29. Pan, X.; Fan, Z.; Chen, W.; Ding, Y.; Luo, H.; Bao, X. Enhanced ethanol production inside carbon-nanotube reactors containing catalytic particles. *Nature Mater*. **2007**, *6*, 507-511 (DOI: 10.1038/nmat1916)

30. Shi, X.; Yao, Y.; Xu, Y.; Liu, K.; Zhu, G.; Chi, L.; Lu, G. Imparting Catalytic Activity to a Covalent Organic Framework Material by Nanoparticle Encapsulation. *ACS Appl. Mater. Interfaces* **2017**, *9*, 7481-7488. (DOI: 10.1021/acsami.6b16267)

31. Nandi, S.; Singh, S. K.; Mullangi, D.; Illathvalappil, R.; George, L.; Vinod, C. P.; Kurungot, S.; Vaidhyanathan, R. Low Band Gap Benzimidazole COF

Supported Ni₃N as Highly Active OER Catalyst. *Adv. Energy Mater.* **2016**, *6*, 1601189 (DOI: 10.1002/aenm.201601189)

32. Peterson, G. V.; Wagner, G. W.; Balboa, A.; Mahle, J.; Sewell, T. C.; Karwacki, C. J. Ammonia Vapor Removal by Cu₃(BTC)₂ and Its Characterization by MAS NMR. *J. Phys. Chem. C* **2009**, *113*, 31, 13906-13917. (DOI: org/10.1021/jp902736z)

33. Gloaguen, F.; Lawrence, J. D.; Rauchfuss, T. B. Biomimetic Hydrogen Evolution Catalyzed by an Iron Carbonyl Thiolate. *J. Am. Chem. Soc.* **2001**, *123*, 9476-9477. (DOI: org/10.1021/ja016516f)

34. Volbeda, A.; Garcin, E.; Piras, C.; de Lacey, A. L.; Fernandez, V. M.; Hatchikian, E. C.; Frey, M.; Fontecilla-Camps, J. Structure of the [NiFe] Hydrogenase Active Site: Evidence for Biologically Uncommon Fe Ligands. *J. Am. Chem. Soc.* **1996**, *118*, 12989-12996. (DOI: org/10.1021/ja962270g)

35. Morales-Guio, G. C.; Stern, L.-A.; Hu, X. Structure of the [NiFe] Hydrogenase Active Site: Evidence for Biologically Uncommon Fe Ligands. *Chem. Soc. Rev.* **2014**, *43*, 6555- 6569. (DOI: org/10.1021/ja962270g)

36. Li, Y.; Wang, H.; Xie, L.; Liang, Y.; Hong, G.; Dai, H. MoS₂ Nanoparticles Grown on Graphene: An Advanced Catalyst for the Hydrogen Evolution Reaction. *J. Am. Chem. Soc.* **2011**, *133*, 7296-7299. (DOI: org/10.1021/ja201269b)

37. Anantharaj, S.; Amarnath, T. S.; Subhashini, E.; Chatterjee, S.; Swaathini, K. C.; Karthick, K.; Kundu, S. Pt Nanoparticle Anchored Molecular Self-Assemblies of DNA: An Extremely Stable and Efficient HER Electrocatalyst with Ultralow Pt Content. *ACS Catal.* **2018**, *8*, 5686-5697. (DOI: org/10.1021/acscatal.6b00965)

38. Anantharaj, S.; Karthik, K.; Amarnath, T. S.; Chatterjee, S.; Subhashini, E.; Swaathini, K. C.; Karthick, P. E.; Kundu, S. Membrane Free Water Electrolysis under 1.23 V with Ni₃Se₄/Ni Anode in Alkali and Pt Cathode in Acid. *Appl. Surf. Sci.* **2019**, *478*, 784-792. (DOI: org/10.1016/j.apsusc.2019.01.231)

39. Dey,K. K.; Jha, S.; Kumar, A.; Gupta, G.; Srivastava, A. K.; Ingole, P. P. Layered vanadium oxide nanofibers as impressive electrocatalyst for hydrogen evolution reaction in acidic medium. *Electrochim. Acta* **2019**, *312*, 89-99. (DOI: org/10.1016/j.electacta.2019.04.185)

40. McKone, J. R.; Sadtler, B. F.; Werlang, C. A.; Lewis, N. S.; Gray, H. B. Ni–Mo Nanopowders for Efficient Electrochemical Hydrogen Evolution. *ACS Catal.* **2013**, *3*, 166-169. (DOI: org/10.1021/cs300691m)

41. Kohl, S. W.; Weiner, L.; Schwartsburd, L.; Konstantinovski, L.; Shimon, J. W.; Ben-David, Y.; Iron, M. A.; Milstein, D. Consecutive thermal H₂ and light-induced O2 evolution from water promoted by a metal complex. *Science* **2009**, *324*, 74-77. (DOI: 10.1126/science.1168600)

42. Ozawa, H.; Haga, M.; Sakai, K. A Photo-Hydrogen-Evolving Molecular Device Driving Visible-Light-Induced EDTA-Reduction of Water into Molecular Hydrogen. *J. Am. Chem. Soc.* **2006**, *128*, 4926-4927. (DOI: org/10.1021/ja058087h)

43. Ahmad, H.; Kamarudina, S. K.; Minggu, L. E.; Kassim, M. Hydrogen from photo-catalytic water splitting process: A review. *Renewable. Sustainable Energy Rev*. **2015**, *43*, 599-610. (DOI: org/10.1016/j.rser.2014.10.101)

44. Hinnemann, B.; Moses, P. G.; Bonde, J.; Jørgensen, K. P.; Nielsen, J. H.; Horch, S.; Chorkendorff, I.; Nørskov, J. K. Biomimetic hydrogen evolution: MoS_2 nanoparticles as catalyst for hydrogen evolution. *J. Am. Chem. Soc*. **2005**, *127*, 5308-5309. (DOI: org/10.1021/ja0504690)

45. Popczun, E. J.; McKone, J. R.; Read, C. G.; Biacchi, A. J.; Wiltrout, A. M.; Lewis, N. S.; Schaak, R. E. *J. Am. Chem. Soc*. **2013**, *135*, 9267-9270. Nanostructured nickel phosphide as an electrocatalyst for the hydrogen evolution reaction. (DOI: 10.1021/ja403440e)

46. Liu, X.; Zheng, H.; Sun, Z.; Han, A.; Du, P. Earth-Abundant Copper-Based Bifunctional Electrocatalyst for Both Catalytic Hydrogen Production and Water Oxidation. *ACS Catal*. **2015**, *5*, 1530-1538. (DOI: org/10.1021/cs501480s)

47. Huot, J. Y. Hydrogen Evolution and Interface Phenomena on a Nickel Cathode in 30 w/o. *J. Electrochem. Soc*. **1989**, *136*, 1933-1939. (DOI: 10.1149/1.2097088)

48. Zenga, M.; Li, Y. Recent advances in heterogeneous electrocatalysts for the hydrogen evolution reaction. *J. Mater. Chem. A*, **2015**, *3*, 14942-14962. (DOI: 10.1039/C5TA02974K)

49. Cherevko, S.; Geiger, S.; Kasian, O.; Kulyk, N.; Grote, J. –P.; Savan, A.; Shrestha, B. R.; Merzlikin, S.; Breitbach, B.; Ludwig, A.; Mayrhofer, K. J. J. Oxygen and hydrogen evolution reactions on Ru, RuO_2, Ir, and IrO_2 thin film electrodes in acidic and alkaline electrolytes: A comparative study on activity and stability. *Catal. Today* **2016**, *262*, 170-180. (DOI: org/10.1016/j.cattod.2015.08.014)

50. Chen, L.; Guay, D.; Lasia, A. Kinetics of the hydrogen evolution reaction on RuO_2 and IrO_2 oxide electrodes in H2SO4 solution: An AC impedance study. J. *Electrochem. Soc*. **1996**, *143*, 3576-3584. (DOI: 10.1149/1.1837255)

51. Miousse, D.; Lasia, A. Hydrogen evolution reaction on RuO_2 electrodes in alkaline solutions. *J. New Mater. Electrochem. Syst*. **1999**, *2*, 71-78.

52. Yang, X.; Zhao, Z.; Yu, X.; Feng, L. Electrochemical hydrogen evolution reaction boosted by constructing Ru nanoparticles assembled as a shell over semimetal Te nanorod surfaces in acid electrolyte. *Chem. Commun*. **2019**, *55*, 1490-1493. (DOI: 10.1039/C8CC09993F)

53. Zhou, W.; Zhou, Y.; Yang, L.; Huang, J.; Ke, Y.; Zhou, K.; Lia, L.; Chen, S. N-doped carbon-coated cobalt nanorod arrays supported on a titanium mesh as highly active electrocatalysts for the hydrogen evolution reaction. *J. Mater. Chem. A* **2015**, *3*, 1915-1919. (DOI: 10.1039/C4TA06284A)

54. Pramoda, K.; Ayyub, M. M.; Singh, N. K.; Chhetri, M.; Gupta, U.; Soni, A.; Rao, C. N. R. Covalently Bonded MoS_2-Borocarbonitride Nanocomposites Generated by Using Surface Functionalities on the Nanosheets and Their Remarkable HER Activity. *J. Phys. Chem. C* **2018**, *122*, 13376-13384. (DOI: org/10.1021/acs.jpcc.7b10782)

55. Liu, Y.; Yu, H.; Quan, X.; Chen, S.; Zhao, H.; Zhang, Y. Efficient and durable hydrogen evolution electrocatalyst based on nonmetallic nitrogen doped hexagonal carbon. *Sci Rep*. **2015**, *4*, 6843. (DOI:10.1038/srep06843)

56. Zhao, Y.; Zhao, F.; Wang, X.; Xu, C.; Zhang, Z.; Shi, G.; Qu, L. Graphitic carbon nitride nanoribbons: graphene-assisted formation and synergic function for highly efficient hydrogen evolution. *Angew. Chem. Int. Ed*. **2014**, *53*, 13934 - 13939. (DOI: 10.1002/anie.201409080)

57. Liu, X.; Zhou, W.L; Yang, L.; Li, L.; Zhang, Z.; Ke, Y.; Chen, S. Correction: Nitrogen and sulfur co-doped porous carbon derived from human hair as highly efficient metal-free electrocatalysts for hydrogen evolution reactions *J. Mater. Chem. A* **2015**, *3*, 8840. (DOI: 10.1039/c5ta90086g)

58. Duan, J.; Chen, S.; Jaroniec, M.; Qiao, S. Z. Porous C_3N_4 nanolayers@N-graphene films as catalyst electrodes for highly efficient hydrogen evolution. *ACS Nano* **2015**, *9*, 1, 931-940. (DOI: org/10.1021/nn506701x)

59. Gu, C.; Hosono, N.; Zheng, J.-J.; Sato, Y.; Kusaka, S.; Sakaki, S.; Kitagawa, S. *Science* **2019**, *363*, 387-391. Design and control of gas diffusion process in a nanoporous soft crystal. (DOI: 10.1126/science.aar6833)

60. Chen, G. J, Li, X. B.; Zhao, C. C.; Ma, H. C.; Kan, J. L.; Xin, Y. B.; Chen, C. X.; Dong, Y. B. Ru Nanoparticles-Loaded Covalent Organic Framework for Solvent-Free One-Pot Tandem Reactions in Air. *Inorg Chem.* **2018**, *57*, 2678-2685. (DOI: 10.1021/acs.inorgchem.7b0307)

61. Uribe-Romo, F. J.; Hunt, J. R.; Furukawa, H.; Klöck, C.; O'Keeffe, M.; Yaghi, O. M. A Crystalline Imine-Linked 3-D Porous Covalent Organic Framework. *J. Am. Chem. Soc.* **2009**, *131*, 4570-4571. (DOI: org/10.1021/ja8096256)

62. Hu, Y.; Goodeal, N.; Chen, Y.; Ganose, A. M.; Palgrave, R. G.; Bronstein, H.; Blunt, M. O. Probing the chemical structure of monolayer covalent-organic frameworks grown via Schiff-base condensation reactions. *Chem. Commun*. **2016**, *52*, 9941-9944. (DOI: 10.1039/C6CC03895F)

63. Tsuchiya, S.; Senō, M.; Lwowski, W. On the nature of nitrogen-nitrogen bonding in cyclic aminimides. *J. Chem. Soc., Perkin Trans*. **1983**, *0*, 887-890. (DOI: 10.1039/P29830000645)

64. Tawil, N.; Sacher, E.; Mandeville, R.; Meunier, M. Strategies for the Immobilization of Bacteriophages on Gold Surfaces Monitored by Surface Plasmon Resonance and Surface Morphology. *J. Phys. Chem. C* **2013,** *117*, 13, 6686-6691. (DOI: org/10.1021/jp400565m)

65. Mu, M.; Wang, Y.; Qin, Y.; Yan, X.; Li, Y.; Chen, L. Two-Dimensional Imine-Linked Covalent Organic Frameworks as a Platform for Selective Oxidation of Olefins. *ACS Appl. Mater. Interfaces* **2017**, *9*, 27, 22856-22863. (DOI: org/10.1021/acsami.7b05870)

66. Guan, Q.; Li, Y.; Chen, Y.; Shi, Y.; Gu, J.; Li, B.; Miao, R.; Chena, Q.; Ning, P. Sulfonated multi-walled carbon nanotubes for biodiesel production through triglycerides transesterification. *RSC Adv*. **2017**, *7*, 7250-7258. (DOI: 10.1039/C6RA28067F).

67. Morgan, D. J. Resolving ruthenium: XPS studies of commonruthenium materials. *Surf. Interface Anal.* **2015**, *47*, 1072-1079. (DOI 10.1002/sia.5852)

68. Bhunia, S.; Das, S. K.; Jana, R.; Peter, S. C.; Bhattacharya, S.; Addicoat, M.; Bhaumik, A.; Pradhan, A. Electrochemical Stimuli-Driven Facile Metal-Free Hydrogen Evolution from Pyrene-Porphyrin-Based Crystalline Covalent Organic Framework. *ACS Appl. Mater. Interfaces* **2017**, *9*, 28, 23843-23851. (DOI: 10.1021/acsami.7b06968).

69. Su, L.; Cui, X.; He, T.; Zeng, L.; Tian, H.; Song, Y.; Qi, K.; Xia, B. Y. Surface reconstruction of cobalt phosphide nanosheets by electrochemical activation for enhanced hydrogen evolution in alkaline solution. *Chem. Sci.* **2019**, *10*, 2019-2024. (DOI: 10.1039/C8SC04589E)

70. Wu, H. B.; Xia, B. Y.; Yu, L.; Yu, X. Y.; Lou, X. W. Porous molybdenum carbide nano-octahedrons synthesized via confined carburization in metal-organic frameworks for efficient hydrogen production. *Nat Commun.* **2015**, *6*, 6512. (DOI:10.1038/ncomms7512)

71. Li, J. S.; Wang, Y.; Liu, C. H.; Li, S. L.; Wang, Y. G.; Dong, L. Z.; Dai, Z. H, Li, Y. F.; Lan, Y. Q. Coupled molybdenum carbide and reduced graphene oxide electrocatalysts for efficient hydrogen evolution. *Nat Commun.* **2016**, *7*, 11204 (DOI: 10.1038/ncomms11204)

72. Hod, I.; Deria, P.; Bury, W.; Mondloch, J. E.; Kung, C. W.; So, M.; Sampson, M. D.; Peters, A. W.; Kubiak, C. P.; Farha, O. K.; Hupp, J. T. A porous proton-relaying metal-organic framework material that accelerates electrochemical hydrogen evolution. *Nat Commun.* **2015**, *6*, 8304. (DOI: 10.1038/ncomms9304)

73. Qin, J. S.; Du, D. Y.; Guan, W.; Bo, X. J.; Li, Y. F.; Guo, L. P.; Su, Z. M.; Wang, Y. Y.; Lan, Y. Q.; Zhou, H. C. Ultrastable Polymolybdate-Based Metal-Organic Frameworks as Highly Active Electrocatalysts for Hydrogen Generation from Water. *J Am Chem Soc.* **2015**, *137*, 7169-7177. (DOI: 10.1021/jacs.5b02688)

74. He, K.; Cao, Z.; Liu, R.; Miao, Y.; Ma, H.; Ding, Y. In situ decomposition of metal-organic frameworks into ultrathin nanosheets for the oxygen evolution reaction. *Nano Res.* **2016**, *9*, 1856-1865. (DOI: 10.1007/s12274-016-1078-x).

75. Wu, D.; Xu, Q.; Qian, J.; Li, X.; Sun, Y. Bimetallic Covalent Organic Frameworks for Constructing Multifunctional Electrocatalyst. *Chem.Eur.J.* **2019**, *25*,3105 –3111. (DOI:10.1002/chem.201805550)

76. Cui, S.; Qian, M.; Liu, X.; Sun, Z.; Du, P. A Copper Porphyrin-Based Conjugated Mesoporous Polymer-Derived Bifunctional Electrocatalyst for Hydrogen and Oxygen Evolution. *ChemSusChem.* **2016**, *9*, 2365-2373. (DOI: 10.1002/cssc.201600452)

Chapter 6
**Conclusion and future aspect**

6.1 Conclusion.

Covalent organic polymers (COPs) or covalent organic frameworks (COFs) have been paid considerable attention due to their emerging controllable nanostructured architecture and structural diversity. The polymeric shape and pore size of COPs can be controlled by pore size tuning, surface active sites, chemical functionalization (presence of hydrophobic and hydrophilic groups) and surface functional group orientation, which can be facilitated in a number of applications such as catalysis, gas sensing, adsorption, detection and electronics.[1-6] This thesis presents a synthesis and characterization of various types of functionalized COPs/COFs materials and investigation their activity or efficiency on respective applications. The pilot investigated in chapter 2, the catalytic activities of sulfonated **COP-2** for biodiesel production through the esterification and transesterification reactions under mild conditions. **COP-2** showed excellent catalytic activity with very short reaction time. The catalyst could be removed by simple filtration techniques and reused for several cycles with the same catalytic activity. Thus **COP-2** was found to be promising in several aspects. In future more of such functionalized **COP-2** will be investigated as heterogeneous catalysts in a variety of chemical reactions due to their structural diversity. In the chapter 3, we designed and synthesized a **COP** for heterogeneous catalysis and promising metal ions adsorbent. In this regard, a new robust covalent organic polymer **COP-3** with a picolinohydrazide linkage was synthesized and explored their properties elaborately in this chapter. We investigated the role of the pyridine and hydrazide moieties in **COP-3** in various applications. **COP-3** acted as a heterogeneous catalyst for Knoevenagel condensation under very mild condition. On the other hand **COP-3** showed promising efficiency in removal of heavy metal ions, including Ca^{2+}, Cu^{2+}, Cd^{2+}, Hg^{2+}, and Pb^{2+}. For all of the mentioned metal ions, **COP-3** showed significant adsorption capacity with removal efficiencies of >95% for Ca^{2+}, Cu^{2+}, Cd^{2+}, and Pb^{2+} and 80% for Hg^{2+}. The unique combination of suitable binding sites, such as pyridine N and hydrazide units, in the polymeric framework was the key reason for such diverse properties of this material. In chapter 4, we used **COP** as an efficient gas sensing material in chemiresistive gas sensor. Here we synthesized a hydrazide-based **COP-4** polymer. The **COP-4** acted as a highly efficient and selective chemiresistive gas sensing material for H_2S at 25 ⁰ C. Gas sensing measurement was performed in a dynamic flow-through resistance measurement system. The sensing effect was fully reversible and operated at room temperature. The maximum response to 200 ppm of H_2S was found to be >50% at 25 ºC with very fast response time of 9 s with a recovery time of 12 s. Here, the gas sensing mechanism of **COP-4** based sensor had been established through a proton conduction process where hydrazide bonds inside the polymeric backbone played a major role in this process. In chapter 5, we synthesized a porous 2D **COF** and Ru encapsulated **COF** (**Ru@COF**). Here we investigated the catalytic activity of **Ru@COF** modified GC electrode in electrochemical HER. **Ru@COF** showed lower overpotential value of 159 mV for HER with

lower Tafel slope of 79 mV dec^{-1}. The lower tafel slope indicated its faster rate and better catalytic activity for H$_2$ generation reaction upon lower cathodic potential. Here **COF** was considered as efficient and better heterogeneous template for the encapsulation of Ru. The 2D **COF** possessed relatively more stable interactions and hydrophobic environment to increase its heterogeneity which enhanced its stability on the GC electrode surface.

6.2 Future aspects.

Development of two dimensional COFs (Reticular chemistry)
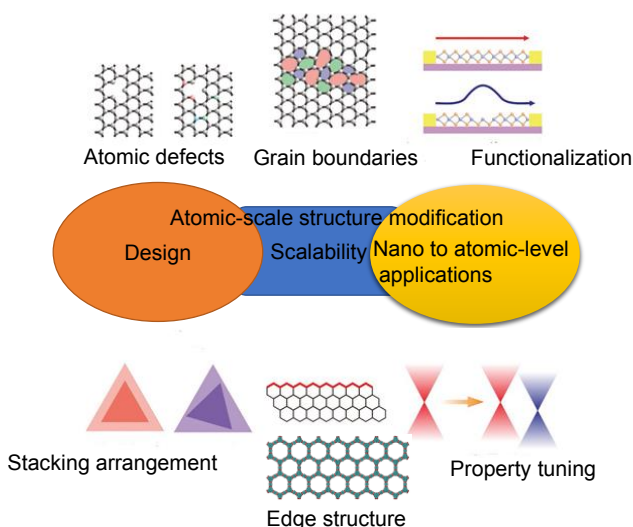
Figure 6.2.1 The design and application of ASSs of 2D materials.

Property modulations of two dimensional frameworks (COFs) towards several applications have attracted extensive attention in recent years. The introduction of new synthetic routes of 2D COFs that exhibits tremendous chemical, thermal stability, structural uniformity and long range order of crystallinity that serve their potential for several applications. However, there are still several obstacles and issues that need to be solved for investigating the structure to properties correlations. It is very difficult to identify a number of defect sites and grain boundaries that prevent the understanding of the inherent properties and growth mechanism of the various 2D polymers.[7-8] If we optimize and control the accurate mechanisms of synthetic conditions for synthesizing the 2D COFs, this will not only scale up production but also structure to properties correlations will be realized. In this regard, we are engaged in the atomic-scale structural (ASS) modification of 2D COFs and the induced property tuning to the respective extension of the application. The ASS modification needs to be established in terms of the different atomic arrangements, atomic defects, edge structure arrangements and stacking configurations. Next, the growth mechanism of ASSs of 2D COFs is still lacking in clear understanding. Advanced high-resolution

characterization analysis such as HRTEM and scanning tunnel microscope (STM) of 2D-COF may give process routes of structural modification on an atomic scale. Theoretical simulations and calculations may also help us understand the mechanisms of growth. The ASS modification of 2D COFs may play a significant role in the property tuning of materials which hold the prospect of structural engineering to improve material diversity towards fundamental chemical research, integrated circuit manufacturing, electrical and optical sensors, and energy storage and transformation devices. We are ensured that the ASSa modification will further promote the development of 2D COFs and tune their properties.

6.3 References.

1. Guo, J.; Jiang, D. Covalent Organic Frameworks for Heterogeneous Catalysis: Principle, Current Status, and Challenges. *ACS Cent. Sci*. **2020**, *6*, 869-879. (DOI: org/10.1021/acscentsci.0c00463)

2. Li, H.; Feng, X.; Shao, P.; Chen, J.; Li, C.; Jayakumar, S.; Yang, Q: *J. Mater. Chem*. A **2019**, *7*, 5482-5492. Synthesis of covalent organic frameworks via in situ salen skeleton formation for catalytic applications. (DOI: 10.1039/c8ta11058a)

3. Meng, Z.; Stolz, R. M.; Mirica, K. A. Two-Dimensional Chemiresistive Covalent Organic Framework with High Intrinsic Conductivity. *J. Am. Chem. Soc*. **2019,** *141*, 11929-11937. (DOI: org/10.1021/jacs.9b03441)

4. Sharma, A.; Malani, A.; Medhekar, N. V.; Babarao, R. CO_2 adsorption and separation in covalent organic frameworks with interlayer slipping. *CrystEngComm*, **2017**, *19*, 6950-6963. (DOI: 10.1039/c7ce01647f)

5. Yang, L.-M.; Pushpa, R. Tuning electronic and optical properties of a new class of covalent organic frameworks. *J. Mater. Chem. C* **2014**, *2*, 2404-2416. (DOI: 10.1039/c3tc32252a)

6. Mandal, A. K.; Mahmood, J.; Baek, J.-B. Two-Dimensional Covalent Organic Frameworks for Optoelectronics and Energy Storage. *ChemNanoMat*. **2017**, *3*, 373-391. (DOI: 10.1002/cnma.201700048)

7. Khan, K.; Tareen, A. K.; Aslam, M.; Wang, R.; Zhang, Y.; Mahmood, A.; Ouyang, Z.; Zhang, H.; Guo, Z. Recent developments in emerging two dimensional materials and their applications. *J. Mater. Chem. C*, **2020**, *8*, 387-440. (DOI: 10.1039/c9tc04187g)

8. Bi, S.; Thiruvengadam, P.; Wei, S.; Zhang, W.; Zhang, F.; Gao, L.; Xu, J.; Wu, D.; Chen, J.-S.; Zhang, F. Vinylene-Bridged Two-Dimensional Covalent Organic Frameworks *via* Knoevenagel Condensation of Tricyanomesitylene. *Journal of the American Chemical Society* **2020**, *142*, 27, 11893-11900 (DOI: 10.1021/jacs.0c04594)
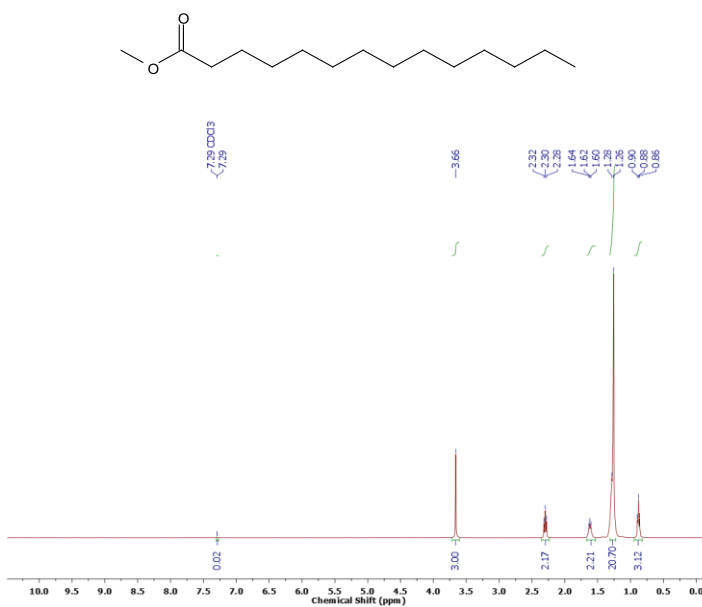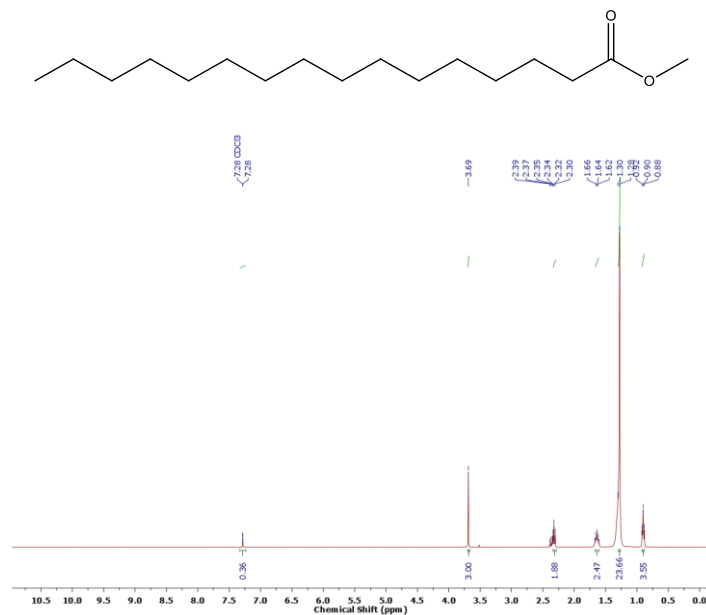
Appendix-A. All NMR, GC-MS data of catalytic reactions by the
COP-2
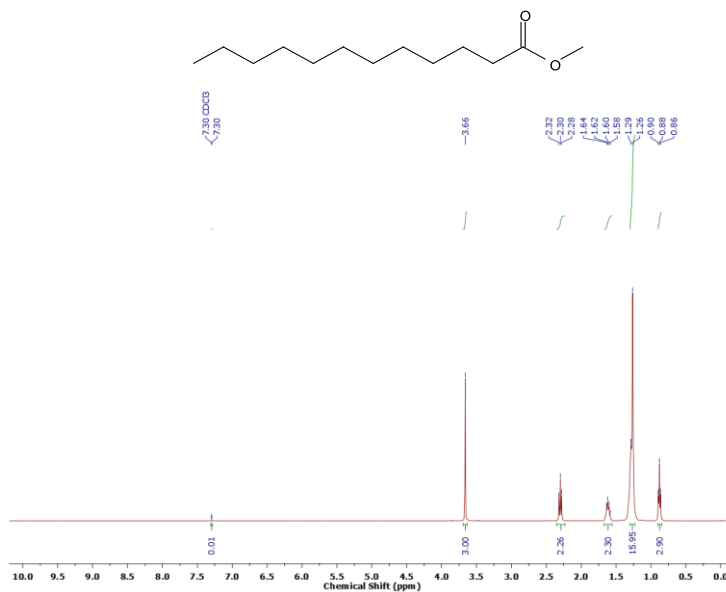
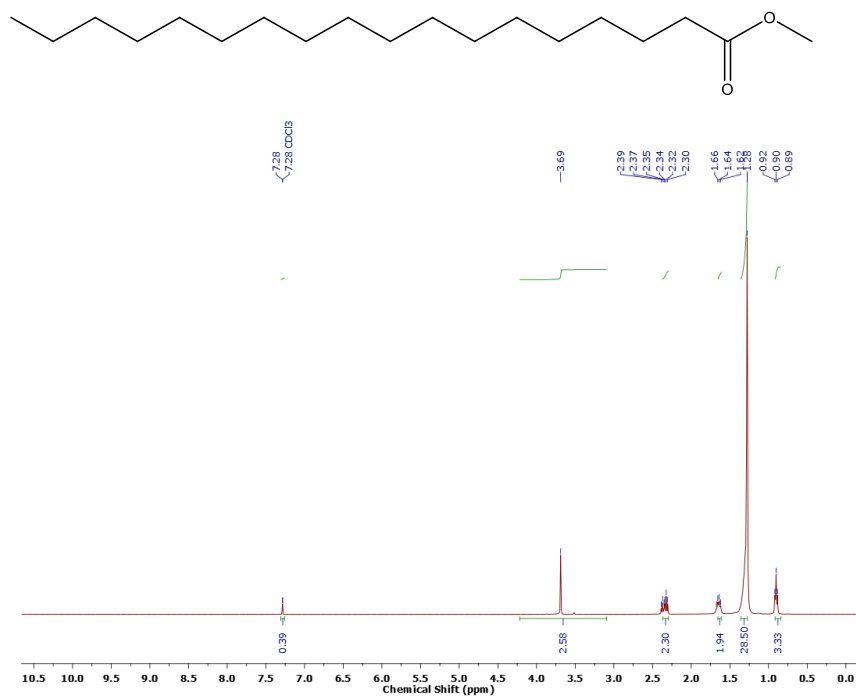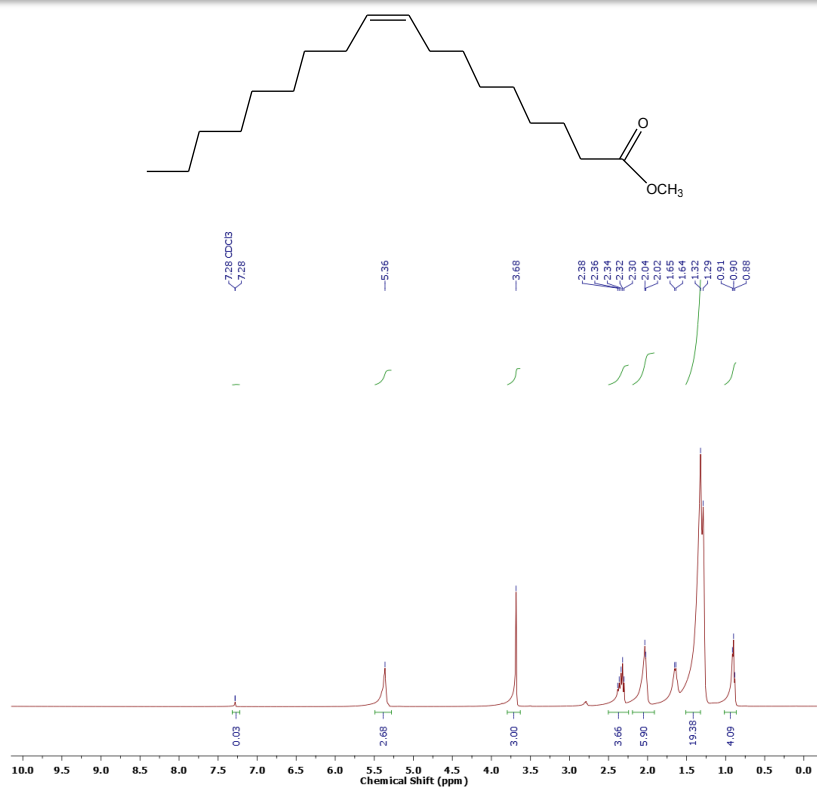A.1. ^{1}H NMR (CDCl$_3$, 400 MHz) of methyl laurate after 7 h reaction.

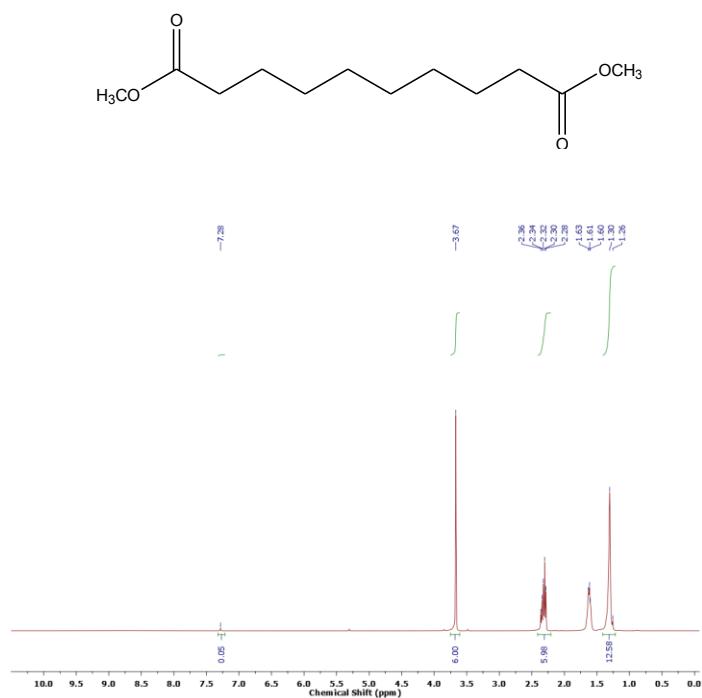A.2. ^{1}H NMR (CDCl$_3$, 400 MHz) of methyl myristate after 7 h reaction.

147

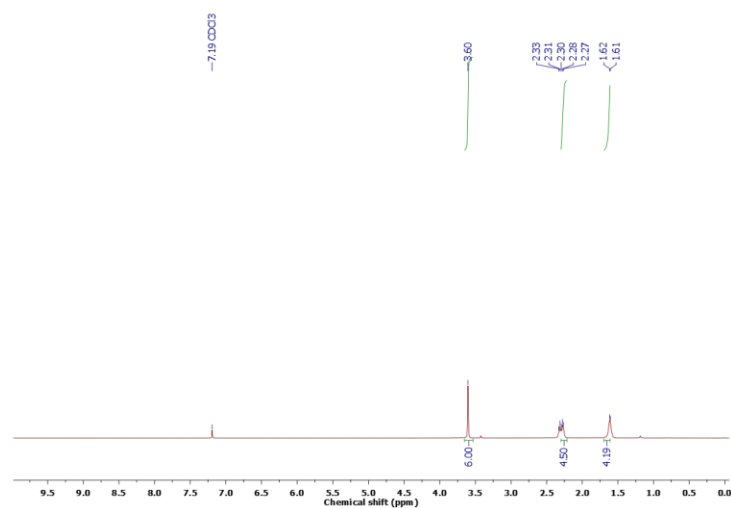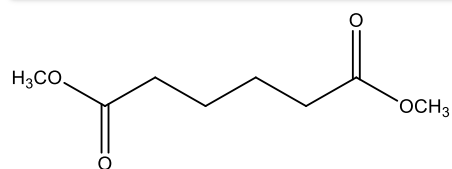A.3. ^{1}H NMR (CDCl$_3$, 400 MHz) of methyl palmitate after 7 h reaction.

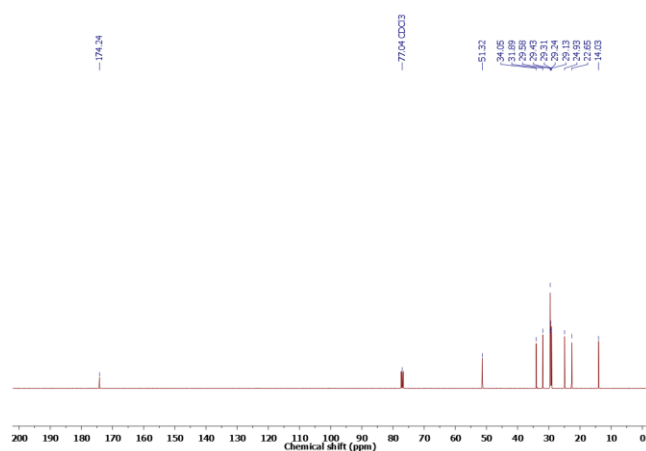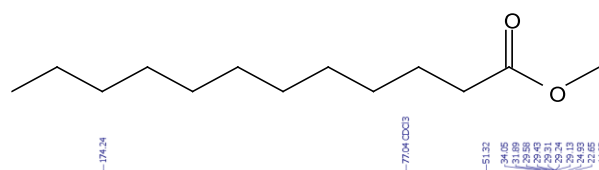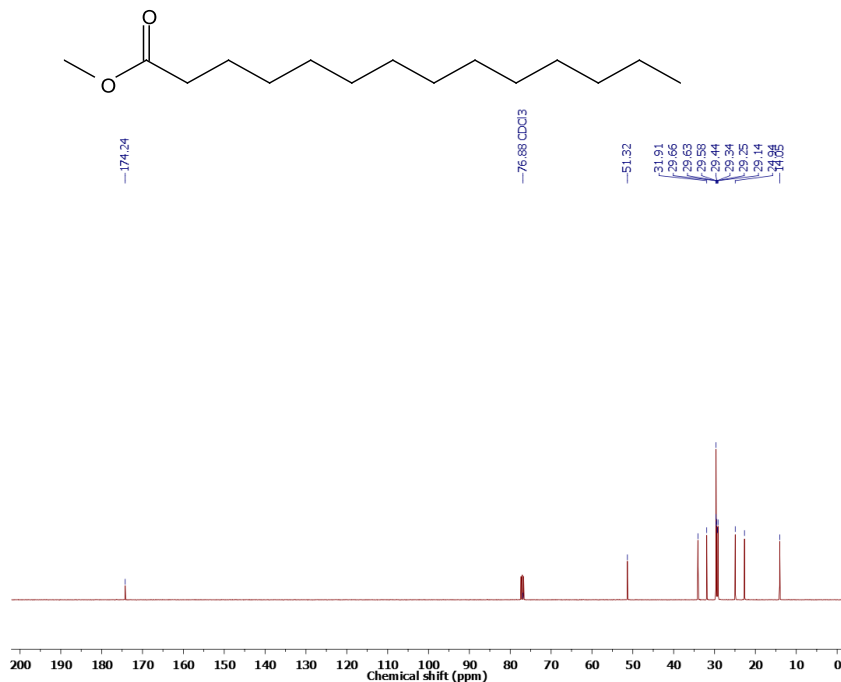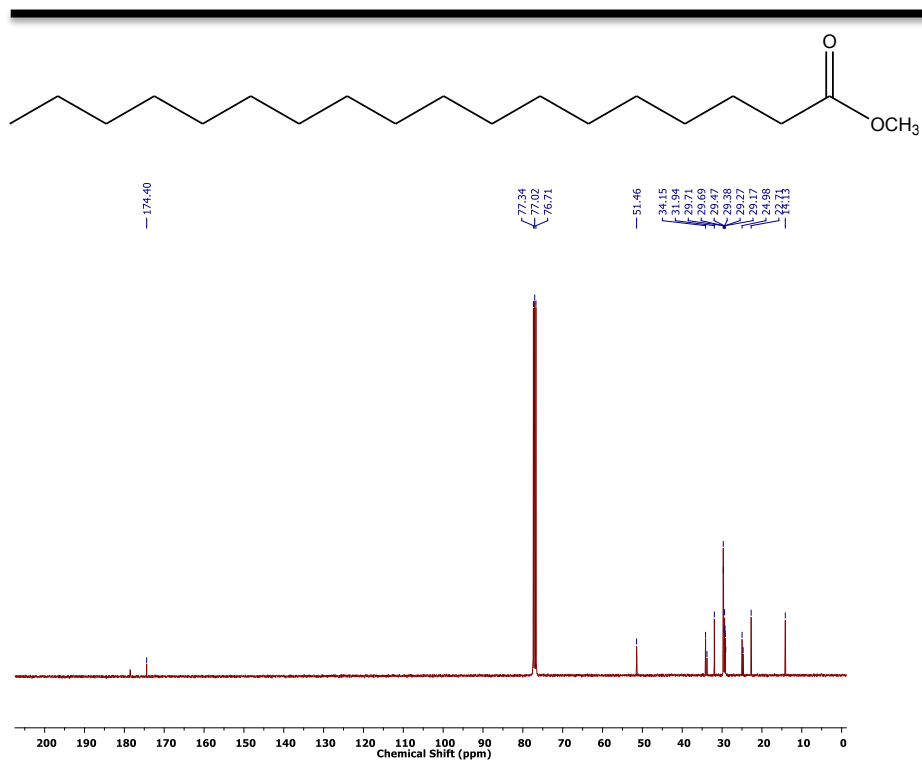A.4. ^{1}H NMR (CDCl$_3$, 400 MHz) of methyl stearate after 7 h reaction.

148

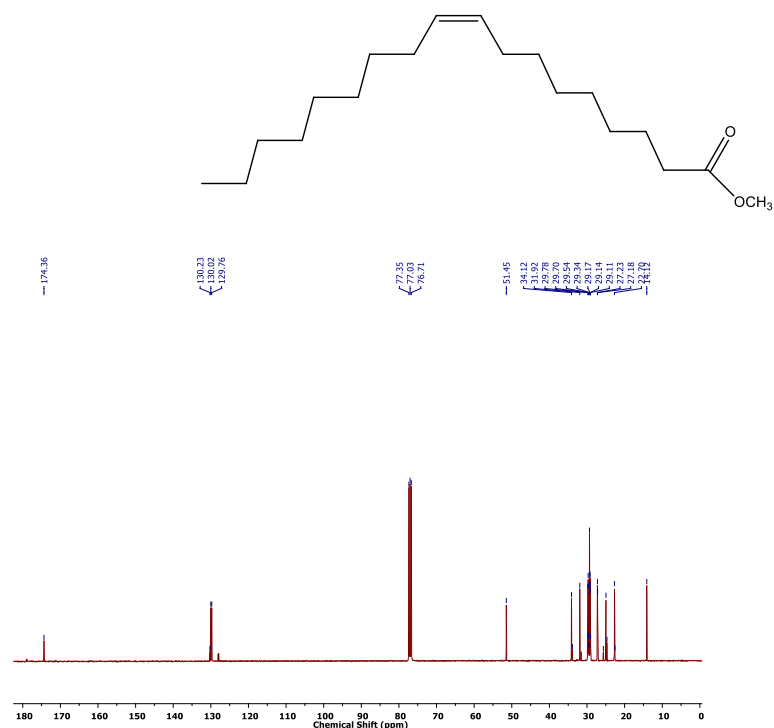A.5. ^{1}H NMR (CDCl$_3$, 400 MHz) of methyl oleate after 7 h reaction.

A.6. ^{1}H NMR (CDCl$_3$, 400 MHz) of dimethyl sebacate after 7 h reaction.

149

A.7. ^{1}H NMR (CDCl$_3$, 400 MHz) of methyl adipate after 7 h reaction.

A.8. ^{13}C NMR (CDCl$_3$, 100 MHz) of methyl laurate after 7 h reaction.

150

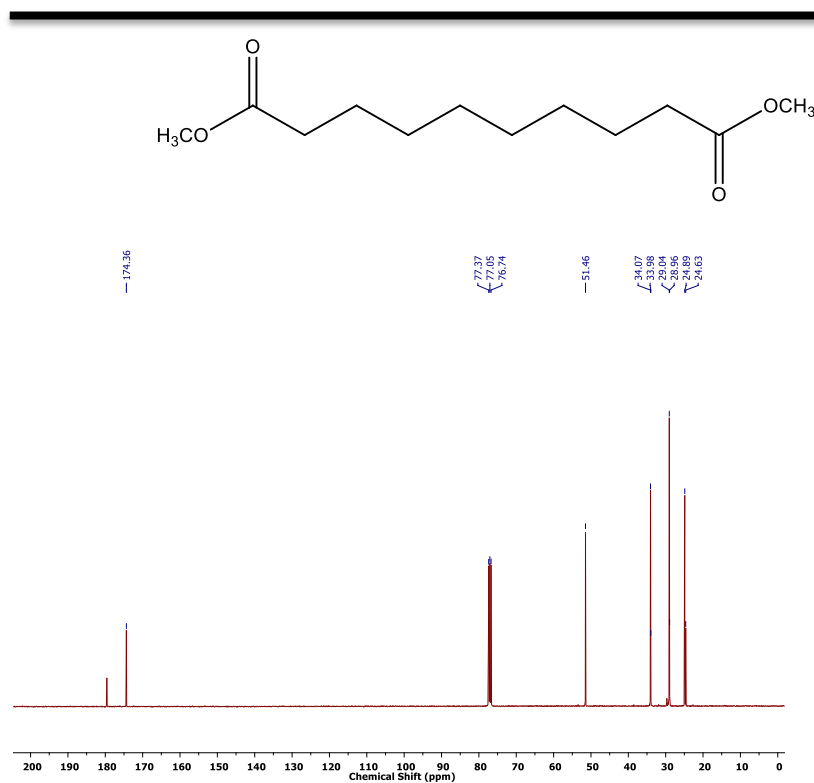A.9. ^{13}C NMR (CDCl$_3$, 100 MHz) of methyl myristate after 7 h reaction.
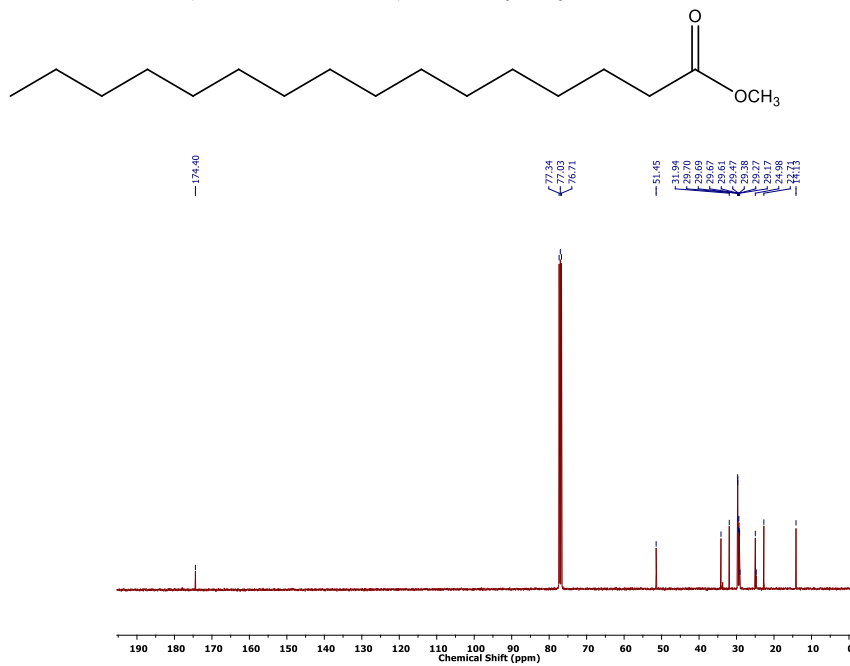
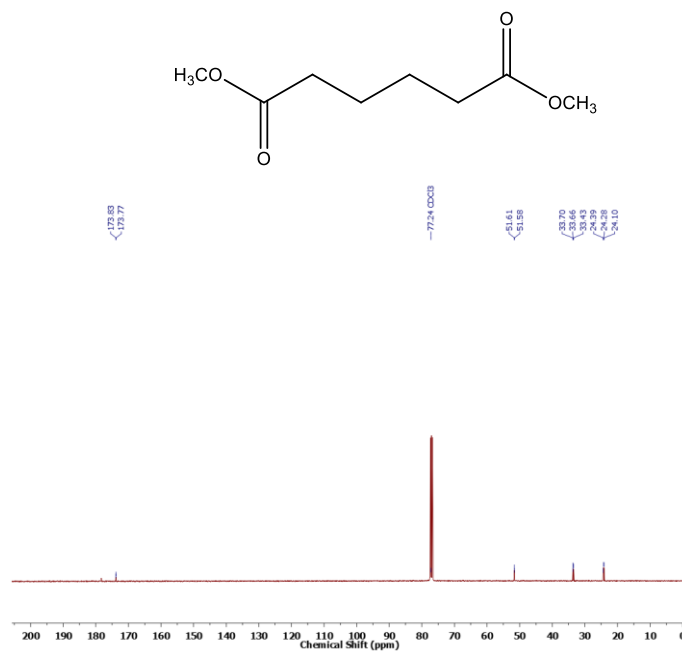A.10. ^{13}C NMR (CDCl$_3$, 100 MHz) of methyl palmitate after 7 h reaction.

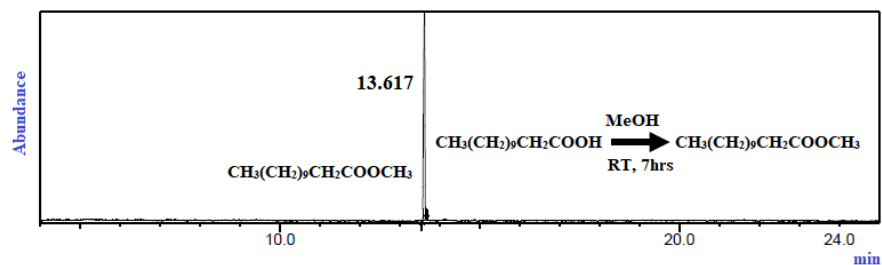A.11. ^{13}C NMR (CDCl$_3$, 100 MHz) of methyl stearate after 7 h reaction.

A.12. ^{13}C NMR (CDCl$_3$, 100 MHz) of methyl oleate after 7 h reaction.

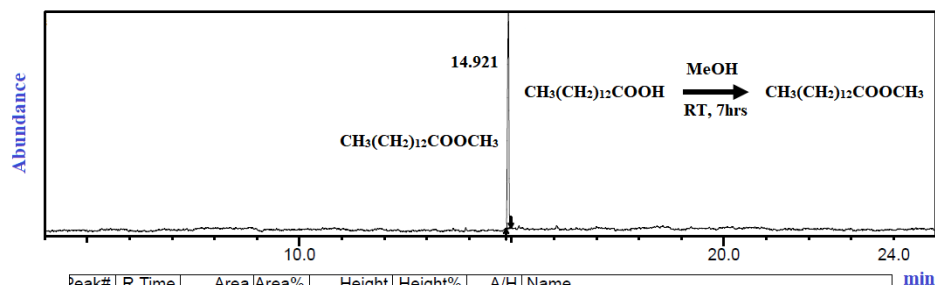A.13. ^{13}C NMR (CDCl$_3$, 100 MHz) of dimethyl sebacate after 7 h reaction.

A.14. ^{13}C NMR (CDCl$_3$, 100 MHz) of methyl adipate after 7 h reaction.

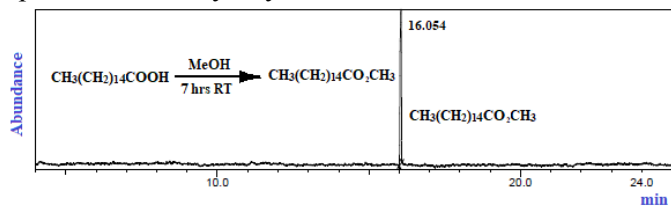| Peak#	R.Time	Area	Area%	Height	Height%	A/H	Name
1	13.617	2394389	100.00	1055627	100.00	2.27	Dodecanoic acid, methyl ester
		2394389	100.00	1055627	100.00		

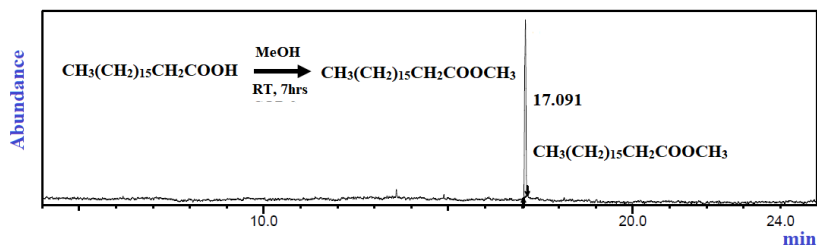A.15. GC spectrum of methyl laurate after 7 h reaction with **COP-2** as catalyst.

Peak#	R.Time	Area	Area%	Height	Height%	A/H	Name
1	14.921	1147866	100.00	502372	100.00	2.28	Methyl myristate
		1147866	100.00	502372	100.00		

A.16. GC spectrum of methyl myristate after 7 h with **COP-2** as catalyst.

Peak#	R.Time	Area	Area%	Height	Height%	A/H	Name
1	16.054	917899	100.00	324840	100.00	2.83	Hexadecanoic acid, methyl este
		917899	100.00	324840	100.00		

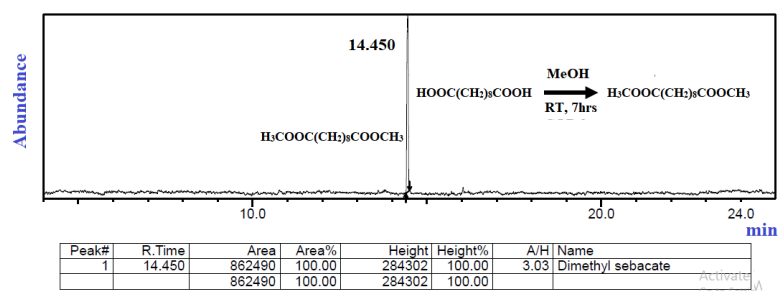A.17. GC spectrum of methyl palmate after 7 h reaction with **COP-2** as catalyst.

Peak#	R.Time	Area	Area%	Height	Height%	A/H	Name
1	17.091	746935	100.00	313911	100.00	2.38	Methyl stearate
		746935	100.00	313911	100.00		

A.18. GC spectrum of methyl stearate after 7 h reaction with **COP-2** as catalyst.
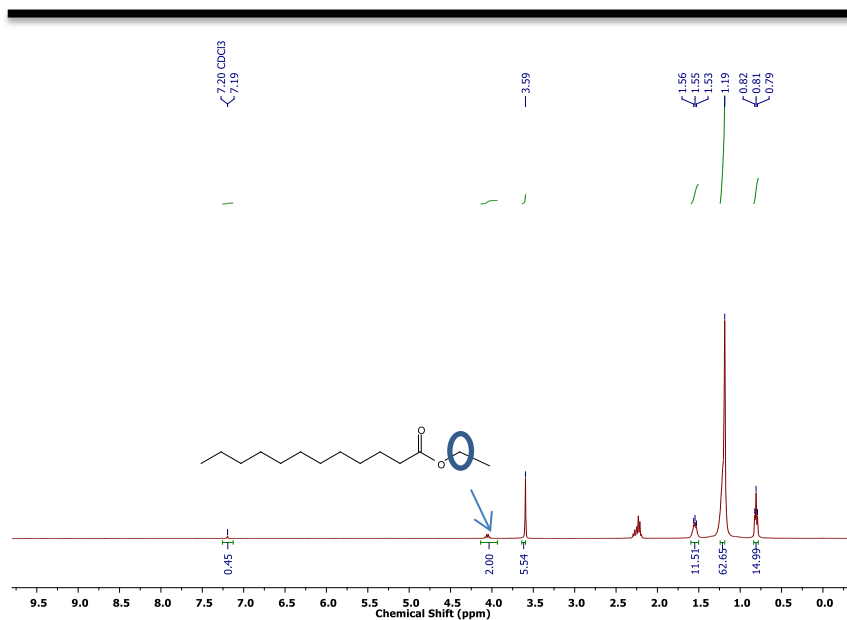
154

Peak#	R.Time	Area	Area%	Height	Height%	A/H	Name
1	17.002	1278218	100.00	356987	100.00	3.58	methyl oleate
		1278218	100.00	356987	100.00		
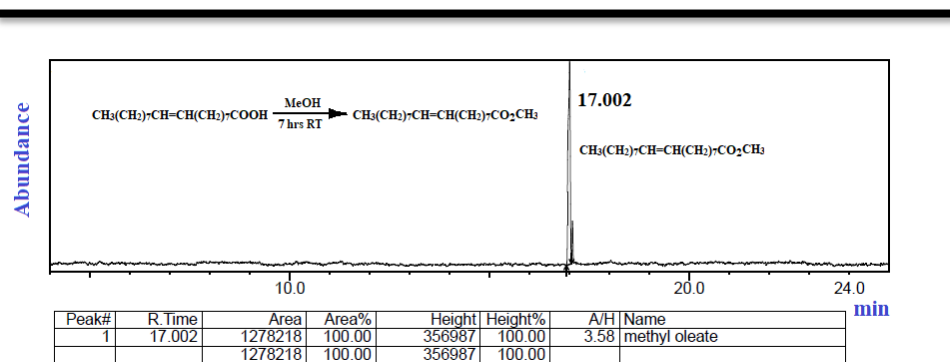
A.19. GC spectrum of methyl oleate after 7 h reaction with **COP-2** as catalyst.

Peak#	R.Time	Area	Area%	Height	Height%	A/H	Name
1	14.450	862490	100.00	284302	100.00	3.03	Dimethyl sebacate
		862490	100.00	284302	100.00		

A.20. GC spectrum of methyl sebacate after 7 h reaction with **COP-2** as catalyst.

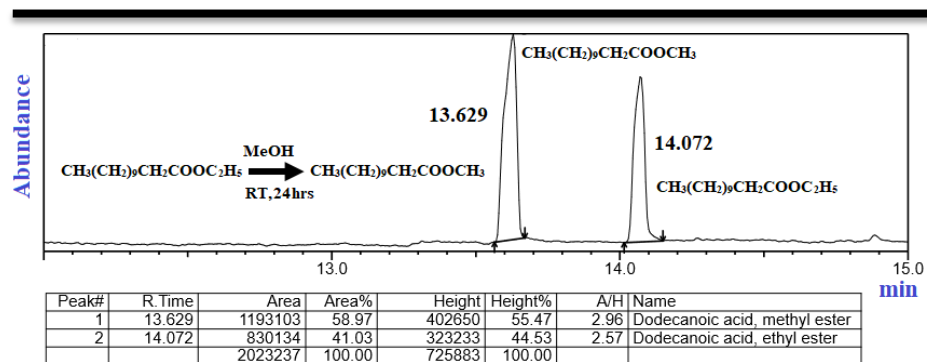| Peak#	R.Time	Area	Area%	Height	Height%	A/H	Name
1	11.509	379910	100.00	230429	100.00	1.65	Hexanedioic acid, dimethyl este
		379910	100.00	230429	100.00		
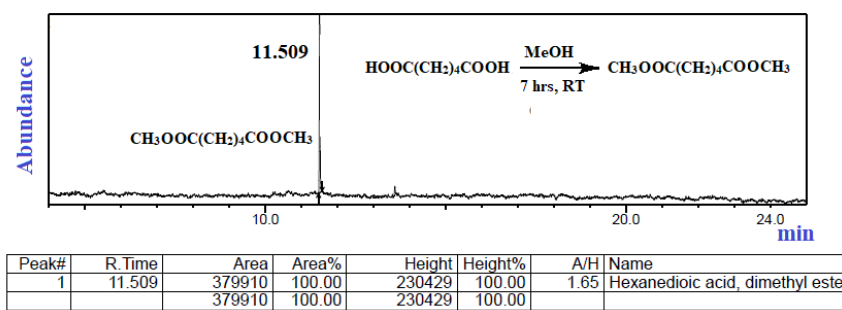
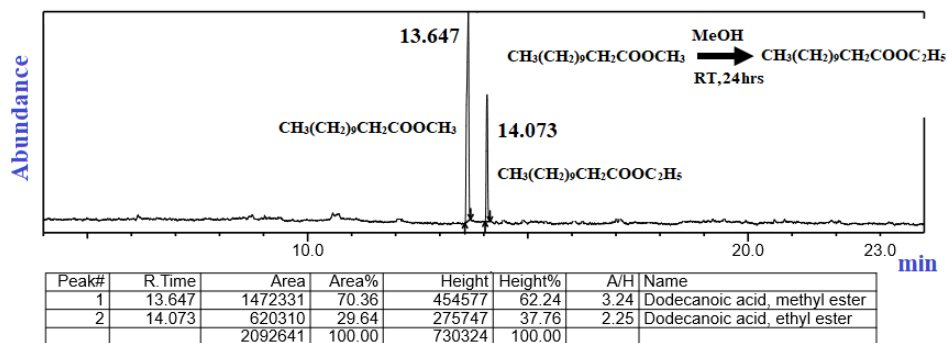A.21. GC spectrum of methyl adipate after 7 h reaction with **COP-2** as catalyst.

A.22. ¹H NMR (CDCl₃, 400 MHz) spectrum of ethyl laurate after transesterification from methyl laurate after 24 h.
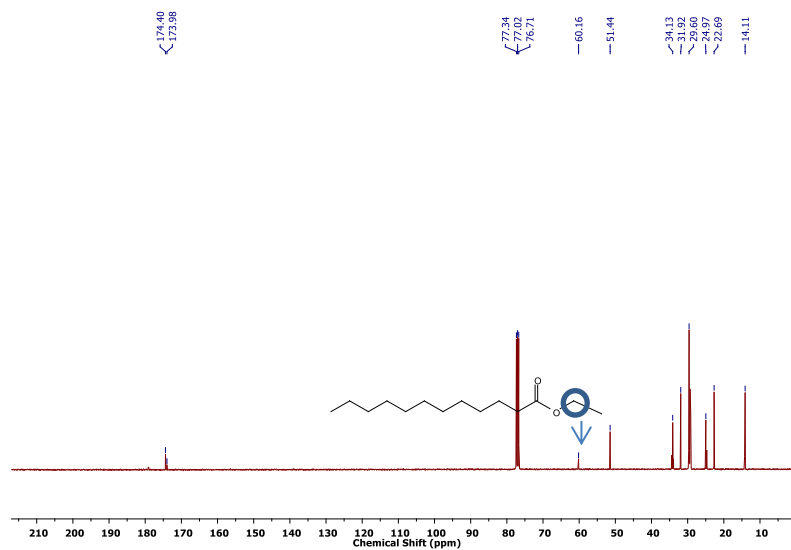
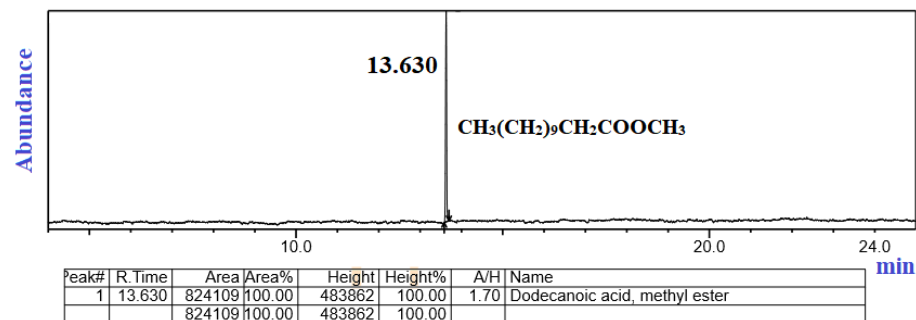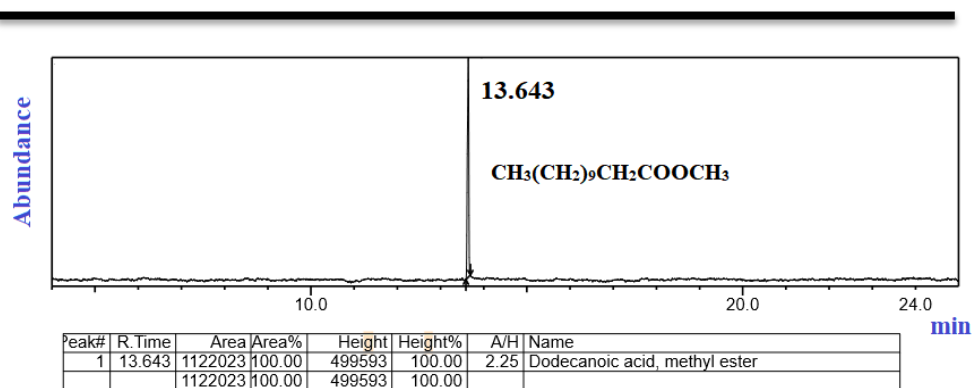A.23. ¹³C NMR (CDCl₃, 100 MHz) spectrum of ethyl laurate after transesterification from methyl laurate after 24 h.

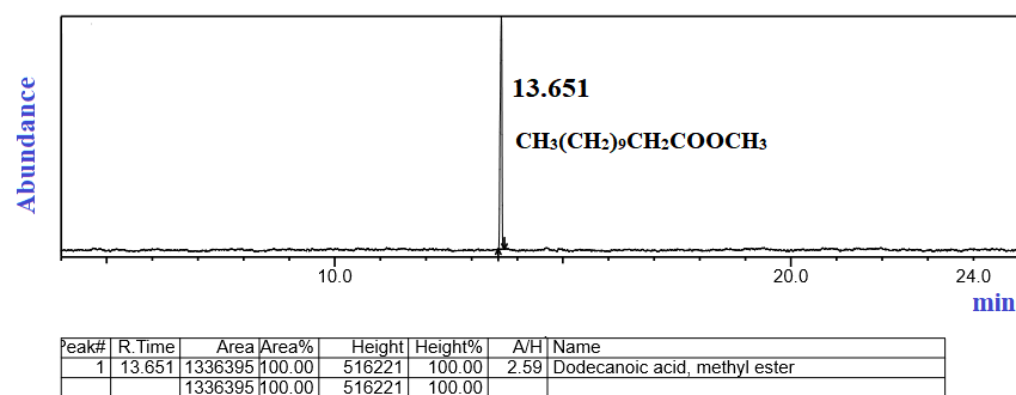| Peak#	R.Time	Area	Area%	Height	Height%	A/H	Name
1	13.629	1193103	58.97	402650	55.47	2.96	Dodecanoic acid, methyl ester
2	14.072	830134	41.03	323233	44.53	2.57	Dodecanoic acid, ethyl ester
		2023237	100.00	725883	100.00		

A.24. GC spectrum of transesterification from ethyl laurate to methyl laurate after 24 h with **COP-2** as catalyst.

Peak#	R.Time	Area	Area%	Height	Height%	A/H	Name
1	13.647	1472331	70.36	454577	62.24	3.24	Dodecanoic acid, methyl ester
2	14.073	620310	29.64	275747	37.76	2.25	Dodecanoic acid, ethyl ester
		2092641	100.00	730324	100.00		

A.25. GC spectrum of the transesterification from methyl laurate to ethyl laurate after 24 h with **COP-2** as catalyst.
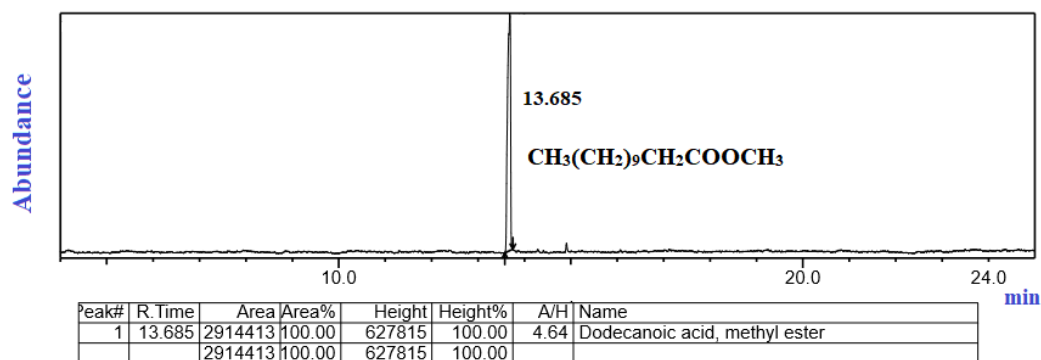

Peak#	R.Time	Area	Area%	Height	Height%	A/H	Name
1	13.630	824109	100.00	483862	100.00	1.70	Dodecanoic acid, methyl ester
		824109	100.00	483862	100.00		

A.26. GC spectrum of the methyl laurate by using 0.5 wt% catalyst **COP-2** after 7 h.

13.643

$CH_3(CH_2)_9CH_2COOCH_3$

Peak#	R.Time	Area	Area%	Height	Height%	A/H	Name
1	13.643	1122023	100.00	499593	100.00	2.25	Dodecanoic acid, methyl ester
		1122023	100.00	499593	100.00		

A.27. GC spectrum of the methyl laurate by using 1 wt% catalyst **COP-2** after 7 h.

13.651

$CH_3(CH_2)_9CH_2COOCH_3$

Peak#	R.Time	Area	Area%	Height	Height%	A/H	Name
1	13.651	1336395	100.00	516221	100.00	2.59	Dodecanoic acid, methyl ester
		1336395	100.00	516221	100.00		

A.28. GC spectrum of the methyl laurate by using 2 wt% catalyst **COP-2** after 7 h.

13.685

$CH_3(CH_2)_9CH_2COOCH_3$

Peak#	R.Time	Area	Area%	Height	Height%	A/H	Name
1	13.685	2914413	100.00	627815	100.00	4.64	Dodecanoic acid, methyl ester
		2914413	100.00	627815	100.00		

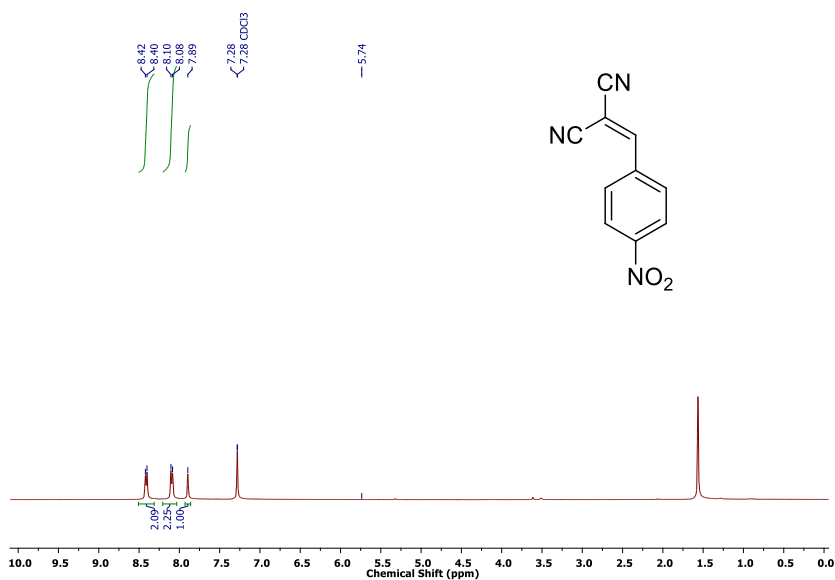A.29. GC spectrum of the methyl laurate by using 3 wt% catalyst **COP-2** after 7 h.
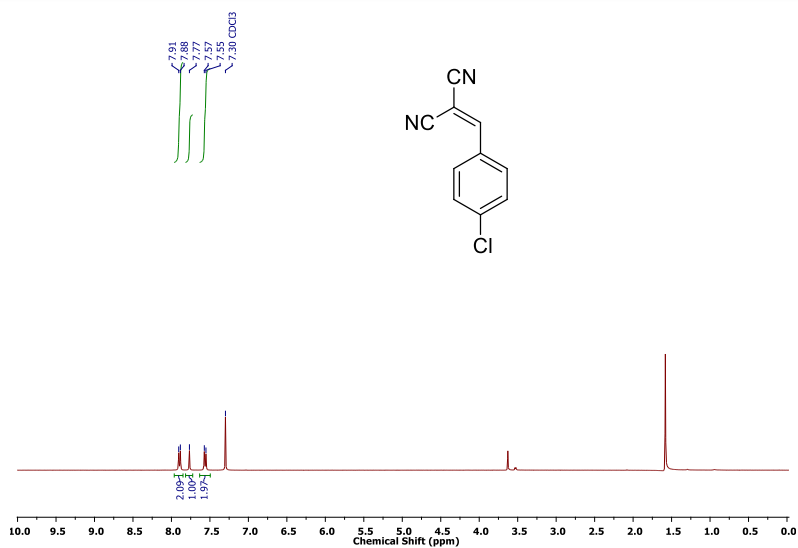
Appendix B.
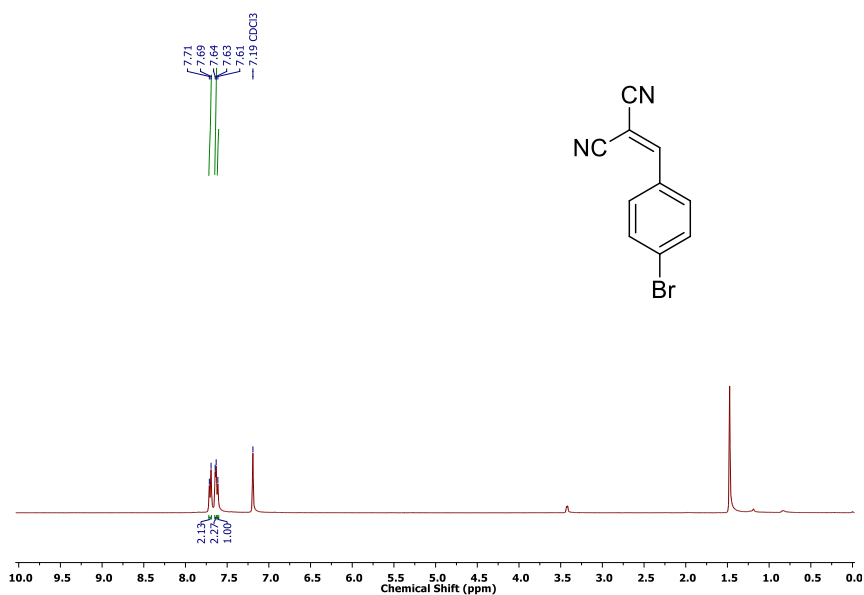**All NMR, GC-MS data of catalytic reactions by the COP-3**
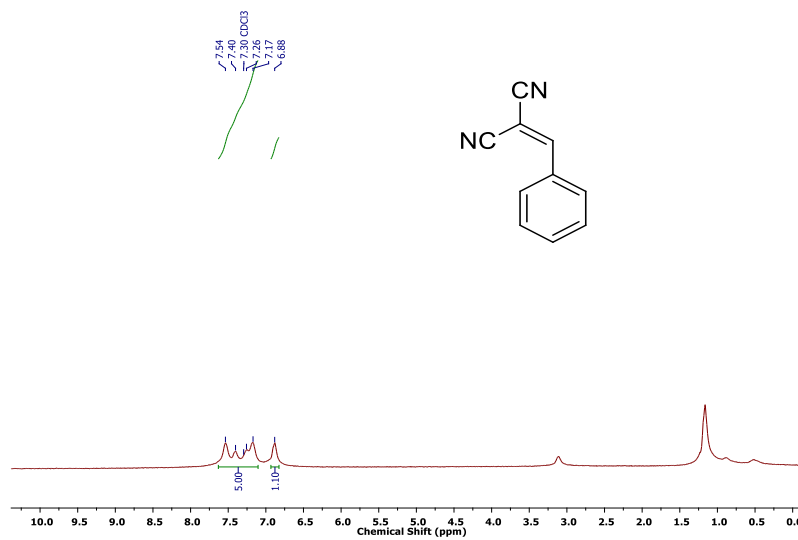
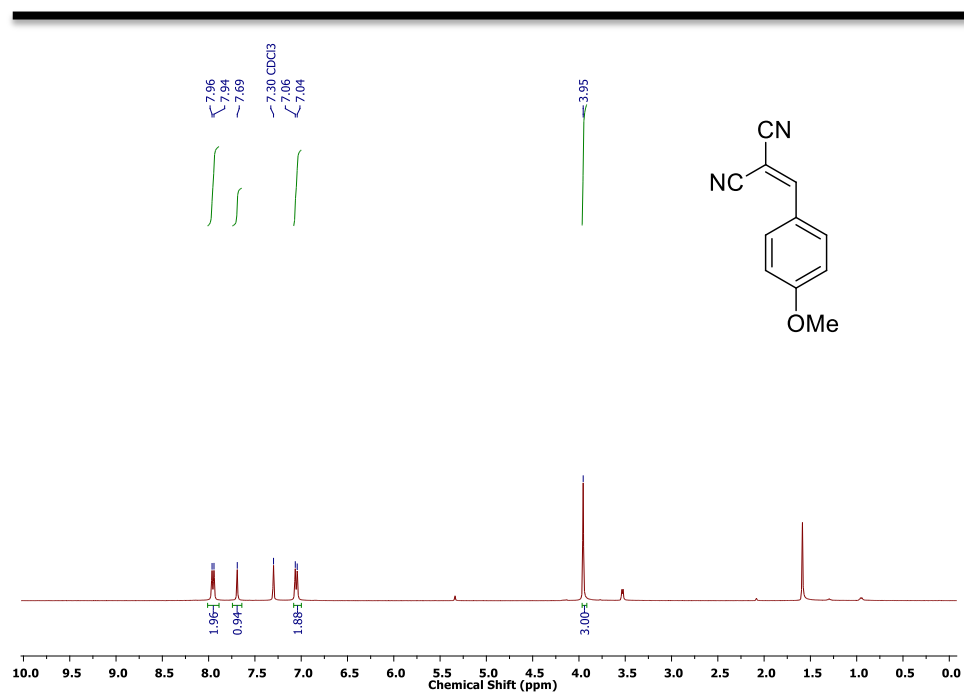B.1. ^{1}H NMR (CDCl$_3$, 400 MHz) spectrum of 2 benzylidenemalononitrile (**1A**).

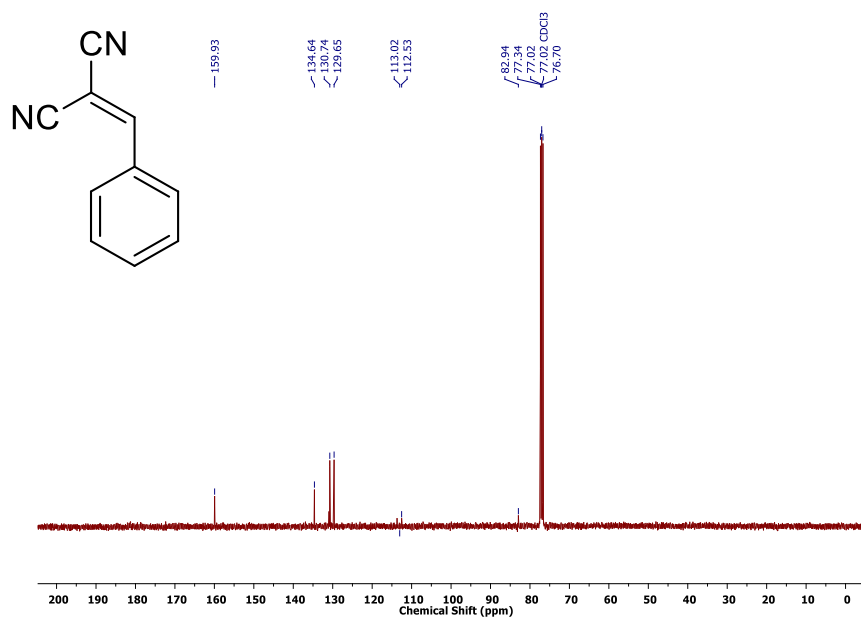B.2. ^{1}H NMR (CDCl$_3$, 400 MHz) spectrum of 2-(4-nitrobenzylidene)malononitrile (**2A**).

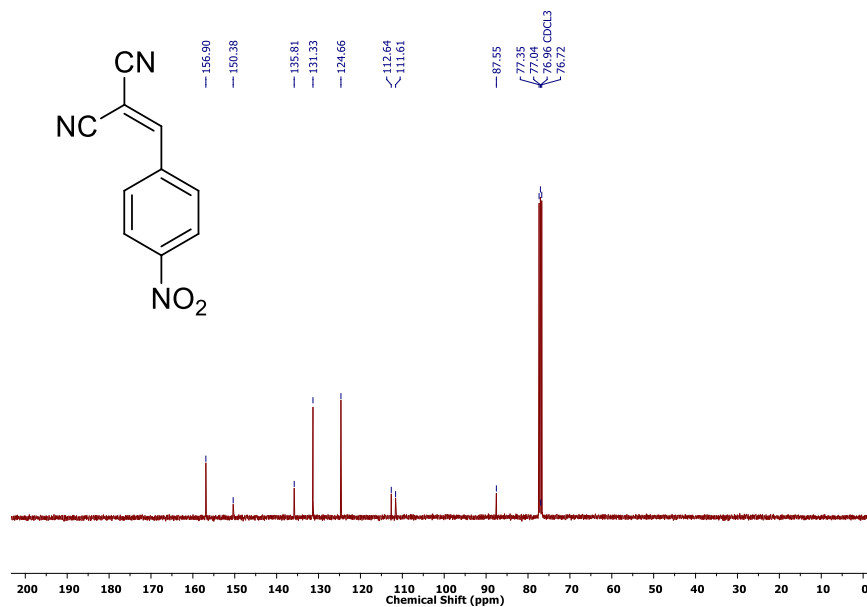B.3. ¹H NMR (CDCl₃, 400 MHz) spectrum of 2-(4-chlorobenzylidene)malononitrile (**3A**).

B.4. ¹H NMR (CDCl₃, 400 MHz) spectrum of 2-(4-bromobenzylidene)malononitrile (**4A**).
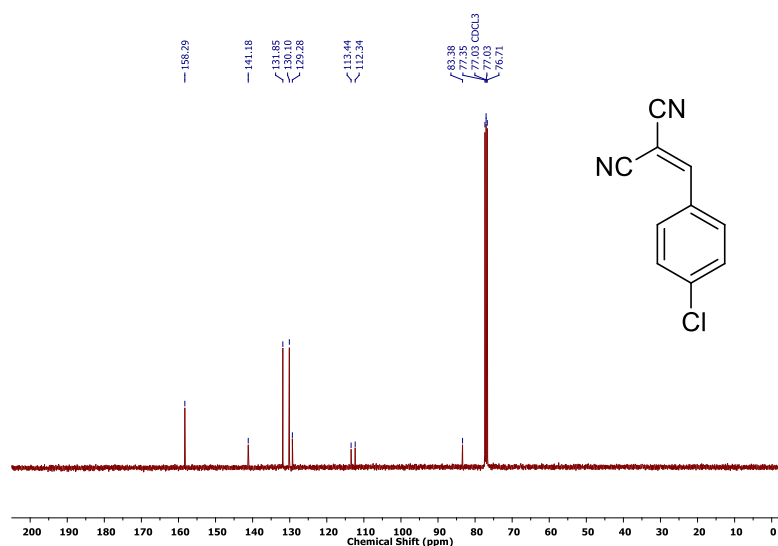
B.5. ¹H NMR (CDCl₃, 400 MHz) spectrum of 2-(4-methoxybenzylidene)malononitrile (**5A**).

B.6. ¹³C NMR (CDCl₃, 400 MHz) spectrum of 2-benzylidenemalononitrile (**1A**).

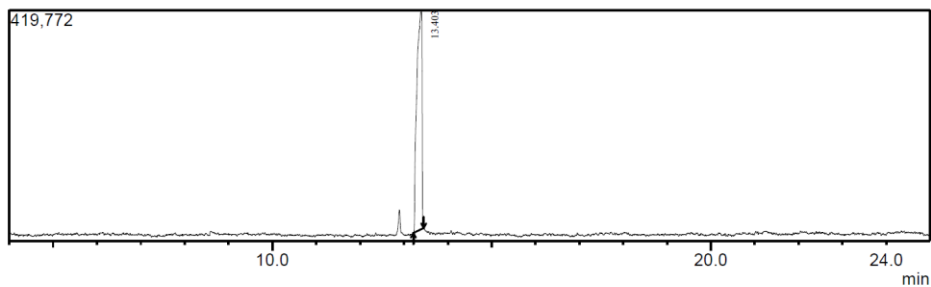B.7. ^{13}C   NMR   (CDCl$_3$,   400   MHz)   spectrum   of   2-(4 nitrobenzylidene)malononitrile (**2A**).

B.8. ^{13}C   NMR   (CDCl$_3$,   400   MHz)   spectrum   of   2-(4-chlorobenzylidene)malononitrile (**3A**).

B.9. ^{13}C NMR (CDCl$_3$, 400 MHz) spectrum of 2-(4-bromolbenzylidene)malononitrile (**4A**).

B.10. ^{13}C NMR (CDCl$_3$, 400 MHz) spectrum of 2-(4-methoxybenzylidene)malononitrile (**5A**).
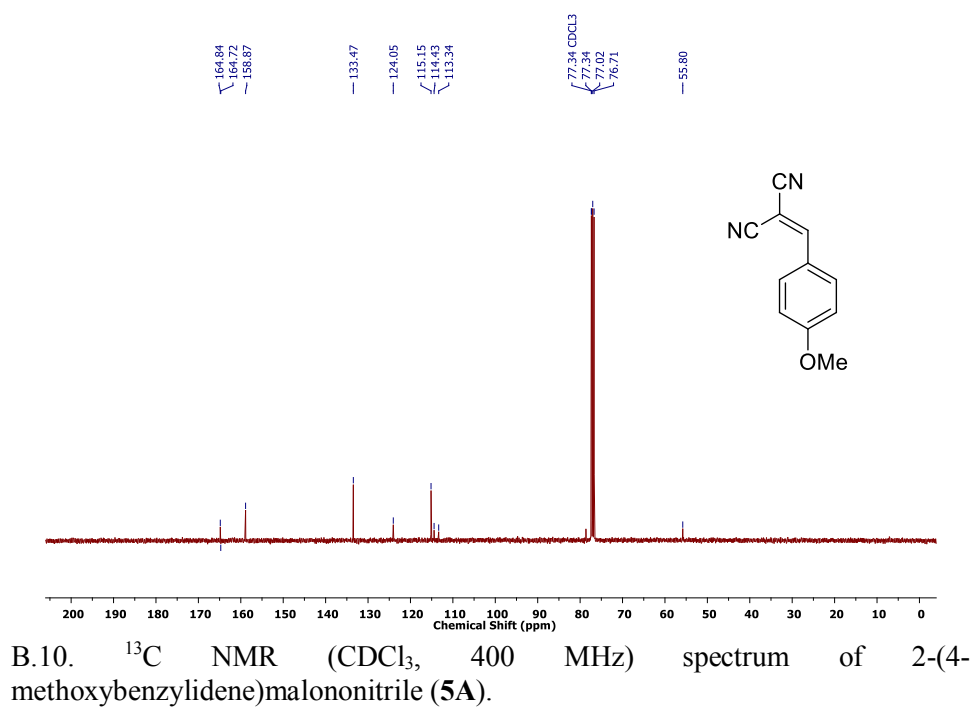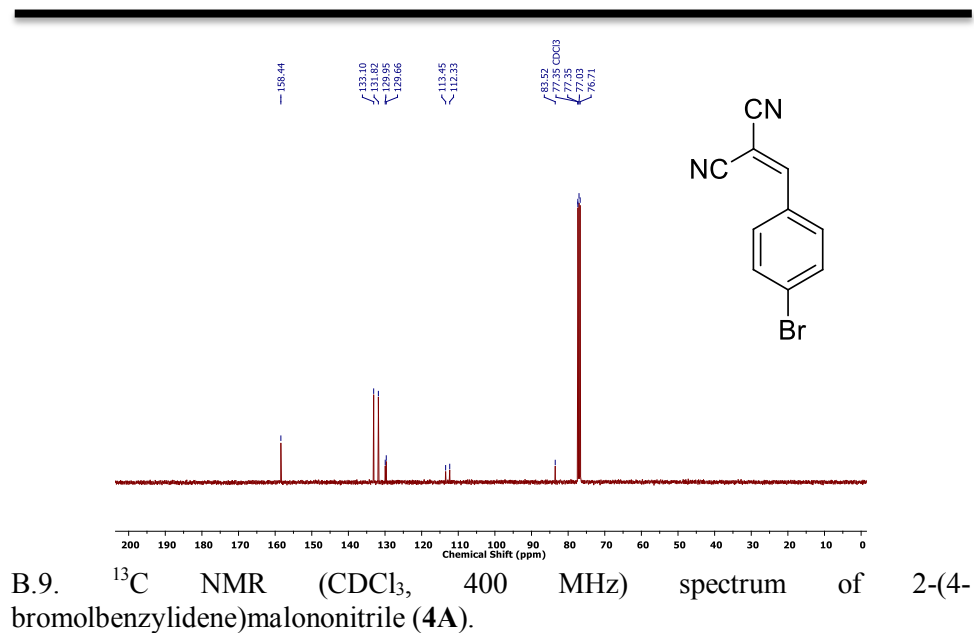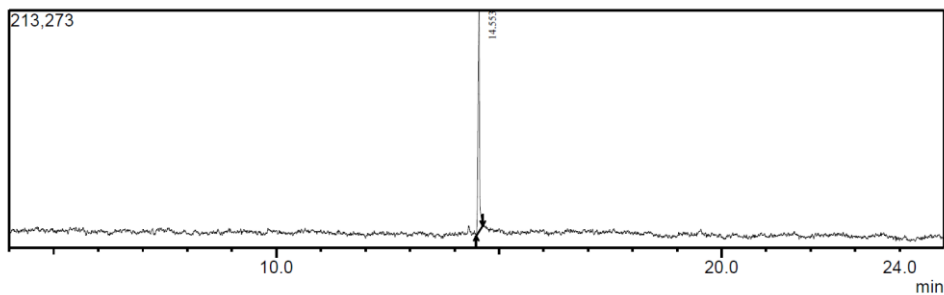
Peak#	R.Time	Area	Area%	Height	Height%	A/H	Name
1	13.403	3205313	100.00	397528	100.00	8.06	Propanedinitrile, (phenylmethylene)-
		3205313	100.00	397528	100.00		

B.11. GC spectrum of 2-benzylidenemalononitrile (**1A**).
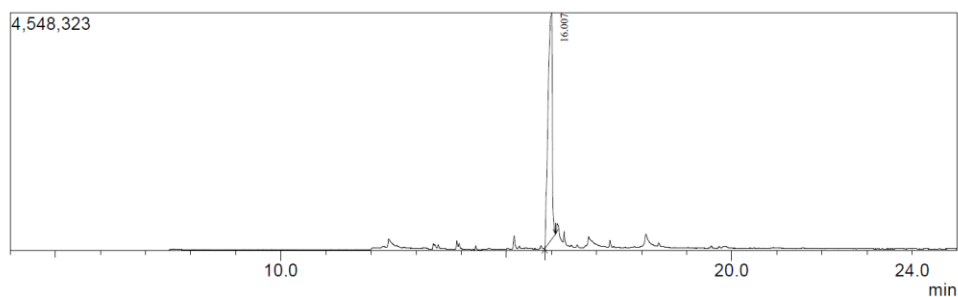
Peak#	R.Time	Area	Area%	Height	Height%	A/H	Name
1	16.007	28581185	100.00	4323328	100.00	6.61	Nitrobenzene, 4-(2,2-dicyanoethenyl)
		28581185	100.00	4323328	100.00		

B.12. GC spectrum of 2-(4-nitrobenzylidene)malononitrile (**2A**).

Peak#	R.Time	Area	Area%	Height	Height%	A/H	Name
1	14.553	521711	100.00	198595	100.00	2.63	Benzene, 1-chloro-4-(2,2-dicyanoethenyl)
		521711	100.00	198595	100.00		

B.13. GC spectrum of 2-(4-chlorobenzylidene)malononitrile (**3A**).

4,150,855

| | | | | | | | | 15.168 | | | | | |

| | | | 10.0 | | | | 20.0 | 24.0 |
| | | | | | | | | min |
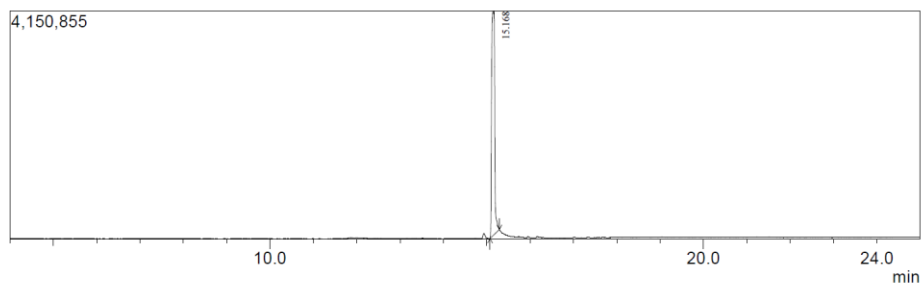
Peak Report TIC

Peak#	R.Time	Area	Area%	Height	Height%	A/H	Name
1	15.168	9731676	100.00	4061147	100.00	4.86	Benzene, 1-bromo-4-(2,2-dicyanoethenyl)
		9731676	100.00	4061147	100.00		

B.14. GC spectrum of 2-(4-bromobenzylidene)malononitrile (**4A**).

TIC

357,074

| | | | 10.0 | | | 20.0 | 24.0 |
| | | | | | | | min |
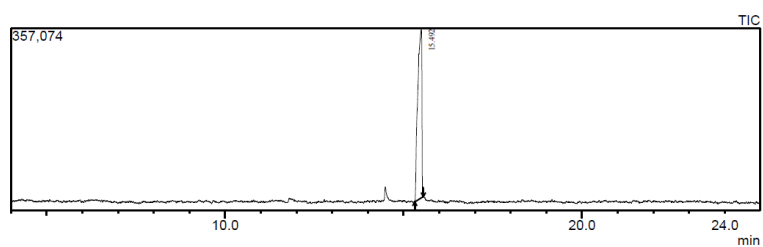
Peak Report TIC

Peak#	R.Time	Area	Area%	Height	Height%	A/H	Name
1	15.492	2611288	100.00	332315	100.00	7.86	Benzene, 1-methoxy-4-(2,2-dicyanoethenyl)

B.15. GC spectrum of 2-(4-methoxybenzylidene)malononitrile (**5A**).